Investigation of the Wind Load on Heliostats in Stow Position

Matthew John Emes

School of Mechanical Engineering

The University of Adelaide

South Australia, 5005

A thesis submitted in fulfilment of the requirements for the Degree of Doctor of Philosophy

November 2017

Abstract

In recent years there has been an increasing effort to lower the capital costs of concentrating solar thermal (CST) power tower (PT) plants to make their levelised cost of electricity (LCOE) more competitive with base-load energy systems. The field of heliostats contributes the most to the capital cost of a PT plant, hence the costs of manufacturing and installation of heliostat components can be reduced by optimising their structural design to withstand the maximum wind loads during high-wind conditions in the stow position. Heliostats are moved from operational positions and aligned parallel to the ground in the stow position during periods of high wind speeds to minimise the effect of fluctuating pressures and unsteady forces that can lead to structural failure. While the effects of temporal variation of turbulence on heliostat design wind loads have been investigated for operational positions, further knowledge of the spatial distribution of turbulence in the frequency domain of the atmospheric boundary layer (ABL) and the dynamic wind loads in stow position needs to be developed. The purpose of this thesis is to develop an understanding of the turbulence effects in the ABL that can lead to maximum wind loads during gusty high-wind conditions. This is achieved by studying the dynamic effects of the wind arising from turbulence characteristics in the lowest 10 m of the ABL and their influence on the peak wind loads on stowed heliostats. With this knowledge, reduction of the design wind loads in the stow position can allow the optimisation of the size and cost of heliostats with respect to the turbulent flow approaching them.

One of the principal factors in the design criteria for a heliostat field is the design wind speed at which the heliostats are moved from operating positions to the stow position. The sensitivity of both the capital cost of heliostats and the LCOE of a PT plant was investigated by developing a statistical model assuming quasi-steady wind loads and simplified cost-area proportionality exponents. A parametric study using wind speed and solar irradiation data showed that a significant reduction in the design wind speed at windy sites can be achieved with only a small reduction in the capacity factor, thus offering potential to reduce the cost of heliostats and the LCOE of a PT plant. Optimal heliostat sizes were found to decrease significantly with increasing stow design wind speed, such as from 50 m^2 to 25 m^2 when the design wind speed increases from 10 m/s to 20 m/s. Velocity measurements in the lowest 25 m of a low-roughness atmospheric surface layer (ASL) were analysed to further understand the relationships between turbulence characteristics and their effect on the velocity gust factor that is widely used in design wind codes to estimate the peak wind loads on physical structures. It was found that the peak wind speeds associated with low-frequency gusts were under-predicted by 5% at heights below 10 m in desert terrain. Hence, simplified gust factor methods and semi-empirical turbulence models can under-estimate the peak wind loads, which are proportional to the square of peak wind speed, by 10% at heights below 10 m in low-roughness terrains where heliostat fields are located.

Subsequently, an experimental investigation was carried out to identify the effects of turbulence characteristics in the lower ABL on the peak wind loads on stowed heliostats. The temporal and spatial turbulence characteristics were characterised over a wide range of turbulence intensities and integral length scales (L_u^x) in a simulated part-depth ABL using two geometries of spires and roughness elements. A range of square heliostat mirror chord lengths (c) was used to investigate the effect of the length-scale-to-chord-length ratio (L_u^x/c) on the peak wind loads on an isolated heliostat in stow position and on a second downstream heliostat in a tandem configuration. It was found that both the peak lift coefficient and the peak hinge moment coefficient on the isolated heliostat increased linearly as L_u^x/c increased from 2.5 to 10 and at longitudinal turbulence intensities greater than 10%. In contrast, the peak lift forces and hinge moments on a second downstream heliostat were up to 30% lower than those on an isolated heliostat at L_u^x/c of 10. Peak energies of measured pressure spectra were an order of magnitude smaller on the downstream heliostat than the isolated heliostat and showed a shift to higher frequencies corresponding to smaller vortices. Peak wind loads on the downstream heliostat were observed to increase to 10% above those on an isolated heliostat as the spacing between the heliostat mirrors in tandem, defined by the gap ratio d/c, was lowered below 1. In contrast, peak wind loads on a downstream heliostat were up to 30% lower than an isolated heliostat at d/c of approximately 2 at intermediate field densities. When stowing the heliostat mirror at a range of elevation heights, it was found that both peak lift forces and hinge moments can be minimised at an elevation axis height equal to or less than half of the mirror chord length. Hence, optimisation of the mirror chord length and the elevation axis height of the stowed heliostat for the approaching turbulence can significantly reduce design wind loads for high-wind events in the atmospheric surface layer and the cost of manufacturing the heliostat components.

The results of the research in the current thesis can be used to optimise the spacing between stowed heliostats at different field densities and the critical scaling parameters of the heliostat, based on known characteristics of the approaching turbulence in a given ABL. Peak wind loads on isolated heliostats in stow position are likely to be over-designed for in-field heliostats positioned in low-density regions of a field, thus offering the potential to manufacture in-field heliostats from lower strength, lighter and cheaper materials. Consequently, uniform designs for heliostats in the first two rows of a field need to consider the critical wind load that leads to failure modes to determine the pylon length and mirror chord length of the heliostat.

Declaration

I, Matthew John Emes, certify that this work contains no material which has been accepted for the award of any other degree or diploma in my name, in any university or other tertiary institution and, to the best of my knowledge and belief, contains no material previously published or written by another person, except where due reference has been made in the text. In addition, I certify that no part of this work will, in the future, be used in a submission in my name, for any other degree or diploma in any university or other tertiary institution without the prior approval of the University of Adelaide and where applicable, any partner institution responsible for the joint-award of this degree.

I give consent to this copy of my thesis, when deposited in the University Library, being made available for loan and photocopying, subject to the provisions of the Copyright Act 1968. The author acknowledges that copyright of published works contained within this thesis resides with the copyright holder(s) of those works.

I also give permission for the digital version of my thesis to be made available on the web, via the University's digital research repository, the Library Search and also through web search engines, unless permission has been granted by the University to restrict access for a period of time.

Signed: __________

Matthew John Emes

Date: 3/11/17

Acknowledgements

I would first like to thank my principal supervisor A/Prof Maziar Arjomandi for his unwavering support and guidance from the first day of my postgraduate study. I am also very grateful for the input and support of my co-supervisors: Prof Gus Nathan, A/Prof Richard Kelso and Dr Farzin Ghanadi. The completion of this thesis would not have been possible without you.

I would like to acknowledge the ongoing support provided by the technical staff of the School of Mechanical Engineering. Garry Clarke for helping me with my experimental rig designs and the Mechanical Workshop technicians, particularly Stephen Kloeden, for manufacturing them. Phil Schmidt and Derek Franklin for sourcing and fabricating my electronics for instrumentation in the wind tunnel. Norio Itsumi for his assistance with controlling servomotors and Lydia Zhang for repairing many hot-wire probes. I would also like to thank Marc Simpson for his assistance when carrying out experimental testing at the Thebarton wind tunnel and Billy Constantine for maintaining my office and lab computers and helping me find software I needed for my experimental instruments.

To my colleagues, thank you for taking the time to show me how to use equipment, provide feedback on presentation slides and my writing, share and discuss research ideas and for organising much needed study breaks to go bowling and go-karting. To my friends and family, thank you for your love and emotional support throughout this period in my life. Especially to my best friends, your positivity and encouragement in the most difficult times helped get me through and I will never forget that.

Finally, I would like to acknowledge the financial support I have received for my research through the provision of an Australian Government Research Training Program Scholarship. In addition, I am grateful for the top-up scholarship provided by the Australian Solar Thermal Research Initiative (ASTRI) through the Australian Renewable Energy Agency (ARENA).

Nomenclature

Acronyms

ABL	Atmospheric boundary layer
ASL	Atmospheric surface layer
ARENA	Australian Renewable Energy Agency
ASTRI	Australian Solar Thermal Research Initiative
CST	Concentrating solar thermal
DOE	Department of Energy
DLR	German Aerospace Center
DNW	German-Dutch wind tunnel
ESDU	Engineering Sciences Data Unit
GBA	Generalised blockage area
HFI	Herman-Föttinger Institut
IEA	International Energy Agency
IRENA	International Renewable Energy Agency
LCOE	Levelised cost of electricity
MAV	Micro-air-vehicle
NSTTF	National Solar Thermal Test Facility
PDF	Probability density function
PSD	Power spectral density
PT	Power tower
RMS	Root-mean-square
VIV	Vortex-induced vibration

Symbols

A	Surface area of heliostat mirror (m^2)
α	Elevation angle of heliostat mirror (°)
β	Azimuth/wind angle or angle of attack (°)
B	Depth of building in the flow direction (m)
b	Width of building or span of roof (m)
C_f	Friction coefficient
c	Chord length of heliostat mirror (m)
c_D	Drag coefficient
c_L	Lift coefficient
c_{M_y}	Overturning moment coefficient
$c_{M_{Hy}}$	Hinge moment coefficient
D	Drag force (N)
d	Separation distance between tandem heliostats (m)
d/c	Gap ratio for tandem heliostats
δ	Atmospheric boundary layer thickness (m)
δ_s	Atmospheric surface layer thickness (m)
θ	Momentum thickness (m)
η	Kolmogorov length scale (m)
f	Non-dimensional frequency $f = nz/\overline{U}$
G_u	Gust factor
g_u	Peak factor
H	Elevation axis height of heliostat mirror (m)
h	Height of building (m)

I_u	Streamwise turbulence intensity (%)
k	von Karman's constant
κ	Surface friction coefficient
K	Kurtosis
L	Lift force (N)
L_u^x	Longitudinal integral length scale (m)
l_p	Distance to the centre of pressure in the flow direction (m)
M_y	Overturning moment (N·m)
M_{Hy}	Hinge moment (N·m)
n	Frequency of velocity/pressure fluctuations (Hz)
ν	Kinematic viscosity of air (m^2/s)
ρ	Density of air (kg/m^3)
p	Fluctuating component of pressure (Pa)
σ_u	Standard deviation of streamwise velocity (m/s)
Re	Reynolds number
R_u	Autocorrelation function of streamwise velocity
S	Skewness
S_p	Power spectral density of pressure fluctuations (Pa^2/Hz)
S_u	Power spectral density of streamwise velocity fluctuations (m^2/s^3)
τ	Time delay (ms)
T	Sampling period (s)
t	Gust period (s)
T_u^x	Longitudinal integral time scale (s)
U	Wind velocity (m/s)

U_∞	Freestream/gradient velocity (m/s)
U_τ	Friction velocity (m/s)
u	Fluctuating component of streamwise/longitudinal velocity (m/s)
v	Fluctuating component of spanwise/lateral velocity (m/s)
w	Fluctuating component of vertical/wall-normal velocity (m/s)
x	Streamwise distance (m)
y	Spanwise distance (m)
z	Height above the ground (m)
z_0	Surface roughness height (m)

Superscripts

$-$	denotes mean value
^	denotes peak value
$+$	denotes viscous time scale and length scale

Table of Contents

Chapter 1

Introduction

1.1. Background and Motivation

Current energy systems, based primarily on the combustion of fossil fuels, are unsustainable in the long term, so that a transition to an environmentally-sustainable energy system with the integration of renewable energy sources is necessary (Hernández-Moro and Martínez-Duart, 2012). Concentrating solar thermal (CST) is one of the most promising renewable technologies capable of large scale electricity production (Hinkley et al., 2013). A CST system operates by focusing direct solar radiation to obtain higher energy densities and thus an improved Carnot efficiency at higher temperatures. Heat collected in the receiver is typically used to heat a working fluid to generate supercritical steam that drives a turbine for electricity generation (IRENA, 2015); although a wide range of alternative power cycles is under development including Brayton and CO_2 power cycles. Parabolic trough systems are the most commercially-deployed CST technology, however power tower (PT) systems have been identified as an emerging concept that can operate at higher concentration ratios and higher working fluid temperatures than parabolic troughs, thus allowing for higher power cycle efficiency (IEA-ETSAP and IRENA, 2013). Although the intermittency of solar irradiation is a practical limitation of CST systems, PT plants can be deployed with thermal energy storage or as a hybrid system with existing fossil fuel power plants for a base-line power supply (Hinkley et al., 2013; Kolb et al., 2011).

PT systems consist of a field of heliostat mirrors reflecting sunlight to the top of a beam-up or beam-down tower containing a receiver. There are two types of heliostat field distributions, as illustrated in Figure 1.1. Heliostats are positioned on one side of an anti-polar facing cavity receiver in a polar field, as shown in Figure 1.1(a) for the PS10 plant in Andalusia, Spain. The PS10 plant contains 624 heliostats, each of 120 m^2 mirror area, with a design capacity of 11 MW and heliostat field optical efficiency of 64% (Noone et al., 2012). Polar fields have very good performance at midday but their performance declines rapidly at larger solar azimuths due to the increased incident angles of the heliostats. In contrast, the annual energy collected by a cylindrical receiver combined with a surround field, such as the 20 MW field in Almeria, Spain in Figure 1.1(b), is significantly higher because the east and west fields contribute strongly at large solar azimuths later in the day (Lovegrove and Stein, 2012). This is shown by a higher optical efficiency of 76% produced by the 884 heliostats, hence surround fields are favourable on a cost-per-unit-energy basis. Noone et al. (2012) found that the heliostat field optical efficiency was increased by 0.19% and the land area was reduced by 10.9% by positioning the heliostats in the PS10 plant closer together to provide higher cosine efficiencies at the expense of lower shading and blocking efficiencies. The diurnal and seasonal variation of solar irradiation varies depending on the solar elevation and azimuth angles that are dependent on the solar position in the terrestrial coordinate system (Lovegrove and Stein, 2012), hence the selection of the shape and distribution of the solar field depends on the location of the field site.

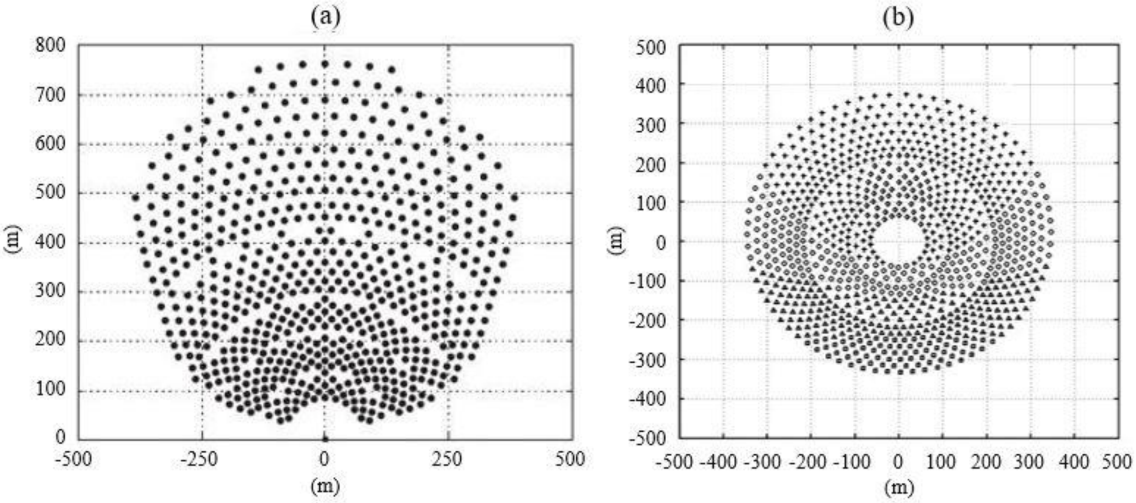

Figure 1.1. Heliostat field distributions of the:
(a) Polar field of an 11 MW plant in Andalusia, Spain. Reproduced from Noone et al. (2012);
(b) Surround field of a 20 MW plant in Almeria, Spain. Reproduced from Talebizadeh et al. (2013).

The main limitation of PT systems is their significantly larger levelised cost of electricity (LCOE), in the range of 0.15-0.19 USD/kWh in 2015 (IRENA, 2015), compared to base-load energy systems such as fossil fuel power plants in the range of 0.06-0.13 USD/kWh in 2011 (IRENA, 2013). Government-funded initiatives that support the research and development of CST systems to make them competitive with base-load energy rates include the SunShot Initiative by the Department of Energy (DOE) in the USA, with a goal LCOE of 0.06 USD/kWh by 2020 (Kolb et al., 2011), and the Australian Solar Thermal Research Initiative (ASTRI) targeting a LCOE of 0.12 AUD/kWh by 2020.

To reduce the LCOE of PT systems there is a need to lower the capital cost of a PT plant, Figure 1.2(a) shows the capital cost breakdown of a PT plant by Pitz-Paal et al. (2004), of which the largest cost is the heliostat field, with an estimated contribution of between 40% and 50% (Coventry and Pye, 2014; Hinkley et al., 2013; IRENA, 2015; Kolb et al., 2007). The baseline capital cost of heliostats was estimated to be \$200 per square metre of heliostat mirror area (\$/m^2) at a Sandia workshop (Kolb et al., 2011). Gary et al. (2011) showed that for a PT plant to achieve a LCOE of \$0.1/kWh, the total capital cost of heliostats must be no more than \$120/m^2 and be further reduced to \$75/m^2 to achieve the DOE target LCOE of \$0.06/kWh. Figure 1.2(b) presents the capital cost breakdown of the components of a heliostat, with mirror chord length c and elevation angle α relative to the horizontal, based on the 2011 Sandia estimates by Kolb et al. (2011) for 30 m^2 and 148 m^2 heliostats. These span a range because the contributions of the different components vary with heliostat size. For example, the relative cost of the pedestal, support structure and foundation increases with size because larger heliostats are subjected to greater wind loads (Kolb et al., 2011). In contrast, the costs of manufacturing, field wiring and controls become more significant for smaller heliostats, due to the increased number of heliostats in the field (Kolb et al., 2011).

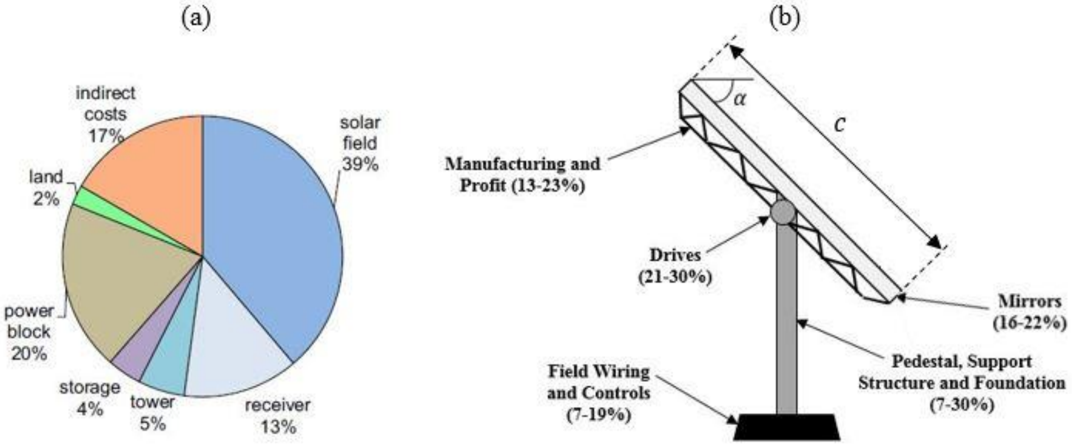

Figure 1.2. Capital cost breakdown of: (a) A power tower plant (Hinkley et al., 2013); (b) A heliostat of mirror chord length c and elevation angle α. Data extracted from Kolb et al. (2011).

Optimisation of the size and position of heliostat components is one opportunity to minimise the manufacturing and installation costs of the solar field in PT plants. Kolb et al. (2007)

estimated the effect of the heliostat mirror area A on the life-cycle costs for the manufacturing and installation of two different heliostat designs based on a large reference ATS heliostat ($A =$ 148 m^2) and a small reference HI heliostat (A = 30 m^2). Following the analysis by Jones of the baseline costs of manufacturing the two heliostat designs of square mirror area at a mass production rate of 50,000 heliostats per year and a total mirror area of 235,000 m^2 over the 30-year life cycle of a PT plant, Kolb et al. (2007) estimated the cost (in 2005 USD) of each heliostat component as a function of the wind loading. Proportionality exponents relating the material cost of each component to the mass of material required to withstand the maximum quasi-static wind loads were derived following the assumption that the material stiffness is constant for varying heliostat sizes. For example, the cost of the pedestal and torque tube were assumed to have a linear variation with wind load, whereas the mass and thus cost of these structural components increases with the heliostat mirror chord length to the power of three, or with the heliostat mirror area to the power of 1.5 (Blackmon, 2013; Lovegrove and Stein, 2012). This is because all of the dimensions of the heliostat need to be increased when the chord length of the mirror and thus mirror area are increased to avoid an increase in stress caused by the peak wind loads (Pfahl et al., 2017). Hence, larger heliostats are exposed to higher wind speeds with increasing height above the ground but fewer units are required for an equivalent mirror area, whereas smaller heliostats can have a lower weight per mirror area for high production rates.

The optimum size of the HI heliostat was 53 m^2, whereas the ATS heliostat had a minimum cost at 214 m^2, as shown in Figure 1.3. Kolb et al. (2007) concluded that the optimum heliostat size for a molten-salt PT plant is between 50 m^2 and 150 m^2, however these two different heliostat designs were not consistent in indicating the optimal size of a heliostat mirror. This is because the optimum heliostat size is dependent on many factors associated with the production volume and manufacturing processes, ease of access to the electricity network in the region and the terrain type and wind conditions at the site. Therefore, further understanding of the relationships between the heliostat cost and the wind loading on heliostats needs to be developed. For example, an investigation of the sensitivity of the heliostat cost to wind speed would allow the optimisation of the design wind speed for moving heliostats from operating positions to the stow position. Heliostats are aligned parallel to the ground in the stow position during periods of high wind speeds to minimise the frontal area and the large drag forces that the heliostat are exposed to in operating positions, however stowed heliostats must withstand maximum lift forces and hinge moments due to the effects of turbulence (gusts) in the atmospheric boundary layer.

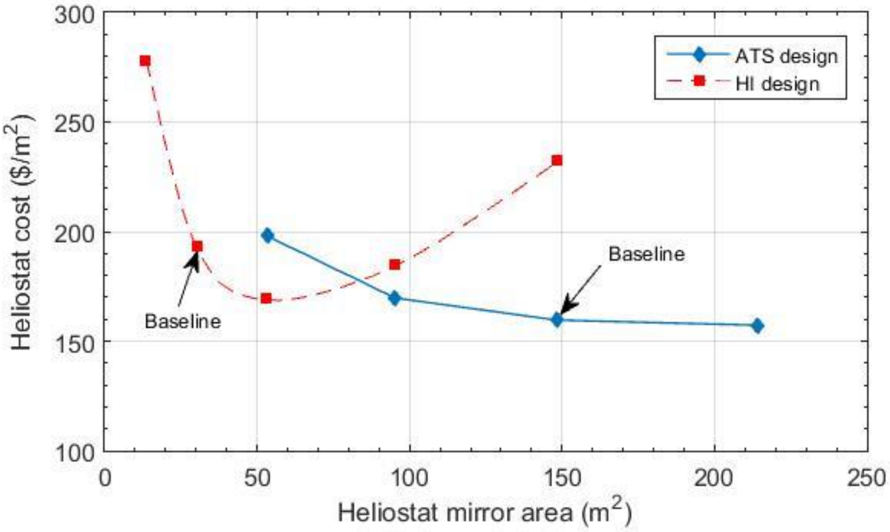

Figure 1.3. Total heliostat cost as a function of heliostat size for two different heliostat designs. The curves were developed through an analysis of lift-cycle costs for the manufacturing and installation of a heliostat field with a total mirror area of 235,000 m^2. Baseline cost estimates by Jones were for reference mirror areas of 148 m^2 for the large ATS heliostat design and 30 m^2 for the small HI heliostat design. Data reproduced from Kolb et al. (2007).

One opportunity to reduce heliostat costs is to improve the structural performance of stowed heliostats during high wind conditions (Kolb et al., 2011). Optimisation of the heliostat structure to wind loads is predicted by Kolb et al. (2011) to lead to a 10% reduction in heliostat cost per unit area (\$/m^2) of PT plants by 2020, which would help achieve the DOE goal of \$75/m^2 heliostat total installed costs. Heliostats need to withstand the maximum wind loads during high-wind conditions when aligned parallel to the ground ($\alpha = 0°$) in the stow position. The motor drives, support structure and mirror must all withstand any forces and moments applied to the heliostat from the wind. Kolb et al. (2011) estimated that these components, which are identified in Figure 1.2(b), account for up to 80% of the heliostat capital cost. A linear cost-load proportionality developed by McMaster Carr suggested that a 40% reduction in the peak hinge moment on the elevation drive of a conventional heliostat can lead to a 24% saving in the representative gear reducer cost (Lovegrove and Stein, 2012). Hence, there is a significant opportunity to minimise the capital cost of a PT plant by optimising the dimensions of heliostats for structural integrity in the stow position. This requires an accurate estimation of wind loading to maintain the structural integrity of the heliostat components while achieving good optical performance (Pfahl et al., 2017).

The motivation for the current research is to develop an understanding of the maximum wind loads on a stowed heliostat in a highly turbulent environment, such as the atmospheric boundary layer (ABL). Stowed heliostats in the outer boundary of the field, typically located in flat open terrains, are exposed to high wind speeds with little protection from upwind heliostats. The interaction of large vortices with the leading edge of the stowed heliostat are likely to cause a wind-induced response that can lead to structural failure from the interaction of vortex-induced vibrations and resonance effects such as galloping. Accurate calculation of the wind loads on an isolated heliostat in stow position is the first stage in the design process to determine the sensitivity of the static and dynamic wind loads to the temporal and spatial turbulence characteristics in the lowest 10 m of the ABL. Further, optimisation of the cornfield and radial stagger arrangements of a heliostat field to peak wind loads can also lead to cost reductions, such as manufacturing in-field heliostats that are exposed to reduced wind loads from lower strength and lighter materials.

1.2. Research Aims and Objectives

The overall aim of the current research is to investigate the peak wind loads on a heliostat in stow position and their sensitivity to the turbulence characteristics in the atmospheric boundary layer (ABL) and the dimensions of the heliostat. A better understanding of the static and dynamic wind loads on heliostats in stow position with respect to the approaching turbulence in the ABL is important to enable optimisation of the size of the heliostat structure and thus reduce the cost of the heliostat's components. As a motivation to reduce the cost of heliostats, the first objective investigates the effect of the stow design wind speed on the heliostat cost and heliostat area by relating the costs of each heliostat component to the quasi-static wind loads and mirror area scaling exponents. The second objective investigates the profiles of turbulence intensity and integral length scales to better understand the temporal and spatial turbulence in the atmospheric surface layer over a low-roughness desert terrain. The maximum gust wind speeds at heights below 10 m, relevant for the design wind loads on stowed heliostats, are calculated from field experiment data and compared with the gust factor approach. The third and fourth objectives investigate the dominant frequencies of pressure fluctuations and the peak wind loads on stowed heliostats in isolation and in tandem arrangements, respectively, and their sensitivity to the turbulence characteristics of the ABL investigated in the second objective. The research objectives can be defined as:

(i) Investigate the effect of the design wind speed for stowing heliostats on the levelised cost of electricity (LCOE) of a power tower plant.

(ii) Investigate the gust characteristics in a low-roughness atmospheric surface layer to determine the suitability of semi-empirical models and the gust factor approach for predicting the peak gust wind speeds and integral length scale profiles.

(iii) Determine the effect of turbulence characteristics in the atmospheric surface layer on the peak wind loads on an isolated heliostat in stow position.

(iv) Determine the effect of gap ratio and heliostat size on the peak wind loads on tandem stowed heliostats in the rows of a solar field in a power tower plant.

In order to achieve the research objectives, the present study involved the following tasks:

- The development of a statistical model to estimate the sensitivity of the cost of heliostats and the levelised cost of electricity of a power tower plant to the design wind speed for stowing heliostats.
- The analysis of velocity data collected in a field experiment in a low-roughness atmospheric surface layer to investigate the relationships between the temporal and spatial characteristics of turbulence in the time and frequency domains.
- Physical modelling of the ABL in a wind tunnel with the required velocity and turbulence intensity profiles approaching full-scale heliostat fields.
- The design, development and manufacture of different sized heliostat mirrors with an adjustable height pylon to investigate the effects of elevation axis height and integral length scales on the mean and peak static wind loads on a scale-model heliostat.

- The design, development and manufacture of a heliostat facet instrumented with differential pressure sensors to monitor the surface pressure distributions and investigate the dynamic wind loads on a scale-model heliostat.

1.3. Thesis Outline

The current thesis is presented in a number of chapters as a collection of manuscripts in a sequence that highlights the chronology of the knowledge development and progress during the course of study. The first chapter provides an overview of the subject matter and details the motivation for pursuing the current research. Chapter 2 provides a comprehensive review of previous studies and the state-of-the-art in the field of research. Knowledge gaps in this research area are highlighted and discussed, followed by a statement of the principal aims and objectives of the current research. Chapters 3 to 6 constitute the main body of the thesis, presented as two conference articles and four manuscripts that have been published, accepted for publication or are currently under review in peer-reviewed international journals. A detailed discussion of the development, validation and interpretation of analytical and experimental methods to simulate the lower atmospheric boundary layer (ABL) in a wind tunnel and an experimental investigation of the peak wind loads on stowed heliostats are presented in these manuscripts. Finally, in Chapter 7 the major findings of the current thesis are summarised, conclusions are drawn and future work in the field of research is proposed. Following is a brief description of the contents of each chapter and how they are related together within the scope of the project.

Chapter 1 introduces the research background of concentrating solar thermal (CST) technology and the motivation to reduce the cost of heliostats to make the levelised cost of electricity

(LCOE) of power tower (PT) systems more competitive with base-load energy sources. This is followed by a summary of the aims and objectives of the current research and a description of the tasks that are required to achieve the objectives. The chapter concludes by listing the publications that form the chapters of the current thesis and the other publications in the present study that are not included in the thesis.

Chapter 2 provides a comprehensive review of the temporal and spatial turbulence characteristics in the lowest 100 m of the ABL known as the atmospheric surface layer (ASL), where heliostats are aligned parallel to the ground in the stow position. This is followed by an extensive literature review of the aerodynamic characteristics of flat plates exposed to smooth and turbulent flow and the dynamic effects of vortex-induced vibrations and galloping on the dynamic wind loads on isolated plates and two plates in tandem. The existing knowledge in the state-of-the-art research of the static and dynamic wind loads on stowed heliostats in PT systems is then discussed in relation to the effects of turbulence in the ABL through the conventional investigation methods using theoretical models, field site measurements, wind tunnel experiments and computational modelling. The literature review concludes with the identification of the research gaps in the existing knowledge and a statement of the aims and objectives of the current research.

Chapter 3 analyses the sensitivity of the LCOE of a PT plant to the design wind speed for moving heliostats from operating positions to the stow position. A statistical model was developed to investigate the effect of the design wind speed at which heliostats are moved to the stow position on the capital cost of the major components of the heliostat and the LCOE of a PT plant. The model assumes quasi-steady wind loads and simplified cost-load and cost-area proportionality exponents to relate the heliostat cost to wind loads and determine the effect of heliostat mirror area on the heliostat cost. The correlation between solar irradiation data and wind speed data allowed the calculation of the capacity factor of the PT plant. The sensitivity of LCOE to the stow design wind speed is calculated based on derived relationships between the cost of materials for manufacturing heliostats and the annual electricity production of a PT plant at six sites in Australia and the USA with a sufficient solar resource. The chapter addresses the motivation to reduce the cost of heliostats by assessing the effect of lowering the design wind speed below the maximum wind speeds at the six sites on the LCOE of a PT plant and the effect of heliostat size on the capital cost of heliostats.

In Chapter 4, the characteristics of turbulence calculated from velocity measurements obtained in a low-roughness desert ABL are analysed and discussed in relation to semi-empirical models developed for homogenous, isotropic turbulence over open country terrains in a neutrally-stable ABL. The temporal and spatial characteristics of turbulence are calculated using field velocity measurements taken in a low-roughness surface layer in the Utah desert during near-neutral conditions. Results from the analysis showed that there are distinct characteristics of a low-roughness surface layer that deviate significantly from semi-empirical relationships derived for open country and urban terrains with larger surface roughness heights. Calculated gust factor profiles following the approach used in wind codes and standards for buildings showed that the peak wind speeds of low-frequency gusts were under-predicted in the low-roughness terrain, thus highlighting the uncertainties associated with using the quasi-steady gust factor method to approximate the peak wind loads on heliostats.

Chapter 5 presents an experimental investigation of the peak wind load coefficients on a heliostat in stow position to optimise the characteristic dimensions of the heliostat to the turbulence characteristics in the atmospheric surface layer. The temporal and spatial turbulence characteristics were characterised in a simulated part-depth ABL representing the gusty wind conditions approaching isolated heliostats in stow position. Peak wind loads were found to be highly dependent on the turbulence intensity and the size of the largest eddies approaching the heliostat with respect to the size of the mirror. Knowledge of both temporal and spatial turbulence in the ABL was found to be important for the design of heliostats in stow position so that they can withstand maximum wind loads during high-wind events. These results can be used in the design of heliostats to further optimise the size and cost of heliostats with respect to the turbulence approaching the outer row of heliostats at a given site.

Chapter 6 presents an experimental investigation of the normalised peak wind load coefficients on two tandem heliostats in stow position on turbulence characteristics in the atmospheric surface layer, such that the spacing between the heliostats and thus their size and cost can be further optimised. Maximum values of the ratio of the peak lift and peak hinge moments on the second downstream heliostat relative to an isolated heliostat in stow position were found to occur at turbulence intensities above 10% and were significantly dependent on the ratio of integral length scale to mirror chord length and the separation distance between the two heliostats in tandem. Peak lift forces and peak hinge moments were reduced by up to 30% on the second tandem heliostat when the gap ratio between the two heliostats was close to 1 and converged to the isolated heliostat for gap ratios greater than 5. The optimal values of these peak wind loads could be achieved by lowering the ratio of elevation axis height to chord length of the mirror H/c to less than 0.5. Peaks of the measured pressure spectra on the downstream mirror surface were an order of magnitude lower than an isolated heliostat mirror and were shifted to frequencies an order of magnitude larger corresponding to smaller vortices.

The final chapter of the current thesis, Chapter 7, summarises the significant findings and the major conclusions of the works undertaken throughout the course of this research and documented in the manuscripts. Future work to further reduce the cost of heliostats is also proposed.

1.4. Publications arising from this thesis

The research presented in the current thesis has resulted in the generation of four journal manuscripts and four peer-reviewed conference articles. The journals and conference proceedings to which the manuscripts have been submitted are closely related to the field of research presented in the current thesis. The following list of manuscripts have been published or submitted for publication as a result of the research:

1.4.1. Journal Articles

[1] Emes, M. J., Arjomandi, M. and Nathan, G. J., 2015, Effect of heliostat design wind speed on the levelised cost of electricity from concentrating solar thermal power tower plants, Solar Energy 115, 441-451.

[2] Emes, M. J., Arjomandi, M., Kelso, R. M. and Ghanadi, F., 2017, Investigation of turbulence characteristics in a low-roughness atmospheric surface layer, Wind and Structures (submitted).

[3] Emes, M. J., Arjomandi, M., Ghanadi, F. and Kelso, R. M., 2017, Effect of turbulence characteristics in the atmospheric surface layer on the peak wind loads on heliostats in stow position, Solar Energy 157, 284-297.

[4] Emes, M. J., Ghanadi, F., Arjomandi, M. and Kelso, R. M., 2017, Investigation of peak wind loads on tandem heliostats in stow position, Renewable Energy (submitted).

1.4.2. Refereed Conference Papers

[1] Emes, M. J., Arjomandi, M., Kelso, R. M. and Ghanadi, F., 2016, 'Integral Length Scales in a Low-Roughness Atmospheric Boundary Layer', *18th Australasian Wind Engineering Society Workshop*, Adelaide, Australia.

[2] Emes, M. J., Ghanadi, F., Arjomandi, M. and Kelso, R. M., 2016, 'An Experimental Technique for the Generation of Large-Scale Spanwise Vortices in a Wind Tunnel', *20th Australasian Fluid Mechanics Society Conference*, Perth, Australia.

[3] Emes, M. J., Arjomandi, M., Ghanadi, F. and Kelso, R. M., 2017, 'Wind Tunnel Investigation of Turbulence Characteristics in the Atmospheric Surface Layer', *Wind Energy Science Conference 2017*, Copenhagen, Denmark.

[4] Emes, M., Ghanadi, F., Arjomandi, M. and Kelso, R., 2017, 'Optimisation of the Size and Cost of Heliostats in a Concentrating Solar Thermal Power Tower Plant', *The European Conference on Sustainability, Energy & the Environment 2017*, Brighton, U.K.

In addition, the author of the current thesis has been closely involved in developing methods for characterising the turbulence approaching heliostats to determine the maximum wind loads for their design in both operating and stow positions in the research fields of concentrating solar thermal and boundary layer turbulence. In the journal article [1] and conference paper [4], the author of the current thesis contributed a method for calculating the integral length scales of turbulence at a given height in the ABL and developed equations to estimate the peak lift coefficient and peak hinge moment on a stowed heliostat based on the heliostat mirror chord length, peak wind speed and integral length scale at the mirror elevation axis height. In the conference paper [2], the current author calculated the velocity, turbulence intensity and gust factor profiles based on velocity data obtained in a low-roughness atmospheric surface layer (ASL) in the Utah desert and contributed to the discussion of results relating to the gust factor and the calculation of wind load on a stowed heliostat. In the conference paper [3], the current author contributed to the discussion of results and editing of the manuscript. The following journal article and conference papers in the research field of concentrating solar thermal produced as part of this work are not included in the current thesis:

[1] Yu, J. S., Emes, M. J., Ghanadi, F., Arjomandi, M. and Kelso, R. M., 2017, Wind load on heliostats – A practical approach, Solar Energy (submitted).

[2] Ghanadi, F., Emes, M., Yu, J., Arjomandi, M. and Kelso, R., 2016, ‘Investigation of the Atmospheric Boundary Layer Characteristics on Gust Factor for the Calculation of Wind Load’, *22nd SolarPACES Conference*, Abu Dhabi, UAE.

[3] Ghanadi, F., Yu, J., Emes, M., Arjomandi, M. and Kelso, R., 2016, ‘Numerical Investigation of Wind Loads on an Operating Heliostat’, *22nd SolarPACES Conference*, Abu Dhabi, UAE.

[4] Ghanadi, F., Yu, J. S., Emes, M. J. and Arjomandi, M., 2016, ‘The effects of heliostat mirror geometry on static and dynamic wind loads’, *3rd Asia-Pacific Solar Research Conference*, Canberra, Australia.

1.5. Thesis Format

The current thesis has been submitted as a portfolio of the above journal manuscripts according to the formatting requirements of the University of Adelaide. The printed and online versions of the thesis are identical. The online version of the thesis is available as a PDF and can be viewed in its original format using Adobe Reader 11.

References for Chapter 1

Blackmon, J.B., 2013, Parametric determination of heliostat minimum cost per unit area, Solar Energy 97, 342-349.

Coventry, J. and Pye, J., 2014, Heliostat cost reduction–where to now?, Energy Procedia 49, 60-70.

Gary, J., Turchi, C. and Sieger, N., 2011, CSP and the DOE sunshot initiative, in: Proc. SolarPACES 2011 Conference, Granada, Spain.

Hernández-Moro, J. and Martínez-Duart, J.M., 2012, CSP electricity cost evolution and grid parities based on the IEA roadmaps, Energy Policy 41, 184-192.

Hinkley, J.T., Hayward, J.A., Curtin, B., Wonhas, A., Boyd, R., Grima, C., Tadros, A., Hall, R. and Naicker, K., 2013, An analysis of the costs and opportunities for concentrating solar power in Australia, Renewable Energy 57, 653-661.

IEA-ETSAP and IRENA, 2013, Concentrating Solar Power Technology Brief.

IRENA, 2013, Renewable Power Generation Costs in 2012: An Overview, Bonn, Germany.

IRENA, 2015, The Power to Change: Solar and Wind Cost Reduction Potential to 2025, Bonn, Germany.

Kolb, G.J., Ho, C.K., Mancini, T.R. and Gary, J.A., 2011, Power Tower Technology Roadmap and Cost Reduction Plan, In: SAND2011-2419, Sandia National Laboratories, Albuquerque, USA.

Kolb, G.J., Jones, S.A., Donnelly, M.W., Gorman, D., Thomas, R., Davenport, R. and Lumia, R., 2007, Heliostat Cost Reduction Study, In: SAND2007-3293, Sandia National Laboratories, Albuquerque, USA.

Lovegrove, K. and Stein, W., 2012, Concentrating solar power technology: principles, developments and applications, Woodhead Publishing Limited, Cambridge, UK.

Noone, C.J., Torrilhon, M. and Mitsos, A., 2012, Heliostat field optimization: A new computationally efficient model and biomimetic layout, Solar Energy 86, 792-803.

Pfahl, A., Coventry, J., Röger, M., Wolfertstetter, F., Vásquez-Arango, J.F., Gross, F., Arjomandi, M., Schwarzbözl, P., Geiger, M. and Liedke, P., 2017, Progress in heliostat development, Solar Energy 152, 3-37.

Pitz-Paal, R., Dersch, J., Milow, B., Ferriére, A., Romero, M., Tellez, F., Zarza, E., Steinfeld, A., Langnickel, U. and Shpilrain, E., 2004, ECOSTAR: European Concentrated Solar Thermal Road-Mapping, In: Report No. SES6-CT-2003-502578, Köln, Germany.

Talebizadeh, P., Mehrabian, M.A. and Rahimzadeh, H., 2013, Optimization of Heliostat Layout in Central Receiver Solar Power Plants, Journal of Energy Engineering 140, 04014005.

Chapter 2

Literature Review

This chapter is focused on previous studies of the static and dynamic wind loads on heliostats and the effects of turbulent phenomena in the atmospheric boundary layer (ABL). To characterise the flow approaching isolated heliostats in stow position, a description of the aerodynamic characteristics of turbulence in the ABL, including velocity profile, surface roughness and vortex structures, is presented in Section 2.1. The effects of these turbulent characteristics on the aerodynamic loads on a flat plate aligned parallel to the ground, representing a heliostat in stow position, that have been investigated in wind tunnel experiments and field measurements are described in Section 2.2. This is followed by an overview of studies on heliostat wind loading in the past few decades in Section 2.3, with an emphasis on wind tunnel experiments on scale-model heliostats in stow position. Moreover, some of the most successful experimental techniques for the generation of the ABL are discussed in regard to their accuracy of reproducing the temporal and spatial distributions of the velocity fluctuations. Subsequently, the turbulence effects that have previously been identified to contribute to the peak wind loads and the structural failure of stowed heliostats during high-wind conditions are summarised in Section 2.4, followed by a statement of the objectives of this research to further optimise the design of heliostats to wind loads in Section 2.5.

2.1. Atmospheric Boundary Layer

Knowledge of the aerodynamic loads on heliostats during high-wind events is critical for their design to maintain structural integrity in stow position, which requires an understanding of the effects of turbulence in the neutrally-stratified wind over flat, uniform terrain within the atmospheric boundary layer (ABL) (Figure 2.1). Large physical structures, such as buildings of height D and heliostats of elevation axis height H, are positioned in the lowest 100 m of the neutral ABL of thickness δ_s, known as the atmospheric surface layer (ASL) (Kaimal and Finnigan, 1994). Full-scale field measurements in the ASL have shown similar turbulence properties to the canonical zero-pressure-gradient turbulent boundary layer along a flat plate in a wind tunnel (Plate, 1974). Similarities in the non-dimensional profiles of mean velocity, turbulence intensity and Reynolds shear stress, following the upper and lower boundary conditions of the logarithmic law defining parameters of friction velocity, surface roughness height and boundary layer thickness, have demonstrated the effective scaling of turbulence parameters between field and wind tunnel measurements (Tennekes and Lumley, 1972). Consequently, wind tunnel experiments have been used to complement the high-resolution velocity measurements in the ASL because of the limited number of vertical data points along the height of a wind mast (Rosi et al., 2013).

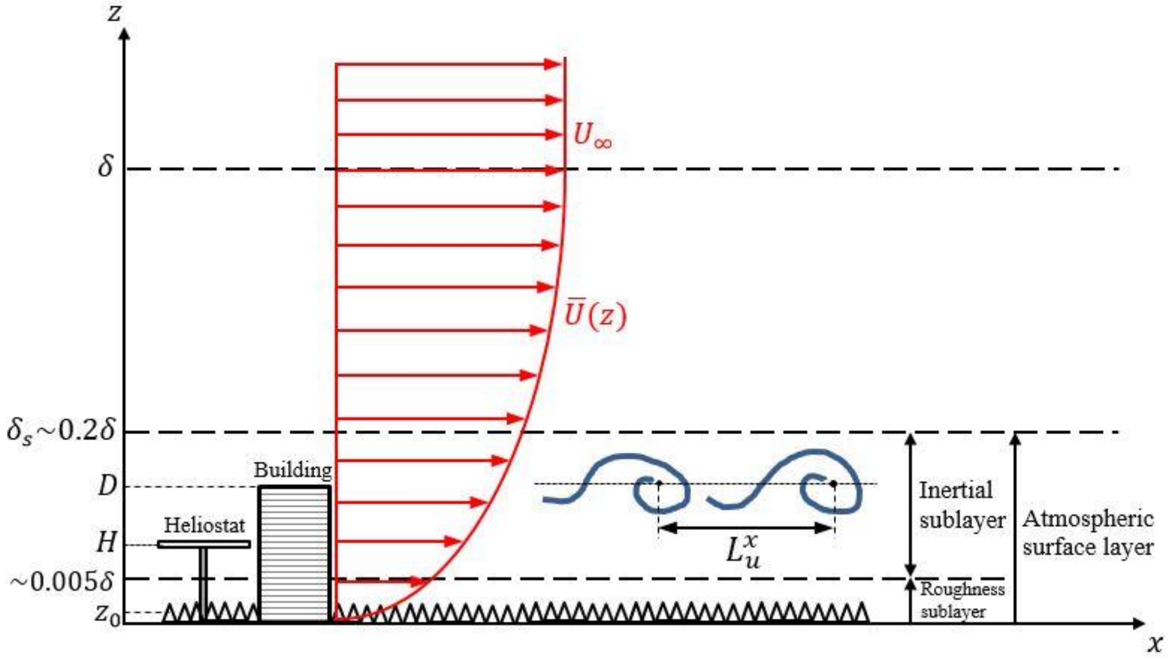

Figure 2.1. Structure and turbulence characteristics of the atmospheric boundary layer.

2.1.1 Velocity Profile

Wind velocity is often thought to consist of a time-averaged mean component and a fluctuating component due to turbulence responsible for the unsteady loads on physical structures, such as buildings and heliostats in the ABL (Figure 2.1). The mean wind velocity varies significantly with height above the Earth’s surface, increasing from zero with a no-slip boundary condition at the surface to the freestream or gradient velocity (U_∞) at the outer edge of the ABL thickness $\delta \approx$ 1-2 km above the surface (Kaimal and Finnigan, 1994; Xu, 2013). The mean velocity profile in the ABL has been modelled to various degrees of accuracy by the logarithmic law, the power law and the Deaves-Harris model (Cook, 1997). Initially derived from the turbulent boundary layer on a flat plate, the logarithmic law has been demonstrated to be the most appropriate for modelling the mean velocity profile at heights below 100 m in the ABL (Sun et al., 2014; Xu, 2013). Following the assumptions of asymptotic similarity and neutral stability with negligible buoyancy effects, the mean velocity profile in the ABL defined by the logarithmic law is:

$$\bar{U}(z) = \frac{U_\tau}{k} \ln\left(\frac{z}{z_0}\right). \tag{2.1}$$

Here $U_\tau = \sqrt{\tau/\rho}$ (m/s) is the friction velocity representing the Reynolds shear stress $\tau = -\rho\overline{u'w'}$ at the surface, k is von Karman's constant (0.4) and z_0 (m) is the surface roughness height as a fraction of the average height of roughness elements in the roughness sublayer (Figure 2.1). The surface roughness height can vary in scale from millimetres in a flat desert to metres in a dense urban area (Xu, 2013). At lower heights in the roughness sublayer ($z \leq 0.005\delta$) and the surface layer ($z \leq 0.2\delta$), velocity and length scales are scaled by the effects of viscosity (Goldstein, 1996). The logarithmic law can therefore be revised as follows:

$$U^+ = \frac{1}{k}\ln(z^+) + A - \frac{\Delta U_r}{U_\tau}, \tag{2.2}$$

where $U^+ = \bar{U}(z)/U_\tau$ and $z^+ = zU_\tau/\nu$ are the viscous velocity and height, respectively, A is an empirical constant ($A = 5$ for a smooth wall boundary layer) and $\frac{\Delta U_r}{U_\tau}$ is a roughness scaling factor. The friction velocity is commonly determined from measurement of the wall shear stress or estimated using the Clauser chart method by defining the friction coefficient $C_f = 2(U_\tau/U_\infty)^2$, such that Equation (2.2) can be written as a function of gradient velocity U_∞ in the following form (Wei et al., 2005):

$$\frac{\bar{U}(z)}{U_\infty} = \frac{1}{k}\sqrt{\frac{C_f}{2}}\ln\left(\frac{zU_\infty}{\nu}\right) + \frac{1}{k}\sqrt{\frac{C_f}{2}}\ln\left(\sqrt{\frac{C_f}{2}}\right) + A\sqrt{\frac{C_f}{2}}, \tag{2.3}$$

Although the lower boundary at the surface is defined in the logarithmic law, there is no upper boundary condition, and thus it is a less accurate description of the mean velocity profile at larger heights in the outer region of the ABL. Consequently, Deaves and Harris (1978) proposed a revised logarithmic profile, known as the Deaves-Harris model, that can also be applied to the outer region of the ABL beyond the surface layer:

$$\frac{\bar{U}(z)}{U_\tau} = \frac{1}{k}\left\{\ln\left(\frac{z}{z_0}\right) + \frac{5.75z}{\delta} - 1.88\left(\frac{z}{\delta}\right)^2 - 1.33\left(\frac{z}{\delta}\right)^3 + 0.25\left(\frac{z}{\delta}\right)^4\right\}, \tag{2.4}$$

where $\delta = U_\tau / Bf$ (m) is the ABL thickness, f (s^{-1}) is the Coriolis parameter and B is an empirical constant determined from observed wind speed profiles. Alternatively, the power law provides a simplified model for the mean velocity profile in the ABL, defined as:

$$\bar{U}(z) = U_\infty \left(\frac{z}{\delta}\right)^\alpha, \tag{2.5}$$

where U_∞ (m/s) is the freestream velocity, δ (m) is the boundary layer thickness and α is a roughness exponent. The power law has been found to be appropriate for modelling the mean velocity profile at heights around 30-300 m and hence, it is most widely used for the calculation of wind loads on tall buildings and other large civil structures (Xu, 2013). However, the height at which heliostats are stowed is below 10 m. Therefore, the logarithmic law is considered the most appropriate to model the mean velocity profile in the lowest 10 m of the ABL.

2.1.2 Turbulence Intensity

Heliostats are positioned in highly turbulent fields, hence the turbulence properties of the approaching flow are an important consideration for the calculation of dynamic wind loads (Peterka and Derickson, 1992). Turbulent velocity fluctuations generate an increased mixing in the inertial sublayer of the ABL, so there is an energy exchange between different eddy length scales in the flow. The simplest and most commonly-used parameter to quantify turbulence in the ABL is the turbulence intensity, defined as the ratio of the root-mean-square (RMS) of the fluctuating velocity in three directions (x, y, z) and the mean velocity as follows:

$$I_i(z) = \frac{\sigma_i}{\bar{U}(z)} \qquad (i = u, v, w) \tag{2.6}$$

Turbulence intensity profiles in the ABL have been found to differ from the simple inner-outer arguments used to define the mean velocity profile in a zero-pressure-gradient turbulent boundary layer (Marusic et al., 2010). Boundary layer data from wind tunnel experiments have shown that the RMS of the streamwise turbulence component, $\overline{u'^2}$, is relatively insensitive to Reynolds number $Re_\theta = U_\infty \theta / \nu$ based on momentum thickness $\theta = \int_0^\infty \frac{u}{U_\infty}\left(1 - \frac{u}{U_\infty}\right) dz$, in the inner region ($z^+ = zU_\tau/\nu < 300$) of the turbulent boundary layer over a flat plate (Marusic et al., 2010). The ratio of the RMS of streamwise turbulence to friction velocity U_τ is highly dependent on the scaled viscous height z^+, particularly in the near-wall viscous sublayer ($z^+ < 5$) and the buffer region ($5 < z^+ < 30$), as shown in Figure 2.2 for turbulent boundary layer data from the Herman-Föttinger Institut (HFI) (Bruns et al., 1992) and the German-Dutch wind tunnel (DNW) (Fernholz et al., 1995). The largest magnitudes of streamwise turbulence intensity, $\overline{u'^2}/U_\tau^2$ between 5 and 10, occur in the buffer region close to the ground, however $\overline{u'^2}/U_\tau^2 \approx$ 5-6 is relatively constant in the inner region ($z^+ < 300$), corresponding to heights $z < 100$ m in the ABL. Heliostat mirrors are stowed at lower heights ($z \leq 6$ m) in the ABL with reduced wind velocities, but they are exposed to larger velocity gradients and magnitudes of streamwise turbulence intensity than tall buildings that can lead to unsteady forces and moments during high-wind conditions.

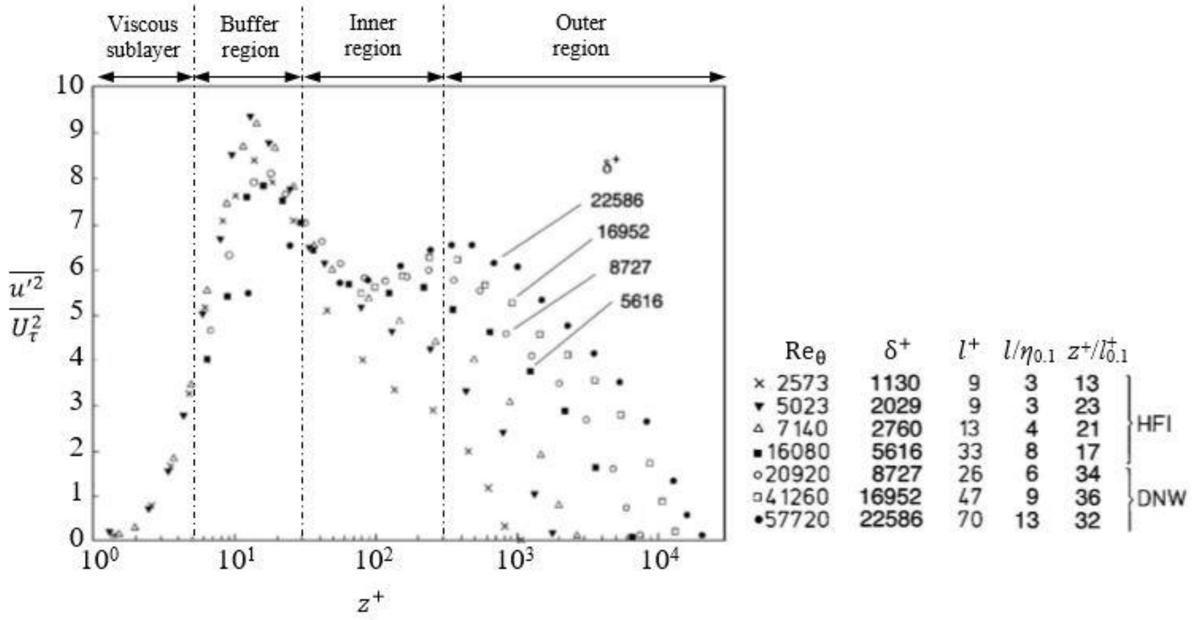

Figure 2.2. Variation of streamwise turbulence intensity scaled to friction velocity $\overline{u'^2}/U_\tau^2$ as a function of viscous height $z^+ = zU_\tau/\nu$ and Reynolds number $Re_\theta = U_\infty\theta/\nu$ in the turbulent boundary layer. Data are from the Herman-Föttinger Institut (HFI) and the German-Dutch wind tunnel (DNW). Reproduced from Marusic et al. (2010).

2.1.3 Neutral Stability

Turbulence characteristics within a shear-driven wall-bounded flow, such as the ABL, that lead to the fluctuating loads on heliostats can be most independently assessed when the atmosphere is neutrally stable. The ABL is defined as neutrally stable during periods of neutral buoyancy when the vertical heat-flux $\overline{w\theta}$ is approximately zero (Hutchins et al., 2012) with temperature stratification corresponding to the adiabatic lapse rate $\frac{d\theta}{dz} \approx$ -1°C/100 m (Kaimal and Finnigan, 1994). Alternatively, the Högström (1988) criterion $|z/L| \leq 0.1$ for a near-neutral condition provides a measure of the stability of the ABL. A common threshold of mean wind speed is 10 m/s at a 10 m height in a neutrally-stratified ABL (Xu, 2013), however Counihan (1975) found that mean wind speeds above 5 m/s at a 10 m height produce adiabatic wind conditions from an analysis of full-scale ABL data sets between 1880 and 1972. This has been supported by recent full-scale surface layer measurements (Anfossi et al., 1997; Chu et al., 1996) at mean wind speeds of 6 m/s. These conditions of neutral stability in surface layer field measurements are critical for comparison with data from canonical laboratory turbulent boundary layers (Metzger et al., 2007; Van den Berg, 2006). Since the ultimate design wind loads have previously been estimated based on scale-model heliostats in wind tunnel experiments (Peterka and Derickson, 1992; Pfahl et al., 2017a), it is assumed that these design coefficients serve as a conservative measure of the maximum wind loads to which full-scale stowed heliostats would be exposed during high wind conditions in a neutral ABL. Hence, the condition of neutral stability is a reasonable and critical assumption for the design of stowed heliostats to withstand the effects of turbulence in the approaching wind.

Mean and peak wind load coefficients of heliostats in stow position have been determined following the theory of stationary random processes that the instantaneous wind velocity comprises a mean component and a fluctuating component due to turbulence in the neutral ABL. Turbulence intensity (Section 2.1.2) provides only a single-point magnitude of the wind fluctuations, whereas the distribution of these fluctuations with time is described by the probability density function (PDF). Higher-order moments and turbulence statistics of the PDF, respectively, such as skewness and kurtosis, provide information on the stability of the ABL and the turbulent motions in the surface layer responsible for the wind fluctuations (gusts). Skewness and kurtosis provide a measure of the symmetry and flatness of the PDF, respectively and are defined for the three components of velocity ($X = u, v, w$) as follows:

$$S(X) = (X - \bar{X})^3 / {\sigma_X}^3 \tag{2.7}$$

$$K(X) = (X - \bar{X})^4 / {\sigma_X}^4 \tag{2.8}$$

The distribution of wind velocity that stowed heliostats are exposed to in a neutral ABL is assumed to follow a Gaussian form after applying a linear filter over the short-time averaging process (Greenway, 1979; Tennekes and Lumley, 1972). However, significant variations in the shape of the PDF that deviate from the Gaussian distribution are believed to be caused by the presence of updrafts and downdrafts from thermal gradients in the convective boundary layer (Anfossi et al., 1997; Hong et al., 2004). Full-scale measurements in a surface layer under different stability conditions were investigated by Chu et al. (1996) at a height of 2 m over the very low roughness terrain (z_0 = 0.13 mm) of a dry lake bed in Owens Valley, California. The PDFs of streamwise velocity in Figure 2.3(a) and vertical velocity in Figure 2.3(b) for a neutral ABL were close to the Gaussian distribution ($S = 0$, $K = 3$). However, the vertical velocity fluctuations in a stable ABL deviated from Gaussian with high kurtosis ($K = 5.78$) due to the intermittent structure and the possible effects of gravity waves (Kaimal and Finnigan, 1994). For unstable stratification, the streamwise PDF was skewed toward negative fluctuations ($S =$ –0.19), whereas the vertical PDF was skewed toward positive fluctuations ($S = 0.31$). Positive skewness of $\widetilde{W}$ indicates the presence of low-speed streaks with prevailing narrow updrafts over wider downdraft motions, but is also associated with large gradients in temperature caused by upward thermal plumes in convective flows (Chu et al., 1996). In the near-wake of a spanwise oscillating wall, Choi and Clayton (2001) observed that logarithmic velocity profiles were shifted upwards and turbulence intensities reduced in the viscous sublayer of the turbulent boundary layer along a flat plate. This thickening of the viscous sublayer was reflected by increasing skewness and kurtosis of velocity fluctuations through an increase in positive-tail probability in the PDF (Choi and Clayton, 2001). The predominantly positive, spiky excursions observed by Choi and Clayton (2001) in the near-wall region of the turbulent boundary layer indicated the existence of coherent structures generated by the ejection of low speed fluid and inrush of high speed fluid through sweep events by the spanwise pressure gradient (Corino and Brodkey, 1969; Grass, 1971). Hence, the assumption of a Gaussian velocity distribution in a neutral ABL with negligible effects of temperature is necessary to accurately predict the maximum wind loads on stowed heliostats that arise from the coherent eddies embedded in the turbulence in the fully-developed boundary layer.

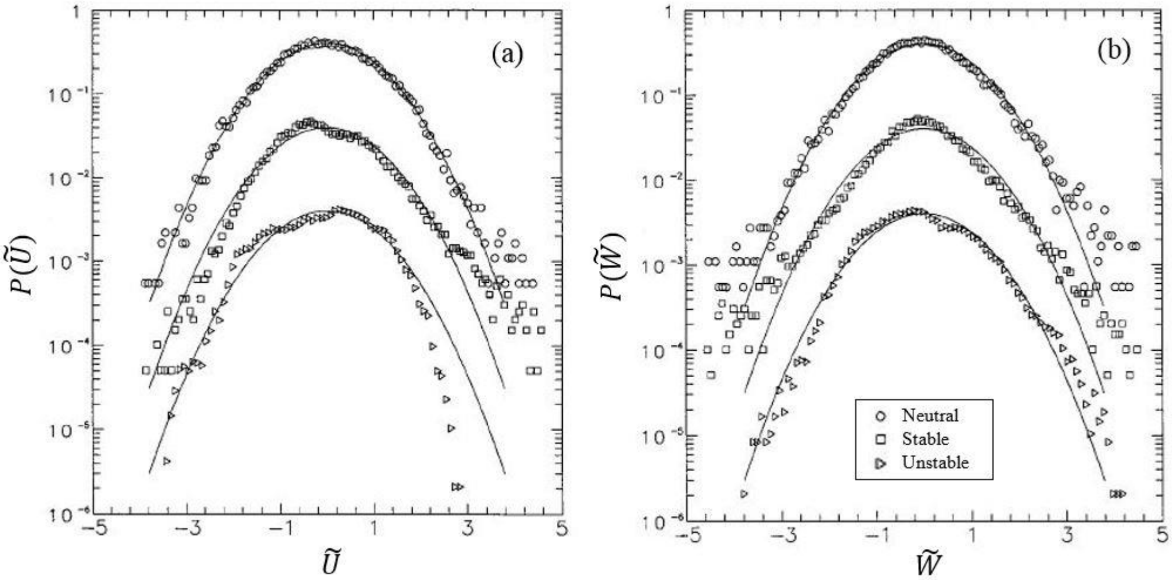

Figure 2.3. Probability density functions of: (a) Streamwise velocity $\tilde{U} = (u - \bar{U})\ /\sigma_u$; (b) Vertical velocity $\tilde{W} = (w - \bar{W})\ /\sigma_w$. Solid lines indicate the Gaussian probability distributions. Reproduced from Chu et al. (1996).

2.1.4 Power Spectral Density (PSD)

The peak wind loads on scale-model physical structures, such as heliostats in wind tunnel experiments, are significantly influenced by the eddy size distribution in the ABL (Pfahl et al., 2015). Turbulence intensities (Section 2.1.2) represent the total intensity of gusts, whereas the power spectral density (PSD) is the distribution of eddy sizes with frequency in the ABL. Analysis of the spectral distribution of the velocity fluctuations is important during heliostat design to identify resonance effects that can arise from fluctuating pressures induced on the structure at frequencies close to the natural frequencies of the heliostat (Pfahl et al., 2017a). Turbulent fluctuations of the instantaneous wind velocity from the mean wind, based on the theory of stationary random processes, arise from eddies (or vortices) of varying sizes within the ABL that are produced by surface roughness and obstacles on the ground (Kristensen et al., 1991; Xu, 2013). Figure 2.4 shows the distribution of energy contained within a cascade of eddies spanning the frequency domain in the ABL. Peak turbulent energy produced by shear and buoyancy is contained in large-scale eddies at low frequencies in region A (Kaimal and Finnigan, 1994). Turbulent mixing without energy production or dissipation leads to a process of vortex stretching and kinetic energy is transferred from the largest vortices with a defined integral length scale, L_u^x, to smaller vortices in the inertial subrange of frequencies in region B. Shearing of the fluid between and within vortices leads to the dissipation of kinetic energy to heat at the Kolmogorov length scale, η, as the vortices become small enough to be suppressed in region C.

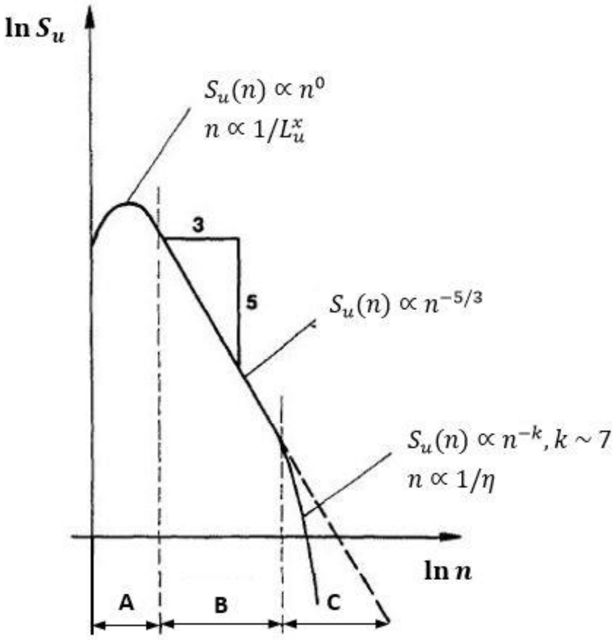

Figure 2.4. Schematic of the energy spectrum in the ABL showing distinct regions of energy production (A) and dissipation (C) and the inertial subrange (B). L_u^x is the integral length scale and η is the Kolmogorov length scale. Reproduced from Solari (1993).

Coherent spanwise vortices have been found to be responsible for most of the entrainment, defined by Head and Bradshaw (1971) as “the volume rate at which fluid is infected with mean vorticity” (Kelso et al., 1993), in the naturally occurring boundary layer that can lead to the dynamic responses of large buildings and the peak wind loads on small physical structures such as heliostats. Coherent structures within turbulent boundary layers have typically been quantified through the measurement of planar vortices, such as very large superstructures observed as counter-rotating pairs of horseshoe vortices in the logarithmic region with length scales of the same order as the ABL thickness δ (Hutchins and Marusic, 2007; Marusic and Hutchins, 2008). Spanwise vortices with an axis of rotation perpendicular to the flow are components of these superstructures, resulting from the interaction of separating and reattaching shear layers and tripping around obstacles on the ground (Sarkar, 2013). The frequency distribution of eddies in the PSD is important for the maximum hinge moments on heliostats in stow position, as the largest eddies at low frequencies cause well-correlated pressures over the surface of a heliostat mirror (Greenway, 1979; Mendis et al., 2007). In addition, resonance effects leading to excessive deflections and stresses and structural failure can occur when the turbulence length scales are comparable to the characteristic length of the heliostat and the frequencies of the velocity fluctuations are close to the natural frequency of the heliostat structure (Gong et al., 2012; Griffith et al., 2015; Nakamura, 1993).

The power spectral density (PSD) method of characterising the distribution of eddy sizes in the turbulent boundary layer assumes that the wind velocity follows a Gaussian distribution (Greenway, 1979). The PSD provides the distribution of energy content in the frequency domain and is defined as the Fourier transform of the autocorrelation function (Goldstein, 1996):

$$S_u(n) = 4\int_0^\infty R\,(\tau)\cos(2\pi n\tau)\,d\tau, \qquad (2.9)$$

where n (Hz) is frequency and $S_u(n)$ is the power spectral density of the fluctuating longitudinal velocity component. There have previously been a number of semi-empirical relations proposed to represent the power spectra in the neutrally-stable ABL. Two commonly used sets of these relations are the von Karman spectrum for isotopic turbulence ($L_u^x = 2L_v^x = 2L_w^x$) in the ABL and those of Kaimal et al. (1972) for the surface layer over flat, uniform terrain (Teunissen, 1980), expressed for the longitudinal direction in non-dimensional form as:

$$\frac{nS_u}{{\sigma_u}^2} = \frac{4\left(\frac{nL_u^x}{\overline{U}}\right)}{\left[1+70.8\left(\frac{nL_u^x}{\overline{U}}\right)^2\right]^{5/6}}, \tag{2.10}$$

$$\frac{nS_u}{{\sigma_u}^2} = \frac{105f}{(1+33f)^{5/3}}. \tag{2.11}$$

Here ${\sigma_u}^2 = \int_0^\infty S_u(n)\, dn$ is the variance of the streamwise velocity fluctuations (Goldstein, 1996) and $f = nz/\overline{U}$ is the non-dimensional frequency.

Experimental field measurements in open country terrains have led to similarity theories concerning the spatial structure of turbulence in the ABL. Semi-empirical models developed on the basis of similarity theory and surface layer measurements describe the flow over rural and urban terrains sufficiently to predict the surface shear stress, roughness height and turbulence intensities in the surface layer (Teunissen, 1980). However, Teunissen (1980) found that both the von Karman and Kaimal models deviated from the measured power spectra, particularly for the latter at low frequencies, as shown in Figure 2.5. Despite the under-prediction of power spectra at low frequencies, the Kaimal model more closely represented the shape of the measured spectra and thus could obtain a more accurate fit by modifying the constants in Equation (2.11) to account for rougher terrains with trees, fences and isolated buildings (Teunissen, 1980).

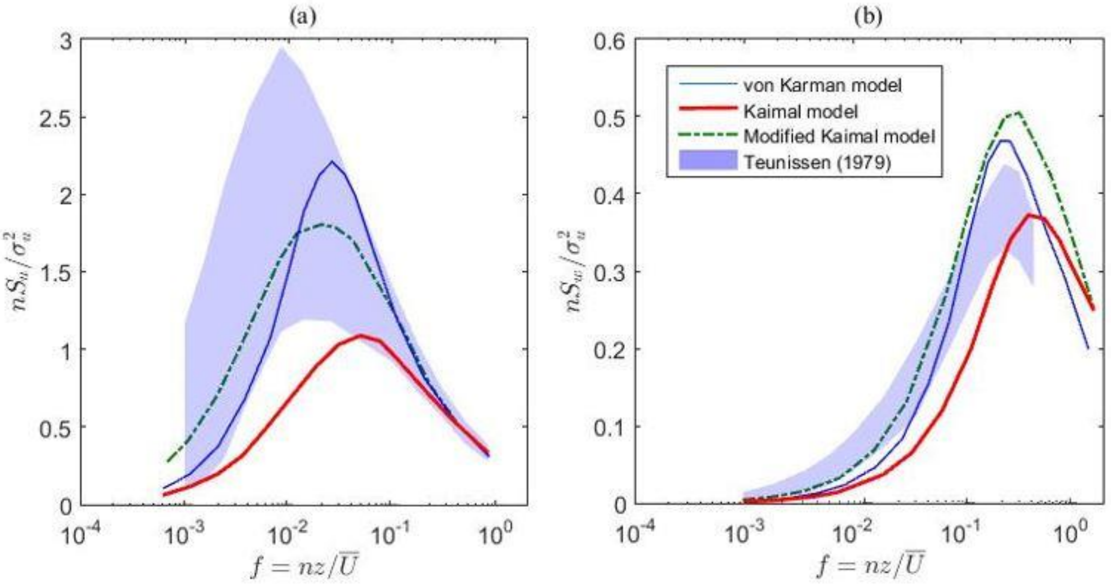

Figure 2.5. Measured power spectra over open country terrain near Woodbridge, Canada: (a) Longitudinal component, (b) Vertical component. Data extracted from Teunissen (1980).

Similarity of the mean wind velocity and turbulence intensity profiles in full-scale ABL field measurements and semi-empirical models with the part-depth ABL generated in wind tunnels has been widely demonstrated (Cook, 1973; Cook, 1978; Counihan, 1973). However, the largest eddies in the low-frequency region of the PSD are difficult to reproduce at smaller scales because of the limited size of wind tunnels. The dimensions of heliostats are an order of magnitude smaller than standard size buildings, hence they need to be modelled at larger scales between 1:10 and 1:50 to position the model at a sufficient height to generate desired velocity and turbulence intensity profiles. However, Banks (2011) noted that typical wind tunnel flow scales are 1:100 to 1:300. These discrepancies in scales are reflected by a shift of the PSD curves to higher frequencies in the ABL generated in wind tunnels. For example, Pfahl et al. (2015) compared measurements in a boundary layer wind tunnel (BLWT) for a 1:20 scale model heliostat mirror of chord length $c = 0.2$ m with Engineering Sciences Data Unit (1985) data at three longitudinal turbulence intensities I_u in a neutral ABL (Figure 2.6). ESDU 85020 is a semi-empirical model developed based on similarity theory and surface layer measurements in an open country terrain ($z_0 \approx 0.03$ m) for a reference mean velocity $\overline{U}_{10r}$ of 20 m/s at a 10 m height. The normalised turbulent energy spectra in the longitudinal and vertical directions from equations B4.1 to B4.4 in ESDU 85020 (Engineering Sciences Data Unit, 1985) are defined as:

$$\frac{nS_u}{\overline{U}^2} = I_u^2\left(\beta_1 \frac{2.987 f\gamma_u}{[1+(2\pi f\gamma_u)^2]^{5/6}} + \beta_2 \frac{1.294 f\gamma_u}{[1+(\pi f\gamma_u)^2]^{5/6}} F_1\right), \tag{2.12}$$

$$\frac{nS_w}{\overline{U}^2} = I_w^2\left(\beta_1 \frac{2.987[1+(8/3)(4\pi f\gamma_w)^2] f\gamma_w}{[1+(4\pi f\gamma_w)^2]^{11/6}} + \beta_2 \frac{1.294 f\gamma_w}{[1+(2\pi f\gamma_w)^2]^{5/6}} F_2\right). \tag{2.13}$$

Here $I_u^2 = \sigma_u^2/\overline{U}^2$ and $I_w^2 = \sigma_w^2/\overline{U}^2$ are the turbulence intensities in the longitudinal and vertical directions, respectively, and the empirical variables are defined as follows:

$$F_1 = 1 + 0.455 e^{-0.76 f\gamma_u \alpha^{1.8}}, \tag{2.14}$$

$$F_2 = 1 + 2.88 e^{-0.218 f\gamma_w \alpha^{1.9}}, \tag{2.15}$$

where $\gamma_u = L_u^x/c\alpha$ and $\gamma_w = L_w^x/c\alpha$ are a function of the integral length scales L_u^x and L_w^x in the longitudinal and vertical directions, respectively, and the characteristic length of the physical structure such as the heliostat chord length c. The empirical variables $\alpha = 0.535$ and $\beta_1 = \beta_2 = 0.5$ are constant because the characteristic length of a stowed heliostat is very small compared to the gradient height or ABL thickness δ (ESDU 85020, B5).

The non-dimensional longitudinal spectra measured by Pfahl et al. (2015) in the BLWT can be matched with ESDU (1985) data for I_u of 22% in the high-frequency region ($nc/\overline{U} > 1$) by lowering I_u to 13% in the BLWT, as shown in Figure 2.6(a). However, the non-dimensional vertical spectra (Figure 2.6(b)) in the BLWT are close to the ESDU (1985) data at the same I_u of 18% and 22%. Consequently, Pfahl et al. (2015) suggested that the vertical power spectra are important for the calculation of peak wind loads on a heliostat in stow position because of the linear relationship found by Rasmussen et al. (2010) between the vertical spectra and the lift forces and hinge moments on a flat plate exposed to low vertical turbulence ($I_w \leq 10\%$). The largest eddies corresponding to lower frequencies at the heights where heliostats are stowed in the ABL are convected at longitudinal mean velocities that are over an order of magnitude larger than the vertical direction, hence Pfahl et al. (2015) concluded that a reduction of turbulence intensity would under-estimate the peak wind loads on stowed heliostats and the common practice of matching the longitudinal turbulence intensity leads to the most realistic results despite a shift to higher frequencies in the BLWT.

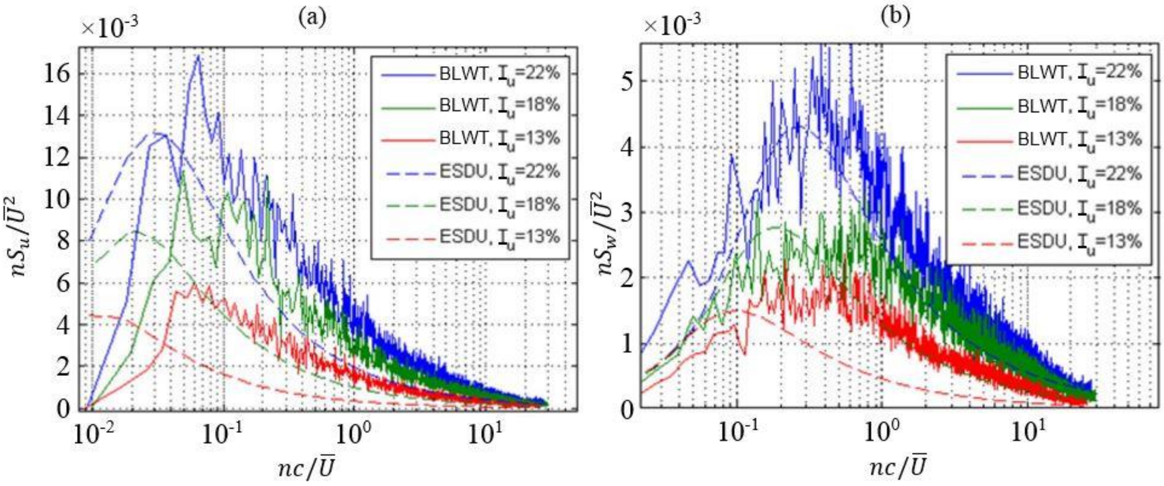

Figure 2.6. Experimental measurements in a boundary layer wind tunnel (BLWT) and ESDU (1985) model predictions of non-dimensional power spectra as a function of non-dimensional frequency $nc/\overline{U}$ based on the heliostat mirror chord length (c = 0.2 m) and longitudinal turbulence intensity I_u: (a) Longitudinal power spectra; (b) Vertical power spectra. Reproduced from Pfahl et al. (2015).

2.1.5 Gust Factor

The ability of physical structures to maintain structural integrity to withstand gusts in the ABL is an important consideration for slender structures with low natural frequencies, such as heliostats, because they are most likely to respond to dynamic instabilities and the effects of resonance (Jain et al., 1996; Mendis et al., 2007). The assumption of continuous turbulence in a Gaussian velocity distribution was found to inadequately account for the strong statistical correlation that exists between phases of Fourier components in the turbulent velocity component (Jones, 1989). Discrete gust models that account for the localised fluctuations characterised by large velocity differences were developed for aircraft with a span that is an appreciable fraction of the integral length scales of turbulence. Non-uniform spanwise gusts were modelled as multiple random inputs, such that the frequency response is calculated for several equally-spaced segments along the span of the aircraft (Jones, 1989). Discrete gust models were predominantly used for determining ultimate phenomena such as structural loading on aircraft, while spectral approaches were considered more applicable for fatigue loading analysis (Roadman and Mohseni, 2009). Typical gust gradient distances of 10 chord lengths and peak gust velocities of 16.76 m/s predicted by discrete gust models were found by Houbolt (1970) to correspond to 15.24 m/s gust velocities in the power spectral density (PSD) method of modelling gusts commonly used in the design of structures for wind.

The gust factor method is widely used in wind load design codes (American Society of Civil Engineers, 2013; Cook, 1985; Engineering Sciences Data Unit, 1985; Standards Australia and Standards New Zealand, 2011) to a series of velocity measurements over a sampling period of 10 minutes or greater, such that the frequency range in the measured PSD is accurately reproduced (Solari, 1993; Wieringa, 1973). The gust factor method uses a finite time response to predict the instantaneous peak velocity of sinusoidal gusts that are assumed to be non-overlapping and normally distributed over the sampling duration (Wieringa, 1973). The expected velocity gust factor that relates the fluctuating longitudinal component of the wind to the mean wind speed can be calculated by (Holmes et al., 2014):

$$G_u = \frac{\hat{U}}{\bar{U}} = \frac{\bar{U}+\sigma_u}{\bar{U}} = 1 + g_u I_u. \tag{2.16}$$

Here the resultant peak velocity ($\hat{U} = \overline{U} + \sigma_u$) of the turbulent wind fluctuations is assumed to be within one standard deviation σ_u of the mean velocity and g_u is the peak factor calculated by (Holmes et al., 2014):

$$g_u = \sqrt{2\ln \nu T} + \frac{0.577}{\sqrt{2\ln \nu T}}, \tag{2.17}$$

where T is the sampling period for the mean velocity usually taken over a duration of 10 minutes or 1 hour (Wieringa, 1973) because of the existence of a spectral gap in this range separating boundary-layer turbulence external fluctuations (Kaimal and Finnigan, 1994). The cycling rate ν representing the average frequency of digital filtering is (Holmes et al., 2014):

$$\nu = \left\{\frac{\int_0^\infty n^2 S_u(n)|H(n)|^2\,dn}{\int_0^\infty S_u(n)|H(n)|^2\,dn}\right\}^{1/2}, \tag{2.18}$$

where $|H(n)|^2 = \left(\frac{\sin n\pi t}{n\pi t}\right)^2$ is the transfer function in the frequency domain for an equivalent moving average filter with a defined gust period t in the time domain.

The expected maximum gust wind speed that is commonly used for the design of physical structures, such as the 40 m/s design wind speed that a second-generation heliostat can withstand in the stow position (Murphy, 1980), is dependent on the duration over which the gusts are averaged and the turbulence intensity. Durst (1960) found that the gust wind speed increased by 15% when the gust period is lowered from 5 s to 0.5 s (Figure 2.7) at a mean wind speed of 18 m/s. A gust duration of 2-3 s, such as the typical response of a Dines anemometer (Holmes and Ginger, 2012), is commonly used in the design wind codes for long-span cable-supported bridges (Xu, 2013) and design standards for large buildings with heights less than 200 m and roof spans less than 100 m (Cook, 1985; Standards Australia and Standards New Zealand, 2011). The significance of the magnitude of the gust period is particularly relevant for AS/NZS 1170.2 because of its redefinition as an equivalent moving average over 0.2 seconds. Holmes et al. (2014) showed that the effect of turbulence intensity becomes significant for shorter duration gusts. As shown in Figure 2.7, the expected 0.1-second gust factor increased by 28% with a doubling of turbulence intensity I_u from 10% to 20%. This spans the range of I_u observed at heights below 10 m in flat desert and open country terrains where heliostat fields are usually located. The redefinition of the gust period in Holmes et al. (2014) from 3 seconds to 0.2 seconds leads to a 10% increase in the velocity gust factor in Figure 2.7. The consideration of short-duration gusts is important for tall buildings with large dynamic responses to very large eddies with low frequencies. However, the effect of the gust period on the estimated peak wind loads using the gust factor approach requires further investigation at heights below 10 m in the ABL where heliostats are stowed.

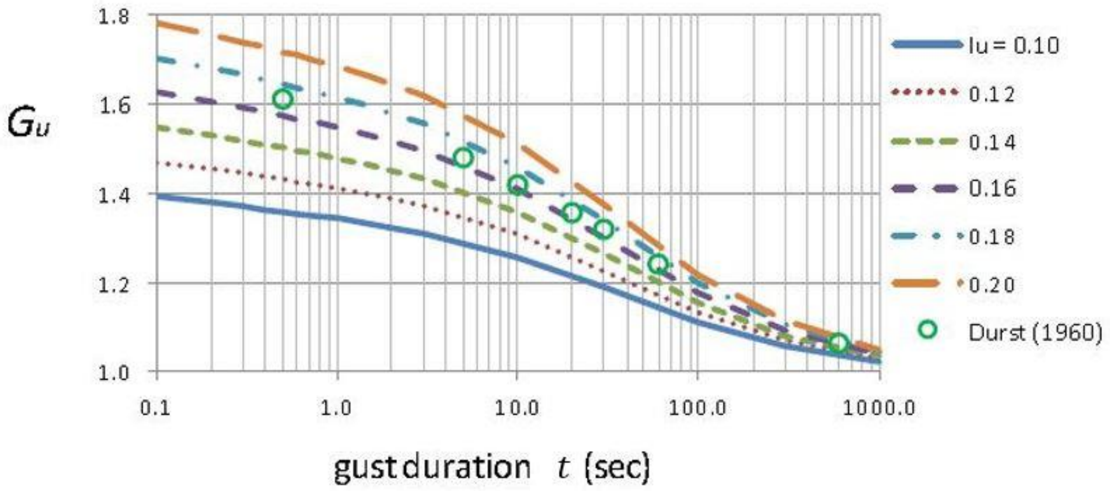

Figure 2.7. Effect of gust period t and turbulence intensity I_u on the velocity gust factor G_u for $L_u^x/\bar{U} = 10$ s and $T = 3600$ s (Holmes et al., 2014).

Atmospheric surface layer turbulence was previously measured by Dines pressure-tube anemometers with a moving average filter of 3 seconds, but the effective gust duration was recognised by Holmes et al. (2014) to be much shorter. As a result, the gust period was changed from 3 to 0.2 s as an equivalent moving average by AS/NZS 1170.2 for buildings with heights less than 200 m (Standards Australia and Standards New Zealand, 2011). Figure 2.8 shows that the use of a 3-second moving average filter truncates a large part of the wind spectrum at a design wind speed of 30 m/s typical for a tall building. The equivalent spatial filter has a frontal area of 3200 m^2 corresponding to a tall building, however for smaller physical structures such as heliostats the calculated gust factor can be underestimated (Holmes et al., 2014). Ghanadi et al. (2016) found that the velocity gust factor increased by 3% at a 10 m height in a low-roughness desert surface layer when the gust period was reduced from 3 s to 0.2 s in the redefinition of AS/NZS 1170.2 (Holmes et al., 2014). This difference increased to more than 5% at lower heights, such as 6 m where the largest 150 m^2 heliostats are conventionally stowed (Téllez et al., 2014). The peak wind loads on the largest stowed heliostats would therefore be under-estimated by approximately 10%, from the proportionality of peak wind load with the gust factor squared, with increasing error at lower heights where smaller heliostat mirrors are stowed. The dynamic response factor C_{dyn} can be calculated in AS/NZS 1170.2 for along-wind dynamic response of tall structures with a natural first-mode fundamental frequency between 0.2 Hz and 1 Hz (Holmes et al., 2012), however the natural frequencies of heliostats is typically larger than 1 Hz (Gong et al., 2012; Griffith et al., 2015). Hence, design wind codes for large buildings, such as AS/NZS 1170.2, are likely to cause errors in the calculation of the dynamic effects of the turbulent velocity fluctuations at lower frequencies and hence can under-estimate the peak wind loads on stowed heliostats.

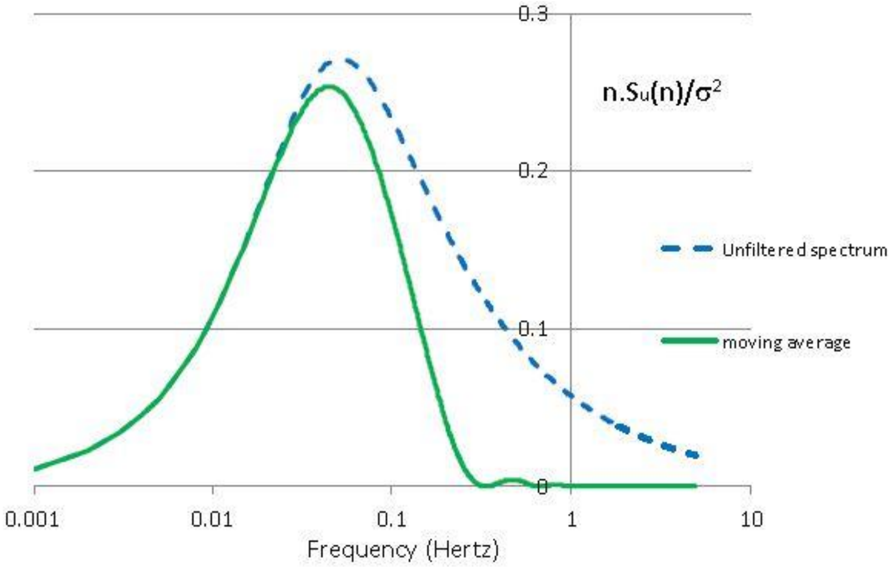

Figure 2.8. Effect of a moving average filter with a 3-second gust period on the longitudinal power spectrum (Holmes et al., 2014).

2.1.6 Integral Length Scales

The distribution of energy in the turbulent velocity fluctuations is proposed by similarity theory to give rise to a cascade of eddies with a range of length scales spanning the inertial subrange of the frequency domain (Tennekes and Lumley, 1972). Turbulent flow fluctuations are often characterised as coherent eddies in order to simplify the descriptions of the random three-dimensional eddying fluid motions in the ABL over a wide range of length scales. Coherent eddies exist for sufficient time periods to have a significant influence on the time-averaged statistics of a turbulent flow field (Venditti et al., 2013). The integral length scales represent the sizes of the largest eddies in a specified direction that correspond to the largest magnitudes of the power spectra in that direction (Milbank et al., 2005; Watkins, 2012). The longitudinal integral length scale L_u^x (m) at a given height H is defined in Figure 2.9(a) as the streamwise spacing between two-dimensional spanwise eddies with a Rankine velocity distribution. The size of the largest eddies increases linearly as the mean convective velocity increases with height relative to the thickness of the lower atmospheric surface layer (ASL) $\delta_s \approx 100$ m in

Figure 2.9(b), such that the ratio of L_u^x to the chord length c of a flat plate increases at larger heights. Small eddies ($L_u^x < c$) result in pressure and load distributions on the plate that become uncorrelated with distance of separation, however large eddies ($L_u^x \geq c$) cause well-correlated pressures over the surface of the plate that tend to lead to the maximum wind loads (Greenway, 1979; Mendis et al., 2007).

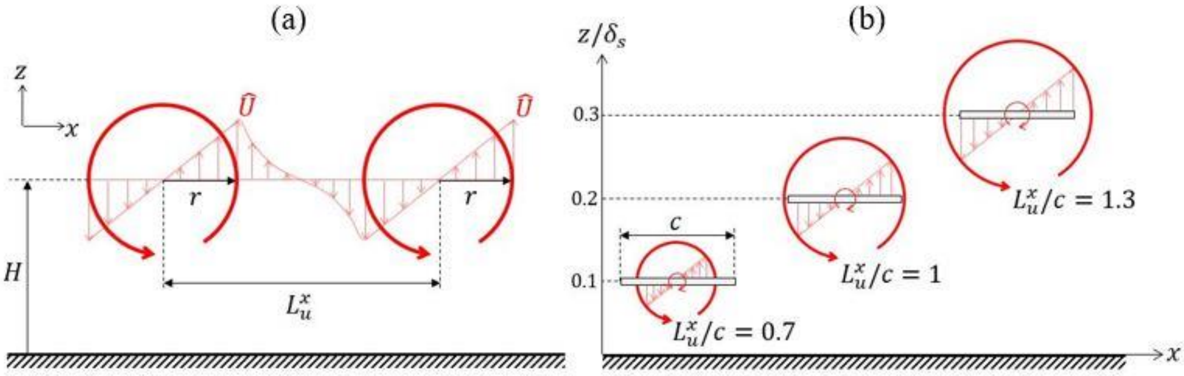

Figure 2.9. (a) Schematic of a Rankine velocity distribution with peak velocity $\hat{U}$ between successive spanwise vortices with an axis of rotation perpendicular to the flow direction x and the definition of the longitudinal integral length scale L_u^x at an elevation axis height H above the ground.
(b) Wind load distribution on a flat plate and approximate values of L_u^x/c calculated at three heights by Emes et al. (2017) in a desert terrain ASL.

The largest eddies in the ABL are spatially extensive structures that require analysis of many points in space. Point velocity measurements, obtained as a function of time, can be transformed to spatially-distributed data by Taylor's hypothesis. This assumes that eddies are embedded in a frozen turbulence field are convected downstream at the mean wind speed $\overline{U}$ (m/s) in the streamwise x direction and hence, do not evolve with time (Kaimal and Finnigan, 1994). The integral length scale at a given height in the ABL is therefore calculated as (Swamy et al., 1979):

$$L_u^x = T_u^x \overline{U}, \tag{2.19}$$

where T_u^x (s) is the integral time scale representing the time taken for the largest eddies to traverse a single point in the ABL. Integral time scales are commonly estimated from the covariance of single point velocity data with a time delay (τ) using the normalised autocorrelation function $R_u(\tau)$ of the fluctuating component of the turbulence velocity (Kaimal and Finnigan, 1994):

$$R_u(\tau) = \frac{\overline{u'(t)u'(t+\tau)}}{{\sigma_u}^2} \tag{2.20}$$

Here $u'(t) = u(t) - \overline{U}$ defines the fluctuating component of streamwise velocity and ${\sigma_u}^2$ is the variance of the streamwise velocity fluctuations. The integral time scale is calculated as the integral of the autocorrelation function in Equation (2.20) up to its first-zero crossing τ_0 in Figure 2.10, assuming that $R_u(\tau)$ fluctuates close to zero after this point (Swamy et al., 1979):

$$T_u^x = \int_0^\infty R_u(\tau)\, d\tau \approx \int_0^{\tau_0} R_u(\tau)\, d\tau, \tag{2.21}$$

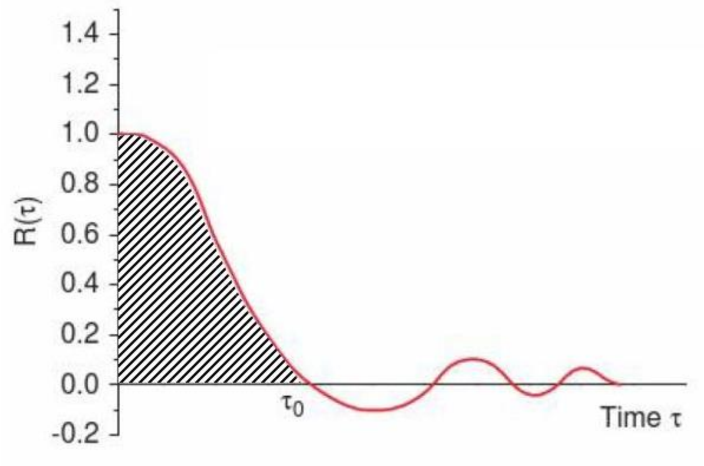

Figure 2.10. Example autocorrelation function of a velocity signal (Xu, 2013). The shaded area indicates the magnitude of the integral time scale calculated to the first-zero crossing τ_0 using Equation (2.21).

The majority of integral length scale data available in the literature has been obtained from field-site anemometer velocity measurements in rural and urban ABLs (Counihan, 1975; Flay and Stevenson, 1988; Teunissen, 1980), however there are few recognised standards due to the diverse spatial turbulence characteristics in the lower surface layer. The model of Counihan (1975) predicts the variation of longitudinal integral length scales with height (10 m $\leq z \leq$ 240 m) as:

$$L_u^x(z) = Cz^{1/n}, \tag{2.22}$$

where C and $1/n$ are empirical variables as a function of the roughness height z_0. Solari and Piccardo (2001) proposed the following equation based on the analysis of integral length scale data in the surface layer ($z \leq$ 200 m) with surface roughness height z_0 ranging from 10 mm to 1 m:

$$L_u^x(z) = 300\left(\frac{z}{200}\right)^{0.67+0.05\ln(z_0)} \tag{2.23}$$

AS/NZS 1170.2 (Standards Australia and Standards New Zealand, 2011) uses the following formula to predict the integral length scales in the surface layer ($z \leq$ 200 m):

$$L_u^x(z) = 85\left(\frac{z}{10}\right)^{0.25} \tag{2.24}$$

The calculated integral length scale using Equation (2.24) gives a value of L_u^x of 85 m at a height of 10 m and is used to estimate the dynamic response factor C_{dyn} for along-wind dynamic response of large physical structures such as tall buildings with heights less than 200 m (Holmes et al., 2012; Standards Australia and Standards New Zealand, 2011). However, the largest heliostats ($A = 150$ m^2) are usually stowed at a height of 6 m (Téllez et al., 2014), hence the values of L_u^x closer to the ground approaching a stowed heliostat are likely to deviate from those adopted in standard design wind codes for tall buildings.

ESDU 85020 is a frequently used data set based on a semi-empirical model for the integral length scales of atmospheric turbulence over uniform terrain in a neutral ABL. The model extends previous empirical formulations for L_u^x to higher equivalent design wind speeds up to 30 m/s at heights corresponding to the taller buildings for which dynamic effects are more significant (Engineering Sciences Data Unit, 1985). Figure 2.11 presents the ESDU 85020 correlations for longitudinal integral length scale L_u^x as a function of height z and surface roughness height z_0. Integral length scales are estimated based on similarity theory predictions of their large dependence on the surface roughness height z_0 in the lower inertial sublayer and on the boundary layer thickness δ in the outer layer of the ABL (Engineering Sciences Data Unit, 1985). The atmospheric surface layer (ASL) in Figure 2.1 is approximated as a constant-stress layer by assuming the Coriolis acceleration f due to the rotation of the Earth and large-scale pressure gradient terms balance the vertical stress gradient in horizontally-homogeneous conditions (Rao et al., 1974). The average thickness of both rural and urban terrain ABLs is estimated as $\delta \approx 600$ m based on the analysis of data for high wind speeds ($\overline{U}_{10m} > 5$–7 m/s) that produce adiabatic conditions (Counihan, 1975). The integral length scales of turbulent eddies and the ABL thickness are influenced by changes in z_0 (Rao et al., 1974), hence δ can be estimated as a function of z_0 from Equations (2.25–2.27) following Xu (2013):

$$\kappa = \left[\frac{k}{\ln(10/z_0)}\right]^2, \tag{2.25}$$

$$U_\tau = \sqrt{\kappa(\overline{U}_{10m})^2}, \tag{2.26}$$

$$\delta = U_\tau/6f. \tag{2.27}$$

Here κ is the surface friction coefficient representing the non-dimensional surface shear stress and $k = 0.4$ is von Karman’s constant and f (m^2/s) is the Coriolis acceleration. Table 2.1 presents the effect of the surface roughness on the characteristic velocity and length scales of the ABL, calculated using Equations (2.25–2.27) for four values of z_0 that closely represent the terrain categories in AS/NZS 1170.2 (Standards Australia and Standards New Zealand, 2011). There is a significant effect of z_0 on the values of surface friction coefficient κ, ABL thickness δ and the longitudinal integral length scales L_u^x at a 10 m height in the ABL predicted by the ESDU (1985) model. Figure 2.11 presents the profiles of L_u^x for the four terrain types in Table 2.1 that are predicted by ESDU 85020 based on a reference mean wind speed $\overline{U}_{10r} = 20$ m/s at a 10 m height over open country terrain (z_0 = 0.03 m) with f = 1×10^{-5} rad/s (Engineering Sciences Data Unit, 1985). The model provides a correction factor k_L to account for the variation of L_u^x with changes in $\overline{U}_{10r}$ and f within an estimated ±8% error.

Table 2.1. Effect of surface roughness on the ABL characteristics (Xu, 2013)

Surface roughness height $\boldsymbol{z_0}$ (m)	Surface friction coefficient $\boldsymbol{\kappa}$	Power law roughness exponent $\boldsymbol{\alpha}$	Boundary layer thickness $\boldsymbol{\delta}$ (m)	Integral length scale at 10 m height $\boldsymbol{L_u^x}$ (m)	AS/NZS 1170.2 terrain category and description
0.001	0.002	0.12	300	175	1 – Very flat (desert)
0.01	0.003	0.16	350	132	2 – Open (grassland)
0.1	0.008	0.22	400	84	3 – Suburban (5 m buildings)
1	0.03	0.30	450	45	4 – Dense (30 m buildings)

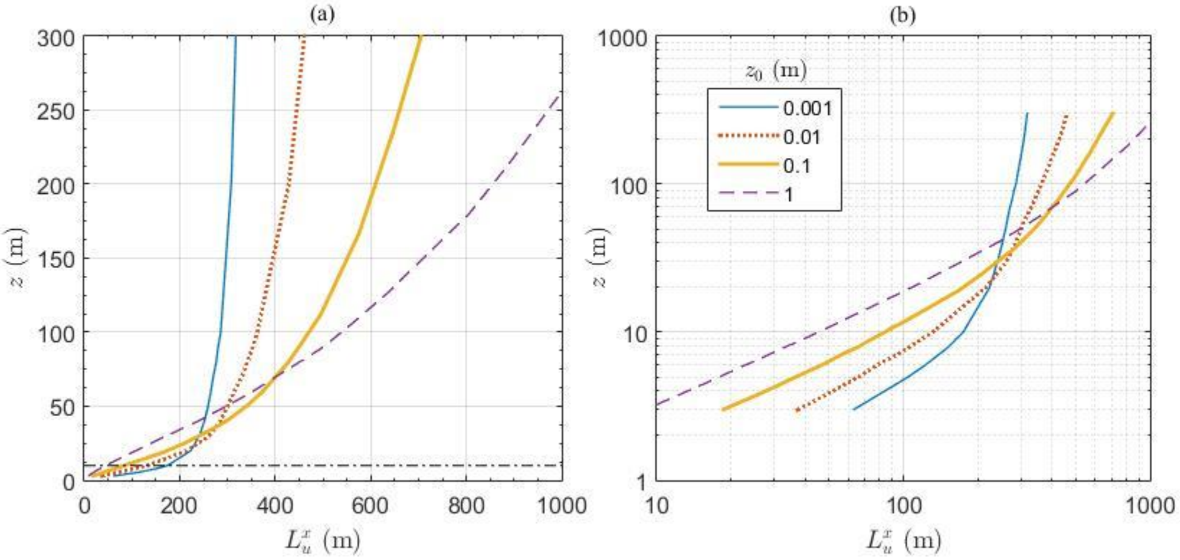

Figure 2.11. (a) Linear and (b) Logarithmic profiles of longitudinal integral length scales L_u^x (m) as a function of height z (m) and surface roughness height z_0 (m) in a neutral ABL predicted by ESDU 85020 for equilibrium conditions U_{10r} = 20 m/s and f = 1×10^{-5} rad/s. The dashed horizontal line in Figure 2.11(a) indicates a height of 10 m commonly used as a reference for field measurements of turbulence in the ASL. Data extracted from Engineering Sciences Data Unit (1985).

For a heliostat stowed at heights between a typical range of 3 m and 6 m, ESDU 85020 predicts L_u^x to range between 37 m and 65 m over an open country terrain ($z_0 = 0.01$ m) and from 63 m to 123 m over a flat desert terrain ($z_0 = 0.01$ m). The sizes of the largest vortices are therefore typically the same order as the chord length of the heliostat and as much as an order of magnitude larger. Eddies that are of the same order and a maximum of one order larger than the heliostat size are presumed to cause the peak wind loads on stowed heliostats because smaller eddies do not cause high net pressures distributed over the heliostat surface, whereas considerably larger eddies have significantly lower vertical velocity fluctuations at the elevation axis height of the heliostat (Pfahl et al., 2015). The effect of the size of the largest eddies on peak wind loads on a stowed heliostat, such as the ratio of L_u^x/c, requires further investigation to better understand the dynamic effects on heliostats such as flutter and galloping.

Experimental field measurements in open country terrains have led to the development of semi-empirical models to predict the spatial structure of turbulence in the atmospheric surface layer (ASL). Semi-empirical models developed on the basis of similarity theory describe the flow over rural and urban terrains sufficiently to predict the surface shear stress, roughness height and turbulence intensities in the surface layer (Teunissen, 1980). However, field measurements in rural terrains have shown a considerable variation of integral length scales using different techniques. Integral length scales have most commonly been approximated from the frequency corresponding to the peak of a von Karman spectrum fitted to the observed spectra in field measurements. As shown in Figure 2.12, Flay and Stevenson (1988) found that the spectral-fit approach tended to underestimate length scales in an open country terrain due to uncertainties associated with the identification of the peak in the broad spectra of slowly-varying turbulent eddies. Teunissen (1980) found that the correlation-integral approach using the autocorrelation function of velocity produced the largest longitudinal integral length scales in reasonable agreement with the ESDU (1974) model but only half of those predicted by the model of Counihan (1975). Deviations from similarity theory of the mean velocity, turbulence variances and length scales are believed to be a result of inherent uncertainties in the surface roughness height in semi-empirical models of turbulence in the ABL, which leads to a scattering of results in the gust-excited response (Solari and Piccardo, 2001). Variations of the surface roughness height over open country and rural terrains result in significant changes to the distribution of integral length scales at lower heights in the surface layer.

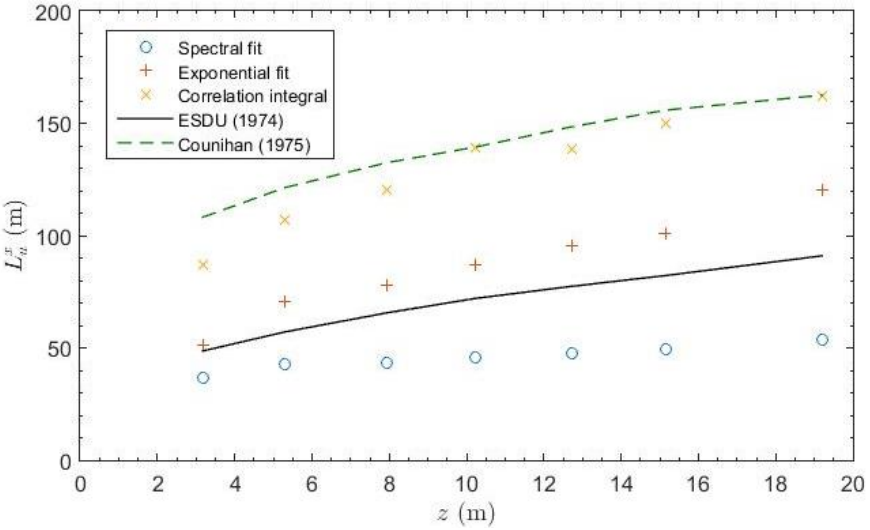

Figure 2.12. Longitudinal integral length scales calculated using different techniques in the lowest 20 m of a neutral ASL over an open country terrain. Data extracted from Flay and Stevenson (1988).

Full-scale field measurements in surface layers over different terrains have shown considerable scatter, which is reflected in the width of the ESDU (1974) and (1985) correlation bands. Farell and Iyengar (1999) observed that field measurements of L_u^x profiles in open country and urban terrains cluster around the ESDU (1985) correlations for the suburb of a large town ($z_0 = 0.3$ m) and for city centres ($z_0 = 0.7$ m), as shown in Figure 2.13. Longitudinal integral length scales in urban terrains from the review of Counihan (1975) by Soma over Tokyo in 1964 and by Ivanov and Klinov (1961) over Moscow vary by over double in magnitude, which is most likely because of the dependence of ESDU L_u^x correlations on reference velocities at design wind speeds that are larger than typical measurement wind speeds and the different techniques used for calculating integral length scales (Farell and Iyengar, 1999). Maximum cross-correlation coefficients of the longitudinal velocity with vertical separations and zero-time-delay decrease by 10% with increasing vertical separations in the lowest 20 m of the ASL, as shown in Figure 2.14. These maxima become negatively skewed with increasing vertical separation, which indicates that the wind gusts at the lowest measurement height of 3 m are delayed with respect to larger heights. The convergence between integral length scales calculated using both autocorrelation and cross-correlation functions at lower heights supports the attached eddy hypothesis of Townsend (1976) that the active (local) eddies in the surface layer are not influenced by inactive (non-local) eddies in the outer layer of the ABL that scale on δ (Hong et al., 2004). The scatter in observed length scale data in different ABLs also supports similarity theory, which proposes that the eddy sizes are more significantly affected by surface roughness than wind speed at lower heights in the surface layer (Engineering Sciences Data Unit, 1985).

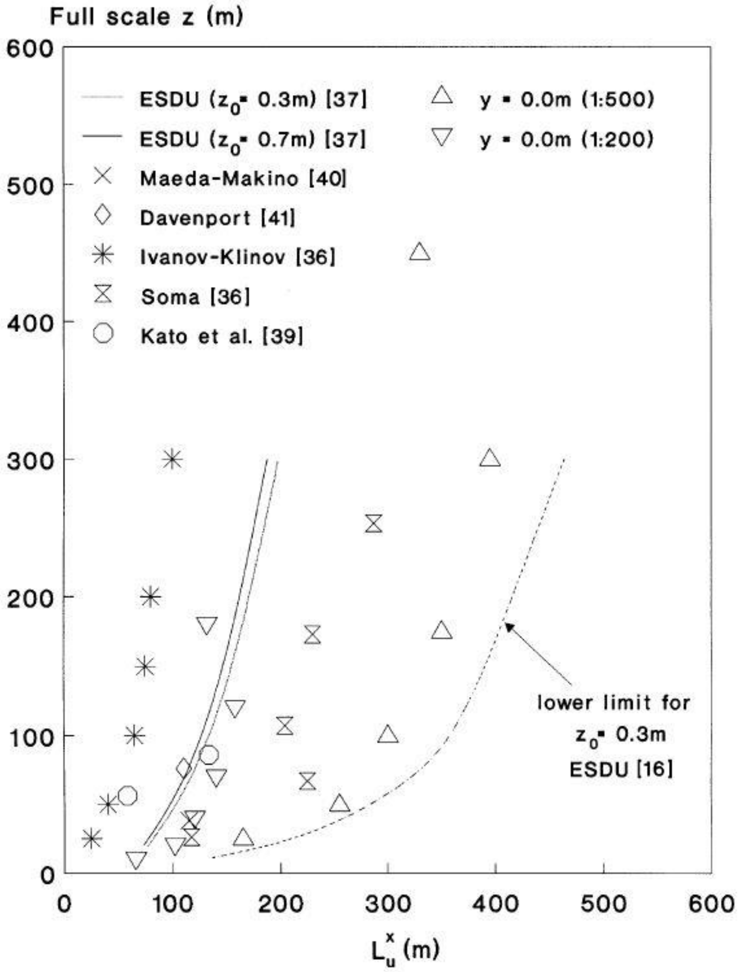

Figure 2.13. Longitudinal integral length scale profiles in the full-scale atmospheric boundary layer (Farell and Iyengar, 1999).

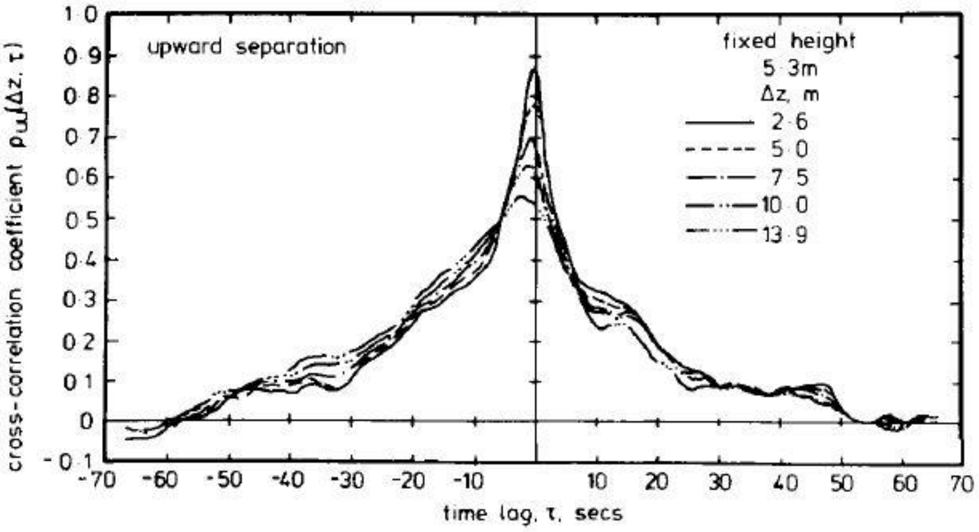

Figure 2.14. Cross-correlations at different heights in the surface layer of a rural terrain (Flay and Stevenson, 1988).

2.2. Aerodynamic Characteristics of Flat Plates

The horizontal alignment of a heliostat mirror in the stow position can be represented as a thin flat plate aligned parallel to the ground, from the assumption that the drives and support structure have a small effect on the pressure distributions and peak wind loads on a heliostat in stow position. This assumption allowed for comparison with the extensive literature of thin longitudinal plates parallel to the flow. The two-dimensional flow around thin bluff bodies, such as square flat plates and airfoils, has been widely investigated in the literature. Extensive research has been undertaken on the transition to turbulence in the development of a boundary layer on a flat plate subjected to uniform flow in wind tunnel experiments. Aerodynamic characteristics of the two-dimensional flow around bluff bodies include a large region of separated flow, a high value of the drag coefficient and the phenomenon of vortex shedding (Roshko, 1993). This section outlines the peak forces and moments on horizontally-aligned flat plates in isolation and in tandem arrangements. Flow-induced vibrations arising from turbulence in the approaching flow are also investigated on the simplified geometries of rectangular prisms commonly used to estimate the peak wind loading on buildings in design wind codes and standards.

2.2.1. Peak Forces and Moments

Flat plates orientated horizontally in a uniform laminar flow experience a friction dominated load with no lift, however the presence of freestream turbulence leads to a pressure difference between the upper and lower surfaces of the plate and thus pressure drag and lift become significant (Chen and Chiou, 1998; Roshko, 1993). Yaghoubi and Mahmoodi (2004) noted large fluctuations of streamwise velocity and turbulence intensity in the leading edge region, particularly for low aspect ratio plates where shear layer growth rate reduces due to the finite plate length. This leads to the dominant effects of the friction coefficient on the plate surface and significant increases in pressure drag. Wind load measurements by Bearman (1971) have shown a strong correlation between the fluctuating drag force on a normal flat plate aligned vertically and the velocity fluctuations in the approaching turbulent flow. Cruz et al. (2008) measured the aerodynamic coefficients on a flat plate airfoil, aligned parallel to the flow direction with a chord length c of 0.15 m and a thickness-to-chord ratio of 1.9%. The plate airfoil was exposed to three variations of grid-generated turbulence, as an application of small-scale micro-air-vehicles (MAVs) at heights below 5 m in the ABL. Figure 2.15(a) shows that the maximum lift coefficient on the plate airfoil increased by 5% with no grid at low turbulence intensity ($I_u = 1.4\%$) and by up to 10% using grid A at a higher turbulence intensity ($I_u = 13.4\%$) with increasing Reynolds numbers from 54,000 to 135,000. However, the maximum lift coefficient was more significantly influenced by the addition of grid-generated turbulence, such as an average increase of 29% at constant Reynolds number. In comparison, the pitching moment coefficient in Figure 2.15(b) increased by 34% on average with the addition of grid-generated turbulence at constant Reynolds number. The effect of turbulence intensity in the approaching flow is therefore more significant than Reynolds number on the maximum wind load coefficients on a flat plate aligned parallel to the ground. It is noted that the load coefficients were measured by Cruz et al. (2008) at moderate I_u up to 13.4% for a flat plate spanning the width of the tunnel, however findings on a flat plate with a finite span are required to determine the effect of turbulence intensity on the peak load coefficients on a stowed heliostat.

Analysis of peak wind loads in wind tunnel experiments based solely on turbulence intensities would represent the total intensity of gusts, however it is known that the eddy size distribution also significantly affects peak wind loads on physical structures (Pfahl et al., 2015). The sizes of the eddies corresponding to the peaks of the turbulent power spectra, defined by the longitudinal integral length scale L_u^x (Section 2.1.6), were reported by Cruz et al. (2008) for the three grid turbulence configurations. The maximum wind load coefficients were found to increase as the ratio of the largest eddies to the chord length of the plate (L_u^x/c) was reduced from 5.3 (no grid) to 1.6 (grid B) at $Re \leq 10{,}000$. The largest load coefficients were measured for grid A with $L_u^x/c = 2.2$ at $Re > 10{,}000$. In comparison, Holdø et al. (1982) found that a logarithmic velocity profile in a neutral ABL ($I_u = 12\%$) produced a 10% increase in the maximum base pressure coefficient on wind tunnel models of low-rise buildings of height D ($L_u^x/D \approx 2.8$) compared to a uniform approaching flow ($L_u^x/D \approx 1.6$). The sizes of the largest vortices generated using grids were limited by the scale of the grid bar width and Cruz et al. (2008) acknowledged that only the high-frequency region of the power spectra could be produced (Milbank et al., 2005). Hence, alternative methods of large-scale vortex generation are required to produce the relevant eddy sizes corresponding to the peaks of the power spectra in the full-scale ABL and hence assess the effects of L_u^x/c on the aerodynamic coefficients on horizontally-aligned plates exposed to turbulence, such as a stowed heliostat in the ABL.

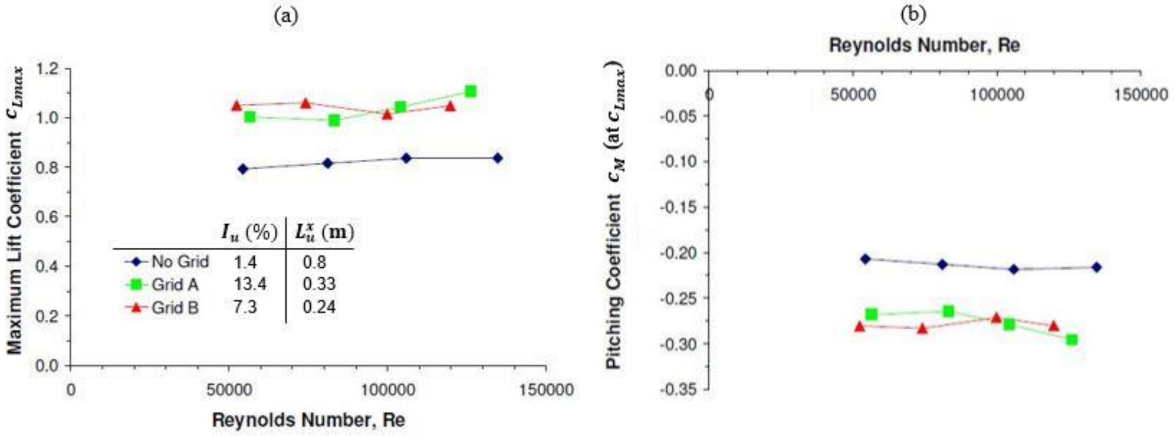

Figure 2.15. Effect of Reynolds number on the aerodynamic coefficients on a flat plate airfoil ($c = 0.15$ m, $t/c = 0.019$) exposed to three variations of grid-generated turbulence: (a) Maximum lift coefficient; (b) Pitching moment at maximum lift coefficient. Reproduced from Cruz et al. (2008).

The position of maximum lift is important for identifying the region on a flat plate that is most vulnerable to stresses and deflections, such as for the analysis of critical failures of heliostat mirrors in stow position (Gong et al., 2013). Maximum lift on a plate is determined from the distribution of non-dimensional pressure coefficients on the upper and lower surfaces, which are independent of the size of the plate (Gong et al., 2013). Chen and Chiou (1998) calculated the lift coefficient on a square plate with chord length c of 120 mm exposed to a turbulent flow ($Re_c = U_\infty c/\nu =$ 20,000) produced by an upstream pitching airfoil vortex generator at different vertical offsets z_V/c from the horizontal plate, as shown in Figure 2.16(a). The maximum lift coefficient of 0.44 occurs at $x/c = 0.1$ downstream of the leading edge at $z_V/c = 0$ in Figure 2.16(b). The effect of increasing z_V/c from 0 to 0.375 flattens the lift coefficient curve over the surface of the plate. The maximum lift coefficient decreases linearly with z_V/c by 43% to 0.25 and its location moves further downstream to $x/c = 0.125$. The lift coefficient distributions over the chord length of the plate, calculated from the integration of the non-dimensional pressure coefficients (Figure 2.16(c)) over the upper and lower surfaces of the plate, showed decreasing and increasing absolute pressures, respectively, as the vortex passes the plate. Figure 2.16(c) shows the effect of changing the leading edge profile of the flat plate on the pressure coefficient distributions. Chen and Chiou (1998) found that the amplitude of lift coefficient variation for the square leading edge plate is greater by at least 25% due to the larger region of low-pressure separated flow produced by the corners of the blunt leading edge. A minimal difference was found between the sharp and elliptical leading edges, except for the pressure on the leading edge which has little influence on the variation of lift (Chen and Chiou, 1998). Hence, the peak lift coefficient on a stowed heliostat can potentially be reduced by altering the square leading edge profile of the mirror. The unsteady pressure distribution due to the interaction with a large vortex is influenced by its vertical offset from the heliostat mirror, however the spatial distribution of vortices in the ABL requires further investigation.

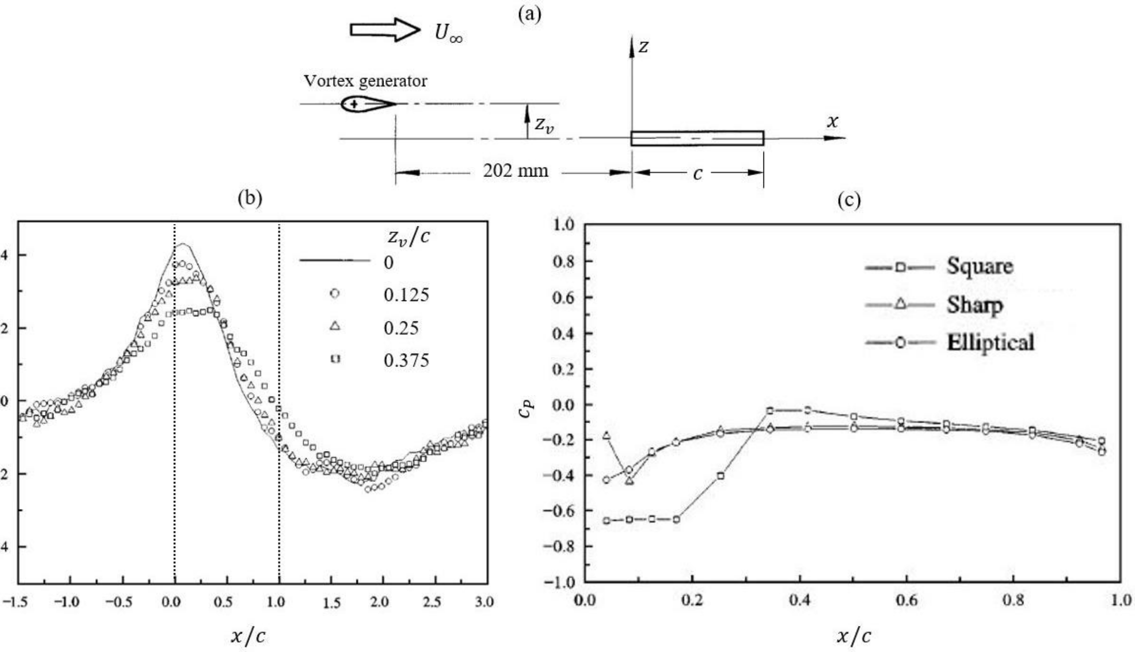

Figure 2.16. (a) Experimental setup for the generation of a spanwise vortex by a pitching NACA 0015 airfoil of 50 mm chord length positioned with a vertical offset z_v upstream of a square flat plate of chord length $c = 120$ mm and thickness-chord ratio $t/c = 0.05$; (b) Variation of lift coefficient measured on a square leading edge flat plate as a function of streamwise location of the vortex x/c and vertical offset z_v; (c) Variation of pressure coefficient along the surface of a flat plate with three leading edge profiles. Reproduced from Chen and Chiou (1998).

Large-scale spanwise vortices can have a significant effect on the peak lift forces on flat plates that are aligned horizontally, such as a heliostat in stow position close to the ground in the ABL. The controlled generation of large-scale spanwise vortices allows the isolation and characterisation of the length scales of vortices. Booth (1990) generated a series of large-scale two-dimensional counter-rotating spanwise vortices with streamwise spacing equivalent to 5 chord lengths apart ($L_u^x \approx 5c$) by the oscillation of a NACA 0012 airfoil ($c = 0.1524$ m) about its quarter chord between pitch angles of 10° and -10°, as shown in Figure 2.17(a). The transient lift coefficient (Figure 2.17(b)) on a downstream blade model, aligned horizontally at an angle of attack α of 0°, was calculated from the integration of the unsteady pressures over the surface of the leading 25% of the blade chord. The amplitude of the blade loading at the largest vertical offset $z/c =$ –0.219 is almost half that of the other three offsets, because of the dissipation of the counter-clockwise (negative) rotating vortices before they pass below the blade. In contrast, clockwise (positive) rotating vortices were found to disrupt rapidly when passing over the top of the blade. Booth (1990) found that the shape of the second maxima of the loading pulses became more rounded with smaller blade-to-vortex miss distance or decreasing absolute magnitude of z/c, as the vortices become more elongated and take longer to traverse the blade. Hence, organised spanwise vortices with a low degree of elongation that pass close to the rotation axis and over the top surface of an airfoil generate significant increases of the maximum lift coefficient near the leading edge. Further understanding of the bursting phenomenon responsible for these peaks in lift coefficient and their application to thin flat plates has significant implications for the large spanwise vortices embedded in the turbulence in the ABL approaching the leading edge of heliostats in stow position.

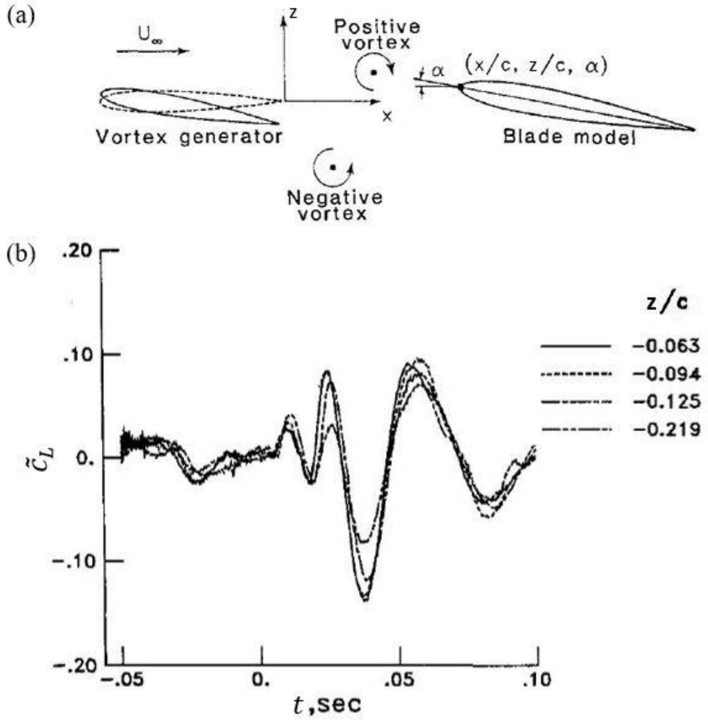

Figure 2.17. (a) Schematic of experimental setup of a pitching NACA 0012 airfoil vortex generator of chord length $c = 0.1524$ m and downstream blade model; (b) Time history of transient lift coefficient $\tilde{c}_L$ on the blade model ($\alpha = 0°$) as a function of the vertical offset z/c of the upstream vortex generator to the blade model. Reproduced from Booth (1990).

2.2.2. Flow-Induced Vibrations

Flow-induced vibrations of long slender bluff bodies from wind excitation are affected by the turbulence in the approaching flow and vortex shedding that results from flow separation from the top and both of the side surfaces of tall buildings and towers (Bearman, 1984; Sakamoto and Arie, 1983). Galloping is a dynamic instability of slender prismatic structures caused by self-excitation at a critical wind speed that leads to an exponentially-growing harmonic oscillation (Jain et al., 1996; Mannini et al., 2013). By contrast, vortex-induced vibration (VIV) is caused by the non-linear response of the fluctuating forces due to the alternate shedding of vortices with one mode of vibration of the structure (Hansen, 2007; Mannini et al., 2013). The critical wind velocity of VIV can be predicted using the Strouhal number, whereas the galloping onset velocity is proportional to the mass-damping parameter known as the Scruton number and can be calculated based on quasi-steady galloping theory (Borri et al., 2012). The effects of both VIV and galloping can occur on slender prismatic structures with a bluff cross-section in the ABL. Although AS/NZS 1170.2 does not specify conditions for VIV and galloping, EN 1991-1.4 (Eurocode, 2010) states that if the ratio of the galloping to VIV critical wind speeds is either lower than 0.7 or larger than 1.5, the two phenomena can be considered separately (Mannini et al., 2013). Hence, the interaction between VIV and galloping on structures is an important consideration for the dynamic wind loads on slender prismatic bodies and thin flat plates.

The dynamic effects on large physical structures in the ABL are commonly assessed using scale models in wind tunnel experiments, such as at the average roof height h of structures with heights $h \leq 200$ m and roof spans $b < 100$ m in AS/NZS 1170.2 (Standards Australia and Standards New Zealand, 2011). Sakamoto (1985) measured the surface pressures on a rectangular prism of constant height $h = 90$ mm and varying square cross-section width b exposed to a turbulent boundary layer of thickness $\delta = 60$ mm ($h/\delta = 1.5$). The fluctuating root-mean-square (RMS) lift coefficient c_{Lf} (Figure 2.18(a)) is largest at a wind angle β of 0° and decreases rapidly with increasing β before it plateaus at $\beta \geq 25°$ at all aspect ratios except $h/b = 1$. Sakamoto (1985) suggested that the lower values of c_{Lf} at $\beta \geq 25°$ is caused by a considerable reduction in strength of the vortices in the separated shear layer because of the reattachment of the shear layer further downstream. This is reflected in a flattening of the power spectrum of the fluctuating lift S_{Lf} (Figure 2.18(b)) at $\beta = 25°$ to lower energy levels and irregular frequencies. In contrast, Sakamoto (1985) found a prominent prevailing frequency $n \approx 65$ Hz for β in the range of 0° and 20° that is shifted to slightly higher frequencies with increasing β at a constant aspect ratio ($h/b = 2$) that correspond to the prominent frequency of vortices shed behind the prism. Hence, the fluctuating lift on rectangular bodies is largest at small wind angles when acting perpendicular to the surface, resulting in the stretching of horseshoe-shaped vortices around the body (Sakamoto and Arie, 1983).

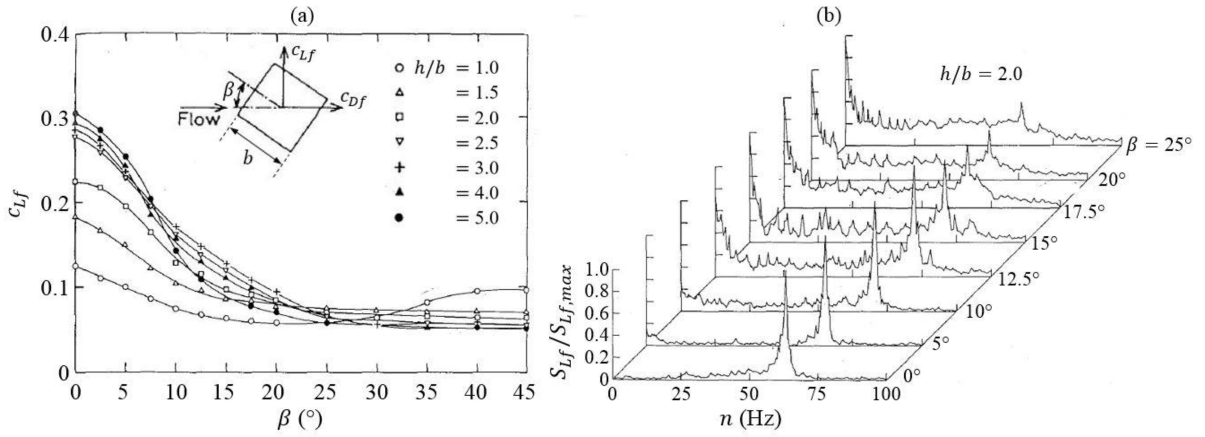

Figure 2.18. Dynamic wind loads on a rectangular prism with height h and square cross-section width b exposed to a turbulent boundary layer: (a) Fluctuating root-mean-square lift coefficient c_{Lf} as a function of the angle of attack of the wind β at different aspect ratios h/b; (b) Ratio of fluctuating lift power spectra S_{Lf} normalised to the peak magnitude of the spectrum ($S_{Lf,max}$) at $\beta = 0°$ as a function of frequency n and wind angle β. Reproduced from Sakamoto (1985).

The turbulence parameters in the ABL are known to influence the fluctuating pressures and unsteady forces on physical structures and amplify the effects of VIV and galloping. In agreement with the results (Figure 2.18) of Sakamoto (1985), Kawai (1995) found that the VIV of a tall building was strengthened by freestream turbulence when the separated flow does not reattach to the side face. The onset velocities of VIV and the galloping vibration were the smallest and the amplitude of the vibrations were the largest when wind attacks normal to the face ($\beta = 0°$). Galloping vibration had the largest effect on a building with a ratio of depth in the flow direction to width (B/b) of 2 when the separated shear layer partially reattaches to the side face, however the amplitude of this vibration in a turbulent boundary layer was much smaller than in smooth flow. In contrast, the largest effect of VIV was found by Kawai (1995) for a building with a shallow section ($B/b = 1/2$) in both smooth and turbulent boundary layer flow when the separated shear layer does not reattach to the side face. In this case, Kawai (1995) suggested that the promotion of flow entrainment of the separated shear layer by freestream turbulence had amplified VIV through the shedding of high-energy vortices into the wake. The critical condition for aerodynamic instability of the building for the level of the normalised RMS displacement $\sigma_y/h = 1/1000$ was found to be at reduced velocities $U/n\sqrt{bB} \geq 5$ and was not significantly affected by B/b (Kawai, 1995). Increasing the ratio L_u^x/h of the sizes of the high-energy eddies, defined in Section 2.1.6 by the longitudinal integral length scale, to the height of a scale-model low-rise building from 1.6 to 2.8 was found by Holdø et al. (1982) to increase the peak drag force by 10%. In contrast, Roadman and Mohseni (2009) observed the maximum wind loads on small-scale micro-air-vehicles (MAVs) when L_u^x was an order of magnitude larger or smaller than their chord length ($c \leq 15$ cm). The effect of increasing the length scale ratio (L_u^x/D) of a 2D short rectangular cylinder of height D to greater than 3 was found by Nakamura (1993) to have a very small effect on the body-scale turbulence ($I_u = 10$-12%) and galloping vibration. The maximum lift forces and hinge moments on a heliostat stowed at elevation axis heights H below 10 m in the ABL are likely to occur from the interaction with eddies of the same order of magnitude as the heliostat mirror chord length c (Pfahl et al., 2015), however this has not previously been studied for an isolated heliostat in stow position.

2.2.3. Effects of Gap Ratio on Tandem Bluff Body Loads

The static and dynamic wind loads on tandem bluff bodies are highly dependent on the spacing between the bluff bodies relative to the characteristic length of the body, defined by the gap ratio d/c, and is an important consideration for the arrangement and density of heliostats in a field. In the case of two circular cylinders in tandem, the fluctuating lift coefficient on the downstream cylinder was larger than that of the upstream cylinder at $d/c > \sim 2.8$ where vortices were shed periodically from both the upstream and downstream cylinders (Arie et al., 1983; Okajima, 1979). Sakamoto et al. (1987) studied the case of two identical square prisms of length $c = 0.4$ m, width $b = 42$ mm and streamwise spacing d in a tandem arrangement (Figure 2.19(a)) exposed to a freestream velocity U_∞ of 20 m/s at low turbulence intensity I_u of 0.2% and Reynolds number Re_∞ of 5.52×10^4. In contrast to the tandem cylinders, Sakamoto et al. (1987) found that the fluctuating RMS lift coefficient c_{Lf} (Figure 2.19(b)) on the upstream prism converged to that of an isolated prism at $d/c \geq 7$ and was approximately 6 times larger than that of the downstream prism at $d/c \geq 3$ due to higher turbulence intensities in the wake and thus larger fluctuating pressures. Hence, the opposite trend was found by Sakamoto et al. (1987) for two tandem prisms with an aspect ratio $b/c = 9.5$ because of the suppression of the fluctuating pressures from reattachment of the separated shear layer at higher gap ratios ($d/c \geq 3$). There is a change in flow regime between the two prisms, shown by a step change in c_{Lf} at $d/c = 3$, as Sakamoto et al. (1987) observed the flow to be very stable around the upstream prism because of the formation of a quasi-steady vortex region between the two prisms. As a result, the separated shear layers from the upstream prism shed onto the side surfaces of the downstream prism. This reattachment regime at lower gap ratios between the two prisms is believed to be the cause of low c_{Lf} on the upstream prism and larger c_{Lf} on the downstream prism (Sakamoto et al., 1987). For the case of two thin ($t/c = 0.03$) bluff plates in a tandem arrangement, Yu et al. (2016) showed that the ratio of the mean drag coefficients on two normal plates orientated perpendicular to the flow direction decreased to a minimum at $d/c \approx 2$ before increasing with larger d/c, whereas this minimum occurred at $d/c \approx 2$ for two plates at an elevation angle of 45°. Hence, the lift forces on the downstream heliostat in a tandem configuration converge to those on an isolated heliostat as the distance between the two heliostats increases. Lift forces and hinge moments on in-field heliostats in the high-density inner regions of a field are likely to be larger than in-field heliostats in the low-density outer regions of a field. Tandem configurations of heliostats have focused on operating positions, whereas the loads on tandem stowed heliostats have been investigated for low-density ($d/c \approx 1.5$) and high-density ($d/c \approx 5.5$) fields. The aerodynamics of slender prisms has been more widely investigated, hence the effect of the gap ratio in this range on the peak wind loads on a thin flat plate is needed to further optimise the layout of heliostat fields during high-wind conditions in the stow position.

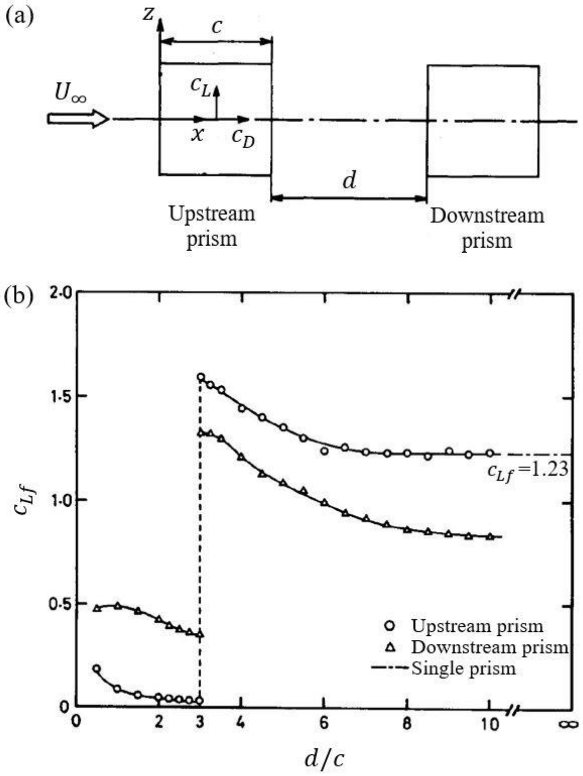

Figure 2.19. (a) Experimental setup of two identical square prisms of chord length $c = 0.4$ m and width $b = 42$ mm in a tandem arrangement with streamwise spacing d in the flow direction at freestream velocity $U_\infty = 20$ m/s and Reynolds number $Re_\infty = 5.52\times10^4$. (b) Fluctuating RMS lift coefficient c_{Lf} on the upstream and downstream prisms as a function of gap ratio d/c and comparison with a single prism ($c_{Lf} = 1.23$). Reproduced from Sakamoto et al. (1987).

The fluctuating lift arising from the vortex shedding behind tandem bluff bodies is significantly dependent on the Reynolds number and the aspect ratio of the geometries. Szepessy and Bearman (1992) investigated a tandem arrangement of movable rectangular end plates of cross-section $8D\times 7D$ connected by a circular cylinder of diameter $D = 6$ cm exposed to a range of Reynolds numbers $Re_\infty = U_\infty D/\nu$ at a low freestream turbulence intensity $I_u < 0.05\%$. As shown in Figure 2.20, the fluctuating lift coefficient c_{Lf} for small aspect ratio flow ($d/D = 1$) is strongly dependent on Reynolds number and increases from 0.27 to 0.78 between Re_∞ of 1.2×10^4 and 7.2×10^4. Szepessy and Bearman (1992) observed a rapid decrease in c_{Lf} above a critical Reynolds number range between 6×10^4 and 1.3×10^5 due to the complete suppression of strong, regular vortex shedding for the small aspect ratio flow. In contrast, only a small variation in c_{Lf} was observed for the large aspect ratio ($d/D = 6.5$) flow. Hence, the aspect ratio of a bluff body was found to have a more significant effect on the fluctuating lift than the Reynolds number, as c_{Lf} reached a maximum at $d/D = 1$ that was almost double the magnitude of c_{Lf} found at larger aspect ratios. The vortex shedding behind a single isolated rectangular prism and a single isolated circular cylinder placed vertically in a turbulent boundary layer ($h/\delta = 0.62$) was observed by Sakamoto and Arie (1983) to change from the Karman-type vortex to the arch-type vortex at small aspect ratios of 2 for a prism and 2.5 for a circular cylinder. Sakamoto and Arie (1983) found that the prominent prevailing frequency of vortex shedding increased by an order of magnitude from 30 Hz to 300 Hz, indicating that the strength of the vortex shedding decreases as the aspect ratio of the prisms increased from 1 to 8. The characteristic dimensions of tandem bluff bodies and the spacing between them can therefore lead to significant changes to the unsteady pressures and peak lift forces. Since the sizes of heliostat mirrors and the elevation axis heights at which they are stowed vary by as much as an order of magnitude, further optimisation of these critical scaling parameters is needed.

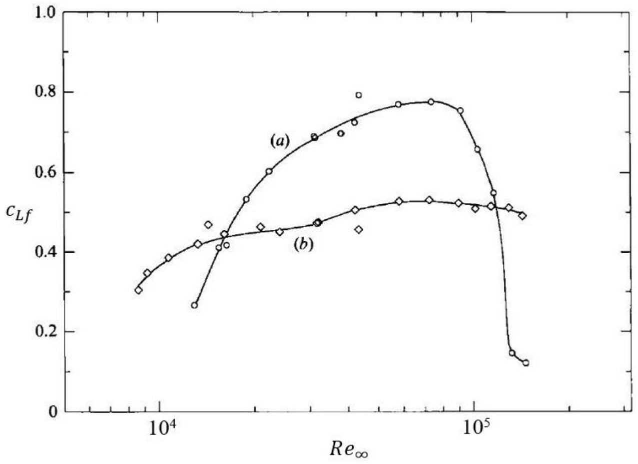

Figure 2.20. Effect of freestream Reynolds number $Re_\infty = U_\infty D/\nu$ on the fluctuating lift coefficient on two identical end plates separated by a distance d with cross-sections of $8D$ width and $7D$ height and connected by a circular cylinder of diameter $D = 6$ cm at constant non-dimensional separation: (a) $d/D = 1$; (b) $d/D = 6.5$. Reproduced from Szepessy and Bearman (1992).

2.3. Wind Loads on Stowed Heliostats

Heliostats are exposed to aerodynamic forces from the wind in the atmospheric boundary layer (ABL). The current practice in the operation of heliostat fields is to move each heliostat mirror to the stow position, aligned parallel to the ground, during periods of extreme wind speeds to minimise loads by reducing the projected frontal area to the wind.

2.3.1 Peak Forces and Moments on Isolated Heliostats

Mean and peak wind loads on heliostats are determined using normalised load coefficients from the heliostat dimensions and the dynamic pressure of the air under different operating positions and turbulence conditions. The orientation of the heliostat is defined in Figure 2.21 by the elevation angle α between the mirror and the horizontal ground plane, and the azimuth angle β between the nominal wind direction and the mirror normal projected on the ground. Figure 2.21 shows the main wind loads on a stowed heliostat, simplified as a thin square flat plate of chord length c at an elevation axis height H above the ground. Stowed heliostats that are aligned horizontally ($\alpha = 0°$) are exposed to smaller drag forces (D) and overturning moments (M_y) than when the heliostat mirrors are inclined during operation. A non-uniform pressure distribution $p(x)$ on the stowed mirror due to turbulent vortices in the ABL leads to large lift forces (L) at the centre of pressure a distance l_p from the centre of the mirror and hinge moments (M_{Hy}) about the elevation axis.

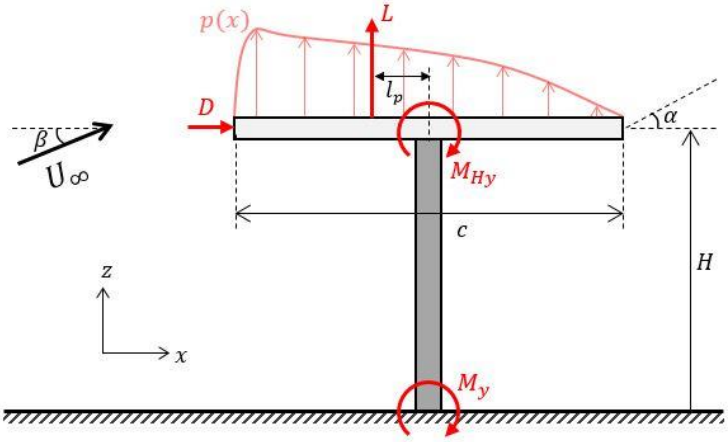

Figure 2.21. Wind loads on a heliostat in stow position.

Wind load coefficients used for the design of heliostats have previously been determined from experimental data measurements on simplified models of heliostats at scales between 1:20 to 1:40 in wind tunnels that reproduce the wind conditions in the lower surface layer of the ABL (Peterka and Derickson, 1992; Pfahl et al., 2017a). Peterka et al. (1989) presented the first set of load coefficients on 1:40 model heliostats for turbulence intensities of up to 18% using a boundary layer wind tunnel at Sandia National Laboratories (Peterka and Derickson, 1992). The lowest wind load coefficients occurred at an elevation angle α of 0° in Figure 2.22, thus representing the most suitable stow position to protect the heliostat components from gusts during high-wind conditions. Although the mean drag and lift coefficients on the stowed heliostat were relatively small compared to operating positions, the peak lift and overturning moment coefficients were at least ten times their mean values in stow position (Peterka and

Derickson, 1992). This indicates the significance of gust and amplification effects of survival high-wind conditions for heliostats in stow position.

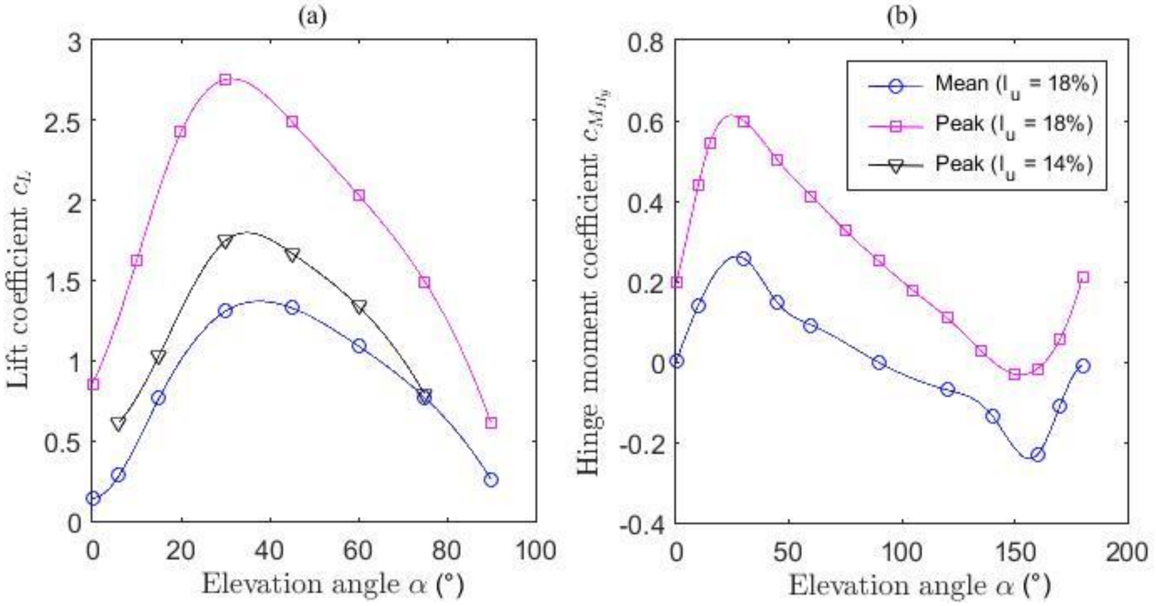

Figure 2.22. Mean and peak wind load coefficients on a 1:40 scale model heliostat ($\beta = 0°$) as a function of elevation angle α: (a) Lift coefficient c_L; (b) Hinge moment coefficient $c_{M_{Hy}}$. Data extracted from Peterka et al. (1989).

Pfahl and Uhlemann (2011) investigated the effect of freestream Reynolds number $Re_d = U_\infty d/\nu$, based on the torque tube diameter d of a 1:50 scale-model stowed heliostat, on the peak wind load coefficients in a high-pressure wind tunnel. The peak lift coefficient was most significantly influenced for load-induced mirror inclination increasing from 0° to 4° due to deflection of the mirror. Hence, Pfahl and Uhlemann (2011) suggested that overturning moments and lift forces were most relevant for the design of heliostats in the stow position during highly turbulent conditions. The dashed lines in Figure 2.23 show that the drag, lift and overturning moment coefficients were independent of Reynolds number at a constant elevation angle α of 4° and wind speeds up to 35 m/s. Therefore, wind tunnel tests at low Reynolds numbers are considered feasible for obtaining reasonable results from conventional boundary layer wind tunnel tests (Pfahl and Uhlemann, 2011).

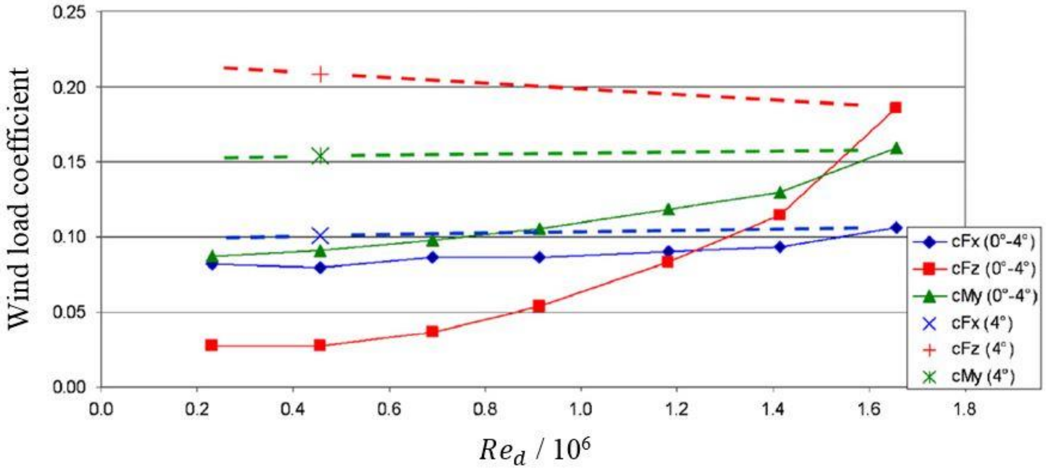

Figure 2.23. Dependence of peak wind load coefficients on freestream Reynolds number for a stowed heliostat. The single markers indicate measured wind load coefficients at a nominal inclination angle of 4° at $Re_d = 0.45 \times 10^6$. The solid lines represent the measured values for the nominal plane inclination of 0°, but the load-induced inclination increases from 0° (low Re_d) to 4° (high Re_d) due to deflection of the mirror. Reproduced from Pfahl and Uhlemann (2011).

Wind tunnel experiments by Peterka et al. (1989) and Pfahl et al. (2011a) showed that peak wind load coefficients increase significantly at longitudinal turbulence intensities above 10%. Peterka et al. (1989) found that the peak lift coefficient doubled for an increase of turbulence intensity from 12% to 18% at an elevation angle α of 30° corresponding to a typical operating position. In contrast for a heliostat in stow position, Pfahl et al. (2015) reported that the peak lift coefficient and peak hinge moment increased by 6.5% and 15%, respectively, when turbulence intensity was increased from 13% to 18% in a range characteristic of the turbulence approaching heliostat fields in an open country terrain. Large-scale turbulence in boundary layer wind tunnels cannot be generated naturally because of a limited working section length, so that turbulence has to be generated artificially. Wind tunnel experiments on scale-model heliostats at Sandia National Laboratories and the German Aerospace Center (DLR) have simulated the velocity and turbulence intensity profiles of the lower region of the full-scale ABL (Peterka and Derickson, 1992; Peterka et al., 1989; Pfahl et al., 2011a; Pfahl et al., 2015). However, Banks (2011) noted that replication of the turbulent power spectra had not been achieved due to discrepancies in scaling between the heliostat model (typically 1:10 to 1:50) and the turbulent eddy length scales (typically 1:100 to 1:300). As shown in Figure 2.24 and discussed in Section 2.1.4, the low-frequency part of the turbulent power spectra cannot be produced because the length scales of the corresponding eddies are limited by the size of the wind tunnel (Pfahl et al., 2017a).

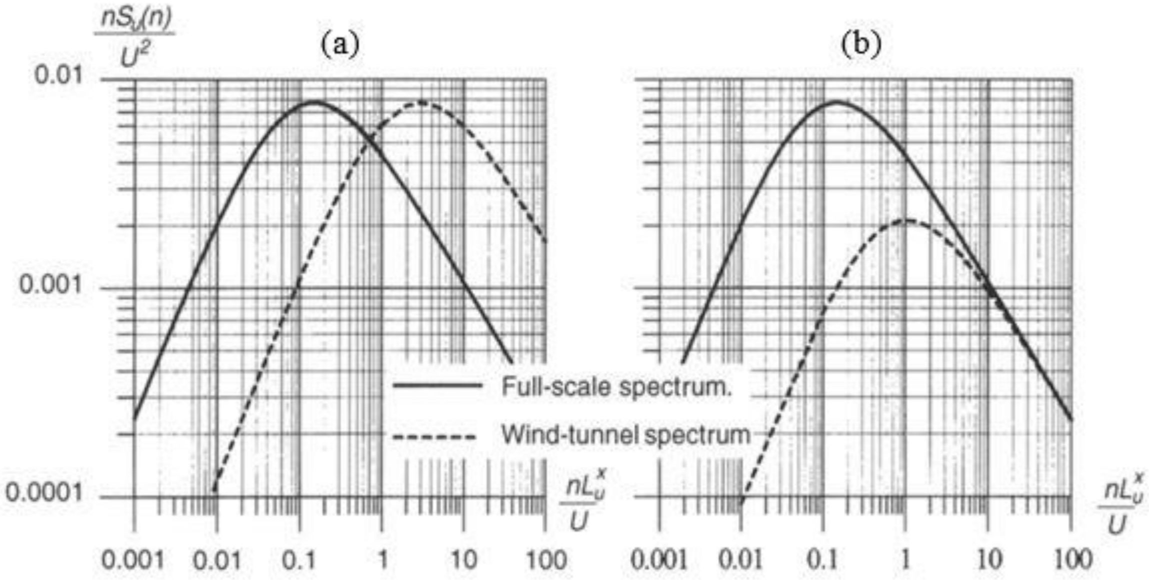

Figure 2.24. Comparison of non-dimensional turbulent power spectra as a function of non-dimensional frequency in the full-scale and wind tunnel atmospheric boundary layers: (a) Same turbulence intensity; (b) Reduced wind-tunnel turbulence intensity to match the power spectra at high frequencies. Reproduced by Pfahl et al. (2015) from Dyrbye and Hansen (1996).

Wind load coefficients for heliostats are usually normalised by the heliostat mirror area so that they apply to any heliostat size. The gust factor method, previously described in Section 2.1.5, for quasi-steady wind loads is widely used in design codes (American Society of Civil Engineers, 2013; Cook, 1985; Engineering Sciences Data Unit, 1985; Standards Australia and Standards New Zealand, 2011) for the estimation of the peak wind loads on large buildings. This quasi-static approach assumes that the unsteady component of the wind, represented by a 3-second gust wind speed, can be related to the mean wind speed by a ratio (gust factor) of 1.6

for an open country terrain, and the gust factor squared gives the ratio of peak force to mean force (Peterka and Derickson, 1992). The gust factor approach can significantly underestimate the peak wind loads on heliostats, as they are an order of magnitude smaller in height and have natural frequencies an order of magnitude larger than standard buildings. Discrepancies in peak wind loads estimated using the gust factor method commonly arise from the high impact of the instantaneous angle of attack for longitudinal wind flows with large vertical components of turbulence caused by vortex structures in the ABL. Hence, Peterka and Derickson (1992) recommended using the peak load coefficient with mean wind speeds measured at the site for the calculation of the design wind loads on heliostats. With a trend towards smaller heliostats in recent years, accurate estimation of the peak and mean wind loads has become more important (Pfahl et al., 2017a). The peak pressure coefficients and peak wind loads in the stow position are most relevant to the sizing of the heliostat dimensions during design (Pfahl et al., 2015), however there exists a wide range of heliostat sizes between 1 m^2 and 150 m^2 that are currently manufactured and installed for PT plants (Coventry and Pye, 2014). Hence, the critical scaling parameters of the heliostat can be further optimised with the knowledge of their sensitivity to the effect of turbulence intensity and the sizes of the largest eddies that cause the unsteady loads and non-uniform pressure distributions on stowed heliostats.

2.3.2 Dynamic Loads and Surface Pressure Distributions

The dynamic response of permanent structures, such as heliostats positioned on the ground, determines their ability to withstand gusts in the ABL and maintain structural integrity for their expected design life. As heliostats are slender in shape and have low natural frequencies less than 10 Hz (Gong et al., 2012; Griffith et al., 2015), they can be exposed to flow-induced vibrations (Section 2.2.2) from the unsteady fluctuating loads caused by turbulence effects. Oscillatory instabilities, such as galloping and flutter arising from one or more vibrational modes, can lead to structural failure from excessive deflections and stresses (Jain et al., 1996; Mendis et al., 2007). Galloping and torsional flutter tend to occur at frequencies on the order of 1 Hz when the turbulence length scales are comparable to the size of the body. A quasi-steady increase in mean velocity occurs when the turbulence scale is increased beyond the order of magnitude of the body scale (Nakamura, 1993) and the galloping effect becomes negligible when the turbulence scale is decreased below the body scale as smaller eddies cannot cause high net pressures (Pfahl et al., 2015). This has particular significance for heliostats because they have natural frequencies between 2 and 5 Hz (Gong et al., 2012; Griffith et al., 2015) and the size of the largest vortices L_u^x has the same order of magnitude as the heliostat chord length when stowed at heights below 10 m in the atmospheric surface layer. Vásquez-Arango et al. (2015) found that the shapes of vibration corresponding to rigid body modes of the mirror frame, such as the oscillation about the elevation axis in Figure 2.25, are most likely excited by fluctuating wind loads using a finite element analysis (FEA) model validated with experimental data. Such numerical methods are capable of determining dynamic wind loads on heliostats, however the computational effort is still very high (Pfahl et al., 2017a).

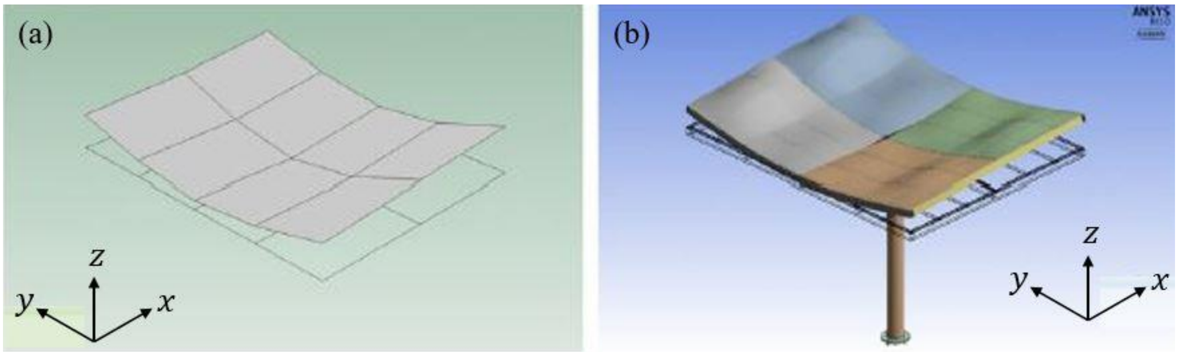

Figure 2.25. Bending mode 7 about the elevation axis of the mirror frame of an 8 m^2 T-shaped heliostat in stow position: (a) Experimental; (b) FEA (Vásquez-Arango et al., 2015).

An alternative method for dynamic wind load analysis on heliostats is to couple transient FEA simulations with experimental data from wind tunnel or full-scale measurements, such as the surface pressure measurements by Gong et al. (2013) on a 1:10 scale model T-shaped heliostat in Figure 2.26. Pressure distributions on the stowed heliostat were most significantly influenced by approaching flow turbulence for wind angles β between 0 and 90 degrees to the horizontal, and less influenced when the incoming wind acts on the back surface of the heliostat due to shielding effects of supporting components. This supports the findings of a numerical analysis by Wu et al. (2010) that the small gaps between mirror facets has a negligible effect on the wind loads on heliostats and hence, the geometry of a heliostat mirror can effectively be modelled as a thin flat plate. Gong et al. (2013) found that large negative peak wind pressure coefficients occurred at the leading edge of the heliostat mirror surface in stow position, suggesting that this region is the most vulnerable to wind-induced mirror damage. It is presumed that the eddies corresponding to the peaks of the power spectra that are comparable in size to the heliostat mirror are responsible for the maximum lift forces and hinge moments on heliostats in stow position (Pfahl et al., 2015). However, the effect of the size of these eddies relative to the size of the heliostat chord length on the unsteady loads and non-uniform pressure distributions on stowed heliostats has not previously been investigated.

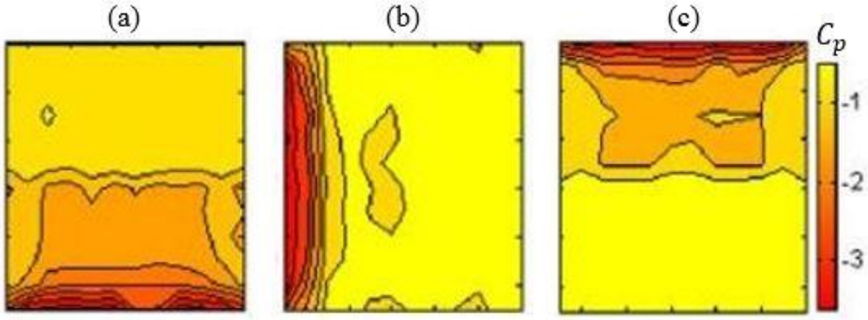

Figure 2.26. Peak pressure coefficient contours on a heliostat in stow position at different wind angles: (a) $\beta = 0°$; (b) $\beta = 90°$; (c) $\beta = 180°$. Reproduced from Gong et al. (2013).

2.3.3 Tandem Heliostats

The layout of heliostat fields in power tower plants has previously been optimised with respect to the optical efficiency of heliostats in operational positions. However, static wind loads on tandem heliostats are highly dependent on the spacing between the heliostat mirrors defined by the gap ratio d/c and the heliostat field density as the ratio of mirror area to land area. Heliostats are arranged in radially staggered rows around a central tower, as shown in Figure 2.27 for a surround field of a 100 MW plant. Heliostats close to the tower have field densities greater than 40% with smaller shading effects and are typically spaced less than 20 m apart for a typical heliostat mirror area of 120 m^2 (Noone et al., 2012). With increasing distance from the central tower, the field density decreases to less than 20% and spacing between heliostats of up to 45 m at the outer boundary of the field (Noone et al., 2012; Pfahl et al., 2011b). Peterka et al. (1987) measured mean and peak wind loads on 1:60 scale-models of a tandem arrangement of five consecutive heliostats in rows of a high-density region of the Barstow heliostat field. Pfahl et al. (2011b) measured peak wind loads on 1:20 scale-models of a tandem arrangement of four consecutive heliostats with 30 m^2 mirror area in operating and stow positions for field densities of 10% and 50% corresponding to gap ratios (d/c) between the mirrors of 5.5 and 1.5, respectively. Peterka et al. (1987) and Pfahl et al. (2011b) reported reductions of up to 50% in peak drag (Figure 2.28) and lift forces on a second normal heliostat relative to the first heliostat in a tandem arrangement at a high field density of 50% ($d/c \approx 1.5$). In comparison for tandem heliostats in stow position, Pfahl et al. (2011b) found that the peak lift forces and hinge moments on a second heliostat were 20% and 60% lower, respectively, relative to the first heliostat at a high field density ($d/c \approx 1.5$). However, a smaller reduction of 20% in peak hinge moment and a 3% increase in peak lift force relative to the first heliostat were measured on the second heliostat at a low field density of 10% ($d/c \approx 5.5$).

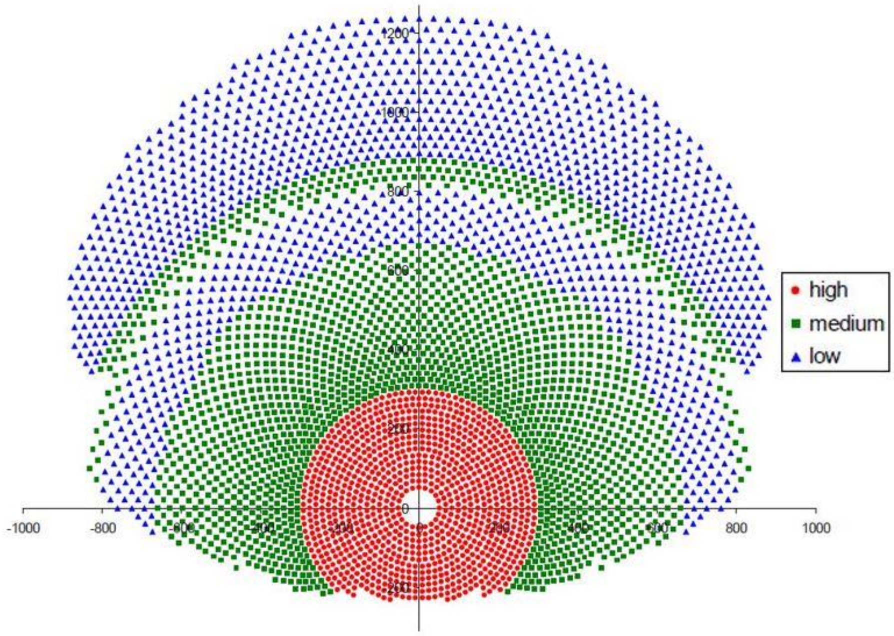

Figure 2.27. Schematic showing the regions of low, medium and high field density of heliostats in a 100 MW power tower plant. Reproduced from Pfahl et al. (2011b).

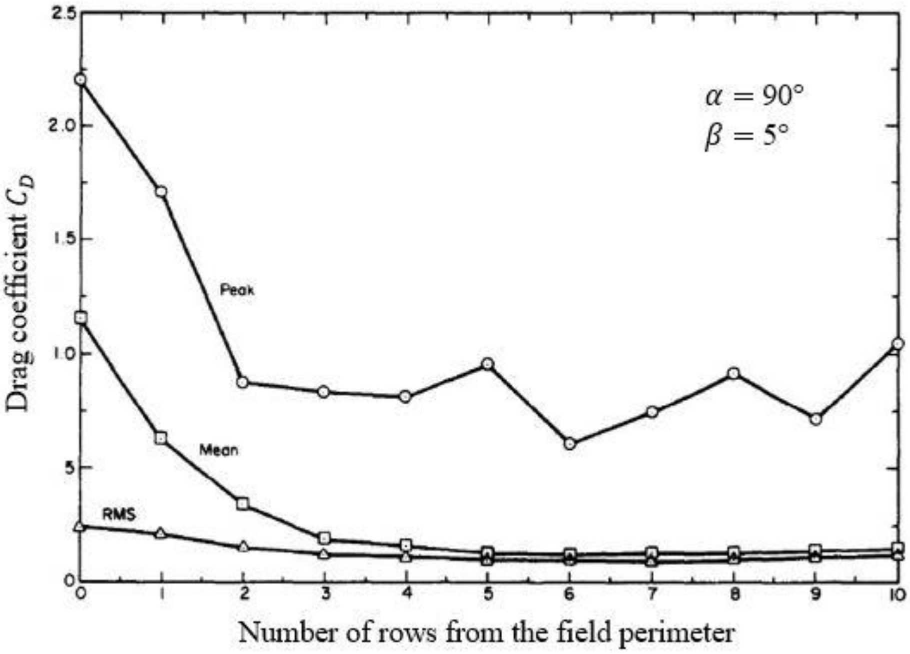

Figure 2.28. Variation of mean and peak drag coefficient on normal heliostats ($\alpha = 90°$) in the outermost rows of a high-density field at a wind angle $\beta = 5°$. Reproduced from Peterka et al. (1987).

The variations in static wind loads on heliostats in the different rows of a field are highly dependent on the elevation angle (α) of the heliostats to the horizontal. Sment and Ho (2014) complemented the findings of Peterka et al. (1987) and Pfahl et al. (2011b) with wind load measurements on instrumented heliostats in a five-row section of the National Solar Thermal Test Facility (NSTTF) heliostat field at Sandia National Laboratories. Figure 2.29(a) shows the mean wind loads measured by Sment and Ho (2014) on five heliostats aligned in a row at two elevation angles, normalised with respect to the first heliostat in a normal orientation ($\alpha = 90°$). Mean drag coefficients measured by Sment and Ho (2014) on normal heliostats were on average 13% lower than those reported by Peterka and Derickson (1992). The mean drag coefficient on the second normal heliostat in a tandem configuration reduced to 40% of that on the first heliostat, in agreement with Peterka et al. (1987) and Pfahl et al. (2011b). The same reduction was observed for the mean drag coefficient on the first heliostat at $\alpha = 45°$ and decreasing to only 7% of the first normal heliostat for a second heliostat at this typical operating position. In contrast, the CFD model of heliostats at $\alpha = 45°$ by Sment and Ho (2014) showed a reduction of 20% relative to the first normal heliostat in the experiment and fluctuated around 90% of the magnitude of the drag coefficient on the first normal heliostat in the subsequent rows. The wind loads on heliostats in a tandem arrangement in Figure 2.28 and Figure 2.29(a) indicate that the largest wind load reductions occur for the second heliostat, beyond which only small variations occur in wind loads relative to the upstream heliostat after the third row.

The mean velocity and turbulence intensity profiles of the approaching boundary layer were characterised by Sment and Ho (2014) using three tri-axial ultrasonic anemometers mounted on a weather tower upstream of the heliostat field. Anemometers were also mounted on the heliostats and on portable towers between the heliostats to develop an understanding of the turbulence characteristics of the flow in the vicinity of the heliostats. Figure 2.29(b) shows that the turbulence intensity increased to over 50% between the third and fifth rows by factors of 3 and 6 for elevation angles of 90° and 45°, respectively. In the stow position however, turbulence intensities on heliostats in downstream rows remained below a maximum of 20% approaching the first row at the outer boundary of the field (Sment and Ho, 2014). Chin et al. (2015) found that an upstream plate aligned horizontally can be used as a large-eddy break-up (LEBU) device to attenuate the energies of the largest spanwise eddies at pre-multiplied energy spectra $\lambda_y^+ > 500$ and redistribute the energy to moderate length scales at $200 < \lambda_y^+ < 500$. Hence, heliostats positioned at in-field rows of a field in stow position are likely to be exposed to lower turbulence intensities and smaller length scales than the first row. The peak wind loads are expected to be lower on a second heliostat in a tandem configuration, compared with an isolated heliostat in stow position that has commonly been investigated in experimental heliostat studies. The effect of an upstream heliostat on the break-up of large-scale eddies and the shift to larger frequencies approaching a second heliostat downstream may reduce the loads if the eddies become smaller than the size of the heliostat mirror. However, vibrations due to galloping can arise if the frequencies are shifted to be closer to the natural frequency of the heliostat. The unsteady wind loads and non-uniform pressure distributions of two tandem stowed heliostats exposed to turbulence in the ABL therefore warrants further investigation.

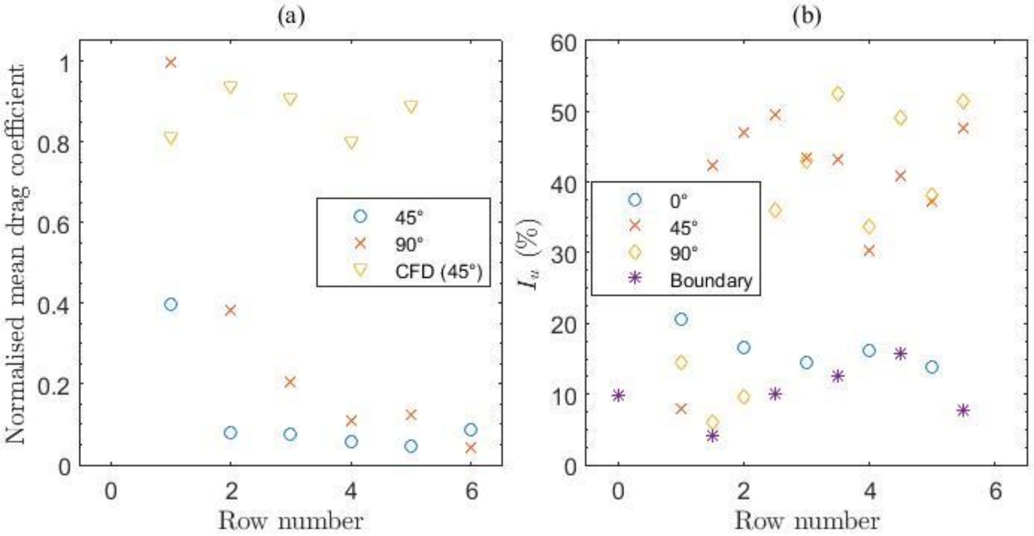

Figure 2.29. (a) Normalised mean drag coefficient in different rows of a heliostat field as a function of elevation angle; (b) Turbulence intensity in different rows of a heliostat field as a function of heliostat elevation angle. Data extracted from Sment and Ho (2014).

2.4. Summary and Discussion of Research Gaps

Stowed heliostats are exposed to the effects of turbulence due to mechanical shear forces produced by the surface roughness of the terrain at mean wind speeds greater than 10 m/s at a 10 m height (Xu, 2013) in a neutrally-stable atmospheric boundary layer (ABL). Short-duration wind fluctuations (gusts) and amplification effects during high-wind conditions need to be considered in the design of heliostat components to maintain their structural integrity. Wind codes and standards for low- to medium-rise buildings adopt a simplified gust factor approach that assumes quasi-steady wind loads based on a maximum gust wind speed. The gust factor generally gives a good approximation of the design wind loads for standard building shapes. However, this approach can lead to significant errors for very tall buildings and smaller physical structures such as heliostats with large dynamic responses to the large amplitude velocity fluctuations arising from gusts over short time intervals. Heliostats in operating positions have a larger projected frontal area to the direction of the wind and thus, the gust factor approach is suitable for calculating the quasi-static drag forces and overturning moments. In contrast for heliostats in stow position, the gust factor method relating the peak gust velocity to mean velocity can lead to significant errors for the calculation of lift forces and hinge moments due to the large vertical components of turbulence in the ABL. Peak lift forces and hinge moments are likely to be under-estimated as the gust factor is not able to account for the dynamic effects of vertical wind pressures and distributed loads on stowed heliostats due to large eddies in the ABL. Design wind codes for large physical structures are also not applicable because stowed heliostats are an order of magnitude smaller in height and have natural frequencies an order of magnitude larger than standard-sized buildings. Consequently, due to their non-standard configurations, heliostats have previously been designed using mean and peak wind load coefficients derived from experimental data in systematic wind tunnel studies. Wind tunnel experiments have developed accurate methods for reproducing theoretical mean velocity and turbulence intensity profiles to represent the lower ABL. However, the spectral distribution of the velocity fluctuations with frequency, commonly modelled by a von Karman spectrum or Kaimal spectrum, is shifted to higher frequencies in smaller-scale boundary layer wind tunnels. Hence, the absence of the largest vortices generated in the lower frequency region of the PSD through wind tunnel experiments can lead to an under-estimation of peak wind loads on stowed heliostats arising from unsteady pressure fluctuations due to short-duration gusts. The frequency distribution of eddies in the PSD is important for the maximum hinge moments on heliostats in stow position, as the largest eddies at low frequencies cause higher pressure differences over the surface of a heliostat mirror. The effect of the fluctuating velocities at lower frequencies, corresponding to the peak magnitudes of the turbulent power spectra, at heights below 10 m in the ABL and how they correlate to the fluctuating pressures on a stowed heliostat requires further investigation to better understand the dynamic wind loads.

The temporal variation of turbulence in the ABL described by the turbulence intensity has been widely studied, however the effect of the spatial distribution of turbulence and the length scales of vortices embedded in the turbulence in the ABL has not been investigated. Peak wind load coefficients on stowed heliostats derived from wind tunnel experiments have shown a large dependence on the turbulence intensity, however the ground effect of the largest eddies at a given height above the ground, defined by the integral length scale, on the fluctuating pressures and unsteady forces on heliostats is not well understood. The natural frequencies of heliostats are on the order of 1 Hz, so that in stow position the effects of resonance and flutter are most likely to occur when the turbulence length scales are comparable to the size of the mirror. The break-up of the largest eddies relative to the size of the mirror is believed to be the factor that is responsible for the peak wind pressures observed at the leading edge of stowed heliostats, however the length scales and dominant frequencies of these eddies have not previously been reported. Therefore, the relationship between peak forces and moments on a heliostat in stow position and the turbulence characteristics in the ABL requires further investigation to improve the accuracy and versatility of the current methods used for calculating the peak wind loads on stowed heliostats.

The layout of heliostat fields has previously been optimised with respect to the optical efficiency of heliostats in operational positions. However, the spacing between heliostats in tandem defined by the field density and the gap ratio also have a significant effect on the wind loads on heliostats in stow position. Previous experimental studies have investigated the static wind loads on stowed heliostats in tandem arrangements representing the rows of a heliostat field, particularly at elevation angles between 30 and 90 degrees within typical operational ranges. It was shown that as the elevation angle is decreased from a normal position to the stow position, the wind loads on the second heliostat in a tandem configuration become closer to those on the first heliostat. The effect of wind direction on the surface pressure distributions is largest for wind angles between 0 and 90 degrees, when the shielding effect of the support structure is negligible. The sharp edges of a square heliostat mirror have the largest effect on the pressure fluctuations over the surface of a mirror and the flow separation downstream of the mirror. In the stow position, different components of the heliostat are exposed to varying wind speeds and turbulence characteristics. Previous experimental studies on tandem heliostats in the rows of a field highlight the significant differences in measured wind loads between wind tunnel experiments with insufficiently defined approaching turbulence characteristics in the simulated ABLs and separation distances between rows in the field. Consequently, the static and dynamic wind loads resulting from non-uniform distributions of fluctuating pressures on the mirror surface requires further investigation. A more detailed characterisation of turbulent characteristics and the spacing between heliostats is required to further understand the flow behaviour between neighbouring heliostats in consecutive rows of a field and their effect on the peak wind loads on tandem heliostats in stow position.

2.5. Aims and Objectives of Current Research

The overall aim of the current research is to investigate the peak wind loads on a heliostat in stow position and their sensitivity to the turbulence characteristics in the ABL and the dimensions of the heliostat. Four objectives (Section 1.2) have been developed to improve the understanding of static and dynamic wind loads on heliostats in stow position. It is important to optimise the size of the heliostat structure and the reduce cost of its components with respect to the turbulence approaching them. As a motivation to reduce the cost of heliostats, the first objective is a structural and cost analysis of one of the principal factors in the design criteria for a heliostat field. The design wind speed at which heliostats are moved to the stow position from operating positions affects the maximum wind loads that heliostats are exposed to and the capacity factor of the heliostat field. The mass of the heliostat components required to withstand the loads in the stow position proportional to the total cost of manufacturing and installing the heliostat and the capacity factor is related to the annual electricity production of a power tower plant. Hence, the scope of the first objective is a sensitivity analysis of the levelised cost of electricity (LCOE) to these two parameters as a function of the stow design wind speed. The statistical analysis was performed from the correlation of wind speed and solar irradiation data at six sites in Australia and the USA with a sufficient solar resource. The model assumes quasi-steady wind loads and simplified cost-area proportionality exponents relating the mass and thus cost of the heliostat components to the total mirror area of heliostats in the field.

The second objective investigates the temporal and spatial characteristics of turbulence and their relationship with the commonly used gust factor approach for estimating peak gust velocities and design wind loads on physical structures in the atmospheric boundary layer (ABL). Peak wind loads estimated using the gust factor method can be conservative for tall buildings and can be under-estimated for smaller physical structures with non-standard configurations that are not accounted for in design wind codes and standards. Heliostats are an order of magnitude smaller in height and have natural frequencies an order of magnitude larger than standard-sized buildings. Heliostats are normally stowed in low-roughness open country and desert terrains in the lowest 6 m of the lower atmospheric surface layer (ASL), where they are exposed to the largest velocity gradients and turbulence intensities in the ABL. These temporal characteristics of turbulence and the spatial characteristics of turbulence in the frequency domain, such as the longitudinal integral length scales, at these lower heights show significant variation with the surface roughness height that characterises the type of terrain. Various semi-empirical models have been developed to correct these turbulent parameters for changes in surface roughness height based on reference data measured for homogenous, isotropic turbulence over open country terrains in a neutrally-stable ABL. The scope of this objective is to compare the predictions of some semi-empirical models with the calculated parameters using field velocity data collected in a low-roughness ASL in the Utah desert. Calculated turbulence profiles in the field ASL are also non-dimensionalised with the defining scale parameters of the ABL used in theoretical models, including the boundary layer thickness and friction velocity, to compare with the turbulent boundary layer on a flat plate in wind tunnel experiments. The filtering of velocity fluctuations in the spectral distribution of frequencies through the definition of a temporal gust period in the gust factor approach is investigated to determine the effect on the estimated gust wind velocities and peak wind loads.

The third objective is focused on the peak wind loads on an isolated heliostat in stow position and their sensitivity to the temporal and spatial characteristics of turbulence in the ASL. Wind load coefficients on heliostats in operating positions have been calculated for a range of turbulence conditions on heliostats in the literature from wind tunnel experiments and field heliostat measurements, however there have been limited sensitivity studies on stowed heliostats. Mean and peak wind load coefficients were measured on a scale-model heliostat exposed to two different combinations of spires and roughness elements in a closed-return wind tunnel to simulate a range of turbulence intensities and integral length scales. The scope of the experimental study is limited to the effects of turbulence intensity and integral length scales on the peak lift and hinge moment coefficients on a stowed heliostat with adjustable mirror chord length and pylon elevation axis height. Dynamic wind loads on a single heliostat mirror and the dominant frequencies of pressure fluctuations were also investigated through the measurement of pressures on the upper and lower surfaces of the stowed heliostat mirror.

The fourth objective is to investigate the peak wind loads on two stowed heliostats in a tandem arrangement to optimise the size and spacing between heliostats to the turbulent flow approaching them in the ABL. Peak wind loads on the second downstream heliostat were normalised with respect to the isolated heliostat in stow position. Wind tunnel experiments were carried out to measure static wind loads and pressure distributions on an isolated heliostat in stow position and a second downstream heliostat in a tandem arrangement. The heliostats were exposed to gusty wind conditions in a simulated part-depth ABL using two configurations of spires and roughness elements to generate a characteristic ABL flow with a power law velocity profile at moderate turbulence intensity and a second wake flow with a linear velocity and higher turbulence intensities. The scaling parameters of the second heliostat, including the chord length of the mirror and the elevation axis height above the ground, were optimised with respect to their height in the ABL and the streamwise spacing between the two tandem heliostats in the flow direction. The effect of turbulence intensity, the ratio of integral length scale to chord length and the peak of the spectral distributions of pressure fluctuations were analysed for the second tandem heliostat with reference to the isolated heliostat in stow position.

References for Chapter 2

ASCE 7-02, 2013, Minimum design loads for buildings and other structures, American Society of Civil Engineers, Reston, Virginia, USA.

Anfossi, D., Ferrero, E., Sacchetti, D. and Castelli, S.T., 1997, Comparison among empirical probability density functions of the vertical velocity in the surface layer based on higher order correlations, Boundary-Layer Meteorology 82, 193-218.

Arie, M., Kiya, M., Moriya, M. and Mori, H., 1983, Pressure fluctuations on the surface of two circular cylinders in tandem arrangement, Journal of fluids engineering 105, 161-166.

Banks, D., 2011, Measuring peak wind loads on solar power assemblies, in: 13th International Conference on Wind Engineering, Amsterdam, Netherlands.

Bearman, P., 1971, An investigation of the forces on flat plates normal to a turbulent flow, Journal of Fluid Mechanics 46, 177-198.

Bearman, P.W., 1984, Vortex shedding from oscillating bluff bodies, Annual review of fluid mechanics 16, 195-222.

Booth, E.R., 1990, Experimental observations of two-dimensional blade-vortex interaction, AIAA journal 28, 1353-1359.

Borri, C., Zhou, S. and Chen, Z., 2012, Coupling investigation on vortex-induced vibration and galloping of rectangular cylinders, in: Proceedings of the Seventh International Colloquium on Bluff Body Aerodynamics and Applications, Shanghai, China, pp. 2-6.

Bruns, J., Dengel, P. and Fernholz, H., 1992, Mean flow and turbulence measurements in an incompressible two-dimensional turbulent boundary layer. Part I: Data, In: 02/92, Institute of Fluid Mechanics and Technical Acoustics, Technische Universität Berlin, Germany.

Chen, J.M. and Chiou, C.-C., 1998, Experimental investigation of a parallel vortex-plate interaction, Journal of Fluids and Structures 12, 295-314.

Chin, C., Monty, J., Hutchins, N., Ooi, A., Orlu, R. and Schlatter, P., 2015, Simulation of a large-eddy-break-up device (LEBU) in a moderate Reynolds number turbulent boundary layer, in: Proc. Turbulence and Shear Flow Phenomena 9, Melbourne, Australia.

Choi, K.-S. and Clayton, B.R., 2001, The mechanism of turbulent drag reduction with wall oscillation, International Journal of Heat and Fluid Flow 22, 1-9.

Chu, C.R., Parlange, M.B., Katul, G.G. and Albertson, J.D., 1996, Probability density functions of turbulent velocity and temperature in the atmospheric surface layer, Water Resources Research 32, 1681-1688.

Cook, N.J., 1973, On simulating the lower third of the urban adiabatic boundary layer in a wind tunnel, Atmospheric Environment (1967) 7, 691-705.

Cook, N.J., 1978, Wind-tunnel simulation of the adiabatic atmospheric boundary layer by roughness, barrier and mixing-device methods, Journal of Wind Engineering and Industrial Aerodynamics 3, 157-176.

Cook, N.J., 1985, The designer's guide to wind loading of building structures, Part 1: Background, damage survey, wind data and structural classification, In: Building Research Establishment, Garston, UK.

Cook, N.J., 1997, The Deaves and Harris ABL model applied to heterogeneous terrain, Journal of Wind Engineering and Industrial Aerodynamics 66, 197-214.

Corino, E.R. and Brodkey, R.S., 1969, A visual investigation of the wall region in turbulent flow, Journal of Fluid Mechanics 37, 1-30.

Counihan, J., 1973, Simulation of an adiabatic urban boundary layer in a wind tunnel, Atmospheric Environment (1967) 7, 673-689.

Counihan, J., 1975, Adiabatic atmospheric boundary layers: a review and analysis of data from the period 1880–1972, Atmospheric Environment 9, 871-905.

Coventry, J. and Pye, J., 2014, Heliostat cost reduction–where to now?, Energy Procedia 49, 60-70.

Cruz, E., Watkins, S., Loxton, B. and Watmuff, J., 2008, A flat plate rectangular wing subjected to grid-generated turbulence, in: 26th AIAA Applied Aerodynamics Conference, pp. 6247.

Deaves, D.M. and Harris, R.I., 1978, A mathematical model of the structure of strong winds, In: Report 76, Construction Industry Research and Information Association, London, UK.

Durst, C.S., 1960, Wind speeds over short periods of time, Meteorological Magazine 89, 181-186.

Dyrbye, C. and Hansen, S.O., 1996, Wind loads on structures, John Wiley & Sons, Chichester, UK.

Emes, M.J., Arjomandi, M., Kelso, R.M. and Ghanadi, F., 2017, Gust characteristics in a low-roughness atmospheric surface layer, Wind and Structures (submitted).

ESDU 85020, 1985, Characteristics of atmospheric turbulence near the ground - Part II: single point data for strong winds (neutral atmosphere), Engineering Sciences Data Unit, London, UK.

Eurocode, Actions on structures, Part 1-4: General actions - Wind actions, EN 1991-1.4, 2010.

Farell, C. and Iyengar, A.K., 1999, Experiments on the wind tunnel simulation of atmospheric boundary layers, Journal of Wind Engineering and Industrial Aerodynamics 79, 11-35.

Fernholz, H., Krause, E., Nockemann, M. and Schober, M., 1995, Comparative measurements in the canonical boundary layer at Reδ2≤ 6× 104 on the wall of the German–Dutch windtunnel, Physics of Fluids 7, 1275-1281.

Flay, R.G.J. and Stevenson, D.C., 1988, Integral length scales in strong winds below 20 m, Journal of Wind Engineering and Industrial Aerodynamics 28, 21-30.

Ghanadi, F., Emes, M., Yu, J., Arjomandi, M. and Kelso, R., 2016, Investigation of the Atmospheric Boundary Layer Characteristics on Gust Factor for the Calculation of Wind Load, In: *Proc., 22nd SolarPACES Conference*, Abu Dhabi, UAE.

Goldstein, R., 1996, Fluid Mechanics Measurements, CRC Press, Philadelphia, Pennsylvania, USA.

Gong, B., Li, Z., Wang, Z. and Wang, Y., 2012, Wind-induced dynamic response of Heliostat, Renewable Energy 38, 206-213.

Gong, B., Wang, Z., Li, Z., Zang, C. and Wu, Z., 2013, Fluctuating wind pressure characteristics of heliostats, Renewable energy 50, 307-316.

Grass, A.J., 1971, Structural features of turbulent flow over smooth and rough boundaries, Journal of Fluid Mechanics 50, 233-255.

Greenway, M.E., 1979, An analytical approach to wind velocity gust factors, Journal of Wind Engineering and Industrial Aerodynamics 5, 61-91.

Griffith, D.T., Moya, A.C., Ho, C.K. and Hunter, P.S., 2015, Structural dynamics testing and analysis for design evaluation and monitoring of heliostats, Journal of Solar Energy Engineering 137, 021010.

Hansen, S.O., 2007, Vortex-induced vibrations of structures, in: Structural engineers world congress, pp. 2-7.

Head, M. and Bradshaw, P., 1971, Zero and negative entrainment in turbulent shear flow, Journal of Fluid Mechanics 46, 385-394.

Högström, U.L.F., 1988, Non-dimensional wind and temperature profiles in the atmospheric surface layer: A re-evaluation, Boundary-Layer Meteorology 42, 55-78.

Holdø, A.E., Houghton, E.L. and Bhinder, F.S., 1982, Some effects due to variations in turbulence integral length scales on the pressure distribution on wind-tunnel models of low-rise buildings, Journal of Wind Engineering and Industrial Aerodynamics 10, 103-115.

Holmes, J.D., Allsop, A.C. and Ginger, J.D., 2014, Gust durations, gust factors and gust response factors in wind codes and standards, Wind and Structures 19, 339-352.

Holmes, J.D. and Ginger, J.D., 2012, The gust wind speed duration in AS/NZS 1170.2, Australian Journal of Structural Engineering 13, 207-217.

Holmes, J.D., Kwok, K.C.S. and Ginger, J.D., 2012, Wind Loading Handbook for Australia and New Zealand: Background to AS/NZS 1170.2 Wind Actions, Australasian Wind Engineering Society, Sydney, Australia.

Hong, J., Choi, T., Ishikawa, H. and Kim, J., 2004, Turbulence structures in the near-neutral surface layer on the Tibetan Plateau, Geophysical Research Letters 31, 15106.

Houbolt, J.C., 1970, Design manual for vertical gusts based on power spectral techniques, In: NO. ARAP-147, Aeronautical Research Associates of Princeton, Inc, Princeton, New Jersey.

Hutchins, N., Chauhan, K., Marusic, I., Monty, J. and Klewicki, J., 2012, Towards reconciling the large-scale structure of turbulent boundary layers in the atmosphere and laboratory, Boundary-Layer Meteorology 145, 273-306.

Hutchins, N. and Marusic, I., 2007, Evidence of very long meandering features in the logarithmic region of turbulent boundary layers, Journal of Fluid Mechanics 579, 1-28.

Jain, A., Jones, N.P. and Scanlan, R.H., 1996, Coupled flutter and buffeting analysis of long-span bridges, Journal of Structural Engineering 122, 716-725.

Jones, J., 1989, Statistical-discrete-gust method for predicting aircraft loads and dynamic response, Journal of Aircraft 26, 382-392.

Kaimal, J., Wyngaard, J., Izumi, Y. and Coté, O., 1972, Spectral characteristics of surface-layer turbulence, Quarterly Journal of the Royal Meteorological Society 98, 563-589.

Kaimal, J.C. and Finnigan, J.J., 1994, Atmospheric Boundary Layer Flows: Their Structure and Measurement, Oxford University Press, New York, USA.

Kawai, H., 1995, Effects of angle of attack on vortex induced vibration and galloping of tall buildings in smooth and turbulent boundary layer flows, Journal of wind engineering and industrial aerodynamics 54, 125-132.

Kelso, R.M., Lim, T.T. and Perry, A.E., 1993, The effect of forcing on the time-averaged structure of the flow past a surface-mounted bluff plate, Journal of Wind Engineering and Industrial Aerodynamics 49, 217-226.

Kristensen, L., Casanova, M., Courtney, M. and Troen, I., 1991, In search of a gust definition, Boundary-Layer Meteorology 55, 91-107.

Mannini, C., Marra, A., Massai, T. and Bartoli, G., 2013, VIV and galloping interaction for a 3: 2 rectangular cylinder, in: Proceedings of EACWE.

Marusic, I. and Hutchins, N., 2008, Study of the log-layer structure in wall turbulence over a very large range of Reynolds number, Flow, Turbulence and Combustion 81, 115-130.

Marusic, I., McKeon, B., Monkewitz, P., Nagib, H., Smits, A. and Sreenivasan, K., 2010, Wall-bounded turbulent flows at high Reynolds numbers: Recent advances and key issues, Physics of Fluids 22, 065103.

Mendis, P., Ngo, T., Haritos, N., Hira, A., Samali, B. and Cheung, J., 2007, Wind loading on tall buildings, EJSE Special Issue: Loading on Structures 3, 41-54.

Metzger, M., McKeon, B.J. and Holmes, H., 2007, The near-neutral atmospheric surface layer: turbulence and non-stationarity, Philosophical Transactions of the Royal Society of London A: Mathematical, Physical and Engineering Sciences 365, 859-876.

Milbank, J., Loxton, B., Watkins, S. and Melbourne, W., 2005, Replication of Atmospheric Conditions for the Purpose of Testing MAVs: MAV Flight Environment Project Final Report, Royal Melbourne Institute of Technology.

Murphy, L.M., 1980, Wind loading on tracking and field-mounted solar collectors, In: SERI-TP-632-958, Solar Energy Research Institute, Golden, USA.

Nakamura, Y., 1993, Bluff-body aerodynamics and turbulence, Journal of Wind Engineering and Industrial Aerodynamics 49, 65-78.

Noone, C.J., Torrilhon, M. and Mitsos, A., 2012, Heliostat field optimization: A new computationally efficient model and biomimetic layout, Solar Energy 86, 792-803.

Okajima, A., 1979, Flows around two tandem circular cylinders at very high Reynolds numbers, Bulletin of JSME 22, 504-511.

Peterka, J.A., Bienkiewicz, B., Hosoya, N. and Cermak, J.E., 1987, Heliostat mean wind load reduction, Energy 12, 261-267.

Peterka, J.A. and Derickson, R.G., 1992, Wind load design methods for ground-based heliostats and parabolic dish collectors, In: SAND92-7009, Sandia National Laboratories, Albuquerque, USA.

Peterka, J.A., Tan, Z., Cermak, J.E. and Bienkiewicz, B., 1989, Mean and peak wind loads on heliostats, Journal of solar energy engineering 111, 158-164.

Pfahl, A., Buselmeier, M. and Zaschke, M., 2011a, Wind loads on heliostats and photovoltaic trackers of various aspect ratios, Solar Energy 85, 2185-2201.

Pfahl, A., Buselmeier, M. and Zaschke, M., 2011b, Determination of wind loads on heliostats, in: Proceedings of the 17th SolarPACES Conference, Granada, Spain.

Pfahl, A., Coventry, J., Röger, M., Wolfertstetter, F., Vásquez-Arango, J.F., Gross, F., Arjomandi, M., Schwarzbözl, P., Geiger, M. and Liedke, P., 2017a, Progress in heliostat development, Solar Energy 152, 3-37.

Pfahl, A., Randt, M., Meier, F., Zaschke, M., Geurts, C. and Buselmeier, M., 2015, A holistic approach for low cost heliostat fields, Energy Procedia 69, 178-187.

Pfahl, A. and Uhlemann, P., 2011, Wind loads on heliostats and photovoltaic trackers at various Reynolds numbers, Journal of Wind Engineering and Industrial Aerodynamics 99, 964-968.

Plate, E.J., 1974, Aerodynamic Characteristics of Atmospheric Boundary Layers, US Atomic Energy Commission, Springfield, Virginia, USA.

Rao, K.S., Wyngaard, J.C. and Coté, O.R., 1974, The structure of the two-dimensional internal boundary layer over a sudden change of surface roughness, Journal of the Atmospheric Sciences 31, 738-746.

Rasmussen, J.T., Hejlesen, M.M., Larsen, A. and Walther, J.H., 2010, Discrete vortex method simulations of the aerodynamic admittance in bridge aerodynamics, Journal of Wind Engineering and Industrial Aerodynamics 98, 754-766.

Roadman, J.M. and Mohseni, K., 2009, Gust characterization and generation for wind tunnel testing of micro aerial vehicles, AIAA paper 1290, 4166.

Roshko, A., 1993, Perspectives on bluff body aerodynamics, Journal of Wind Engineering and Industrial Aerodynamics 49, 79-100.

Rosi, G., Martinuzzi, R. and Rival, D., 2013, A conditional analysis of spanwise vortices within the lower atmospheric log layer, Journal of Wind Engineering and Industrial Aerodynamics 119, 89-101.

Sakamoto, H., 1985, Aerodynamic forces acting on a rectangular prism placed vertically in a turbulent boundary layer, Journal of wind engineering and industrial aerodynamics 18, 131-151.

Sakamoto, H. and Arie, M., 1983, Vortex shedding from a rectangular prism and a circular cylinder placed vertically in a turbulent boundary layer, Journal of Fluid Mechanics 126, 147-165.

Sakamoto, H., Hainu, H. and Obata, Y., 1987, Fluctuating forces acting on two square prisms in a tandem arrangement, Journal of Wind Engineering and Industrial Aerodynamics 26, 85-103.

Sarkar, P.P., 2013, Advances in wind tunnel simulation, techniques and tools for assessing extreme-wind hazard to structures, in: The Eighth Asia-Pacific Conference on Wind Engineering, Chennai, India.

Sment, J. and Ho, C., 2014, Wind patterns over a heliostat field, Energy Procedia 49, 229-238.

Solari, G., 1993, Gust buffeting. I: Peak wind velocity and equivalent pressure, Journal of Structural Engineering 119, 365-382.

Solari, G. and Piccardo, G., 2001, Probabilistic 3-D turbulence modeling for gust buffeting of structures, Probabilistic Engineering Mechanics 16, 73-86.

AS/NZS 1170.2, Structural Design Actions - Part 2: Wind actions, Standards Australia and Standards New Zealand, Sydney, Australia.

Sun, H., Gong, B. and Yao, Q., 2014, A review of wind loads on heliostats and trough collectors, Renewable and Sustainable Energy Reviews 32, 206-221.

Swamy, N.V.C., Gowda, B.H.L. and Lakshminath, V.R., 1979, Auto-correlation measurements and integral time scales in three-dimensional turbulent boundary layers, Applied Scientific Research 35, 237-249.

Szepessy, S. and Bearman, P., 1992, Aspect ratio and end plate effects on vortex shedding from a circular cylinder, Journal of Fluid Mechanics 234, 191-217.

Téllez, F., Burisch, M., Villasente, Sánchez, M., Sansom, C., Kirby, P., Turner, P., Caliot, C., Ferriere, A., Bonanos, C.A., Papanicolas, C., Montenon, A., Monterreal, R. and Fernández, J., 2014, State of the Art in Heliostats and Definition of Specifications, In: 609837, STAGE-STE Project, Madrid, Spain.

Tennekes, H. and Lumley, J.L., 1972, A First Course in Turbulence, MIT press, Cambridge, Massachusetts, USA.

Teunissen, H.W., 1980, Structure of mean winds and turbulence in the planetary boundary layer over rural terrain, Boundary-Layer Meteorology 19, 187-221.

Townsend, A.A., 1976, The Structure of Turbulent Shear Flow, Cambridge University Press, New York, USA.

Van den Berg, G.P., 2006. The sound of high winds: The effect of atmospheric stability on wind turbine sound and microphone noise, Ph.D. Dissertation, Groningen University, Groningen, Netherlands.

Vásquez-Arango, J.F., Buck, R. and Pitz-Paal, R., 2015, Dynamic Properties of a Heliostat Structure Determined by Numerical and Experimental Modal Analysis, Journal of Solar Energy Engineering 137, 051001.

Venditti, J.G., Best, J.L., Church, M. and Hardy, R.J., 2013, Coherent Flow Structures at Earth's Surface, John Wiley & Sons.

Watkins, S., 2012, Turbulence Characteristics of the Atmospheric Boundary Layer and Possibilities of Replication for Aircraft, in: Third Symposium "Simulation of Wing and Nacelle Stall", Braunschweig, Germany.

Wei, T., Schmidt, R. and McMurtry, P., 2005, Comment on the Clauser chart method for determining the friction velocity, Experiments in Fluids 38, 695-699.

Wieringa, J., 1973, Gust factors over open water and built-up country, Boundary-Layer Meteorology 3, 424-441.

Wu, Z., Gong, B., Wang, Z., Li, Z. and Zang, C., 2010, An experimental and numerical study of the gap effect on wind load on heliostat, Renewable Energy 35, 797-806.

Xu, Y.L., 2013, Wind Effects on Cable-Supported Bridges, John Wiley & Sons, Singapore.

Yaghoubi, M. and Mahmoodi, S., 2004, Experimental study of turbulent separated and reattached flow over a finite blunt plate, Experimental Thermal and Fluid Science 29, 105-112.

Yu, J.S., Arjomandi, M., Ghanadi, F. and Kelso, R.M., 2016, The Effect of Inclination Angle on the Flow Characteristics of Tandem Bluff Plates, In: *Proc., 20th Australasian Fluid Mechanics Society Conference*, Perth, Australia.

Chapter 3

Stow Design Wind Speed of Heliostats

3.1. Section Overview

This chapter addresses the motivation to reduce the cost of heliostats by investigating the effect of the design wind speed at which heliostats are moved to the stow position, one of the principal factors in the design of a heliostat field. Second-generation heliostats developed by the Department of Energy (DOE) were designed to maintain a total optical error in any orientation during operation up to the stow design wind speed of 22 m/s and maintain the structural strength to withstand wind speeds up to 40 m/s in the stow position. A statistical model was developed to investigate the effect of lowering the design wind speed at which heliostats are moved to the stow position on the capital cost of the major components of the heliostat and the levelised cost of electricity (LCOE) of a PT plant. The model, assuming quasi-steady wind loads and simplified cost-area proportionality exponents, used the correlation between solar irradiation data and wind speed data to determine the capacity factor of the PT plant and the effect of heliostat size on the capital cost of heliostats. Furthermore, the model assessed the sensitivity of the LCOE to stow design wind speed through both the capital cost and the annual electricity production of a PT plant at six sites in Australia and the USA with a sufficient solar resource. The total capital cost of a heliostat field was highly dependent on the stow design wind speed, where the optimal heliostat size decreased from 50 m^2 to 25 m^2 with increasing design wind speed from 10 m/s to 20 m/s. In addition, the capacity factor of a heliostat field and power output of a PT plant showed small reductions when lowering the design wind speed from the maximum recorded at the site. Consequently, the sensitivity analysis found that lowering the design wind speed for stowing a heliostat at sites with mean wind speeds greater than 10 m/s, can lead to an 18% reduction in LCOE through manufacturing and installation costs with only a 2% loss in heliostat field capacity factor.

3.2. Effect of Stow Design Wind Speed on LCOE

Statement of Authorship

Title of Paper	Effect of heliostat design wind speed on the levelised cost of electricity from concentrating solar thermal power tower plants	
Publication Status	☑ Published ☐ Submitted for Publication	☐ Accepted for Publication ☐ Unpublished and Unsubmitted work written in manuscript style
Publication Details	Emes, M.J., Arjomandi, M. and Nathan, G.J., 2015, Effect of heliostat design wind speed on the levelised cost of electricity from concentrating solar thermal power tower plants, Solar Energy 115, 441-451	

Principal Author

Name of Principal Author (Candidate)	Matthew Emes		
Contribution to the Paper	Performed data analysis and interpretation, wrote manuscript and acted as corresponding author.		
Overall percentage (%)	70		
Certification:	This paper reports on original research I conducted during the period of my Higher Degree by Research candidature and is not subject to any obligations or contractual agreements with a third party that would constrain its inclusion in this thesis. I am the primary author of this paper.		
Signature		Date	3/11/17

Co-Author Contributions

By signing the Statement of Authorship, each author certifies that:

i. the candidate's stated contribution to the publication is accurate (as detailed above);

ii. permission is granted for the candidate in include the publication in the thesis; and

iii. the sum of all co-author contributions is equal to 100% less the candidate's stated contribution.

Name of Co-Author	Maziar Arjomandi		
Contribution to the Paper	Supervised development of work, helped in data interpretation and manuscript evaluation.		
Signature		Date	3/11/17

Name of Co-Author	Graham Nathan		
Contribution to the Paper	Supervised the research and contributed in academic discussion and manuscript review.		
Signature		Date	3/11/17

ELSEVIER
Available online at www.sciencedirect.com
ScienceDirect
Solar Energy 115 (2015) 441–451
SOLAR ENERGY
www.elsevier.com/locate/solener

Effect of heliostat design wind speed on the levelised cost of electricity from concentrating solar thermal power tower plants

Matthew J. Emes [*], Maziar Arjomandi, Graham J. Nathan

Centre for Energy Technology, School of Mechanical Engineering, The University of Adelaide, SA 5005, Australia

Received 23 November 2014; received in revised form 15 February 2015; accepted 17 February 2015

Communicated by: Associate Editor Ranga Pitchumani

Abstract

This paper assesses the influence on the levelised cost of electricity (LCOE) of the design wind speed at which heliostats in concentrating solar thermal (CST) power tower (PT) plants are stowed. Lowering the design wind speed for parking heliostats in the stow position reduces the cost of the heliostat field at the expense of a reduction in the energy harvested. However, both influences are highly non-linear and also vary from site to site, so that new understanding is needed to guide the optimisation of this parameter. The capacity factor and the power output for a PT plant without thermal storage are calculated for six locations by mapping hourly solar irradiance data to the Weibull probability distribution of mean wind speed. The cost of materials for the heliostat components and their sensitivity to heliostat size are estimated as a function of the design (stow) wind speed based on the specification of the structural design for quasi-static wind loads. The sensitivity of the LCOE to the design is assessed statistically. The results show that the materials cost of structural components in larger heliostats are most sensitive to the design wind speed, so that a 34% reduction in cost can be achieved by lowering the design wind speed from 15 m/s to 10 m/s. In contrast, the optimum design wind speed for smaller heliostats between 20 m^2 and 50 m^2 is typically above 10 m/s. The LCOE can be reduced by as much as 18% by lowering the design wind speed from the maximum recorded wind speeds at the three Australian sites. Hence there is significant economic benefit from optimising the minimum design at sites with high wind speeds.

Keywords: Levelised cost of electricity; Concentrating solar thermal; Power tower; Heliostat

1. Introduction

Current energy systems based on the consumption of fossil fuels are unsustainable in the long term, so that a transition to an environmentally sustainable energy system with the integration of renewable energy sources is necessary (Hernández-Moro and Martínez-Duart, 2013). Concentrating solar thermal (CST) power tower (PT) is one of the most promising renewable technologies capable of large scale electricity production (Hinkley et al., 2013). It offers both thermal energy storage and relative ease of integration with existing fossil fuel power plants and hybridisation for a base line power supply (Kolb et al., 2011). Government funded initiatives that are supporting the research and development of CST systems to make them competitive with base load energy rates include the US Department of Energy's SunShot Initiative, with a goal of \$0.06/kW h by 2020 (Kolb et al., 2011), and the more conservative Australian Solar Thermal Research Institute (ASTRI) program targeting \$0.12/kW h by 2020. To achieve these targets there is a need to lower the capital cost of a PT plant, of which the largest cost is the heliostat field.

---

[*] Corresponding author.

http://dx.doi.org/10.1016/j.solener.2015.02.047

One opportunity to lower the heliostat cost is through careful selection of the design wind speed. Here this is demonstrated by the assumption of quasi-static wind loads with a peak-load coefficient derived from wind tunnel data, although the use of site-specific data, if available, would make the estimates more accurate.

The opportunities identified to reduce heliostat costs through technical advances in a recent Sandia workshop (Kolb et al., 2011) are through improved materials, and through improved structural performance of stowed heliostats during survival high wind conditions. Optimisation of the heliostat structure is predicted by Kolb et al. (2011) to enable a 10% reduction in heliostat cost per unit area ($\$/m^2$) of PT plants by 2020, which would help achieve the DOE goal of $\$75/m^2$ heliostat total installed costs. The scaling relationships of Kolb et al. (2007) were used to estimate that the heliostat costs scale with the mirror area to the power of 1.5, which is consistent with the quasi-static wind load approach by Lovegrove and Stein (2012) and by Blackmon (2013) applied to the three cost categories of a heliostat. There is also currently no consensus on the optimum size of a heliostat. Hence an aim of this investigation is to develop cost-load relationships that can be used to estimate the cost of a single heliostat as a function of the design (stow) wind speed and the heliostat mirror area.

The current practice in the operation of heliostat fields is to move each heliostat to a parked (or stowed) position during periods of high wind speeds, which reduces loads by greatly reducing the cross projected area to the wind. Peak wind loads associated with gusts and dynamic amplification on stowed heliostats have been measured to be more than 10 times larger in magnitude than the mean loads on heliostats in the stow position (Peterka et al., 1989). Currently the design wind speed for stowing heliostats is 22 m/s, according to specifications for Department of Energy (DOE) second generation heliostats (Murphy, 1980). Stowing the heliostats lowers the effective capacity factor of the plant if the periods of high wind speed occur during periods of good solar irradiance. However, the probability distribution of wind speed typically follows a Weibull distribution so that the most extreme wind speeds are highly improbable. Furthermore, the probability that the periods of extreme wind coincide with a period of high solar irradiance is even lower. Hence there is an opportunity to lower costs by optimising the trade-off between losses in capacity factor and lowering the cost of the heliostat array through lowering the design wind speed at which the heliostats are parked. A systematic study of the trade-off between capacity factor and design wind speed has not been reported before. Hence the present investigation aims to meet this need.

The economic feasibility of renewable energy technologies such as CST relative to fossil fuel plants is often assessed by levelised cost of electricity (LCOE) (IEA, 2010). The current LCOE of CST PT systems is estimated to be \$0.223/kW h in Australia (Hinkley et al., 2013) and \$0.137/kW h in USA (Turchi et al., 2010), so that significant reductions are needed to reach the ASTRI and SunShot targets of \$0.12/kW h and \$0.06/kW h respectively by 2020. The LCOE is influenced by the capital cost of the plant, of which the field of heliostats is estimated to constitute 39% (Hinkley et al., 2011), and by the capacity factor. Both of these are dependent on the design wind speed for stowing the heliostat. A recent sensitivity analysis about a \$0.25/kW h baseline cost of CST in Australia (Lovegrove et al., 2012) showed that a 10% reduction in the capital cost of a PT plant results in a 9% reduction in LCOE. However, while the influence of the local variation in solar irradiation on LCOE has been reported to decrease by 4.5% for each 100 kW h/m^2-year between 2000 kW h/m^2-year and 2800 kW h/m^2-year (IEA-ETSAP and IRENA, 2013), the effect of wind speed has not been reported before. The aim of the present paper is therefore to address the economic viability of CST PT technology on the basis of selection of the design wind speed for stowing heliostats.

The overall aim of this paper is to determine the trade-off between lowering the design wind speed for stowing heliostats, which reduces the capital cost of heliostats, and the losses in capacity factor and power output of a PT plant. The first aim is to estimate the relationship between wind load and the material costs of manufacturing heliostat fields as a function of the design wind speed. The second aim is to calculate the reduction to capacity factor associated with lowering heliostat cost through lowering the design wind stow-speed for heliostats. The third aim is to calculate the relative influences of the design stow speed on the LCOE of a PT plant through its impact on heliostat cost and the capacity factor.

2. Methodology

Six sites were selected for assessment based on the joint criteria of a good solar resource with an annual average DNI greater than 2000 kW h/m^2-year and the availability of good quality records of both wind speed and solar DNI. Here the value of 2000 kW h/m^2-year, which corresponds to an annually averaged flux of 228 W/m^2, has been estimated to be the minimum threshold needed for a solar thermal plant to be economically viable (IEA-ETSAP and IRENA, 2013). The solar energy input was calculated from historical time series of direct normal irradiance (DNI) measured using a pyrheliometer, which can achieve an accuracy of 15 W/m^2 on a regional scale (Arvizu et al., 2011). This is more reliable than satellite measurements. Similarly, wind speed data must also be based on local measurements, since it is too difficult to predict the effects of topography and weather from other data. Hence the six sites in Table 1 were identified with good quality data of hourly average DNI and hourly average wind speed (Bureau of Meteorology, 2014; National Climatic Data Center, 2014; NREL, 2010).

2.1. Variation of mean wind speed with height

The log law was used to estimate the vertical profile of the wind speed under the assumption of asymptotic

Table 1
Details of the six sites selected for analysis of hourly average DNI and hourly average wind speed data.

Station	Latitude (°)	Longitude (°)	Elevation (m)	Barometer height (m)	Annual average DNI (kW h/m^2-year)
Alice Springs, Australia	−23.7951	133.8890	546	1	2771
Mildura, Australia	−34.2358	142.0867	50	2.8	2251
Darwin, Australia	−12.4239	130.8925	30.4	4.6	1970
Las Vegas, USA	36.0719	−115.1634	664.5	1.5	1875
Bakersfield, USA	35.4344	−119.0542	149	1.5	2387
Phoenix, USA	33.4277	−112.0038	337.4	1.5	1964

similarity for a neutral atmospheric boundary layer, following earlier work (Cook, 1997; Li et al., 2010)

$$U(z) = \left(\frac{U_\tau}{\kappa}\right) \ln\left(\frac{z}{z_0}\right), \tag{1}$$

where $U(z)$ is the wind speed at height z, U_τ is the surface friction velocity, κ is von Karman's constant (0.4) and z_0 is the surface roughness length. This is preferable to the power law and Deaves–Harris model (Sun et al., 2014) at heights of up to 100 m above the ground surface (Cook, 1997; Li et al., 2010; Sun et al., 2014). The standard specification height for design wind speed is 10 m according to ANSI/ASCE 7-88 (Peterka and Derickson, 1992). Mean wind speed data was therefore scaled to a 10 m height using Eq. (2) for effective comparison of the six locations. The quasi-static approach assumes that the unsteady component of the wind, represented by a 3-s gust wind speed, can be related to the mean wind speed at this height by a ratio of 1.6 for an open country terrain (Peterka and Derickson, 1992). The annual average ratio of gust speed to mean speed was calculated to be 1.34, 1.44 and 1.46 at Darwin, Alice Springs and Mildura, respectively.

$$\frac{U(z)}{U(z_{\text{ref}})} = \frac{\ln\left(\frac{z}{z_0}\right)}{\ln\left(\frac{z_{\text{ref}}}{z_0}\right)} \tag{2}$$

A surface roughness length z_0 of 0.015 m characterises the terrain as open country with flat grassy plains (Peterka and Derickson, 1992; Peterka et al., 1988). This represents the typical surroundings of solar thermal power plants (Peterka and Derickson, 1992).

2.2. Probability distribution of mean wind speed

The two-parameter Weibull probability distribution function $f(U)$ of mean wind speed was calculated as:

$$f(U) = \left(\frac{k}{c}\right)\left(\frac{U}{c}\right)^{k-1} \exp\left[-\left(\frac{U}{c}\right)^{k}\right], \tag{3}$$

where k is the shape parameter and the c (m/s) is the scale parameter. The probability of a given wind speed being exceeded at the site is one important consideration when selecting the design wind speed that a structure can withstand. The Weibull function is used for fitting a frequency curve to a wide range of recorded wind data (Dorvlo, 2002; Garcia et al., 1998; Lun and Lam, 2000; Stewart and Essenwanger, 1978; Weisser, 2003). The mean standard deviation method adopted from Hennessey (1977) is used in this investigation to calculate the two Weibull parameters below due to the simplicity of obtaining mean wind speed $\overline{U}$ and standard deviation σ_U from a collection of wind speed data (Ahmed et al., 2006).

$$k = \left(\frac{\sigma_U}{\bar{U}}\right)^{-1.086} \tag{4}$$

$$c = \frac{\bar{U}}{\Gamma\left(1 + \frac{1}{k}\right)} \tag{5}$$

Here Γ is the gamma function. The two Weibull parameters in Eqs. (4), (5) were calculated for the 10 m mean wind speed data at the six weather stations listed in Table 1.

2.3. Capacity factor

The capacity factor, CF, was calculated as the joint probability of wind speed being below the maximum wind speed U_{des} and the probability of solar irradiance being above the minimum threshold specified in Section 2:

$$CF = \mathrm{P}(U \leqslant U_{des}) \cdot \mathrm{P}(DNI \geqslant 228\ \mathrm{W/m^2}), \tag{6}$$

where the CF was calculated from hourly DNI and hourly wind speed data at each location. A PT plant without thermal storage is assumed to only operate at times when the solar irradiation meets the condition in Eq. (6) estimated from a sensitivity analysis in Section 3.2. The reference case for the design wind stow-speed was selected to be the maximum wind speed that provides the full load capacity. The design wind speed of so called "second generation" heliostats is specified to be 22 m/s for stowing the heliostat (Murphy, 1980), which is the maximum mean wind speed that can be tolerated by the heliostat in any orientation. Hence, it is assumed that the heliostats will be able to survive gusts of a higher speed for a particular ratio of gust to mean wind speed that is relevant at the site. An additional sensitivity analysis in Section 3.2 has been conducted to determine the sensitivity of capacity factor to stowing the heliostat at a lower design wind speed than the specified value. This is relevant because plant operators may choose to operate the plant conservatively and park the heliostats below the maximum design wind speed.

2.4. Power output

The power output of a PT plant was calculated by incorporating the joint probability of operating hours and heliostat field output:

$$P = DNI|_{>228\ \mathrm{W/m^2}} \cdot \eta_f \cdot \eta_t \cdot \psi_{CF}, \qquad (7)$$

where (W/m^2) is the instantaneous solar irradiance, where it exceeds a minimum threshold, taken here to be 228 W/m^2, η_f is the heliostat field efficiency, is the thermal-to-electric conversion efficiency of the turbine in the power block, which was assumed to be 42% (Kolb et al., 2011), and ψ_{CF} is a binary parameter for capacity factor that is unity when the wind speed is below the design threshold and zero when it is above it. The method for calculating field efficiency adopted by Kueh et al. (2014) was calculated by, where θ_i is the incidence angle of the sun. This angle is a function of the time of the year, time of the day and the location of the site. Annual and seasonal average daily profiles of power output were generated by averaging the output calculated at each hour of the day. The analysis assumes that the thermal efficiency of the power block is constant and that the plant only generates electricity at times when the DNI is above the threshold and the wind speed is less than the design threshold. While the analysis assumes that the optical efficiency is independent of the stow speed of the heliostat field, in practice these are linked. Hence, there is a need for more information on the relationships between the cost of the heliostat field, its optical efficiency and wind stow speed.

2.5. Capital cost of heliostats

The cost of heliostat components were calculated as a function of design wind speed from the cost-load and cost-area proportionality exponents in Table 2. Fig. 1 presents a breakdown of the relative contribution of a heliostat to the capital cost based on the 2011 Sandia estimates (Kolb et al., 2011) for 30 m^2 and 148 m^2 heliostats. These span a range, in part because the relative contributions vary with heliostat size. For example, the relative cost of the pedestal, support structure and foundation increases with size because larger heliostats are subjected to greater wind loads (Kolb et al., 2011). In contrast, the costs of manufacturing, field wiring and controls become more significant for smaller heliostats, due to the increased number of heliostats in the field (Kolb et al., 2011).

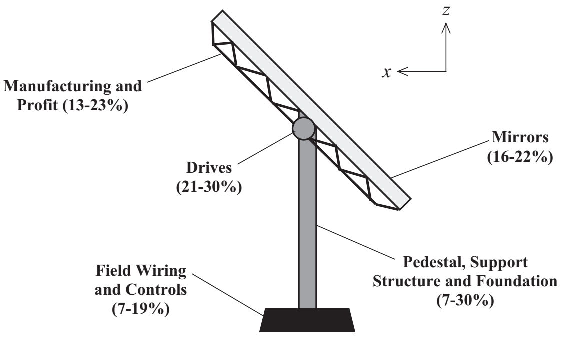

Fig. 1. Relative contribution of heliostat components to capital cost from a 2011 cost reduction study (Kolb et al., 2011).

Cost-area proportionality exponents, shown in Table 2, for all components of the heliostat were sourced directly from the Sandia heliostat cost reduction study (Kolb et al., 2007). Cost-load proportionality exponents for the drives and the controls were also sourced from Kolb et al. (2007), while the cost of structural components was estimated to be a function of design wind speed, consistent with the quasi-static wind load approach and cost categorisation of heliostat components used by Lovegrove and Stein (2012) and by Blackmon (2013). The key assumptions made in the cost analysis are:

- Reference wind load coefficients were assumed to be as measured in the Sandia wind tunnel tests (Peterka et al., 1989) for a mean wind speed of 12 m/s at the heliostat elevation axis height.
- Reference wind loads were calculated for a 120 m^2 heliostat with an elevation axis height of 5.4 m and torque tube diameter of 0.6 m (Pfahl and Uhlemann, 2011).
- The heliostat was assumed to have square mirror area with constant density of materials used in the construction of components at a mass production rate of 50,000 heliostats per year (Kolb et al., 2007).

Table 2
Proportionality relationships used in cost scaling analysis.

Heliostat component	Cost-load proportionality	Cost-area proportionality	Source
Azimuth drive	$C \propto 0.3068 M_z$	$C \propto A^{0.6}$	Lovegrove and Stein (2012)
Elevation drive	$C \propto 0.3068 M_{H_y}$	$C \propto A^{0.6}$	Lovegrove and Stein (2012)
Pedestal	$C \propto M_y$	$C \propto A^{1.5}$	–
Foundation	$C \propto M_y^{0.5}$	$C \propto A^{1.5}$	International Code Council (2010)
Torque tube	$C \propto M_{H_y}$	$C \propto A^{1.5}$	–
Truss	$C \propto F_x^{0.5}$	$C \propto A^{1.5}$	Farkas and Jármai (2013)
Braces	$C \propto F_x^{0.5}$	$C \propto A^{1.5}$	Farkas and Jármai (2013)
Mirror	$C = \text{constant}$	$C = \text{constant}$	Blackmon (2013)
Wiring	$C = \text{constant}$	$C \propto A^{0.448}$	Kolb et al. (2007)
Controls	$C_{\text{motor}} \propto M_y^{0.436}$	$C \propto A^{0.185}$	Kolb et al. (2007)

- Heliostat component costs were based on material and labour costs in 2006 for deployment of 600 MW of power towers per year (Kolb et al., 2007).
- The cost of structural components vary with the cube of the chord length of the heliostat following Kolb et al. (2007) – see Table 2.
- The profit margin for the manufacturer is 20% of the total direct cost (Kolb et al., 2007; Sargent & Lundy LLC Consulting Group, 2003).

Wind loads on the reference 120 m^2 heliostat were calculated from the component geometry using the peak wind load coefficients measured in the Sandia wind tunnel (Peterka et al., 1989) in combination with the mean wind speed for the site following Peterka and Derickson (1992) to account for the effects of wind gusts. The wind loads on the structural components of a heliostat are the drag force F_x, azimuth moment M_z, hinge moment M_{H_y} and overturning moment M_y, were calculated as follows:

$$F_x = C_{F_x}\frac{1}{2}\rho U^2 A \tag{8}$$

$$M_z = C_{M_z}\frac{1}{2}\rho U^2 Ab \tag{9}$$

$$M_{H_y} = C_{M_{H_y}}\frac{1}{2}\rho U^2 Ab \tag{10}$$

$$M_y = C_{M_y}\frac{1}{2}\rho U^2 Ah, \tag{11}$$

where $C_{F/M}$ is the peak force/moment coefficient, ρ (kg/m^3) is the density of air, U (m/s) is the mean wind speed at the elevation axis height h (m), A (m^2) is the heliostat mirror area and b (m) is the chord length of the heliostat.

The cost of materials for the structural components of a 120 m^2 heliostat as a function of wind load were estimated following Kolb et al. (2007). Table 2 shows the derived cost-load proportionality approximations. The azimuth drive must resist the moment M_z about the vertical azimuth (z) axis in Fig. 1 and the elevation drive must resist the hinge moment M_{Hy} about the elevation axis (Pfahl and Uhlemann, 2011). The dependence of the cost of the drives was estimated by scaling both the azimuth and hinge moments using the linear fit from Lovegrove and Stein (2012) because it showed a better agreement with manufacturer data than the proportionality exponent (Kolb et al., 2007). The cost of both drive units in Table 2 was assumed to vary with mirror area by a constant proportionality exponent of 0.6 used by Kolb et al. (2007).

The pedestal and foundation must withstand the overturning moment M_y at the pylon base of the heliostat (Pfahl and Uhlemann, 2011). The foundation depth d (m), converted from imperial to SI units, required to resist lateral loads for a constrained ground surface is given by

$$d = \sqrt{\frac{0.00425M_y}{S_3 b}}, \tag{12}$$

where M_y (Nm) is the overturning moment at the base of the pedestal, S_3 (kPa) is the allowable soil-bearing pressure and b (m) is the pedestal diameter (International Code Council, 2010). Foundation costs for concrete were assumed to be \$91/m and the cost of steel to be \$0.5/kg for the pedestal (Kolb et al., 2007). Stress analysis of a hollow cylindrical cantilever beam using Eqs. (13) and (14) allows the thickness of the pedestal tube and torque tube to be estimated from the maximum bending moment applied for the selected range of wind speeds.

$$\sigma = \frac{M_y y}{I_{cyl}} \tag{13}$$

$$I_{cyl} = \frac{\pi}{4}(r_2^4 - r_1^4) \tag{14}$$

Here σ (kPa) is the bending stress, y (m) is the distance from the neutral axis, I_{cyl} (m^4) is the moment of inertia of a hollow cylinder, r_2 (m) is the cylinder outer radius and r_1 (m) is the cylinder inner radius. The cost of the torque tube was assumed to be \$0.684/kg (Kolb et al., 2007). Costs of the foundation, pedestal and torque tube were estimated from the mass of material required to withstand the wind loads at the given design wind speed. The stowed heliostat was also assumed to have sufficient strength to withstand wind loads according to the quasi-static expressions developed by Peterka et al. (1989). The dependence on wind loading of cost of the pedestal and torque tube was taken to be linear, as shown in Table 2. The cost of structural components was scaled with the mirror area to the power of 1.5 under the assumption that the stiffness is constant for varying heliostat sizes, following the quasi-static wind load approach by Kolb et al. (2007) together with the cost categories of Lovegrove and Stein (2012) and that of Blackmon (2013).

Cost relationships for the truss and braces of the support structure were estimated using optimum design of steel tubular structures for displacement (Farkas and Jármai, 2013). The thickness of the steel support rods in tension and compression from the applied drag force of the wind was determined for steel with a yield stress of 355 MPa, Young's modulus of 210 MPa and a circular hollow section slenderness of 50. The effective buckling length factor was assumed to be 0.9 for vertical rods and 0.75 for horizontal and diagonal rods (Farkas and Jármai, 2013).

2.6. Levelised cost of electricity (LCOE)

For this analysis, LCOE is calculated using the following equation (IEA, 2010)

$$\mathrm{LCOE} = \frac{\sum_{t=1}^{n}(I_t + M_t)\cdot(1+r)^{-t}}{\sum_{t=1}^{n}(E_t)\cdot(1+r)^{-t}}, \tag{15}$$

where I_t (\$/kW) is the capital costs of constructing and installing all components of the PT plant in the year t, M_t (\$/kW) is the operational and maintenance costs of the plant in the year t, E_t (kW h) is the electricity

Table 3
Main assumptions for LCOE analysis of a 20 MW CST PT plant.

Parameter	Value	Source
Tower-receiver capital cost ($/kW)	200	Kolb et al. (2011)
Power block capital cost ($/kW)	1000	Kolb et al. (2011)
Operation and maintenance cost ($/kW-year)	65	Beath (2012)
Discount rate (%)	14	Sargent & Lundy LLC Consulting Group (2003)
Power block thermal-electric efficiency (%)	42	Kolb et al. (2011)
Useful plant life (years)	30	Kolb et al. (2007)
Plant capacity (MW)	20	NREL (2011)
Heliostat mirror area (m^2)	120	NREL (2011)
Number of heliostats in field	1255	NREL (2011)
Number of heliostat fields	1	NREL (2011)

production in the year t, r is the discount rate and n(years) is the useful plant life.

The LCOE is a function of both the heliostat cost and the power output from the PT plant, which were calculated as a function of the design wind speed using the parameters shown in Table 3. The total power from the dynamic solar resource was calculated assuming a minimum DNI threshold of 228 W/m^2 together with the maximum wind speed design threshold. Operational and maintenance costs are assumed to be constant throughout the plant life with no dependence on design wind speed. The output capacity of the PT plant was assumed to be 20 MW for a single heliostat field with the same number of 120 m^2 heliostats as Abengoa Solar's PS20 plant (NREL, 2011).

3. Results and discussion

3.1. Probability distribution of mean wind speed

Fig. 2(a) presents the Weibull probability distribution function using Eq. (3) for one year of mean wind speed data in each of the six locations. The shape of the Weibull curves at the three Australian sites shows that the highest mean wind speeds throughout the year are not likely to occur very frequently. For example, an 18 m/s wind speed is only likely to occur in Alice Springs for 0.1545% of the year or a return period of 647 days, while the corresponding values in Mildura and Darwin are 391 years and 1370 years in Mildura and Darwin, respectively. The Weibull probability curves for the three US locations span a narrower range of wind speeds. The return period at a 9 m/s design wind speed is 6 years in Las Vegas and 78 years in Bakersfield indicating that, at the three US sites, the maximum wind speeds can be selected as the design wind speed for stowing heliostats.

Operation of heliostats is limited to the daytime hours in which the DNI is above the threshold of minimum irradiance to be useful. Hence, it is necessary to calculate the wind speed as a function of DNI. Fig. 2(b) presents the Weibull probability distribution of mean wind speed as a function of DNI at Bakersfield, USA in 2010. It is clear that the probability of high wind speeds increases with DNI. For example, there is a 30% probability of a 6 m/s mean wind speed occurring at DNI > 800 W/m^2, compared with a zero probability at DNI < 200 W/m^2. Maximum mean wind speeds at Bakersfield therefore tend to coincide with times of high solar irradiance. Similar trends were observed at the other locations, although the shape of the Weibull curves exhibits a weaker dependence on solar irradiance.

3.2. Capacity factor

Fig. 3(a) presents the dependence of the capacity factor on the design wind speed for the six sites selected for analysis. The capacity factor can be seen to increase significantly with the design wind speed at the US sites to maximum values of 41.6% in Las Vegas and 44.3% in Bakersfield and Phoenix. Lowering the design wind speed by 3 m/s from the maximum in these three locations reduces the CF by

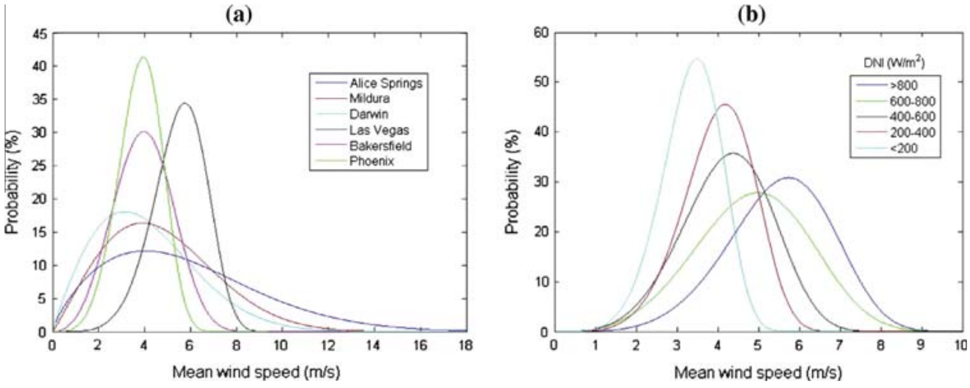

Fig. 2. (a) Weibull probability distributions of mean wind speed for one year at the six sites; (b) Joint Weibull probability distributions of mean wind speed for different DNI ranges at Bakersfield, USA in 2010.

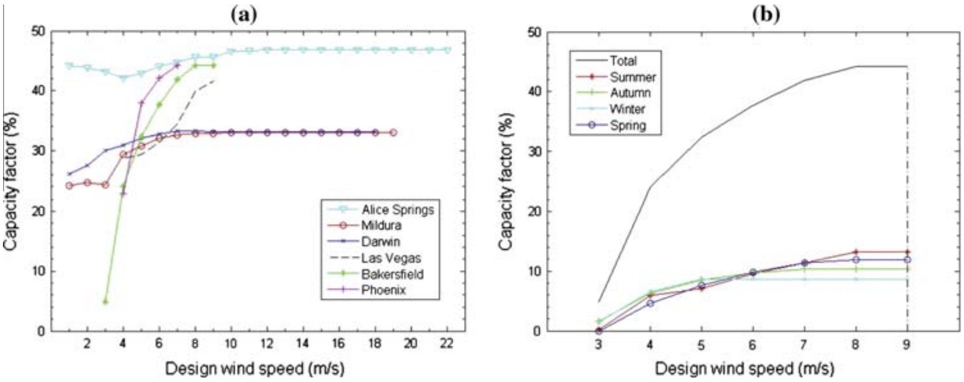

Fig. 3. (a) Dependence of capacity factor on design wind speed U_{des} for the six sites selected for analysis; (b) Seasonal variation of *CF* with U_{des} at Bakersfield, USA in 2010.

10%, 12% and 21%, respectively. The capacity factor is less sensitive to design wind speed at the three Australian sites, as shown by the lower design wind speeds of 10 m/s, 12 m/s and 6 m/s in Alice Springs, Mildura and Darwin, respectively. The corresponding reduction in is 2%, 9% and 7%, respectively. Hence, for most sites and over most of the wind-speed range, a small reduction in the design wind speed typically only has a small impact on *CF*.

The seasonal dependence of capacity factor on design wind speed is reported in Fig. 3(b) for each of the four seasons at Bakersfield in 2010. The capacity factor of a PT plant increases significantly at higher wind speeds, particularly during summer and spring. Decreasing the design wind speed from 9 m/s to 5 m/s results in a 6% loss in capacity factor in summer compared to a negligible loss in winter. This indicates that times of the strongest DNI in Bakersfield, which are most favourable for CST generation, tend to coincide with the highest wind speed conditions.

The influence of traversing the heliostat to the stow position at a lower wind speed than the specified design wind speed on the capacity factor of the heliostat field is shown by a sensitivity analysis in Fig. 4(a). The capacity factor is relatively insensitive to small reductions in design wind speed from the maximum recorded speed at the three sites. The largest reduction in capacity factor is 4.1% at Las Vegas for a 10% reduction in design wind speed from the peak value, compared with only a 0.1% lower capacity factor for a 40% reduction in design speed at Mildura. The peak capacity factors are therefore unlikely to be overestimated at high wind speed sites such as Mildura. Fig. 4(b) presents the sensitivity of the capacity factor to the minimum hourly average DNI threshold for PT plant operation without thermal storage at Phoenix. The capacity factor shows an increasing dependence on the design threshold with design wind speed, where the smallest change in capacity factor occurs between the 200 W/m^2 and 300 W/m^2 lines. The chosen threshold of 228 W/m^2 is therefore considered acceptable for the analysis, and is broadly consistent with the operating threshold of 300 W/m^2 for system start-up of a CST PT plant (Romero-Alvarez and Zarza, 2007).

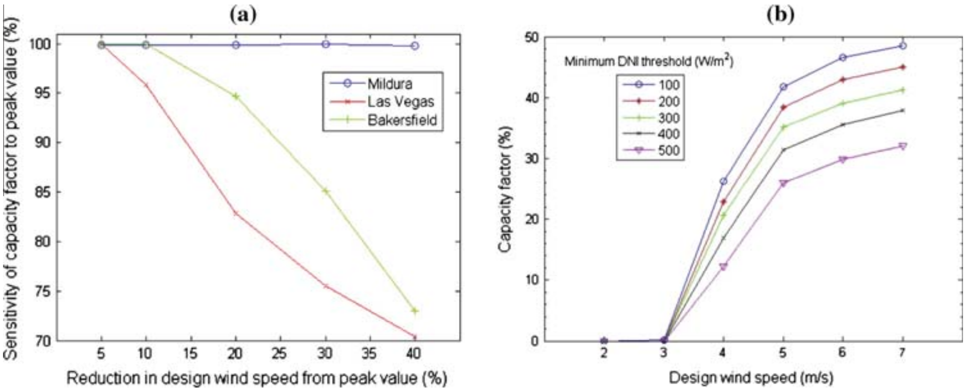

Fig. 4. (a) Sensitivity analysis of capacity factor to a reduction in stow speed from the maximum recorded at selected sites; (b) Sensitivity analysis of capacity factor to the minimum hourly average DNI threshold for plant operation at Phoenix, USA in 2010.

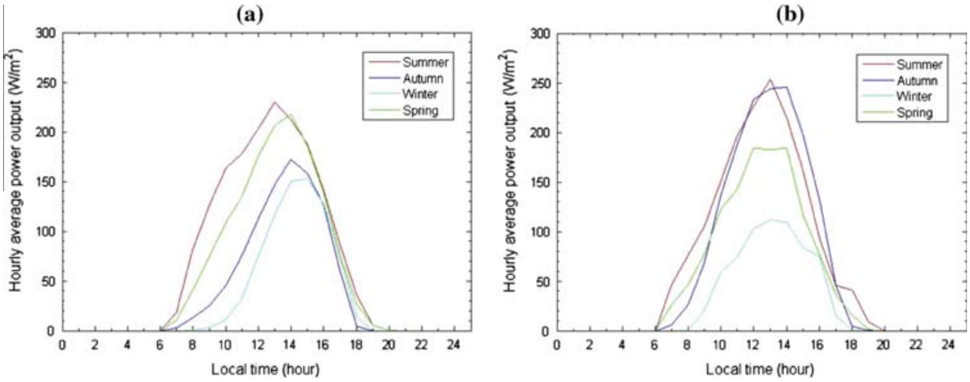

Fig. 5. Average hourly variation of plant power output for the four seasons at (a) Alice Springs, Australia in 2012 for a 10 m/s design wind speed; (b) Las Vegas, USA in 2010 for a 9 m/s design wind speed.

3.3. Power output

Fig. 5 presents the hourly average power output from a 20 MW PT plant for each season at two sites. Of these, the total annual output at Las Vegas is greatest at 929 MW for a maximum design wind speed of 9 m/s, with a peak hourly average power output over 250 W/m^2 at 1 pm in summer. In comparison, the same PT plant at Alice Springs can only produce 831 MW of power for a 10 m/s design wind speed that optimises capacity factor (see Section 3.1). The peak hourly average power output is also lower – 230 W/m^2 at 1 pm in summer. The operating times of a PT plant are similar at both sites for all seasons and the power output profile in Las Vegas is approximately symmetric about the maximum value. However, the variation of power output through the year is less at Alice Springs, where there is only a 34% difference between the summer and winter peak averages compared with a 56% difference at Las Vegas.

Fig. 6 presents the dependence of hourly average power output averaged throughout the year on the design wind speed at Alice Springs and Las Vegas. Consistent with expectation, the power output decreases with a reduction in the design wind speed at both locations. However, the trends are highly non-linear. For example, lowering the design wind speed by 5 m/s (25%) from 20 m/s to 15 m/s in Alice Springs only reduces the total and peak power output by 1.6% and 2%, respectively. In contrast, a reduction in the design wind speed by a further 5 m/s to 10 m/s leads to equivalent reductions of 14% and 12.5%, respectively. This suggests that, at this site, it may be possible to reduce the LCOE by lowering the design wind speed to below 20 m/s, in which case there will be an optimal speed for lowest LCOE. In contrast, even a reduction in the design wind speed by 1 m/s (10%) in Las Vegas results in a reduction in the total and peak power output by 11% and 0%, respectively, while the equivalent reductions are 70% and 59%, respectively when the wind speed is decreased by 3 m/s (30%). This, together with the relatively low magnitude of wind speeds at this site, suggests that any benefits in lowering the design wind speed there will be small.

3.4. Capital cost of heliostats

Fig. 7 presents the dependence of heliostat component costs per unit of mirror area ($/m^2) on the heliostat design wind speed for a 120 m^2 heliostat. The total cost can be

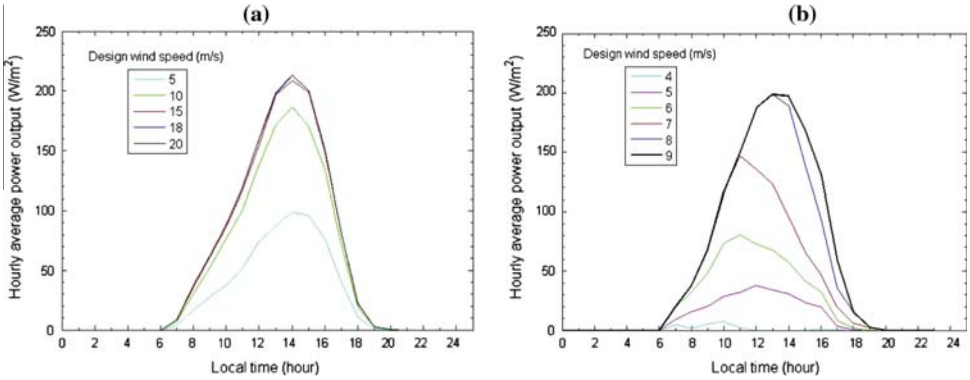

Fig. 6. Dependence of average hourly power output of a PT plant on design wind speed U_{des} at (a) Alice Springs, Australia in 2012; (b) Las Vegas, USA in 2010.

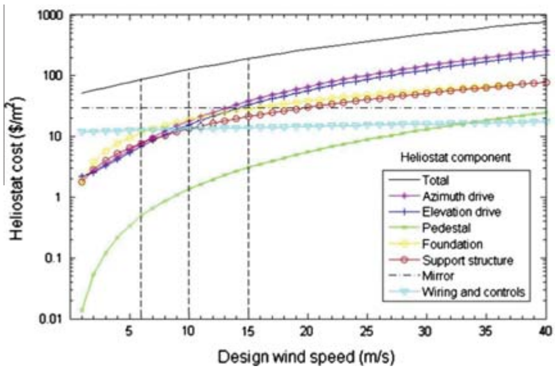

Fig. 7. Calculated dependence of the capital cost of the components of a single 120 m^2 heliostat as a function of design wind speed using the costing in Table 2.

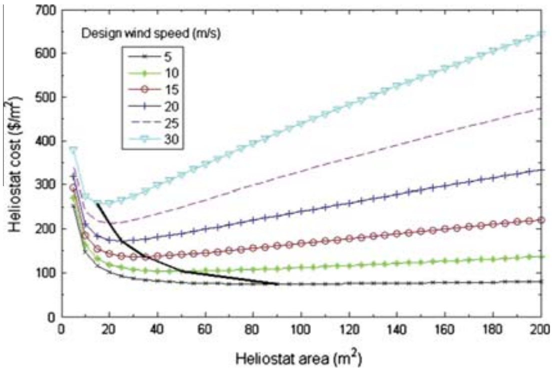

Fig. 8. Calculated dependence of heliostat capital cost on design wind speed as a function of heliostat area using the cost-area scaling relationships in Table 2. The solid black line corresponds to the locus of minimum heliostat cost.

seen to increase almost logarithmically from \$51/m^2 to \$728/m^2 as the design wind speed is increased from 1 m/s to 40 m/s. The total installed cost of the heliostat shows good agreement with the \$126/m^2 estimate by Kolb et al. (2007) at the design wind speed of 12 m/s used as a reference for peak wind load coefficients measured by Peterka et al. (1989). The pedestal, support structure and foundation components of a heliostat are most sensitive to wind loads for this heliostat, since capital cost increases at higher wind speeds due to the larger quantity of steel (per m^2 of surface area) in larger heliostats to maintain a rigid structure (Kolb et al., 2011). These structural components constitute only 6% of the heliostat cost at a 1 m/s design wind speed, compared with 22% at 10 m/s and 23% at 15 m/s. Wiring and controls are almost independent of the design wind speed, especially as the design wind speed is increased.

The design wind speed can be seen to have a significant influence on the capital cost of a heliostat. For example, lowering the design wind speed from 15 m/s to 10 m/s yields a 34% reduction of the total capital cost of a single heliostat, which is equivalent to a saving of approximately \$7100 per heliostat of 120 m^2 mirror area. This is a significant saving when compared with the deduction of Kolb et al. (2011) that only a 10% improvement in heliostat cost could be achieved by 2020 with wind load measurement and mitigation to optimise heliostat structural performance.

Fig. 8 presents the dependence of heliostat component costs on the mirror area for six design wind speeds. This shows that the optimal size of the heliostat is a function of the design wind speed because the influence of the design wind speed increases with the size of the heliostats. The sensitivity of cost to wind speed is relatively weak for lower design wind speeds of around 5 m/s, but is significant by 10 m/s. The predicted minimum costs for the 15 m/s design wind speed are comparable with those shown by Lovegrove and Stein (2012). Interestingly, the optimal size is always less than 120 m^2, even for a design wind speed of 5 m/s, and is down to 50 m^2 for a design wind speed of 10 m/s and 25 m^2 for a design wind speed of 20 m/s. Thus heliostat cost can be minimised, particularly in regions with wind peak speeds of approximately 10 m/s and above, by manufacturing smaller heliostats.

3.5. Sensitivity of LCOE to heliostat design wind speed

Fig. 9 presents the dependence of LCOE of a PT plant on the heliostat design wind speed at the six sites selected for analysis in Table 1. It can be seen that, in all cases, the optimal design wind speed is less than 13 m/s while, in cases such as Phoenix, it is as low as 7 m/s. Lowering the design wind speed from the maximum recorded at the three Australian sites is found to yield a significant economic benefit, such that the LCOE of a PT plant at Alice Springs, Mildura and Darwin can be reduced by 18%, 17% and 15%, respectively. In contrast, the optimised LCOE at the three US sites, including \$0.07/kW h at Las Vegas and \$0.05/kW h at Bakersfield and Phoenix, occurs for a design wind speed at the maximum corresponding wind speed because the wind speeds there are relatively low. However, it is evident that the LCOE is more sensitive to the capacity factor and field efficiency of a plant than to the cost of the heliostats. Hence, the heliostat design wind speed can only be lowered to a point where the plant output is not significantly reduced.

The influence of lower capacity factors at the wind speeds of Mildura and Darwin in Fig. 3(a) can be seen by LCOEs that are at least \$0.1/kW h higher than in the other locations at design wind speeds above 6 m/s. Despite a lower design wind speed of 9 m/s in Darwin yielding a cheaper heliostat to manufacture than in Alice Springs, the low capacity factor there leads to the highest LCOE of \$0.202/kW h of the six locations in. In contrast, the optimal LCOE is significantly lower at \$0.083/kW h for a PT plant in Alice Springs because of a 14% higher optimal capacity factor (see Section 3.2). Hence, the LCOE of CST generated electricity at windy sites tends to be more sensitive to capacity factor than the cost of the heliostat.

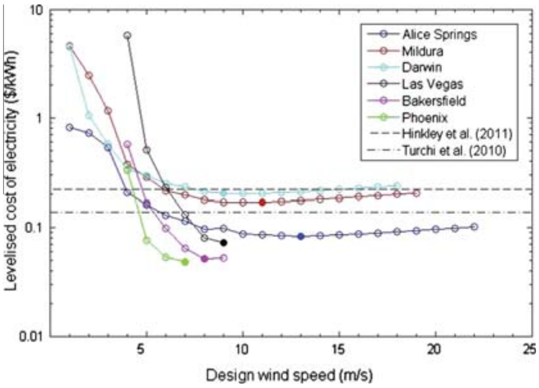

Fig. 9. Sensitivity of the calculated LCOE of a 20 MW CST PT plant to heliostat design wind speed at the six locations. Solid symbols indicate the local minimum LCOE. Dashed lines indicate the LCOE estimated at different sites and for different conditions by Hinkley et al. (2011) and by Turchi et al. (2010).

The present estimates of LCOE were compared with those of two recent studies by CSIRO in Australia (Hinkley et al., 2011) and NREL in the USA (Turchi et al., 2010). The Australian study estimated the LCOE to be \$0.223/kW h for a 100 MW PT plant in Longreach, Queensland with 6 h thermal storage, 20 year economic life and a 7% discount rate. The US study estimated the LCOE to be \$0.137/kW h for a 111 MW PT plant at Daggett, California with 6 h thermal storage, molten salt working fluid and assuming large heliostats, such as the 148 m^2 ATS heliostat, consistent with the 2007 Sandia study (Kolb et al., 2007). Given these differences, the agreement between the presently calculated LCOE and the reference values is good, with the optimised LCOE in some locations approaching the SunShot and ASTRI targets of \$0.06/kW h and \$0.12/kW h respectively.

4. Conclusions

There is significant potential to lower the LCOE in windy sites by careful choice both of the design wind speed at which heliostats are parked in stow position and of the size of the heliostats. Lowering the design wind speed has the potential to reduce the LCOE of a PT plant at windy sites because of the strong dependence of the cost of the heliostat field on the design wind speed. For example, the relative cost of the structural components increases from 6% to 23% as the design wind speed is increased from 1 m/s to 15 m/s. Hence, at the three Australian sites assessed here, a significant reduction in the design wind speed is associated with only a small reduction to the capacity factor, which lowers the LCOE. For example, lowering the design wind speed by 9 m/s from the maximum 22 m/s measured wind speed at Alice Springs yields a 0.3% lower capacity factor and a 18% reduction in LCOE. The optimal size of a heliostat is also dependent on the design wind speed. For example, the optimal heliostat size is 50 m^2 for a design wind speed of 10 m/s, while it is only 25 m^2 for a design wind speed of 20 m/s. Hence, the design wind speed and the size of the heliostat need to be considered together because the optimal heliostat area decreases with increasing design wind speed based on the assumption of quasi-static loads for the heliostat design. Additionally, heliostat costs can be minimised in regions of wind speeds above 10 m/s by manufacturing smaller heliostats than those commonly employed today. However, this requires that the heliostat structure be optimised to account for wind speed, which would reduce the number of sites to which any given design applies and, in turn, reduce the economies of scale. This suggests that there may be a trade-off between site specific designs and a more robust design that is applicable at all practical sites, such as a heliostat with an increased mirror area at a low wind speed site.

Acknowledgements

The authors would like to acknowledge the contributions of Kimberley Kueh and Associate Professor Eric Hu to the heliostat field efficiency equations used in the power output calculations, and for the constructive and insightful comments by the anonymous reviewers of the paper. Support for the work has been provided by the Centre for Energy Technology and the Australian Solar Thermal Research Initiative (ASTRI), through funding provided by the Australian Renewable Energy Agency (ARENA).

References

Ahmed, M.A., Ahmad, F., Akhtar, M.W., 2006. Assessment of wind power potential for coastal areas of Pakistan. Turk. J. Phys. 30, 127–135.

Arvizu, D., Balaya, P., Cabeza, L., Hollands, T., Jäger-Waldau, A., Kondo, M., Konseibo, C., Meleshko, V., Stein, W., Tamaura, Y., Xu, H., Zilles, R., 2011, Direct Solar Energy. In: Cambridge University Press, Cambridge, United Kingdom.

Beath, A., 2012. Overarching Economic Model, in: ASTRI Planning Phase, CSIRO.

Blackmon, J.B., 2013. Parametric determination of heliostat minimum cost per unit area. Sol. Energy 97, 342–349.

Bureau of Meteorology, 2014. Data Services. <http://www.bom.gov.au/climate/data-services/> (last accessed 29.08.14).

Cook, N.J., 1997. The Deaves and Harris ABL model applied to heterogeneous terrain. J. Wind Eng. Ind. Aerodyn. 66, 197–214.

Dorvlo, A.S.S., 2002. Estimating wind speed distribution. Energy Conserv. Manage. 43, 2311–2318.

Farkas, J., Jármai, K., 2013. Optimum Design of Steel Structures. Springer-Verlag, New York.

Garcia, A., Torres, J.L., Prieto, E., Francisco, A.D., 1998. Fitting wind speed distributions: a case study. Sol. Energy 62, 139–144.

Hennessey, J.P., 1977. Some aspects of wind power statistics. J. Appl. Meteorol. 16, 119–128.

Hernández-Moro, J., Martínez-Duart, J.M., 2013. Analytical model for solar PV and CSP electricity costs: Present LCOE values and their future evolution. Renew. Sustain. Energy Rev. 20, 119–132.

Hinkley, J., Curtin, B., Hayward, J., Wonhas, A., Boyd, R., Grima, C., Tadros, A., Hall, R., Naicker, K., Mikhail, A., 2011, Concentrating solar power - drivers and opportunities for cost-competitive electricity. In: CSIRO Energy Technology. Newcastle.

Hinkley, J.T., Hayward, J.A., Curtin, B., Wonhas, A., Boyd, R., Grima, C., Tadros, A., Hall, R., Naicker, K., 2013. An analysis of the costs and opportunities for concentrating solar power in Australia. Renewable Energy 57, 653–661.

IEA-ETSAP, IRENA, 2013. Concentrating Solar Power Technology Brief.

IEA, 2010. Projected Costs of Generating Electricity: 2010 Edition, 9 rue de la Fédération, 75739 Paris Cedex 15, France.

IEA, 2010. Technology Roadmap – Concentrating Solar Power, 9 rue de la Fédération, 75739 Paris Cedex 15, France.

International Code Council, 2010. Chapter 18A - Soils and Foundation. <http://publicecodes.cyberregs.com/st/ca/st/b200v10/st_ca_st_b200v10_18a_sec007.htm>, (last accessed 12.06.14).

Kolb, G.J., Ho, C.K., Mancini, T.R., Gary, J.A., 2011, Power Tower Technology Roadmap and Cost Reduction Plan. In: Sandia Report SAND2011-2419. Sandia National Laboratories. Albuquerque, New Mexico, USA.

Kolb, G.J., Jones, S.A., Donnelly, M.W., Gorman, D., Thomas, R., Davenport, R., Lumia, R., 2007, Heliostat Cost Reduction Study. In: Sandia Report SAND2007-3293. Sandia National Laboratories. Albuquerque, New Mexico, USA.

Kueh, K., Nathan, G.J., Saw, W.L., 2014. Sizing a solar thermal plant for continuous power output. Centre Energy Technol. Internal Rep.

Li, Q.S., Zhi, L., Hu, F., 2010. Boundary layer wind structure from observations of a 325 m tower. J. Wind Eng. Ind. Aerodyn. 98, 818–832.

Lovegrove, K., Stein, W., 2012. Concentrating Solar Power Technology: Principles, Developments and Applications. Elsevier.

Lovegrove, K., Watt, M., Passey, R., Pollock, G., Wyder, J., Dowse, J., 2012. Realising the Potential of Concentrating Solar Power in Australia: Summary for Stakeholders. Australian Solar Institute Pty Limited.

Lun, I.Y.F., Lam, J.C., 2000. A study of Weibull parameters using long-term wind observations. Renewable Energy 20, 145–153.

Murphy, L.M., 1980. Wind loading on tracking and field mounted solar collectors. Technical Report for Colorado State University Report No. SERI/TP-632-958.

National Climatic Data Center, 2014. Datasets, <http://www.ncdc.noaa.gov/cdo-web/datasets> (last accessed 29.08.14).

NREL, 2010. National Solar Radiation Data Base. <http://rredc.nrel.gov/solar/old_data/nsrdb/1991-2010/hourly/list_by_state.html#N> (last accessed 29.08.14).

NREL, 2011. Power Tower Projects. <http://www.nrel.gov/csp/solarpaces/power_tower.cfm> (last accessed 10.06.14).

Peterka, J.A., Derickson, R.G., 1992, Wind load design methods for ground based heliostats and parabolic dish collectors. In: Report SAND92-7009. Sandia National Laboratories. Springfield.

Peterka, J.A., Derickson, R.G., 1992, Wind load design methods for ground based heliostats and parabolic dish collectors. In: Sandia National Laboratories. Springfield.

Peterka, J.A., Tan, Z., Bienkiewicz, B., Cermak, J.E., 1988, Wind Loads on Heliostats and Parabolic Dish Collectors; Final Subcontract Report. In: Report SERI/STR-253-3431. Sandia National Laboratories. Fort Collins, Colorado.

Peterka, J.A., Tan, Z., Cermak, J.E., Bienkiewicz, B., 1989. Mean and peak wind loads on heliostats. J. Sol. Energy Eng. 111, 158–164.

Pfahl, A., Uhlemann, P., 2011. Wind loads on heliostats and photovoltaic trackers at various Reynolds numbers. J. Wind Eng. Ind. Aerodyn. 99, 964–968.

Romero-Alvarez, M., Zarza, E. Concentrating solar thermal power, Handbook of energy efficiency and renewable energy; 2007.

Sargent & Lundy LLC Consulting Group, 2003, Assessment of parabolic trough and power tower solar technology cost and performance forecasts. In: NREL/SR-550-34440. National Renewable Energy Laboratory (NREL). 1617 Cole Boulevard, Golden, Colorado, USA.

Stewart, D.A., Essenwanger, O.M., 1978. Frequency distribution of wind speed near the surface. Amer. Meteorol. Soc. 78, 1633–1642.

Sun, H., Gong, B., Yao, Q., 2014. A review of wind loads on heliostats and trough collectors. Renew. Sustain. Energy Rev. 32, 206–221.

Turchi, C., Mehos, M., Ho, C.K., Kolb, G.J., 2010. Current and future costs for parabolic trough and power systems in the US market. In: Proc., SolarPACES 2010, Perpignan, France.

Weisser, D., 2003. A wind energy analysis of Grenada: an estimation using the 'Weibull' density function. Renewable Energy 28, 1803–1812.

Chapter 4

Atmospheric Surface Layer Turbulence

4.1. Section Overview

This chapter reports some characteristics of the turbulence in a low-roughness atmospheric surface layer (ASL). The temporal and spatial characteristics of turbulence were calculated using field velocity measurements taken in a low-roughness surface layer in the Utah desert during near-neutral conditions for comparison with laboratory data of turbulent boundary layers. Velocity, turbulence intensity and integral length scale profiles (Appendix A) were analysed and discussed in relation to semi-empirical models developed for homogenous, isotropic turbulence over open country terrains in a neutrally-stable ABL. Calculated gust factor profiles following the approach used in wind codes and standards for buildings showed that the peak wind speeds of low-frequency gusts were under-predicted in the low-roughness terrain. Hence, these discrepancies highlight the uncertainties associated with using the quasi-steady gust factor method to approximate the peak wind loads on stowed heliostats.

4.2. Field Experiment Wind Measurements

Statement of Authorship

Title of Paper	Investigation of turbulence characteristics in a low-roughness atmospheric surface layer	
Publication Status	☐ Published ☑ Submitted for Publication	☐ Accepted for Publication ☐ Unpublished and Unsubmitted work written in manuscript style
Publication Details	Emes, M.J., Arjomandi, M., Kelso, R.M. and Ghanadi, F., 2017, Investigation of turbulence characteristics in a low-roughness atmospheric surface layer, Wind and Structures	

Principal Author

Name of Principal Author (Candidate)	Matthew Emes		
Contribution to the Paper	Performed data analysis and interpretation, wrote manuscript and acted as corresponding author.		
Overall percentage (%)	70		
Certification:	This paper reports on original research I conducted during the period of my Higher Degree by Research candidature and is not subject to any obligations or contractual agreements with a third party that would constrain its inclusion in this thesis. I am the primary author of this paper.		
Signature		Date	3/11/17

Co-Author Contributions

By signing the Statement of Authorship, each author certifies that:

i. the candidate's stated contribution to the publication is accurate (as detailed above);
ii. permission is granted for the candidate in include the publication in the thesis; and
iii. the sum of all co-author contributions is equal to 100% less the candidate's stated contribution.

Name of Co-Author	Maziar Arjomandi		
Contribution to the Paper	Supervised development of work, helped in data interpretation and manuscript evaluation.		
Signature		Date	3/11/17

Name of Co-Author	Richard Kelso		
Contribution to the Paper	Supervised the research and contributed in academic discussion and manuscript review.		
Signature		Date	3/11/17

Name of Co-Author	Farzin Ghanadi		
Contribution to the Paper	Supervised the research and contributed in academic discussion and manuscript review.		
Signature		Date	3/11/2017

Investigation of turbulence characteristics in a low-roughness atmospheric surface layer

Matthew J. Emes*[1], Maziar Arjomandi[1a], Richard M. Kelso[1b] and Farzin Ghanadi[1c]

[1]*School of Mechanical Engineering, The University of Adelaide, SA 5005, Australia*

(Received keep as blank , Revised keep as blank , Accepted keep as blank)

Abstract. This paper investigated the sizes and frequencies of gusts in the lower surface layer of a flat, low-roughness atmospheric boundary layer (ABL), based on the high-fidelity measurements of wind velocity in the Utah desert during near-neutral conditions. The observations in the field experiment were used to evaluate the correctness of the predictions obtained from theoretical and empirical models used frequently in quasi-steady gust factor analysis for the design of physical structures in wind load codes and standards. Results from the analysis showed that there are distinct characteristics of a low-roughness ABL that deviate significantly from semi-empirical relationships derived for open country and urban terrains with larger surface roughness heights. Longitudinal integral length scales followed a linear relationship with height, compared to a logarithmic relationship predicted by the Engineering Sciences Data Unit (ESDU) 85020 model. Longitudinal power spectral densities in the desert surface layer were consistent with the von Karman equation, however the calculated velocity gust factor was 3% larger for a 0.2 second-gust compared with a 3 second-gust. Gust periods above 1 s were found to under-predict peak wind speeds of low-frequency gusts in the low-roughness terrain compared to open country terrains with an order of magnitude larger roughness height.

Keywords: atmospheric surface layer; gust factor; turbulence intensity; integral length scale; eddy; surface roughness; power spectral density.

1. Introduction

Wind codes and standards for low- to medium-rise buildings adopt a simplified gust factor approach that assumes quasi-steady wind loads based on a maximum gust wind speed. This can lead to significant errors for very tall buildings with large dynamic responses to the large amplitude fluctuations during high-wind events such as gusts over short time intervals (Durst, 1960; Mendis et al., 2007). Gusts are a rapid fluctuation of the instantaneous wind velocity from the mean wind over a specified sampling duration (Kristensen et al., 1991). These flow fluctuations arise from eddies of varying sizes within the atmospheric boundary layer (ABL) that are produced by surface roughness and obstacles on the ground and large-scale superstructures in the outer layer (Hutchins et al., 2012; Hutchins and Marusic, 2007).

---

[*] Corresponding author, Ph.D. Student, E-mail: matthew.emes@adelaide.edu.au

[a] Associate Professor, E-mail: maziar.arjomandi@adelaide.edu.au

[b] Associate Professor, E-mail: richard.kelso@adelaide.edu.au

[c] Ph.D., E-mail: farzin.ghanadi@adelaide.edu.au

The sizes of the largest eddies in the lower surface layer are defined by the longitudinal integral length scale L_u^x and they have a significant effect on the fluctuating pressures and unsteady forces on physical structures, which can result in fatigue damage and structural collapse. Small eddies result in wind loads on various parts of a structure that become uncorrelated with distance of separation, however large eddies whose size is comparable with the structure result in well correlated pressures over its surface as the eddy engulfs the structure, leading to maximum wind loads (Greenway, 1979; Mendis et al., 2007). Maximum wind loads at lower heights in the ABL will therefore tend to occur from the interaction of the largest eddies in the flow with a structure. Holdø et al. (1982) found that the drag force on a scale model low-rise building of height D increased by 10% in an ABL with a turbulence intensity of 25% (L_u^x/D = 2.8) compared to a uniform approaching flow (L_u^x/D = 1.6). Hence, consideration of the size of the largest eddies in the ABL relative to the characteristic length of a physical structure can lead to significant savings in costs due to the reduced design wind loading.

The dynamic response of permanent structures positioned on the ground is important as it determines their ability to withstand gusts. The turbulence structure of neutrally-stratified wind with negligible thermal effects over large, flat, uniform terrain has been widely investigated for the purposes of determining wind loads on physical structures. Tall or slender structures with low natural frequencies are most likely to respond to the dynamic effects of gusts, which can lead to failure from excessive deflections and stresses due to flutter and random turbulent buffeting in the direction of the wind (Jain et al., 1996; Mendis et al., 2007). The surface layer, usually in the lowest 100m of the neutral ABL, has been shown to have similar turbulence properties as the canonical turbulent boundary layer along a flat plate in a wind tunnel, including a logarithmic mean velocity profile (Plate, 1974). Based on the theory of stationary random processes, the fluctuating component of wind velocity due to turbulence in the ABL is assumed to be a Gaussian random variable, such that the distribution of wind velocity follows a Gaussian form after applying a linear filter over the short-time averaging process (Greenway, 1979). Significant variations in shape from the Gaussian distribution of wind velocity is believed to be caused by the presence of updrafts and downdrafts from thermal gradients in the convective boundary layer (Anfossi et al., 1997; Hong et al., 2004). Higher-order moments and turbulence statistics of the probability density function (PDF) such as skewness and kurtosis provide information on the stability of the ABL and the turbulent motions in the surface layer responsible for the wind fluctuations (gusts). Hence, the first objective of this study is to investigate the turbulence structure close to the ground in the surface layer of a near-neutral low-roughness ABL in the Utah desert from the analysis of PDF and higher-order turbulence statistics of velocity measurements by Hutchins et al. (2012).

Experimental field measurements in open country terrains have led to similarity theories concerning the spatial structure of turbulence in the surface layer. Semi-empirical models developed on the basis of similarity theory describe the flow over rural and urban terrains sufficiently to predict the surface shear stress, roughness height and turbulence intensities in the surface layer (Teunissen, 1980). However, field measurements in rural terrains have shown considerable variation of integral length scales using different techniques. Teunissen (1980) found that the correlation-integral approach using the autocorrelation function of velocity produced the largest longitudinal integral length scales in reasonable agreement with the ESDU (1974) model but only half those predicted by the model of Counihan (1975). Flay and Stevenson (1988) suggested that the spectral-fit approach tended to underestimate length scales due to uncertainties associated with the identification of the peak in the broad spectra of slowly-varying turbulent eddies. Turbulent power spectra observations in the atmospheric surface layer have suggested that only the deviations of mean velocities, turbulence variances and length scales of the vertical component show consistent Monin-Obukhov scaling from site to site because of the absence of low-frequency components (Panofsky et al., 1982; Panofsky et al., 1977). In contrast, the low-frequency components of longitudinal turbulence cannot be consistently scaled from site to site because they are "very substantially enhanced by the 'memory' of upstream terrain" (Panofsky et al., 1982). As a result, variation of the surface roughness height in open country and rural terrain ABLs has a significant effect on the distribution of longitudinal integral length scales at lower heights in the surface layer. Hence, the second objective of this study is to characterise the integral length scales in the surface layer of a low-roughness ABL using field measurements by Hutchins et al. (2012) and compare with length scales measured in rural terrains and predicted by semi-empirical models.

The gust factor method uses a finite time response to predict the instantaneous peak velocity of sinusoidal gusts that are assumed to be non-overlapping and normally distributed over the sampling duration (Wieringa, 1973). This approach is widely used in wind load design codes (American Society of Civil Engineers, 2013; Cook, 1985; Engineering Sciences Data Unit, 1985; Standards Australia and Standards New Zealand, 2011) to estimate the peak (gust) wind speeds within a series of velocity measurements over a sampling period of 10 minutes or greater, such that the frequency range in the measured PSD is accurately reproduced (Solari, 1993; Wieringa, 1973). The maximum gust wind speed is dependent on the duration over which the gusts are averaged, as shown by Durst (1960) for a 15% increase in gust wind speed at 18 m/s mean wind speed when the gust period is lowered from 5 s to 0.5 s. A gust duration of 2-3 s, such as the typical response of a Dines anemometer (Holmes and Ginger, 2012), is commonly used in the design wind codes for long-span cable-supported bridges (Xu, 2013) and design standards for large buildings with heights less than 200 m and roof spans less than 100 m (Cook, 1985; Standards Australia and Standards New Zealand, 2011). The significance of the magnitude of the gust period is particularly relevant for AS/NZS 1170.2 because of its redefinition in Holmes et al. (2014) as an equivalent moving average over 0.2 seconds that can be converted to the frequency domain using a transfer function containing the PSD following random process theory. Hence, the third objective of this paper is to investigate the relationship between time and frequency domains using the PSD and determine the effect of the gust period on the gust factor using the spectral method of characterising gusts in a low-roughness ABL field experiment (Hutchins et al., 2012).

The overall aim of this paper is to estimate the sizes and frequencies of gusts in the neutral surface layer using field experiment measurements in a low-roughness ABL compared with widely accepted semi-empirical models developed from theory and experimental data. To achieve this aim it is required to quantify the effect of shortening the gust period and lowering the non-dimensionalised height in the ABL on the gust factor calculated using the PSD and a transfer function defined in Holmes et al. (2014) and from the turbulence intensity in a semi-empirical equation proposed by Ashcroft (1994). Further, the sizes of the largest eddies in the surface layer of the field experiment ABL (Hutchins et al., 2012) are calculated using the autocorrelation function and non-dimensionalised with the boundary layer thickness for comparison with the integral length scales predicted by empirical data including the Engineering Sciences Data Unit (1985) model. This will be used to provide recommendations for improving the accuracy and versatility of the current methods used for calculating wind loads on permanent structures exposed to gusty wind conditions in the ABL.

2. Gust characteristics

Engineering structures that are exposed to gusts in a turbulent environment are commonly designed to withstand a maximum gust wind speed. Peak wind loads are commonly estimated from the measurement of gust wind speeds at a reference position such as the roof height of scale-model buildings in boundary layer wind tunnels (Mendis et al., 2007; Standards Australia and Standards New Zealand, 2011). Alternatively, peak wind loads can be derived from the product of mean wind loads and velocity gust factor squared by assuming that the resultant peak longitudinal velocity is within one standard deviation of the mean longitudinal velocity following a Gaussian normal distribution (Holmes et al., 2014; Xu, 2013). The characteristics of turbulence that are required to define a gust in terms of the temporal and spatial distributions of wind velocity are detailed in this section. The relationships between these turbulence parameters in the time and frequency domains are described in the context of a turbulent boundary layer along a flat plate, as analogous to similarity theory and semi-empirical models of the surface layer in a neutrally-stratified ABL.

2.1 Mean velocity and turbulence statistics

For the design of physical structures such as buildings with height D less than 100m corresponding to the surface layer in Fig. 1, the logarithmic law is most appropriate for modelling the mean longitudinal velocity profile under the assumption of asymptotic similarity in a neutral ABL (Cook, 1997)

$$\bar{U}(z) = \frac{U_\tau}{k}\ln\left(\frac{z}{z_0}\right) \tag{1}$$

Here $U_\tau = \sqrt{\tau/\rho}$ (m/s) is the friction velocity representing the Reynolds shear stress $\tau = -\rho\overline{u'w'}$ at the surface, k is von Karman's constant (0.41) and z_0 (m) is the surface roughness height as a fraction of the average height of roughness elements on the ground in Fig. 1, which can vary in scale from millimetres in a flat desert to metres in a dense urban area (Xu, 2013). At lower heights in the roughness sublayer and the surface layer, velocity and length scales are scaled by the effects of viscosity as follows (Goldstein, 1996)

$$U^+ = \frac{1}{k}\ln(z^+) + A - \frac{\Delta U_r}{U_\tau} \tag{2}$$

Here $U^+ = \bar{U}(z)/U_\tau$ and $z^+ = zU_\tau/\nu$ are the viscous velocity and height respectively, A is an empirical constant (5.0) for a smooth wall boundary layer and $\frac{\Delta U}{U_\tau}$ is a roughness scaling factor. The friction velocity is commonly estimated using the Clauser chart method and defining the friction coefficient $C_f = 2(U_\tau/U_\infty)^2$ such that Equation (2) can be written in the form (Wei et al., 2005)

$$\frac{\bar{U}(z)}{U_\infty} = \frac{1}{k}\sqrt{\frac{C_f}{2}}\ln\left(\frac{zU_\infty}{\nu}\right) + \frac{1}{k}\sqrt{\frac{C_f}{2}}\ln\left(\sqrt{\frac{C_f}{2}}\right) + A\sqrt{\frac{C_f}{2}}, \tag{3}$$

where U_∞ is the freestream or gradient velocity shown in Fig. 1.

The design wind speed at the height of a physical structure in the ABL is normally calculated from measured gust velocities at the standard specification height of 10 m (American Society of Civil Engineers, 2013; Engineering Sciences Data Unit, 1985; Standards Australia and Standards New Zealand, 2011). For example, the minimum design wind speed is 30 m/s for permanent structures such as buildings less than 200 m in height and roof spans less than 100 m in AS/NZS 1170.2 (Standards Australia and Standards New Zealand, 2011). Hence, mean wind speeds are typically scaled to a 10 m reference height for the calculation of turbulence intensity, $I_u(z) = \sigma_u(z)/\bar{U}(z)$, where σ_u (m/s) is the standard deviation of the fluctuating component of the instantaneous streamwise velocity. Turbulence intensity provides only a single-point magnitude of the wind fluctuations, however the distributions of these fluctuations with time given by the PDF were also investigated to provide information on the distribution of wind velocity as a stationary random variable with a zero-mean value (Tennekes and Lumley, 1972). Skewness and kurtosis are two higher-order statistics that provide a measure of the symmetry and flatness of the PDF respectively and are defined for the three components of velocity $(X = u, v, w)$ as follows:

$$S(X) = (X - \bar{X})^3/{\sigma_X}^3 \tag{4}$$

$$K(X) = (X - \bar{X})^4/{\sigma_X}^4 \tag{5}$$

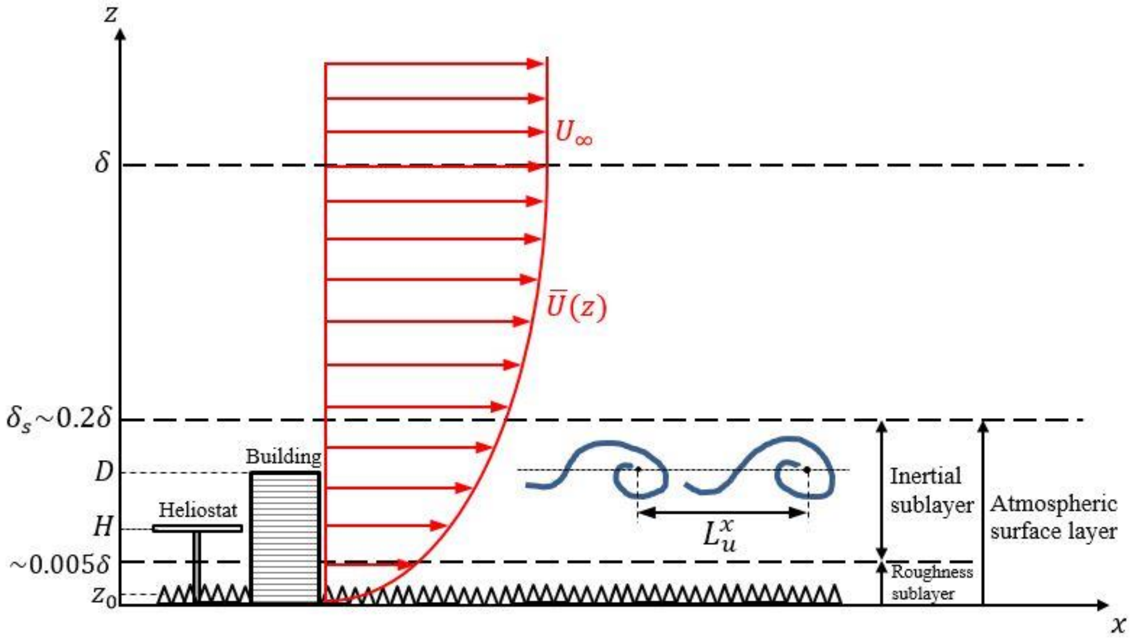

Fig. 1 Turbulence characteristics and structure of the atmospheric boundary layer

The lower surface layer of the ABL in Fig. 1 is approximated as a constant-stress layer by assuming the Coriolis acceleration f (m/s^2) due to the rotation of the Earth and large-scale pressure gradient terms balance the vertical stress gradient in horizontally-homogeneous conditions (Rao et al., 1974). Hence, similarity theory predicts that the size of the largest eddies are most dependent on the surface roughness height z_0 in the lower surface layer and on the boundary layer thickness δ in the outer layer of the ABL (Engineering Sciences Data Unit, 1985). The average thickness of both rural and urban terrain ABLs is estimated as $\delta \approx 600$ m based on the analysis of data for high wind speeds ($\bar{U}_{10m} > 5$-7 m/s) that produce adiabatic conditions (Counihan, 1975). The scale of turbulent eddies and the height of the ABL are influenced by changes in z_0 (Rao et al., 1974), hence δ is estimated as a function of z_0 from Equations (6)-(8) following (Xu, 2013)

$$\kappa = \left[\frac{k}{\ln(10/z_0)}\right]^2 \tag{6}$$

$$U_\tau = \sqrt{\kappa(\bar{U}_{10m})^2} \tag{7}$$

$$\delta = U_\tau/6f, \tag{8}$$

where κ is the surface friction coefficient representing the non-dimensional surface shear stress, $\bar{U}_{10m}$ is the mean wind speed at a 10 m height and $f = 2\omega \sin|\lambda| = 9.5\times10^{-5}$ is the Coriolis parameter at the latitude ($\lambda = 40.8°$ N) of the Bonneville salt flats in western Utah. The near-neutral surface layer thickness, denoted by δ_s in Fig. 1, is considered as an effective boundary layer thickness for the purposes of comparing with laboratory data of a turbulent boundary layer along a flat plate (Metzger et al., 2007).

2.2 Integral length scales

The longitudinal integral length scale L_u^x (m) at a given height z is defined in Fig. 1 as the streamwise spacing between two-dimensional spanwise eddies orientated in the axial direction. Point velocity measurements as a function of time are transformed to spatially distributed data by Taylor's hypothesis. This assumes that eddies are embedded in a frozen turbulence field convected downstream at the mean wind speed $\overline{U}$ (m/s) in the streamwise x direction and hence do not evolve with time (Kaimal and Finnigan, 1994). The integral length scale at a given height in the ABL is therefore calculated as (Swamy et al., 1979)

$$L_u^x = T_u^x \overline{U}, \tag{9}$$

where T_u^x (s) is the integral time scale representing the time taken for the largest eddies to traverse the inertial subrange in the ABL before they are dissipated by viscosity at the Kolmogorov length scale η. The integral time scale is calculated using Equation (10) by the integral of the autocorrelation function in Equation (11) to its first-zero crossing τ_0, assuming that $R(\tau)$ fluctuates close to zero after this point (Swamy et al., 1979).

$$T_u^x = \int_0^\infty R(\tau)\, d\tau \approx \int_0^{\tau_0} R(\tau)\, d\tau \tag{10}$$

$$R(\tau) = \frac{\overline{u'(t)u'(t+\tau)}}{{\sigma_u}^2} \tag{11}$$

The majority of integral length scale data available in the literature has been obtained from field-site anemometer velocity measurements in rural and urban ABLs (Counihan, 1975; Flay and Stevenson, 1988; Teunissen, 1980), however there are few recognised standards due to the diverse turbulence characteristics and scales in the lower surface layer. The model of Counihan (1975) predicts the variation of longitudinal integral length scale with height as

$$L_u^x(z) = Cz^{1/n}, \tag{12}$$

where C and $1/n$ are empirical variables as a function of the roughness height z_0. Solari and Piccardo (2001) proposed the following equation ($z \leq 200$ m) based on the analysis of integral length scale data in terrains with surface roughness height z_0 ranging from 10 mm to 1 m:

$$L_u^x(z) = 300\left(\frac{z}{200}\right)^{0.67+0.05\ln(z_0)} \tag{13}$$

AS/NZS 1170.2 uses the following formula to predict the integral length scale in the ABL for the design of buildings ($z \leq 200$ m)

$$L_u^x(z) = 85\left(\frac{z}{10}\right)^{0.25} \tag{14}$$

The calculated integral length scale from Equation (14) gives a value of L_u^x of 85 m at a height of 10 m and is used to estimate the dynamic response factor C_{dyn} for along-wind dynamic response of tall structures (Holmes et al., 2012; Standards Australia and Standards New Zealand, 2011). ESDU 85020 is a data set based on a semi-empirical model for integral length scales of atmospheric turbulence over uniform terrain in a neutral ABL based on a reference mean wind speed $\overline{U}_{10r}$ = 20 m/s at a 10 m height over open country terrain (z_0 = 30 mm) with $f = 1\times10^{-5}$ rad/s (Engineering Sciences Data Unit, 1985). A correction factor k_L is provided to account for the variation of L_u^x with changes in $\overline{U}_{10r}$ and f within an estimated ±8% error (Engineering Sciences Data Unit, 1985).

2.3 Power spectral density

The power spectral density (PSD) provides the distribution of energy content in the frequency domain and is defined as the Fourier transform of the autocorrelation function (Goldstein, 1996)

$$S_u(n) = 4\int_0^{\infty} R\,(\tau)\cos(2\pi n\tau)\,d\tau, \tag{15}$$

where n (Hz) is frequency and $S_u(n)$ is the power spectral density of the fluctuating longitudinal velocity component. The PSD of wind turbulence in the ABL is commonly modelled in wind codes and standards as a von Karman spectrum, which can be written in non-dimensional form as (Holmes and Ginger, 2012)

$$\frac{nS_u}{{\sigma_u}^2} = \frac{4\left(\frac{nL_u^x}{\bar{U}}\right)}{\left[1+70.8\left(\frac{nL_u^x}{\bar{U}}\right)^2\right]^{5/6}} \tag{16}$$

Here ${\sigma_u}^2$ is the variance of the streamwise velocity fluctuations defined by (Goldstein, 1996)

$${\sigma_u}^2 = \int_0^{\infty} S_u(n)dn \tag{17}$$

2.4 Velocity gust factor

The expected velocity gust factor that relates the fluctuating longitudinal component of the wind to the mean wind speed can be calculated by (Holmes et al., 2014)

$$G_u = \frac{\hat{U}}{\bar{U}} = \frac{\bar{U}+\sigma_u}{\bar{U}} = 1 + g_u I_u \tag{18}$$

Here the resultant peak velocity ($\hat{U} = \bar{U} + \sigma_u$) of the turbulent wind fluctuations is assumed to be within one standard deviation σ_u of the mean velocity and g_u is the peak factor derived by Davenport (1964) from the distribution of the largest instantaneous value of a stationary random function

$$g_u = \sqrt{2\ln \nu T} + \frac{0.577}{\sqrt{2\ln \nu T}} \tag{19}$$

where T is the sampling period for the mean velocity usually taken over a duration of 10 minutes or 1 hour (Wieringa, 1973) because of the existence of a spectral gap in this range separating boundary-layer turbulence external fluctuations (Kaimal and Finnigan, 1994). The cycling rate ν represents the average frequency of a time history and is calculated as (Holmes et al., 2014)

$$\nu = \left\{\frac{\int_0^{\infty} n^2 S_u(n)|H(n)|^2\,dn}{\int_0^{\infty} S_u(n)|H(n)|^2\,dn}\right\}^{1/2} \tag{20}$$

where $|H(n)|^2 = \left(\frac{\sin n\pi t}{n\pi t}\right)^2$ is the transfer function in the frequency domain for an equivalent moving average filter with a defined gust period t in the time domain. Peak gusts were previously assumed to be measured by standard Dines anemometers over a duration of 3 seconds, however the effective gust duration was recognised by Holmes et al. (2014) to be much shorter. As a result, the equivalent moving average definition of the gust period adopted by AS/NZS 1170.2 was changed to 0.2 s for buildings with heights less than 200 m (Standards Australia and Standards New Zealand, 2011). The dynamic response factor C_{dyn} can be calculated in AS/NZS 1170.2 for along-wind dynamic response of tall structures with a natural first-mode fundamental frequency between 0.2 Hz and 1 Hz (Holmes et al., 2012).

Empirical measurements of wind velocities at meteorological stations have been used to formulate relationships between gust factor and turbulence intensity following the form of Equation (18). Ashcroft (1994) adapted the following semi-empirical fit by Cook (1985) to a 1 s gust factor of 1.6 at a 10 m height over open country terrain (z_0 = 30 mm)

$$G_u = 1.0 + 0.42\, I_u\, \ln(3600/t) \tag{21}$$

Here t (s) is the gust period over which the maximum gust wind speed is averaged and $T = 3600$s represents the averaging period of one hour for the mean wind speed. The dependence of the gust factor upon the type of terrain is implicit as the turbulence intensity is a function of both the surface roughness height z_0 of the terrain and the non-dimensional height z/δ in the ABL (Ashcroft, 1994). Ishizaki (1983) developed Equation (21) but with a coefficient of 0.5, based on measurements in typhoon-prone regions.

3. Analysis of field measurement data

Gusts in the ABL can be most independently assessed and thus accurately characterised by a time series of wind velocity data measurements in a neutral ABL with negligible thermal effects. In the absence of a fully developed boundary layer wind tunnel for testing scale models of structures and buildings, high fidelity measurements of wind velocity were acquired from a field experiment study carried out by Hutchins et al. (2012) at the SLTEST facility in the western Utah Great Salt Lake desert. The unique geography of the site enabled measurements to be taken in a very high Reynolds number ABL ($Re_\tau = \delta U_\tau/\nu \approx 6\times10^5$) that has developed over 100km of low surface roughness salt flats in Dugway Proving Grounds, Utah (Hutchins and Marusic, 2007; Marusic and Hutchins, 2008). Raw velocity data were collected at SLTEST between 4am-5am on 2nd June 2005 by Hutchins et al. (2012) during a one hour period of neutral buoyancy and steady wind conditions when the vertical heat-flux $\overline{w\theta}$ was approximately zero (Hutchins et al., 2012), such that the velocity profiles and shear forces in the surface layer are expected to be generated by a shear-driven wall-bounded flow (Marusic and Hutchins, 2008). The atmosphere during the hour was considered to be near-neutral by Hutchins et al. (2012) following the Högström (1988) criterion $|z/L| \leq 0.1$ for the stability parameter. Conditions of neutral stability with negligible buoyancy effects were required to effectively compare statistically stationary data from canonical laboratory turbulent boundary layers (Metzger et al., 2007; Van den Berg, 2006). The mean wind speed $\overline{U}$ of 6.19 m/s at a 10 m height in the SLTEST field experiment is smaller than the common threshold of 10 m/s for a neutrally-stratified atmosphere (Xu, 2013), however Counihan (1975) found that mean wind speeds above 5 m/s at a 10 m height produce adiabatic wind conditions from an analysis of full-scale ABL data sets between 1880-1972, which has been supported by recent full-scale surface layer measurements (Anfossi et al., 1997; Chu et al., 1996) with mean wind speeds of 6 m/s. The steadiness of the wind for an approximately constant streamwise velocity was also satisfied, however the mean flow angle was established to be –12° (Hutchins et al., 2012). There is some uncertainty regarding the convergence of the turbulence statistics for one hour of velocity measurements in the SLTEST field experiment. Nevertheless, this sampling duration is sufficient for gust analysis to capture the low frequency events in the turbulent boundary layer (Hutchins et al., 2012; Solari, 1993).

Velocities in the streamwise x, spanwise y and vertical z directions were measured using sonic anemometers at a sampling frequency of 20 Hz using a wall-normal array of 9 logarithmically-spaced sonic anemometers at heights between 1.42 m and 25.69 m (z/δ_s = 0.02 to 0.43). The spatial resolution of 100mm for the sonic anemometers was shown by Kunkel and Marusic (2006) to be adequate for resolving the measured velocities and turbulence intensities in the SLTEST field experiment ABL. The measurement heights in the field experiment have been scaled on an estimated surface layer thickness δ_s of 60 m from two-point correlations of velocity data and prior radiosonde measurements (Metzger et al., 2007), however these techniques introduce some experimental uncertainties in the estimation of δ_s compared to an independent measurement of the wall shear stress. Hutchins et al. (2012) confirmed that $\delta_s \approx 60$ m returned the optimum consistency of two-point correlations with laboratory data of turbulent boundary layers using the estimated friction velocity U_τ of 0.19 m/s within a maximum experimental error of 10%. Hence, the expected error of both the surface layer thickness δ_s and the boundary layer thickness δ is 10% due to the proportionality between δ and U_τ in Equation (6) following similarity theory. The boundary layer thickness δ of the very flat terrain at the SLTEST site in the Utah desert is estimated to be 333 m from similarity theory using Equations (6)-(8), corresponding to errors of 18% and 10%, respectively, when comparing to values in standards of 274 m for open terrain (ASCE 1988) and 300 m for very flat terrain (Xu, 2013).

In this study, wind tunnel tests were used for comparison to demonstrate the similarities of turbulence parameters near the ground in the neutral atmospheric surface layer and along a flat plate in a zero-pressure-gradient turbulent boundary layer. This would allow the SLTEST surface layer to be compared with the logarithmic law mean velocity profile and turbulence intensity profiles that have been non-dimensionalised with the boundary layer thickness on a flat plate in a wind tunnel.

3.1 Mean velocity and turbulence statistics

Fig. 2(a) shows the mean streamwise velocity profile for one hour of velocity data collected at the SLTEST site, compared with the logarithmic law using Equation (2) for $U^+ = \overline{U}/U_\tau$ as a function of height $z^+ = zU_\infty/\nu$. The SLTEST mean velocity profile in Fig. 2(a), with an experimental uncertainty of 10% expected by Hutchins et al. (2012) in the estimation of U_τ, shows good agreement with the smooth wall logarithmic law profile. The terrain is best approximated as a mildly transitional rough surface with an equivalent sand-grain roughness height $k_s^+ \approx 21$ and an aerodynamic roughness height $z_0 \approx 2$ mm (Hutchins et al., 2012). The error bars on the field experiment velocity profile indicate a maximum 10% error in the estimated U_τ using the Clauser chart method in Fig. 2(b) following the equation for $\overline{U}/U_\infty$ in Wei et al. (2005). The SLTEST data closely fits the line for a constant friction coefficient of 0.0016 and by definition $C_f = 2(U_\tau/U_\infty)^2$ the friction velocity is calculated as $U_\tau = 0.19$ m/s by assuming the freestream velocity U_∞ can be approximated by the sonic anemometer at the largest height. This value for friction velocity was also confirmed from the definition $U_\tau = (\overline{uv}^2 + \overline{vw}^2)^{1/4}$ (Stull, 1988) as the vector sum of the along-wind and across-wind components of the Reynolds shear stress at the lowest sonic anemometer (z = 1.42 m) in agreement with Kunkel and Marusic (2006) and Metzger et al. (2007).

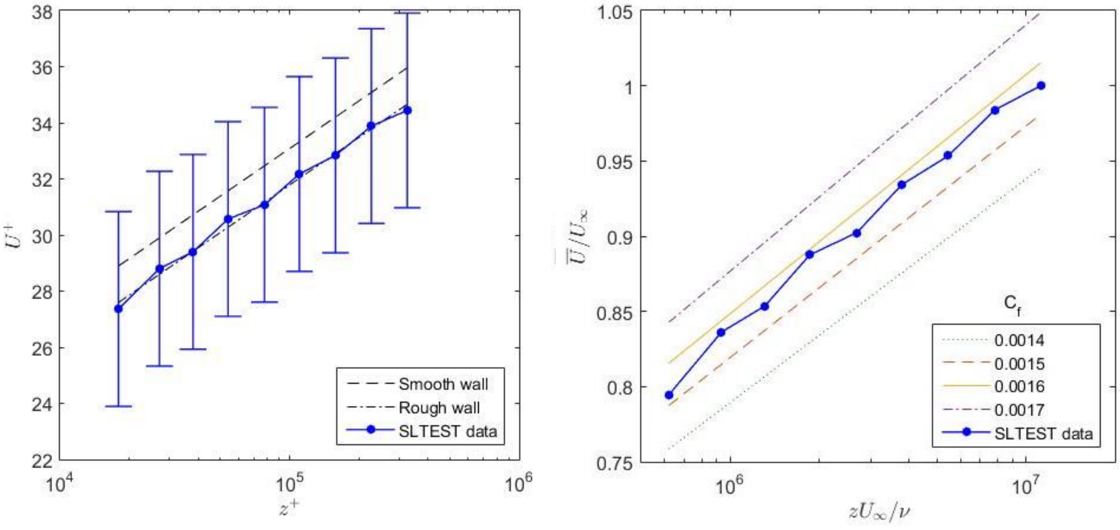

(a) Mean velocity profile $U^+ = \overline{U}/U_\tau$ of SLTEST field experiment data compared with the logarithmic profile in Equation (2) for U_τ = 0.19 m/s, A = 5.0 (smooth wall) and $\Delta U/U_\tau$ = 1.3 (rough wall)

(b) Clauser chart method used to estimate friction velocity U_τ. Lines of constant skin friction coefficient C_f are shown in comparison with the SLTEST field experiment data

Fig. 2 Comparison of surface layer velocity data measured in the SLTEST field experiment with theoretical models for a logarithmic velocity profile of the boundary layer on a flat plate. Error bars on the SLTEST mean velocity profile indicate a maximum 10% error in the estimate of friction velocity U_τ

Fig. 3 presents turbulence intensity profiles of the SLTEST data in the streamwise, spanwise and vertical directions with a maximum 10% experimental error in the estimate of friction velocity. The height is non-dimensionalised with respect to the surface layer thickness δ_s = 60 m in the SLTEST field experiment for comparison with smooth and rough wall laboratory data from Hinze (1975) in a zero-pressure-gradient turbulent boundary layer. Although Re_τ is an order of magnitude larger in the SLTEST field experiment, the turbulence intensity profiles show good agreement with laboratory data for a smooth wall within the estimated experimental error of the friction velocity in the SLTEST data and thus, provide further verification of the 60 m estimate for surface layer thickness. The difference in Fig. 3(a) between the SLTEST data and the smooth wall boundary layer remains relatively constant with decreasing height in the surface layer, however the differences in Fig. 3(b) and Fig. 3(c) become larger with decreasing height because sonic anemometers are expected to degrade significantly in accuracy at lower heights where the vertical velocity gradients are typically the largest and the eddy scales of interest are too small to be resolved accurately (Kaimal and Finnigan, 1994).

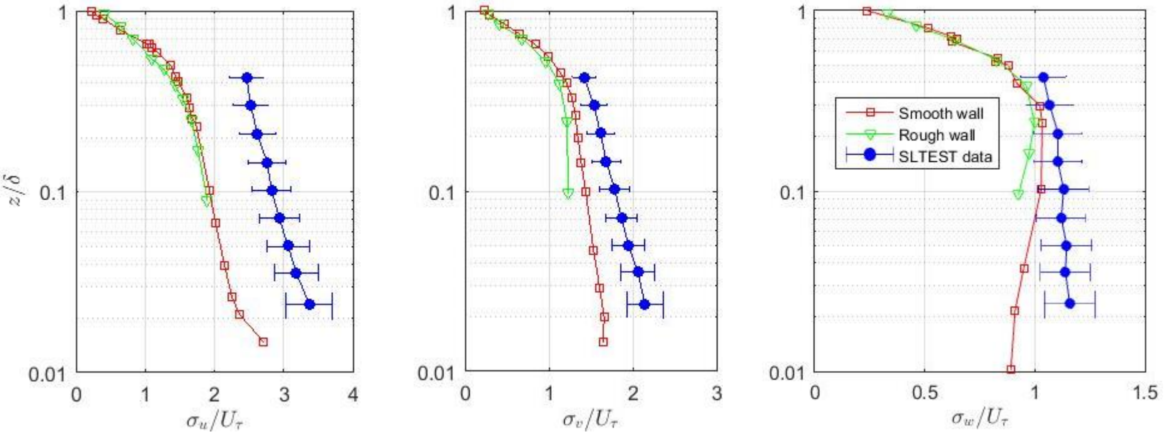

(a) Streamwise (b) Spanwise (c) Vertical

Fig. 3 Turbulence intensity profiles of SLTEST field experiment data as a function of height in the ABL non-dimensionalised with the surface layer thickness δ_s = 60m. Error bars on the SLTEST data indicate a maximum 10% error in the estimate of friction velocity U_τ. Smooth and rough wall data were taken from Hinze (1975) for a zero-pressure-gradient turbulent boundary layer along a flat plate. The smooth wall has $U_\tau/U_\infty \approx 0.037$ and Re_τ = 75,000 and the rough wall has $U_\tau/U_\infty \approx 0.055$ and Re_τ = 67,000

Fig. 4(a) presents the PDF of the streamwise velocity u at the lowest measurement height (z = 1.42 m) in the SLTEST field experiment, compared with full-scale neutral surface layer measurements at z = 2 m by Chu et al. (1996) in very low roughness terrain (z_0 = 0.13 mm) of a dry lake bed in Owens Valley, California and by Hong et al. (2004) in a flat Tibetan plateau at heights of 3 m and 20 m. The skewness in Fig. 4(b) and kurtosis in Fig. 4(c) of the SLTEST data show nearly Gaussian probability distributions ($S(u)$ = 0, $K(u)$ = 3) that are consistent with full-scale surface layer studies (Chu et al., 1996; Hong et al., 2004) and laboratory measurements (Klebanoff, 1955) at lower heights ($z \leq 3$ m) in the surface layer. Skewness of the SLTEST streamwise velocity data increases and remains positive (i.e. skewed to the left in Fig. 4(b)) at heights above 3 m (z/δ_s > 0.05), however laboratory measurements by Klebanoff (1955) calculated negative skewness at larger heights ($z/\delta > 0.05$) in a zero-pressure gradient turbulent boundary layer on a flat plate.

Fig. 5(a) presents the PDF of the vertical velocity w at the lowest measurement height (z = 1.42 m) in the SLTEST field experiment, compared with full-scale neutral surface layer measurements (Chu et al., 1996). Values of skewness and kurtosis of w in Fig. 5(b) and Fig. 5(c), respectively, are relatively larger than the streamwise velocity and are consistent with other surface layer measurements at lower heights in a neutrally-stratified atmospheric boundary layer (Chu et al., 1996; Hong et al., 2004). Positive skewness of w indicates the presence of low-speed streaks with prevailing narrow updrafts over wider downdraft motions in the Utah desert (Hong et al., 2004).

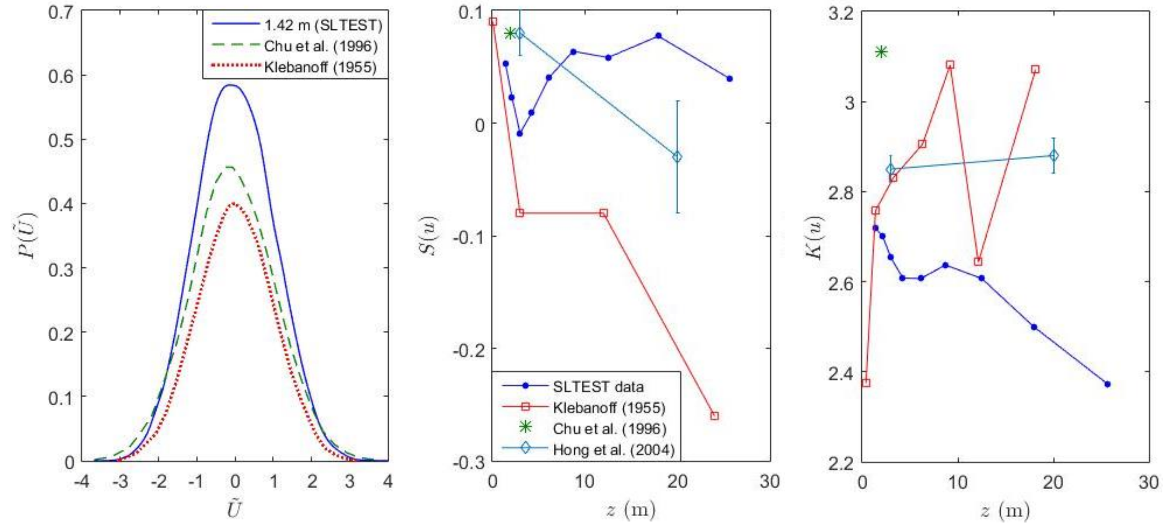

(a) Probability density functions $\tilde{U} = (u - \bar{U})\,/\sigma_u$ (b) Skewness profiles (c) Kurtosis profiles

Fig. 4 Statistics of streamwise velocity u in the SLTEST field experiment compared with full-scale surface layer measurements (Chu et al., 1996) and empirical equation fit (Klebanoff, 1955) for $z/\delta \leq 0.4$ in a zero-pressure-gradient turbulent boundary layer on a flat plate

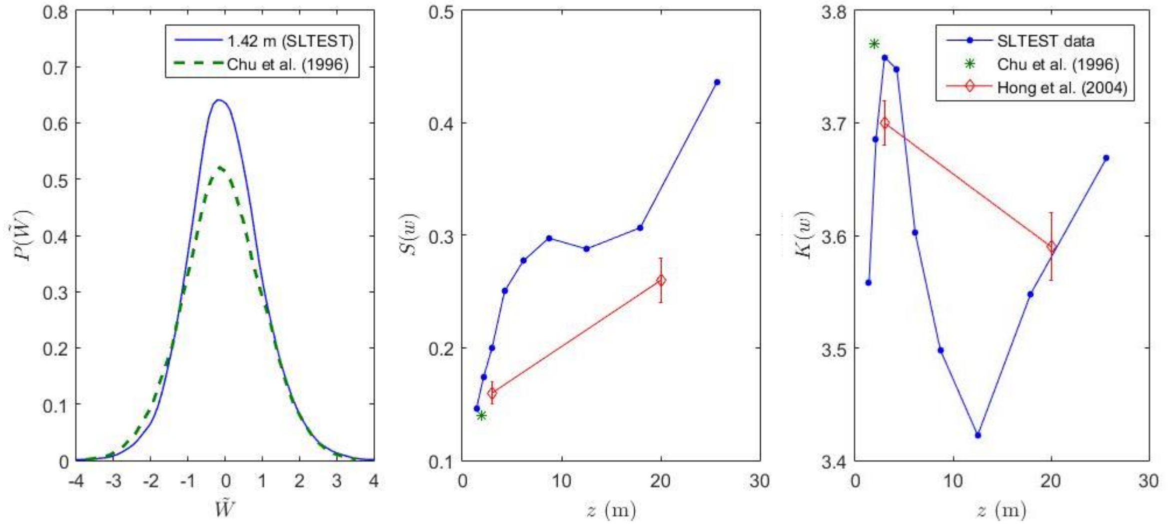

(a) Probability density functions $\tilde{W} = (w - \bar{W})\,/\sigma_w$ (b) Skewness profiles (c) Kurtosis profiles

Fig. 5 Statistics of vertical velocity w in the SLTEST field experiment compared with full-scale surface layer measurements (Chu et al., 1996; Hong et al., 2004)

3.2 Integral length scales

Fig. 6(a) shows the autocorrelation function of streamwise velocity at three heights in the SLTEST field experiment. It is noted that R_u decreases quickly with time lag τ towards the first-zero crossing before a small localised peak at τ = 6 s. The shape of R_u is not well represented by an exponential fit and thus the longitudinal integral length scales L_u^x are under-predicted using this method, as shown in

Fig. 6(b). The spectral fit method using the von Karman spectrum in Equation (16) more closely estimated the integral length scales at lower heights (z < 10 m), however locating the peak of the PSD was difficult because of the relatively smooth terrain of the Utah desert. Integrating under the R_u curve to the first-zero crossing τ_0 yielded the largest values of L_u^x and was considered the most appropriate method because of clearly defined limits of integration, consistent fluctuation of R_u about zero after τ_0 and relatively smaller errors compared to the other two methods. Fig. 6(c) shows the integral length scales estimated using the correlation integral method of the three velocity components as a function of height in the SLTEST surface layer. The ratios of the integral length scales for separations in the longitudinal direction are $L_u^x/L_v^x \approx 4.3$, $L_u^x/L_w^x \approx 25$ and $L_v^x/L_w^x \approx 9.3$. The corresponding ratios for isotropic turbulence are 2, 2 and 1, respectively, indicating the significant elongation of eddies in the longitudinal direction and the extremely small scale of the w-component fluctuations in the desert surface layer. The linear variation of L_u^x with height z in Fig. 6(c) suggests that physical structures such as buildings of height D in the surface layer of low-roughness terrains are exposed to eddies that are a similar size ($L_u^x/D \approx 1$), leading to the maximum wind loads due to turbulent buffeting (Greenway, 1979; Mendis et al., 2007).

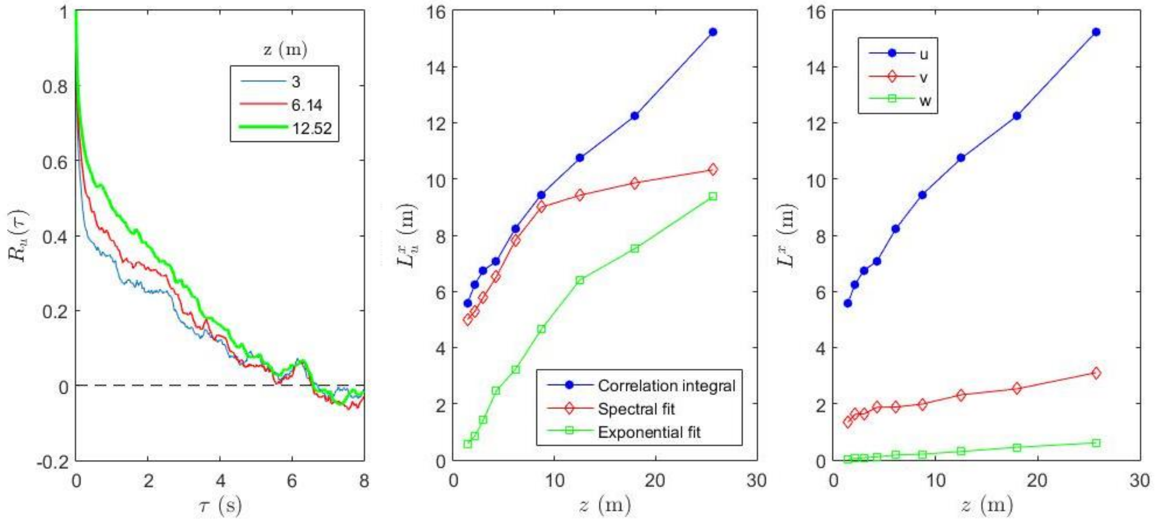

(a) Autocorrelation function of streamwise velocity as a function of time lag τ at three heights in the SLTEST surface layer

(b) Longitudinal integral length scales calculated using three different methods: first-zero crossing of R_u, fitting of von Karman Equation (16) to PSD data and exponential fit by integrating to $R_u = 1/e$

(c) Distributions of streamwise u, spanwise v and vertical w velocities with height for separations in the longitudinal x direction.

Fig. 6 Distributions of integral length scales with height calculated from measured velocity data in the SLTEST field experiment

Fig. 7(a) presents the distribution of longitudinal integral length scales with height in the SLTEST surface layer, estimated using the correlation integral method in comparison with experimental measurements in low-roughness surface layers and semi-empirical equations. It is observed that the profile of L_u^x over a very low roughness ($z_0 \approx 2$ mm) desert terrain follow a similar trend with height in the surface layer as other field measurements in open country terrains ($z_0 \approx 30$ mm) such as those reported by Flay and Stevenson (1988) on short grassy plains near Christchurch. However L_u^x at heights above 10 m are an order of magnitude lower than previous field measurements in low roughness terrains reported by Counihan (1975) and three semi-empirical models developed on the basis of field measurements in open country terrains. Integral length scale profiles predicted by ESDU 85020 correlations were previously observed by Farell and Iyengar (1999) to be an upper bound to field measurements in larger roughness surface layers with open country and urban terrains. Length scales at lower heights (z < 10 m) are over-estimated by the semi-empirical equations in the SLTEST desert surface layer ($z_0 \approx$ 2 mm) and in the majority of field measurements in low-roughness ($z_0 \approx$ 10 mm) terrains (Counihan, 1975).

The discrepancies between empirical data and models of L_u^x and the role of inactive non-local eddies in the outer layer of the ABL can be more effectively analysed by using outer-layer scaling parameters such as the boundary layer thickness δ, as shown in Fig. 7(b). The value of δ in the SLTEST field experiment over the Utah desert was estimated as 333 m using Equation (8) for U_τ of 0.19 m/s. The ESDU (2002) data had $\delta \approx$ 480 m following similarity theory using Equations (6)-(8) for z_0 of 1 mm and $\overline{U}_{10m}$ of 6.19 m/s and the full-scale rural and urban terrain ABLs were estimated to be 600 m in height following the recommendation of Counihan (1975). The ratio of length scales to the boundary layer thickness L_u^x/δ in the SLTEST field experiment compare well to full-scale measurements by Ivanov and Klinov (1961) over an urban terrain in Moscow and reported in Farell and Iyengar (1999). However, they are significantly lower than L_u^x/δ over an open country terrain (Flay and Stevenson, 1988) and are approximately four times lower than those predicted by Engineering Sciences Data Unit (1985) in the lowest 10% of a 1 mm desert terrain. The values of L_u^x/δ are predicted by ESDU 85020 to follow a logarithmic relationship with z/δ, however the calculated length scales in the SLTEST field experiment follow a linear relationship with height in the lowest 25 m of the surface layer (z/δ < 0.08) in agreement with Townsend's attached eddy hypothesis (Townsend, 1976). This supports Townsend's theory that the active (local) eddies in the surface layer are not influenced by inactive (non-local) eddies in the outer layer of the ABL that scale on δ (Hong et al., 2004). Hence, the characteristics of low-roughness ABLs in deserts appear to differ considerably from rural, open country and urban terrains with larger roughness heights. Furthermore, the significance of the relationship between L_u^x and z_0 has major implications for the dynamic wind loads on physical structures exposed to gusts in the ABL.

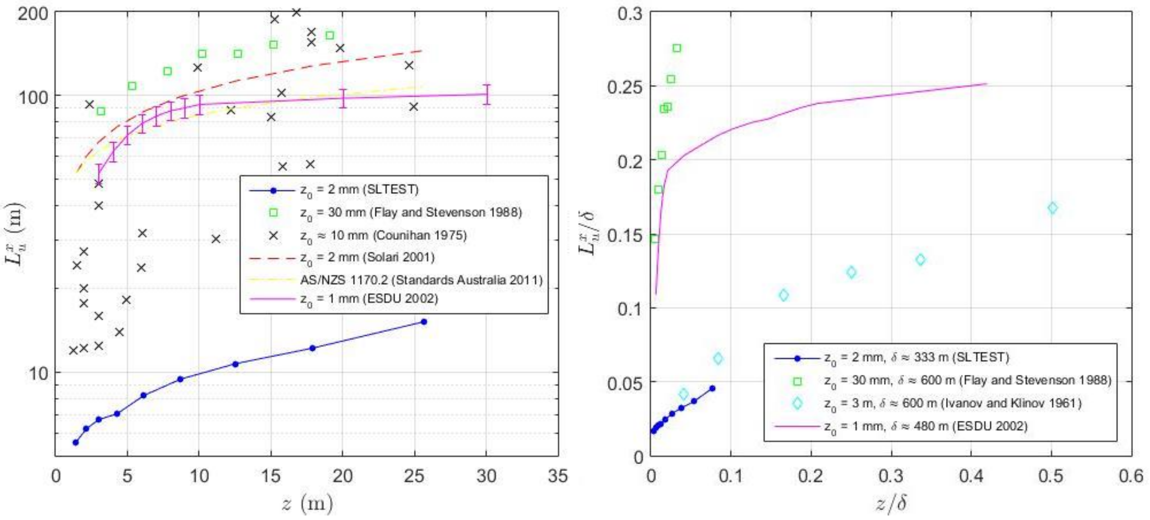

(a) Calculated longitudinal integral length scale profiles. Error bars on the ESDU curve indicate a ±8% error in the variation of L_u^x with changes in mean wind speed

(b) Ratio of longitudinal integral length scales to estimated boundary layer thickness L_u^x/δ as a function of non-dimensional height in the SLTEST field experiment ABL compared with full-scale measurements and the ESDU 85020 (2002) model

Fig. 7 Longitudinal integral length scales calculated using the correlation integral method as a function of height in the SLTEST field experiment compared with those measured in low-roughness surface layers (Counihan, 1975; Flay and Stevenson, 1988) and predicted by semi-empirical equations (Engineering Sciences Data Unit, 1985; Solari and Piccardo, 2001; Standards Australia and Standards New Zealand, 2011)

3.3 Power spectral density

Fig. 8(a) presents the relationship between the gust period τ and the cycling rate ν using the transfer function in Equation (20) from Holmes et al. (2014) to convert between the time domain and the frequency domain using the longitudinal PSD. It is observed that lower values of τ correspond to a higher average frequency of the velocity signal and has the largest effect on ν at lower heights closer to the ground. The differences in ν between gust periods of 0.2 s and 3 s are of particular interest because of their re-definition in AS/NZS 1170.2 (Standards Australia and Standards New Zealand, 2011) for the design wind loads on buildings and physical structures. Lowering the gust period from 3 s to 0.2 s results in the average frequency of the velocity fluctuations decreasing from 0.47 Hz to 0.09 Hz, as shown in Fig. 8(b) on the longitudinal PSD at a 3 m height in the SLTEST surface layer. It is observed that the lower gust period (τ = 0.2 s) corresponds to integral length scales at lower frequencies described by a linear relationship between S_u and n with a –5/3 slope. Although the larger gust period (τ = 3 s) may correspond to eddies with lower average frequencies and potentially larger length scales, the resolution of filtering becomes less precise at such low frequencies and hence large length scales cannot be captured as effectively at the sampling frequency of 20 Hz in the SLTEST field experiment. Sonic anemometers are expected to degrade significantly in accuracy at lower heights where the vertical velocity gradients are typically the largest and the eddy scales of interest are too small to be resolved accurately (Kaimal and Finnigan, 1994). Fig. 8(c) shows the range of non-dimensional PSDs as a function of non-dimensional frequency at the 9 heights in the SLTEST desert surface layer. The shape and magnitudes of the non-dimensional functions agree well with the von Karman spectrum in Equation (16) and are similar to other spectral turbulence data collected in other full-scale measurements in low-roughness terrains (Hong et al., 2004).

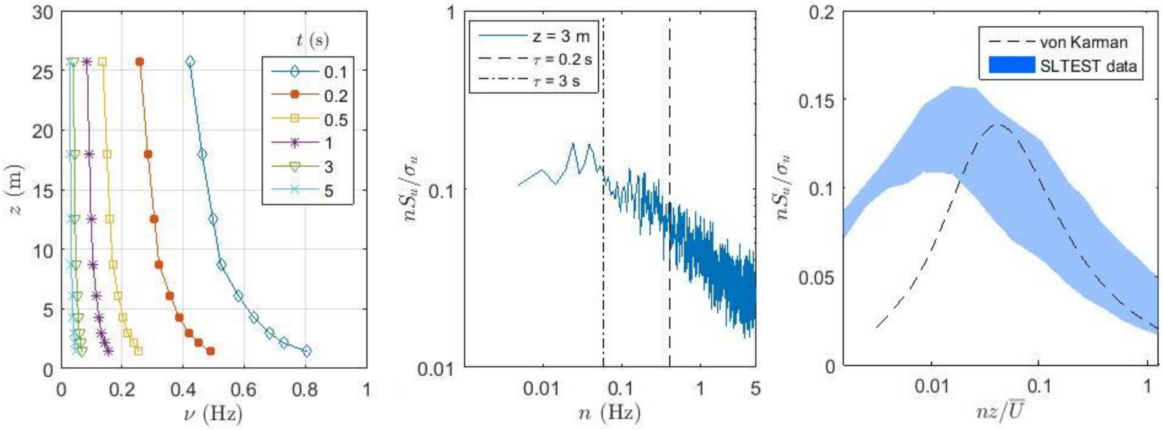

(a) Distribution of cycling rate ν and relationship with gust period τ using the transfer function in Equation (20) from Holmes et al. (2014)

(b) Non-dimensional longitudinal power spectrum nS_u/σ_u at z = 3 m as a function of frequency n. The two dashed lines indicate the cycling rate ν from Fig. 8(a) at gust periods τ of 0.2s and 3s

(c) Non-dimensional longitudinal power spectra nS_u/σ_u as a function of non-dimensional frequency $nz/\overline{U}$ compared with the von Karman form in Equation (16). The shaded area shows the range of variation of power spectra at the 9 heights of the vertical SLTEST tower

Fig. 8 Gust frequency characteristics in the SLTEST field experiment

3.4 Velocity gust factor

Fig. 9(a) presents the velocity gust factor calculated using the ratio of peak wind speed to mean wind speed at different heights in the SLTEST surface layer, in comparison to the expected peak factor in Equation (18) as a function of the gust period. Gust factors range between 1.3 and 1.5 at the measurement heights and increase with decreasing gust period as expected. The expected gust factor G_u increases by 3% from 1.35 to 1.39 at the standard measurement height of 10 m as the gust period is lowered from 3 s to 0.2 s because the average frequency of the velocity fluctuations is increased to resolve the largest eddies in the SLTEST surface layer. These values of G_u correspond to peak factors g_u of approximately 3.5 and 4, respectively and hence, the adopted value of 3.4 for g_u in AS/NZS 1170.2 (Standards Australia and Standards New Zealand, 2011) is not appropriate for a 0.2-second gust in this low-roughness desert surface layer. In addition, the 3-second gust factors are under-estimated at lower heights ($z \leq 6$ m) compared to G_u calculated from the peak-to-mean values of the SLTEST velocity data. Despite these differences, the predicted gust factors in Fig. 9(a) are in agreement with those reported in Holmes et al. (2014) for flat, uniform terrains at the same turbulence intensity of 10% at a 10 m height. Fig. 9(b) presents the maximum gust wind speed $\hat{U}$ in the longitudinal direction, calculated from G_u in Fig. 9(a) and the mean wind speed $\overline{U}$, as a function of height and gust period in the SLTEST surface layer. Values of $\hat{U}$ in the lowest 25 m or lowest 50% of this low-roughness surface layer are less than 9 m/s for the range of gust periods investigated. Maximum gust wind speed at a 10 m height increases from 8.3 m/s to 8.56 m/s as the gust period decreases from 3 s to 0.2 s. Hence, a design wind speed of 10 m/s at the standard 10 m specification height would be a conservative value for this low-roughness desert terrain.

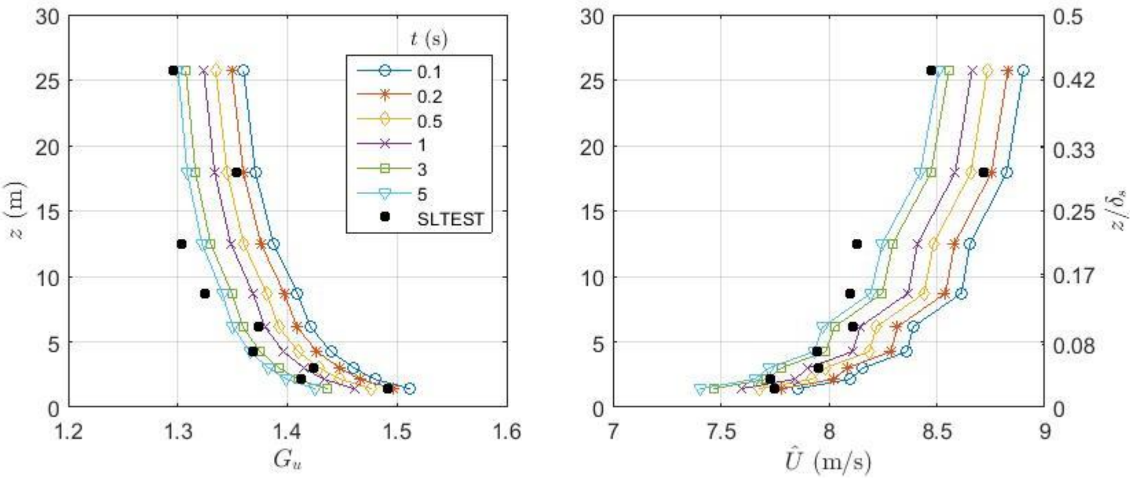

(a) Effect of gust period t on velocity gust factor G_u using the expected peak factor in Equation (19)

(b) Effect of gust period t on maximum gust wind speed $\hat{U}$ using Equation (18) from the velocity gust factor G_u in Fig. 9(a) and the mean wind speed $\overline{U}$

Fig. 9 Velocity gust factors and maximum gust wind speeds calculated from the peak-to-mean ratio of the SLTEST velocity data using Equation (18) at 9 heights in the Utah surface layer compared with the empirical expression for peak factor in Equation (19) following Holmes et al. (2014) as a function of gust period

Fig. 10 compares the gust factor method using the expected peak factor by Holmes et al. (2014) with a semi-empirical equation adapted by Ashcroft (1994) for open country terrains. Fig. 10(a) presents the streamwise turbulence intensity as a function of height in the surface layer of the SLTEST field experiment. The turbulence intensity I_u is approximately 10% at a height of 10 m and reaches a maximum of 12.3% at the lowest height of 1.42 m above the ground. The turbulence intensities in the surface layer can be related to the estimated surface roughness of the terrain by $I_u = 1/\ln(z/z_0)$ (Holmes, 2015; Xu, 2013), such that the turbulence intensity at a constant height of 10 m increases from approximately 11% to 17% when z_0 increases from 2 mm to 30 mm for flat desert and open country terrains, respectively (Ashcroft, 1994). The relationship between gust factor and turbulence intensity as a function of height in the SLTEST field experiment in Fig. 10(b) is well represented by the Ashcroft (1994) equation within a 1% average error for a 0.2-second gust, however the average error for a 3-

second gust is 4.3% at the measurement heights in the surface layer. This suggests that the Ashcroft (1994) equation can be acceptable for short-duration gusts but tends to under-predict the peak wind speeds of low-frequency gusts because it assumes the gust factor is only a function of turbulence intensity. The relationship between gust factor and turbulence intensity also appears to be a function of the terrain roughness, such that there is a positive horizontal shift in the gust factor profile with increasing surface roughness from a desert terrain to an open country terrain.

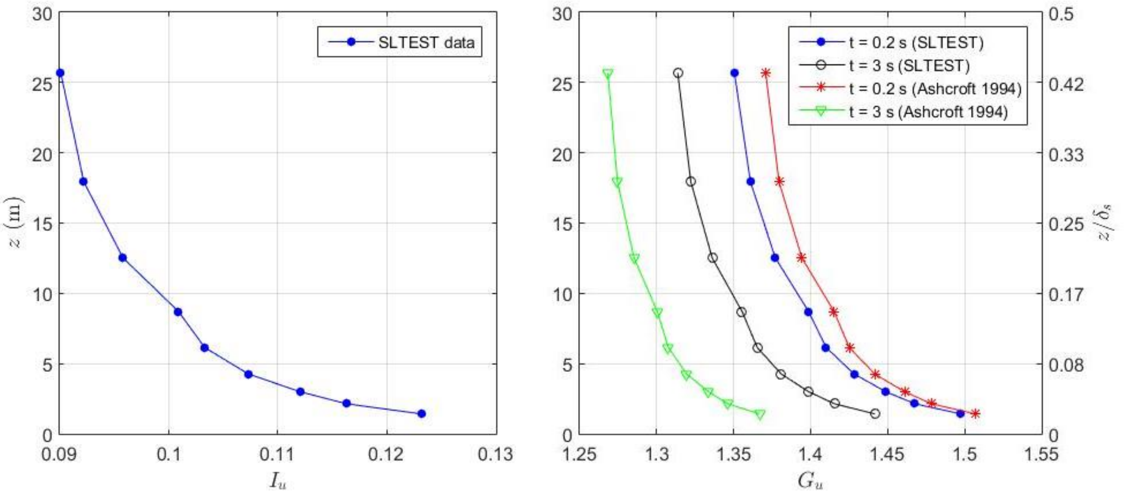

(a) Calculated turbulence intensity $I_u = \sigma_u/\bar{U}$ as a function of height z in the 60m-thickness (δ_s) surface layer of the SLTEST field experiment

(b) Calculated gust factor profiles using Equation (18) from SLTEST experiment data and comparison with Equation (21) proposed by Ashcroft (1994) for gust periods of 0.2 s and 3 s

Fig. 10 Gust factors calculated at 9 heights in the SLTEST surface layer using Equation (18) following Holmes et al. (2014) compared with those predicted by Equation (21) following Ashcroft (1994)

4. Conclusions

The wind characteristics used to define the size and frequencies of gusts over a very flat, open terrain in a desert surface layer have been investigated based on one hour of velocity data measurements by Hutchins et al. (2012) during near-neutral conditions. The following major conclusions can be drawn:

- For the purposes of studying the effects of gusts in a neutrally-stratified ABL, the mean velocity profile in the SLTEST field experiment agrees well with the logarithmic law within a 10% experimental error in the estimate of friction velocity from the Clauser chart method and Reynolds stresses close to the ground. Turbulence intensity profiles in the streamwise, spanwise and vertical directions show good agreement with laboratory data from Hinze (1975) for a smooth wall when the height is non-dimensionalised with respect to an estimated surface layer thickness δ_s of 60 m. The skewness and kurtosis of the PDF of vertical velocity w are consistent with other surface layer measurements at lower heights in the neutrally-stratified atmospheric boundary layer (Chu et al., 1996; Hong et al., 2004), where positive skewness of w indicates the presence of low-speed streaks with prevailing narrow updrafts over wider downdraft motions in the Utah desert.
- The size of gusts defined by the integral length scales found that the autocorrelation function of velocity R_u to the first-zero crossing τ_0 yielded the largest values and was considered the most appropriate method because of clearly defined integration limits, consistent fluctuation of R_u about zero after τ_0 and relatively smaller errors than locating the peak of the PSD in the spectral fit method and approximating R_u as an exponential function. Large eddies are elongated

significantly in the longitudinal direction for length scale ratios of 4.3, 25 and 9.3 in the 3 directions, respectively, due to the extremely small scale of the w-component fluctuations in the desert surface layer.

- The variation of the longitudinal integral scale L_u^x with height in the SLTEST field experiment is consistent with semi-empirical models (Counihan, 1975; Engineering Sciences Data Unit, 1985; Solari and Piccardo, 2001), however these models over-predict the size of the largest eddies by more than double in the lowest 10 m of the low-roughness desert surface layer. The active eddies in the surface layer are not influenced by the inactive eddies in the outer layer that scale on the ABL thickness δ, as shown by the closely linear variation of L_u^x with non-dimensional height z/δ in the lowest 25 m ($z/\delta < 0.08$) of the SLTEST surface layer in agreement with Townsend's attached eddy hypothesis (Townsend, 1976). Hence, the sizes of eddies close to the ground in the surface layer in a low-roughness desert ABL appear to differ considerably from rural, open country and urban terrains that have commonly been the basis of semi-empirical models.
- For the purposes of deriving design wind loads on physical structures in the ABL from the calculation of the gust factor, the longitudinal PSD functions at the 9 measurement heights in the SLTEST surface layer are considered reasonably close to the von Karman spectrum. The maximum gust velocity is less than 9 m/s for the range of gust periods tested in the desert terrain, however the velocity gust factor at a 10 m height increases by 3% as the gust period is lowered from 3 s to 0.2 s, such as in the redefinition of the equivalent moving average in AS/NZS 1170.2. Gust factor calculated using the Ashcroft (1994) equation is consistent with the expected gust factor following Holmes et al. (2014) for short duration 0.2-second gusts, however tends to under-predict the peak wind speeds of low-frequency gusts in the low-roughness SLTEST desert terrain compared to open country terrains with an order of magnitude larger roughness height.

Acknowledgments

I acknowledge the support I have received for my research through the provision of an Australian Government Research Training Program Scholarship. Further support for the work has been provided by the Australian Solar Thermal Research Initiative (ASTRI), through funding provided by the Australian Renewable Energy Agency (ARENA). The authors also acknowledge Associate Professor Nicholas Hutchins and Dr Kapil Chauhan at the University of Melbourne for their contribution of velocity data obtained from the SLTEST facility in Utah, USA.

References

American Society of Civil Engineers, 2013, Minimum design loads for buildings and other structures, Reston, Virginia, USA, ASCE 7-02.

Anfossi, D., Ferrero, E., Sacchetti, D. and Castelli, S.T., 1997, Comparison among empirical probability density functions of the vertical velocity in the surface layer based on higher order correlations, Boundary-Layer Meteorology 82, 193-218.

Ashcroft, J., 1994, The relationship between the gust ratio, terrain roughness, gust duration and the hourly mean wind speed, Journal of Wind Engineering and Industrial Aerodynamics 53, 331-355.

Chu, C.R., Parlange, M.B., Katul, G.G. and Albertson, J.D., 1996, Probability density functions of turbulent velocity and temperature in the atmospheric surface layer, Water Resources Research 32, 1681-1688.

Cook, N.J., 1985, The designer's guide to wind loading of building structures, Part 1: Background, damage survey, wind data and structural classification, In: Building Research Establishment, Garston, UK.

Cook, N.J., 1997, The Deaves and Harris ABL model applied to heterogeneous terrain, Journal of Wind Engineering and Industrial Aerodynamics 66, 197-214.

Counihan, J., 1975, Adiabatic atmospheric boundary layers: a review and analysis of data from the period 1880–1972, Atmospheric Environment 9, 871-905.

Davenport, A.G., 1964, Note on the distribution of the largest value of a random function with application to gust loading, Proceedings of the Institution of Civil Engineers 28, 187-196.

Durst, C.S., 1960, Wind speeds over short periods of time, Meteorological Magazine 89, 181-186.

Engineering Sciences Data Unit, 1985, Characteristics of atmospheric turbulence near the ground - Part II: single point data for strong winds (neutral atmosphere), London, UK, ESDU 85020.

Farell, C. and Iyengar, A.K., 1999, Experiments on the wind tunnel simulation of atmospheric boundary layers, Journal of Wind Engineering and Industrial Aerodynamics 79, 11-35.

Flay, R.G.J. and Stevenson, D.C., 1988, Integral length scales in strong winds below 20 m, Journal of Wind Engineering and Industrial Aerodynamics 28, 21-30.

Goldstein, R., 1996, Fluid Mechanics Measurements, CRC Press, Philadelphia, Pennsylvania, USA.

Greenway, M.E., 1979, An analytical approach to wind velocity gust factors, Journal of Wind Engineering and Industrial Aerodynamics 5, 61-91.

Hinze, J.O., 1975, Turbulence, McGraw-Hill, New York, USA.

Högström, U.L.F., 1988, Non-dimensional wind and temperature profiles in the atmospheric surface layer: A re-evaluation, Boundary-Layer Meteorology 42, 55-78.

Holdø, A.E., Houghton, E.L. and Bhinder, F.S., 1982, Some effects due to variations in turbulence integral length scales on the pressure distribution on wind-tunnel models of low-rise buildings, Journal of Wind Engineering and Industrial Aerodynamics 10, 103-115.

Holmes, J.D., 2015, Wind Loading of Structures, FL CRC Press, Boca Raton, Florida, USA.

Holmes, J.D., Allsop, A.C. and Ginger, J.D., 2014, Gust durations, gust factors and gust response factors in wind codes and standards, Wind and Structures 19, 339-352.

Holmes, J.D. and Ginger, J.D., 2012, The gust wind speed duration in AS/NZS 1170.2, Australian Journal of Structural Engineering 13, 207-217.

Holmes, J.D., Kwok, K.C.S. and Ginger, J.D., 2012, Wind Loading Handbook for Australia and New Zealand: Background to AS/NZS 1170.2 Wind Actions, Australasian Wind Engineering Society, Sydney, Australia.

Hong, J., Choi, T., Ishikawa, H. and Kim, J., 2004, Turbulence structures in the near-neutral surface layer on the Tibetan Plateau, Geophysical Research Letters 31, 15106.

Hutchins, N., Chauhan, K., Marusic, I., Monty, J. and Klewicki, J., 2012, Towards reconciling the large-scale structure of turbulent boundary layers in the atmosphere and laboratory, Boundary-Layer Meteorology 145, 273-306.

Hutchins, N. and Marusic, I., 2007, Evidence of very long meandering features in the logarithmic region of turbulent boundary layers, Journal of Fluid Mechanics 579, 1-28.

Ishizaki, H., 1983, Wind profiles, turbulence intensities and gust factors for design in typhoon-prone regions, Journal of Wind Engineering and Industrial Aerodynamics 13, 55-66.

Jain, A., Jones, N.P. and Scanlan, R.H., 1996, Coupled flutter and buffeting analysis of long-span bridges, Journal of Structural Engineering 122, 716-725.

Kaimal, J.C. and Finnigan, J.J., 1994, Atmospheric Boundary Layer Flows: Their Structure and Measurement, Oxford University Press, New York, USA.

Klebanoff, P.S., 1955, Characteristics of turbulence in boundary layer with zero pressure gradient, In: NACA-TR-1247, National Advisory Committee for Aeronautics, Springfield, USA.

Kristensen, L., Casanova, M., Courtney, M. and Troen, I., 1991, In search of a gust definition, Boundary-Layer Meteorology 55, 91-107.

Kunkel, G.J. and Marusic, I., 2006, Study of the near-wall-turbulent region of the high-Reynolds-number boundary layer using an atmospheric flow, Journal of Fluid Mechanics 548, 375-402.

Marusic, I. and Hutchins, N., 2008, Study of the log-layer structure in wall turbulence over a very large range of Reynolds number, Flow, Turbulence and Combustion 81, 115-130.

Mendis, P., Ngo, T., Haritos, N., Hira, A., Samali, B. and Cheung, J., 2007, Wind loading on tall buildings, EJSE Special Issue: Loading on Structures 3, 41-54.

Metzger, M., McKeon, B.J. and Holmes, H., 2007, The near-neutral atmospheric surface layer: turbulence and non-stationarity, Philosophical Transactions of the Royal Society of London A: Mathematical, Physical and Engineering Sciences 365, 859-876.

Panofsky, H., Larko, D., Lipschutz, R., Stone, G., Bradley, E., Bowen, A.J. and Højstrup, J., 1982, Spectra of velocity components over complex terrain, Quarterly Journal of the Royal Meteorological Society 108, 215-230.

Panofsky, H.A., Tennekes, H., Lenschow, D.H. and Wyngaard, J., 1977, The characteristics of turbulent velocity components in the surface layer under convective conditions, Boundary-Layer Meteorology 11, 355-361.

Plate, E.J., 1974, Aerodynamic Characteristics of Atmospheric Boundary Layers, US Atomic Energy Commission, Springfield, Virginia, USA.

Rao, K.S., Wyngaard, J.C. and Coté, O.R., 1974, The structure of the two-dimensional internal boundary layer over a sudden change of surface roughness, Journal of the Atmospheric Sciences 31, 738-746.

Solari, G., 1993, Gust buffeting. I: Peak wind velocity and equivalent pressure, Journal of Structural Engineering 119, 365-382.

Solari, G. and Piccardo, G., 2001, Probabilistic 3-D turbulence modeling for gust buffeting of structures, Probabilistic Engineering Mechanics 16, 73-86.

Standards Australia and Standards New Zealand, 2011, Structural Design Actions - Part 2: Wind actions, Sydney, Australia, AS/NZS 1170.2.

Stull, R.B., 1988, An introduction to boundary layer meteorology, Kluwer Academic, Dordrecht.

Swamy, N.V.C., Gowda, B.H.L. and Lakshminath, V.R., 1979, Auto-correlation measurements and integral time scales in three-dimensional turbulent boundary layers, Applied Scientific Research 35, 237-249.

Tennekes, H. and Lumley, J.L., 1972, A First Course in Turbulence, MIT press, Cambridge, Massachusetts, USA.

Teunissen, H.W., 1980, Structure of mean winds and turbulence in the planetary boundary layer over rural terrain, Boundary-Layer Meteorology 19, 187-221.

Townsend, A.A., 1976, The Structure of Turbulent Shear Flow, Cambridge University Press, New York, USA.

Van den Berg, G.P., 2006, The sound of high winds: The effect of atmospheric stability on wind turbine sound and microphone noise. Ph.D. Dissertation, Groningen University, Groningen, Netherlands.

Wei, T., Schmidt, R. and McMurtry, P., 2005, Comment on the Clauser chart method for determining the friction velocity, Experiments in Fluids 38, 695-699.

Wieringa, J., 1973, Gust factors over open water and built-up country, Boundary-Layer Meteorology 3, 424-441.

Xu, Y.L., 2013, Wind Effects on Cable-Supported Bridges, John Wiley & Sons, Singapore.

Chapter 5

Peak Wind Loads on an Isolated Heliostat

5.1. Section Overview

This chapter reports an experimental investigation of the peak wind load coefficients on a heliostat in stow position and their sensitivity to turbulence characteristics in the atmospheric surface layer discussed in Chapter 4. The turbulence parameters were characterised experimentally in a simulated part-depth ABL (Appendices B and C) representing the gusty wind conditions approaching isolated heliostats in stow position. Knowledge of both temporal and spatial turbulence in the ABL was found to be important for the design of heliostats in stow position so that they can withstand maximum wind loads during high-wind events. Peak wind loads were found to be highly dependent on the size of the largest eddies approaching the heliostat with respect to the size of the mirror. The results can be used in the design of heliostats to further optimise the size (Appendix D) and thus cost of manufacturing heliostats with respect to the turbulence approaching the solar field at a given site.

5.2. Experimental Measurements in a Simulated ABL

Statement of Authorship

Title of Paper	Effect of turbulence characteristics in the atmospheric surface layer on the peak wind loads on heliostats in stow position
Publication Status	☑ Published ☐ Accepted for Publication ☐ Submitted for Publication ☐ Unpublished and Unsubmitted work written in manuscript style
Publication Details	Emes, M.J., Arjomandi, M., Ghanadi, F. and Kelso, R.M., 2017, Effect of turbulence characteristics in the atmospheric surface layer on the peak wind loads on heliostats in stow position, Solar Energy 157, 284-297

Principal Author

Name of Principal Author (Candidate)	Matthew Emes		
Contribution to the Paper	Carried out wind tunnel experiments, performed data analysis and interpretation, wrote manuscript and acted as corresponding author.		
Overall percentage (%)	70		
Certification:	This paper reports on original research I conducted during the period of my Higher Degree by Research candidature and is not subject to any obligations or contractual agreements with a third party that would constrain its inclusion in this thesis. I am the primary author of this paper.		
Signature		Date	3/11/17

Co-Author Contributions

By signing the Statement of Authorship, each author certifies that:

i. the candidate's stated contribution to the publication is accurate (as detailed above);
ii. permission is granted for the candidate in include the publication in the thesis; and
iii. the sum of all co-author contributions is equal to 100% less the candidate's stated contribution.

Name of Co-Author	Maziar Arjomandi		
Contribution to the Paper	Supervised development of work, helped in data interpretation and manuscript evaluation.		
Signature		Date	3/11/17

Name of Co-Author	Farzin Ghanadi		
Contribution to the Paper	Supervised development of work, assisted in carrying out wind tunnel experiments, helped in data interpretation and manuscript evaluation.		
Signature		Date	03/11/2017

Name of Co-Author	Richard Kelso		
Contribution to the Paper	Supervised the research and contributed in academic discussion and manuscript review.		
Signature		Date	3/11/17

Solar Energy 157 (2017) 284–297

Contents lists available at ScienceDirect

Solar Energy

journal homepage: www.elsevier.com/locate/solener

Effect of turbulence characteristics in the atmospheric surface layer on the peak wind loads on heliostats in stow position

Matthew J. Emes*, Maziar Arjomandi, Farzin Ghanadi, Richard M. Kelso

School of Mechanical Engineering, The University of Adelaide, SA 5005, Australia

ARTICLE INFO

Keywords:
Heliostat
Stow position
Wind load
Atmospheric surface layer

ABSTRACT

This study investigates the dependence of peak wind load coefficients on a heliostat in stow position on turbulence characteristics in the atmospheric surface layer, such that the design wind loads, and thus the size and cost of heliostats, can be further optimised. Wind tunnel experiments were carried out to measure wind loads and pressure distributions on a heliostat in stow position exposed to gusty wind conditions in a simulated part-depth atmospheric boundary layer (ABL). Force measurements on different-sized heliostat mirrors at a range of heights found that both peak lift and hinge moment coefficients, which are at least 10 times their mean coefficients, could be optimised by stowing the heliostat at a height equal to or less than half that of the mirror facet chord length. Peak lift and hinge moment coefficients increased linearly and approximately doubled in magnitude as the turbulence intensity increased from 10% to 13% and as the ratio of integral length scale to mirror chord length L_u^x/c increased from 5 to 10, compared to a 25% increase with a 40% increase in freestream Reynolds number. Pressure distributions on the stowed heliostat showed the presence of a high-pressure region near the leading edge of the heliostat mirror that corresponds to the peak power spectra of the fluctuating pressures at low frequencies of around 2.4 Hz. These high pressures caused by the break-up of large vortices at the leading edge are most likely responsible for the peak hinge moment coefficients and the resonance-induced deflections and stresses that can lead to structural failure during high-wind events.

1. Introduction

The concentrating solar thermal (CST) power tower (PT) is one of the most promising renewable technologies for large-scale electricity production with thermal energy storage, and it can be deployed as a hybrid system with existing fossil fuel power plants for a base-line power supply (Hinkley et al., 2013). The main limitation of PT systems is their significantly larger levelised cost of electricity (LCOE) relative to base-load energy systems (IRENA, 2013). To reduce the LCOE of PT systems there is a need to lower the capital cost of a PT plant, of which the largest cost is the heliostat field, with an estimated contribution of between 40% and 50% (Coventry and Pye, 2014; Hinkley et al., 2013; IRENA, 2015; Kolb et al., 2007). One opportunity to lower the heliostat cost is through optimisation of the size and position of heliostat mirrors to withstand maximum wind loads during high-wind conditions when in the stow position, aligned parallel to the ground ($\alpha = 0°$). The motor drives, support structure and mirror must all withstand any forces and moments, shown in Fig. 1(a), applied to the heliostat from the wind. These components, which are identified in Fig. 1(b), account for up to 80% of the heliostat capital cost according to research by Kolb et al. (2011). A cost analysis of quasi-static wind loads on individual heliostat components by Emes et al. (2015) found that the sensitivity of the total heliostat cost to the stow design wind speed increased by 34% for an increase in mean wind speed from 10 m/s to 15 m/s. Following the linear cost-load proportionality developed by McMaster Carr, a 40% reduction in the peak hinge moment on the elevation drive of a conventional heliostat can lead to a 24% saving in the representative gear reducer cost (Lovegrove and Stein, 2012). Hence, there is significant potential to minimise the capital cost of a PT plant through optimising the structural design of heliostats in the stow position.

Knowledge of the aerodynamic loads on heliostats during high-wind events is critical for their design to maintain structural integrity in stow position, and requires an understanding of the turbulent effects of neutrally-stratified wind over flat, uniform terrain in the atmospheric boundary layer (ABL). Large physical structures such as buildings and heliostats are positioned in the lowest 200 m ($\delta_s \approx 0.2\,\delta$) of the neutral ABL, known as the atmospheric surface layer (ASL). Full-scale field measurements in the ASL were shown to have similar turbulence properties to the canonical turbulent boundary layer along a flat plate in a wind tunnel (Plate, 1974). For example, the wind velocity profile

---

* Corresponding author.
E-mail address: matthew.emes@adelaide.edu.au (M.J. Emes).

http://dx.doi.org/10.1016/j.solener.2017.08.031
Received 24 February 2017; Received in revised form 1 August 2017; Accepted 11 August 2017
0038-092X/

Nomenclature

A	heliostat mirror area (m^2)
α	power law roughness exponent
b	spire base width (m)
c	heliostat mirror chord length (m)
c_L	peak lift coefficient
c_{MHy}	peak hinge moment coefficient
c_P	pressure coefficient
D	drag force on heliostat in stow position (N)
d	spire base depth in flow direction (m)
δ	ABL thickness (m)
f	frequency of velocity/pressure fluctuations (Hz)
H	elevation axis height of stowed heliostat mirror above the ground (m)
h	spire height (m)
I_u	turbulence intensity (%)
L_u^x	longitudinal integral length scale (m)
L	lift force on the flat plate (N)
$L_{heliostat}$	lift force on the heliostat assembly with pylon and plate (N)
L_{pylon}	lift force on the heliostat pylon without the plate (N)
l_p	distance to the centre of pressure in the flow direction (m)
M_{Hy}	hinge moment on heliostat in stow position (N·m)
M_y	overturning moment on heliostat in stow position (N·m)
P_i^f	pressure fluctuations on the upper surface of the stowed heliostat mirror (Pa)
P_i^b	pressure fluctuations on the lower surface of the stowed heliostat mirror (Pa)
Re_∞	freestream Reynolds number $Re_\infty = U_\infty \delta / \nu$
S_p	power spectrum of pressure fluctuations (Pa^2/Hz)
S_u	power spectrum of streamwise velocity fluctuations (m^2/s^3)
σ_u	standard deviation of streamwise velocity fluctuations (m^2/s^3)
T_u^x	longitudinal integral time scale (s)
U_∞	freestream velocity (m/s)
$\overline{U}$	mean velocity (m/s)
u	streamwise velocity fluctuations (m/s)
x	longitudinal direction (m)
y	spanwise direction (m)
z	height above the ground (m)

$\overline{U}(z)$ in the ABL (Fig. 2) can be accurately modelled by the power law and log law to a theoretical maximum gradient or freestream velocity U_∞ at the boundary layer thickness δ (Kaimal and Finnigan, 1994), however Banks (2011) noted that replication of the turbulent power spectra in boundary layer wind tunnels cannot be achieved due to discrepancies in scaling between heliostat models (typically 1:10 to 1:50) and the turbulent eddy length scales (typically 1:100 to 1:300). Heliostats are typically stowed at heights below 10 m in the ASL and hence they are exposed to large velocity gradients and rapid fluctuations of the instantaneous wind velocity relative to the mean, also known as gusts (Kristensen et al., 1991). These flow fluctuations arise from eddies of varying sizes within the ABL that are produced by surface roughness and obstacles in the viscous sublayer near the ground. The sizes of the largest eddies, defined by the longitudinal integral length scale L_u^x, that are the same order of magnitude as the characteristic length of a physical structure have a significant effect on the fluctuating pressures and unsteady forces, which can result in fatigue damage and lead to structural collapse. Small eddies result in pressures on various parts of a structure that become uncorrelated with distance of separation, however large eddies whose sizes are comparable with the structure result in well-correlated pressures over its surface as the eddies engulf the structure, leading to maximum wind loads (Greenway, 1979; Mendis et al., 2007). Maximum wind loads on a stowed heliostat at heights H below 20 m in the ASL will therefore tend to occur from the interaction of the largest eddies with the heliostat facet. Holdø et al. (1982) found that the drag force on a scale model low-rise building of height D increased by 10% in an ABL with a turbulence intensity of 25% ($L_u^x/D = 2.8$) compared to a uniform approaching flow ($L_u^x/D = 1.6$). However, Roadman and Mohseni (2009) observed the maximum wind loads on small-scale micro-air-vehicles (MAVs) when the sizes of the eddies were an order of magnitude larger or smaller than their chord length ($c \leq 15$ cm). Hence, consideration of the sizes of the largest eddies in the ABL relative to the characteristic length of a physical structure can lead to significant savings in costs due to the reduced design wind loading.

Wind codes and standards for low- to medium-rise buildings adopt a simplified gust factor approach that assumes quasi-steady wind loads based on a maximum gust wind speed, however due to their non-standard shapes, heliostat components have previously been designed from mean and peak wind load coefficients derived from experimental data in systematic wind tunnel studies. Peterka et al. (1989) found that the lowest drag forces on a 1:40 scale heliostat modelled as a thin flat plate occurred at an elevation angle α of 0°, however the peak lift and hinge moment coefficients were approximately 10 times their mean values in stow position. This indicates the significance of gust and amplification effects of survival high-wind conditions for heliostats in

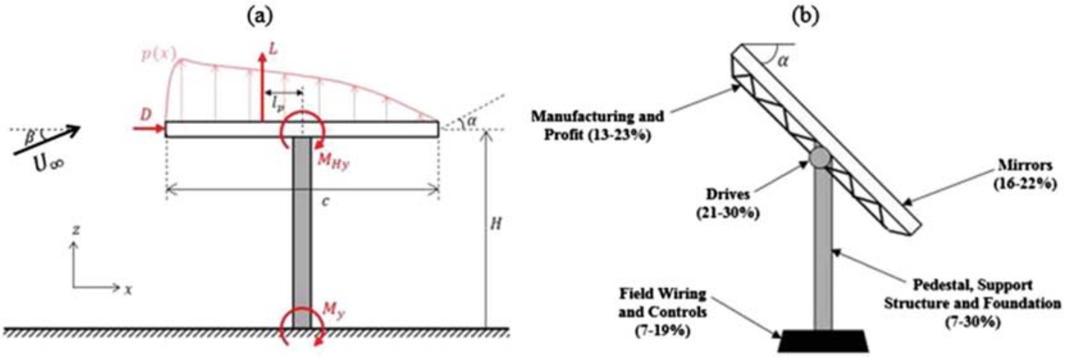

Fig. 1. (a) Main wind loads acting at the centre of pressure l_p due to a non-uniform pressure distribution $p(x)$ on a heliostat in stow position with a chord length c and an elevation axis height H; (b) Breakdown of heliostat cost by component (reproduced from Kolb et al. (2011)).

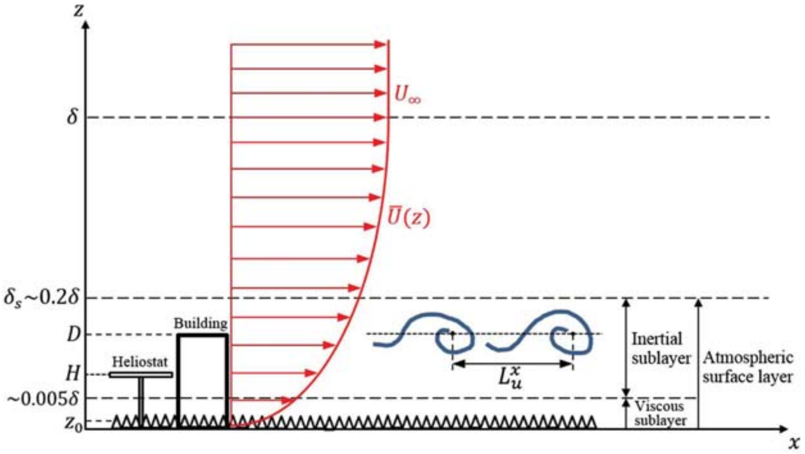

Fig. 2. Structure and turbulence characteristics of the atmospheric boundary layer.

stow position. Wind tunnel experiments by Peterka et al. (1989) and Pfahl et al. (2011) showed that peak wind load coefficients increase significantly at turbulence intensities I_u above 10%. Pfahl et al. (2015) found that the peak lift coefficient and peak hinge moment increased by 6.5% and 15%, respectively, when the freestream longitudinal turbulence intensity was increased from 13% to 18% in a range characteristic of the turbulence within heliostat fields in an open country terrain. The temporal variation of turbulence has been widely studied, however the effect of the spatial distribution of turbulence and the length scales of vortices embedded in the turbulence in the ABL has not been investigated in a systematic study. Analysis of the peak wind loads on heliostats in wind tunnel experiments has previously yielded the most realistic results by matching the longitudinal turbulence intensity, however the sizes of the relevant eddies that are the same order of magnitude as the chord length of the heliostat are presumed to be responsible for the peak wind loads (Pfahl et al., 2015). The ratio of integral length scale to building height L_u^x/D was found to have a greater effect than Reynolds number on peak drag coefficient for turbulence intensities between 2% and 25% (Holdø et al., 1982). The effect of increasing the length scale ratio (L_u^x/D) of a 2D short rectangular cylinder of height D to greater than 3 was found by Nakamura (1993) to have a very small effect on the body-scale turbulence ($I_u = 10$–12%) and galloping vibration. Hence, this paper aims to investigate the effect of the ratio of integral length scale to heliostat chord length L_u^x/c on the peak lift and hinge moment coefficients on a heliostat in stow position.

The dynamic wind-excited response of permanent structures such as heliostats positioned on the ground determines their ability to withstand gusts in the ABL. Tall or slender structures with low natural frequencies are most likely to respond to the dynamic effects of gusts, which can lead to failure from excessive deflections and stresses due to galloping and torsional flutter (Jain et al., 1996; Mendis et al., 2007). Flutter is an oscillatory instability from one or more vibrational modes at a critical wind velocity leading to an exponentially-growing response that often leads to structural failure, whereas buffeting is the random response due to turbulence in the oncoming wind flow that does not generally lead to catastrophic failures but is important for serviceability considerations (Jain et al., 1996). Nakamura (1993) found that galloping and torsional flutter tend to occur on short rectangular cylinders of height D ($Re_\infty = \overline{U}D/\nu$ from 0.14 to 30 $\times$ 10^4) at frequencies of the order of 1 Hz when the turbulence length scales are comparable to the size of the body ($L_u^x/D \approx 1$). This has a particular significance for heliostats with natural frequencies between 2 Hz and 5 Hz (Gong et al., 2012) that are stowed in the lowest 10 m of the ASL. The longitudinal integral length scales were calculated by Emes et al. (2016) to be $L_u^x/z \geqslant 1$ in the lowest 10 m of a low-roughness desert terrain, hence stowed heliostats in open country and low roughness terrains are likely to be exposed to vortices of sizes that are the same order as the heliostat chord length c. The gust factor method assuming quasi-steady wind loads is widely used in design codes (American Society of Civil Engineers, 2013; Cook, 1985; Engineering Sciences Data Unit, 1985; Standards Australia and Standards New Zealand, 2011) to estimate the peak wind loads on large buildings with heights less than 200 m and calculation of an along-wind dynamic response factor with a natural first-mode fundamental frequency between 0.2 Hz and 1 Hz (Holmes et al., 2012). However, this standard approach is not suitable for heliostats as they have chord lengths and heights that are an order of magnitude smaller and typically have natural frequencies that are at least an order of magnitude larger than standard-sized buildings. Discrepancies in peak wind loads estimated using the gust factor method commonly arise from the high impact of the instantaneous angle of attack for longitudinal wind flows with large vertical components of turbulence and the shift of the turbulent energy spectra to higher frequencies in boundary layer wind tunnels (Banks, 2011; Pfahl et al., 2015). This is the case for a heliostat in stow position, as the mean wind load is near zero for longitudinal wind flow but reaches significant values for high vertical turbulence components caused by vortex structures. The eddies corresponding to the peaks of the power spectra that are comparable in size to the heliostat mirror are important for the maximum lift forces and hinge moments on heliostats in stow position, as these eddies cause the maximum pressure differences over the surface of the heliostat mirror. Gong et al. (2013) found that large negative peak wind pressure coefficients occurred at the leading edge of the mirror surface in stow position, suggesting that this region was the most vulnerable to wind-induced mirror damage. The size of the largest eddies relative to the size of the mirror is believed to be the factor that is responsible for these peak wind pressures, however the length scales and dominant frequencies of these eddies were not previously reported. Hence, the present study investigates the distribution of pressure coefficients and peak wind loads on a stowed heliostat and the correlation of loads and eddy frequencies at different points near the leading edge of the heliostat mirror.

The overall aim of this paper is to investigate the dependence of peak wind load coefficients on a heliostat in stow position on three turbulence characteristics in the atmospheric surface layer: freestream Reynolds number, turbulence intensity and the ratio of integral length scale to chord length of the stowed heliostat mirror. To achieve this aim it is required to fully characterise the temporal and spatial distribution of velocity to represent the eddies in the lower ABL, to which stowed heliostats are exposed, during gusty high-wind conditions. Force measurements on different-sized heliostat mirrors at a range of elevation axis heights were used to derive relationships for the peak lift and peak hinge moment coefficients as a function of these turbulent characteristics and the height of the stowed heliostat mirror in the ABL. Pressure distributions over the surface of the stowed heliostat facet were measured for analysis of their correlation with load fluctuations, particularly close to the leading edge of the facet, from the interaction with large vortices so that the turbulence conditions that would most likely lead to critical failures and fatigue could be determined. The results will be used to provide recommendations for improving the accuracy and versatility of the current methods used for calculating the ultimate design wind loads on heliostats in stow position, based on the temporal and spatial turbulence characteristics of gusts in the lower ABL. Further, the derived relationships can be used to optimise the dimensions of the stowed heliostat mirror chord length and elevation axis height, based on known characteristics of the approaching turbulence in a given ABL.

2. Experimental method

2.1. Experimental setup

Experimental measurements were taken in a closed-return wind tunnel at the University of Adelaide. The test section of the tunnel has a development length of 17 m and a cross-section expanding to 3 m × 3 m to allow for a pressure gradient resulting from growth of the boundary layer. The tunnel can be operated at speeds of up to 20 m/s with a low level of turbulence intensity, ranging between 1% and 3%. The unperturbed boundary layer formed in smooth flow is 0.2 m thick at the location of the turntable, 15 m downstream of the turning vanes. Accurate representation of a part-depth ABL in the wind tunnel is required to replicate similar turbulence properties that heliostats are exposed to in the lower surface layer of the ABL, including a logarithmic mean velocity profile. It is generally accepted that the most effective wind tunnel simulation of the ABL is obtained when a flow passes over a rough surface producing a natural-growth boundary layer (De Bortoli et al., 2002). The most commonly-used passive devices include spires to generate turbulent mixing through separation of flow around their edges, fence barriers to increase the height of the boundary layer and floor roughness to develop the velocity deficit near the ground (Cook, 1978; Counihan, 1973). The present study uses spires and roughness elements shown in Fig. 3(a) to generate a power law mean velocity profile of the form

$$\overline{U}(z) = U_\infty \left(\frac{z}{\delta}\right)^{\alpha}, \tag{1}$$

where U_∞ (m/s) is the freestream velocity, δ is the boundary layer thickness and α is the power law exponent. Dimensions of two different triangular spire designs and the timber roughness blocks are shown in Fig. 3(b). These dimensions were derived following a theoretical design method outlined by Irwin (1981) such that the height h, base width b and depth d of the spire could be determined based on the desired power law profile with exponent α of 0.2 and boundary layer thickness δ of 1.2 m. This gives a ratio of boundary layer thickness to wind tunnel height of 0.33, for which Irwin (1981) showed that the experimental boundary layer velocity profile based on the spire dimensions ratio b/h can be generated to within 3% of a power law velocity profile. Lateral homogeneity of the fully developed boundary layer was found to occur after a minimum streamwise distance of 6 spire heights (6h) downstream of the spires, whereas the effect of the roughness elements on the velocity deficit of the boundary layer becomes smaller with

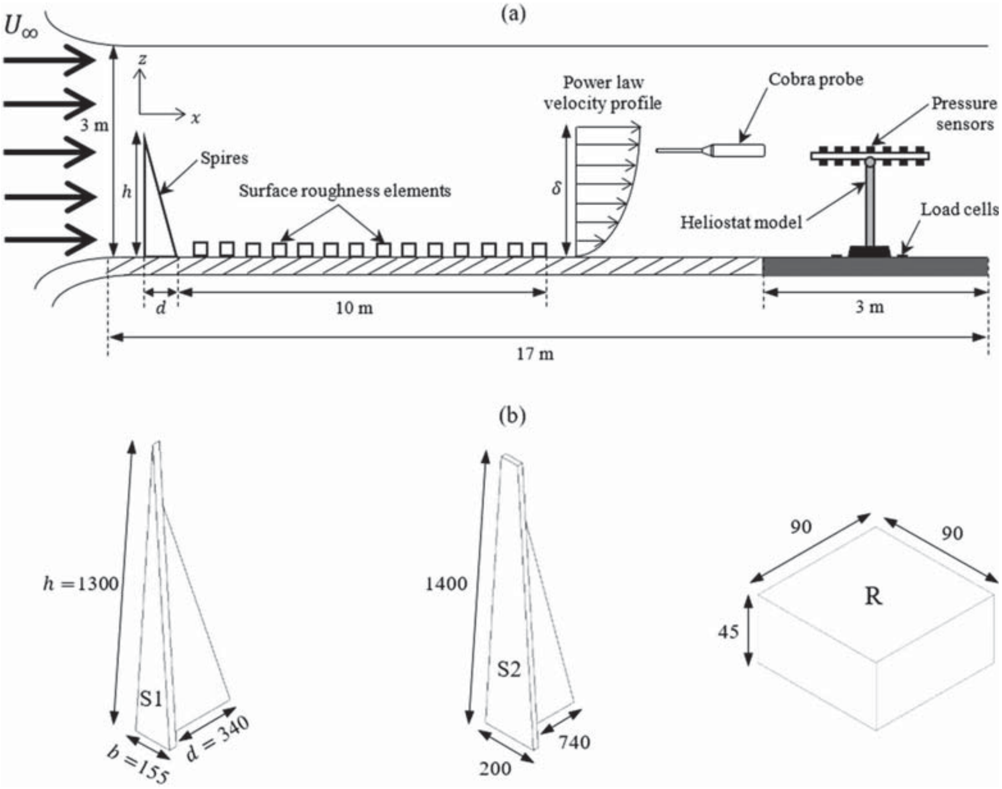

Fig. 3. (a) Schematic diagram with labelled dimensions of the wind engineering test section in the closed-return wind tunnel containing spires and roughness elements and a stowed heliostat; (b) Schematic diagram showing the dimensions (mm) of the two spires and the roughness elements (R) used for generation of the lower ABL.

increasing downstream distance. The mounting point of the stowed heliostat is 9*h* downstream of the spires in the current study, hence the development length of the tunnel is expected to be sufficient for lateral flow homogeneity.

The experimental setup in the wind tunnel is shown in Fig. 9 for one of the two spire and roughness configurations tested, hereafter referred to as SR1 and SR2, with dimensions shown in Fig. 3(b). The spires were separated by a distance of 650 mm at their centrelines followed by a 10 m fetch of wooden roughness elements. Three components of velocity were measured using a Turbulent Flow Instrumentation (TFI) Cobra probe at a sampling frequency of 1 kHz with an oversampling ratio of 5 to satisfy the Nyquist criterion and prevent aliasing. Data were taken at two freestream velocities U_∞ of 11 m/s and 15.5 m/s, corresponding to freestream Reynolds numbers $Re_\infty = U_\infty \delta/\nu$ of 0.88×10^6 and 1.24×10^6, respectively. The forces and pressures at these velocities fill the measurement span of the devices so that errors remain small.

Fig. 4 presents the mean velocity and turbulence intensity profiles as a function of non-dimensional height z/δ at three spanwise locations in the lower ABL generated by SR1 with a freestream velocity U_∞ of 11 m/s, boundary layer thickness of δ of 1.2 m and Reynolds number Re_∞ of 880,000. Velocity profiles at the tunnel centreline ($y = 0$ m) in Fig. 4(a) show lateral homogeneity within a maximum error of ± 5% of the values at the outer boundaries of a 1 m × 1 m grid at the position of the heliostat. The heliostat was stowed at heights relative to the boundary layer thickness z/δ between 0.3 and 0.5, as indicated by the shaded region in Fig. 4. Turbulence intensities at the two outer lateral boundaries in Fig. 4(b) are within 1% and 2% of the centreline values, respectively, which are considered to be sufficient for using centreline profiles for the calculation of turbulence parameters and wind loads. Mean velocity profiles are well approximated by the theoretical power law curve $\overline{U}(z) = 11(z/1.2)^{0.18}$ to represent a low-roughness atmospheric surface layer in an open country terrain, as is commonly modelled for the region surrounding heliostat fields. The power law curve can be shown to correspond to a logarithmic mean velocity profile with roughness height z_0 of 2 mm within a maximum 1% error.

Fig. 5 shows the mean velocity and turbulence intensity profiles (I_u) as a function of non-dimensional height z/δ behind two different configurations of spires and roughness elements, hereafter referred to as SR1 and SR2. It can be seen in Fig. 5(a) that SR1 more closely represents the power law and log law profiles than SR2, within a maximum error of ± 5% in the range of heights ($0.3 < z/\delta < 0.5$) at which the heliostat mirror is stowed. Although the relative errors in turbulence intensity profiles using SR1 and SR2 are more significant, the values of I_u in the SR1 profile are within ± 2% of the ESDU 85020 profile of I_u within the shaded range of heights ($0.3 < z/\delta < 0.5$) of the stowed heliostat in Fig. 5(b). Turbulence intensities ranged between 6% and 13% at the range of stowed heliostat elevation axis heights in the current study, hence the effect of turbulence intensity on the peak wind loads could be investigated by positioning the heliostat mirror at different heights using SR1 and SR2.

Fig. 6 compares the Reynolds stress profiles, normalised with respect to the freestream velocity U_∞, as a function of non-dimensional height z/δ of SR1 and SR2 in the current study with the wind tunnel experiment by Farell and Iyengar (1999) in a simulated ABL with $\delta = 1.2$ m and a power law velocity profile with roughness exponent $\alpha = 0.28$. The magnitudes of Reynolds stresses of SR1 in the current study are significantly lower than SR2, however the largest Reynolds stresses occur in the middle region of the ABL at non-dimensional heights z/δ between 0.3 and 0.5 where the heliostat mirror was stowed. This indicates that the heliostat is exposed to the region of the ABL where the largest turbulent stress production occurs, leading to the generation of the largest eddies. The differences between the Reynolds stress profiles of SR1 and the study by Farell and Iyengar (1999) in this middle region of the ABL are due to the larger velocity gradient $d\overline{U}/dz = 14$ at $z/\delta = 0.5$ in the urban power law ($\alpha = 0.28$) terrain compared to $d\overline{U}/dz = 2.8$ at $z/\delta = 0.5$ in the low-roughness power law ($\alpha = 0.18$) terrain represented by SR1. Further, the packing density, defined as the ratio of roughness element area projected onto a plane perpendicular to the flow direction to the unit ground area surrounding the roughness elements, in the study by Farell and Iyengar (1999) was 7.84% compared to 5% in the current study. In contrast, the magnitudes of Reynolds stresses of SR2 are closer to the study by Farell and Iyengar (1999) because of the larger velocity gradient $d\overline{U}/dz = 5.8$ at $z/\delta = 0.5$ for SR2. Despite the differences in magnitude between the Reynolds stress profiles of SR1 and SR2, the Reynolds stresses are relatively constant at the heights ($0.3 < z/\delta < 0.5$) of the stowed heliostat in the middle region of the simulated ABL. Hence, the effect of the largest eddies can be most independently assessed within this range of heights.

Fig. 7 presents the non-dimensional power spectra in the streamwise and vertical directions as a function of non-dimensional frequency $fc/\overline{U}$ based on the chord length ($c = 0.8$ m) of the stowed heliostat and the mean wind speed. It can be seen in Fig. 7(a) and (b) that both the

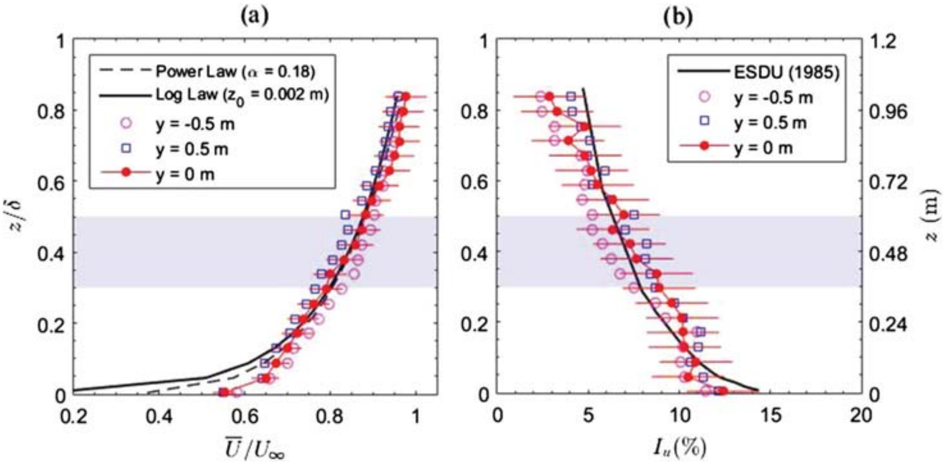

Fig. 4. Flow profiles at three spanwise y locations in the ABL generated using spire and roughness configuration SR1: (a) Mean velocity profiles normalised with respect to the freestream velocity U_∞ and compared with power law ($\alpha = 0.18$) and log law ($z_0 = 0.002$ m) profiles; (b) Turbulence intensity profiles compared with ESDU 85020 (1985) for $U_{10r} = 10$ m/s, $z_0 = 0.002$ m and $\delta = 350$ m. Error bars show maximum errors of ± 5% of the centreline velocity profile and ± 2% of the centreline I_u profile.

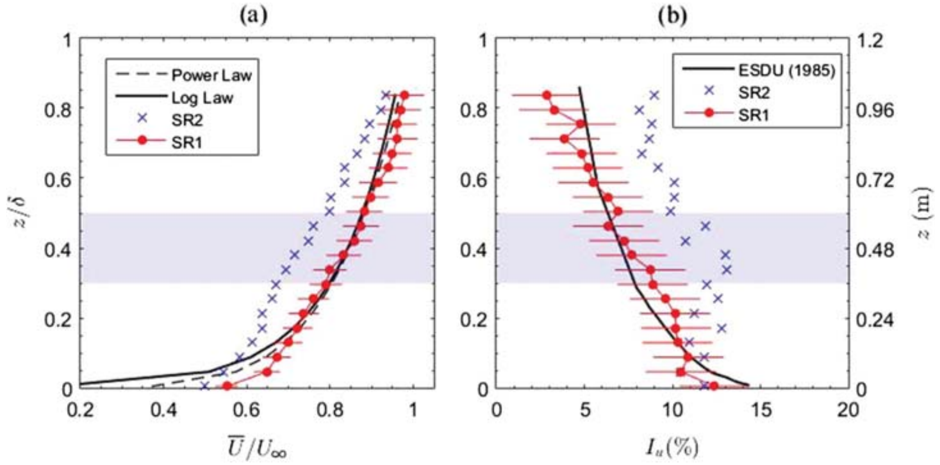

Fig. 5. Centreline flow profiles using two configurations of spires and roughness elements: (a) Mean velocity profiles normalised with respect to the freestream velocity U_∞ and compared with power law ($\alpha = 0.18$) and log law ($z_0 = 0.002$ m) profiles; (b) Turbulence intensity profiles compared with ESDU 85020 (1985) for $U_{10r} = 10$ m/s, $z_0 = 0.002$ m and $\delta = 350$ m. Error bars indicate a maximum error of ± 5% of the SR1 velocity profile and ± 2% of the SR1 turbulence intensity profile for comparison with the log law profiles.

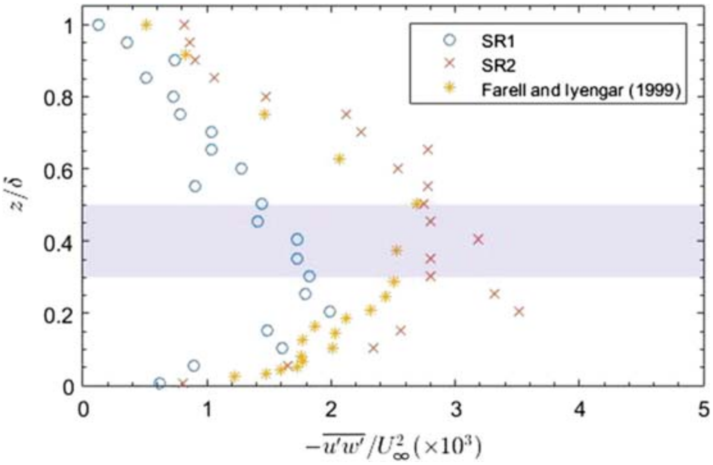

Fig. 6. Reynolds shear stress profiles non-dimensionalised with respect to the freestream velocity and compared with the wind tunnel experiment by Farell and Iyengar (1999) in a simulated ABL with $\delta = 1.2$ m and power law velocity profile ($\alpha = 0.28$). The shaded region indicates the range of heights at which the heliostat mirror was stowed.

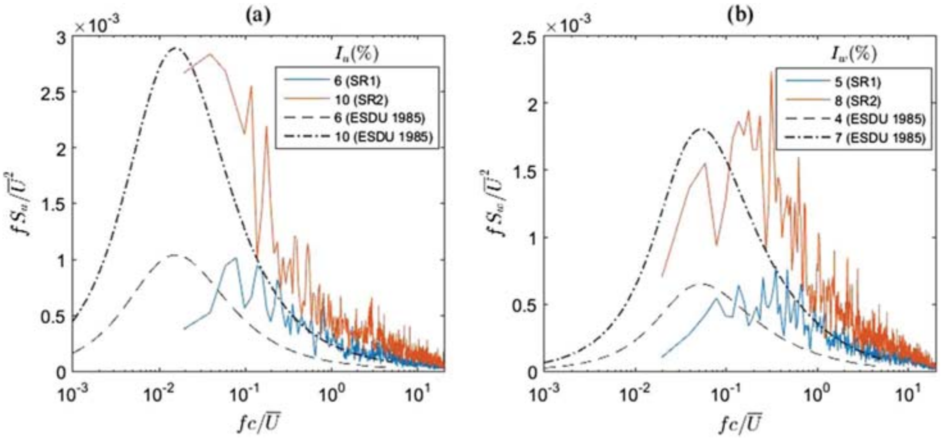

Fig. 7. Non-dimensional power spectra as a function of non-dimensional frequency $fc/\overline{U}$ of the two spire and roughness configurations (SR1 and SR2) compared with Engineering Sciences Data Unit (1985) correlations: (a) Longitudinal power spectra of turbulence $fS_u/\overline{U}^2$; (b) Vertical power spectra of turbulence $fS_w/\overline{U}^2$.

longitudinal power spectra $fS_u/\overline{U}^2$ and the vertical power spectra $fS_w/\overline{U}^2$ for both SR1 and SR2 were similar in magnitude to the Engineering Sciences Data Unit (1985) data for a neutral ABL. The peak energy of eddies at lower frequencies for SR1 is smaller than SR2 because of a lower turbulence intensity of 6%, as the area under the curve of the PSD function is equivalent to the variance σ_u^2 of the streamwise velocity fluctuations. However, the frequency domain of the experimental measurements in the current study is limited due to the differences between heliostat model scales and the wind tunnel flow scales and hence, the low frequency region of the full-scale turbulent power spectra cannot be replicated in boundary layer wind tunnel experiments (Banks, 2011; Pfahl et al., 2015). This is indicated in Fig. 7(a) by a horizontal shift of $fS_u/\overline{U}^2$ for SR1 and SR2 to higher frequencies when the longitudinal turbulence intensity I_u is matched to ESDU 85020. Fig. 7(b) shows that the vertical spectra $fS_w/\overline{U}^2$ are also shifted to higher frequencies, however the vertical turbulence intensities I_w of SR1 and SR2 are 1% larger than the ESDU (1985) data at the same I_u due to the differences in scaling between the longitudinal and vertical components of turbulence in the ABL and the current study. Despite the limitation of wind tunnel experiments at lower frequencies, velocity fluctuations measured at the frequencies corresponding to the peak values of the power spectra were considered sufficient for the calculation of longitudinal integral length scales L_u^x to provide a measure of the largest eddies in the flow.

Fig. 8(a) presents the longitudinal integral length scales as a function of height in the ABL with δ of 1.2 m for two combinations of the spires with surface roughness elements (SR1 and SR2). Although there is some scatter, the general trend indicates that the eddies approaching the stowed heliostat at heights between 0.35 m and 0.6 m tend to have length scales between 1.5 m and 3 m. Larger length scales were generated in the middle region of the simulated ABL for SR1 and SR2 compared to S1 and S2 in Fig. 8(a), suggesting that floor roughness can more effectively maintain the larger-scale eddies developed in the near wake of the spires. The average model-scale integral length scales L_{uM}^x for an assumed surface roughness height z_{0M} of 2 mm were converted to a full-scale ABL using the average scale factor $S = 91.3z_M^{0.491}/L_{uM}^{x\ 1.403}z_{0M}^{0.088}$ from Cook (1978) for comparison with other experimental measurements and a semi-empirical model in Fig. 8(b). Length-scale data in the current study showed good agreement with the wind tunnel simulation of an urban terrain ABL by Counihan (1973) in the lowest 100 m, commonly known as the surface layer, although integral length scales were 37% smaller on average than Counihan (1973) at heights greater than 100 m. This difference is most likely because of the larger gradient or freestream wind speed U_∞ of 31 m/s in the experiments by Counihan (1973) compared to 11 m/s in the current study. The opposite trend was found when comparing the current study with full-scale field measurements by Ivanov and Klinov (1961) over an urban terrain in Moscow and reported in Farell and Iyengar (1999). These discrepancies highlight the difficulties in comparing absolute length scales between full-scale and model-scale experiments.

Integral length scales predicted by the ESDU 85020 model following similarity theory were compared for an assumed logarithmic roughness height z_0 of 1 mm, boundary layer thickness δ of 480 m and mean wind speed $\overline{U}_{10m}$ of 6 m/s at a 10 m height for consistency with the current study. Integral length scales are predicted by ESDU 85020 within a maximum error of ± 8% from changing the 10 m height mean wind speed to 6 m/s from the reference 20 m/s wind speed over open country terrain in the ESDU (1985) model. The semi-empirical model underestimated the length scales by as much as 28% at heights between 100 m and 200 m, as shown Fig. 8(b). Farell and Iyengar (1999) previously observed ESDU 85020 data to be an upper bound to field measurements of L_u^x profiles in open country and urban terrains, however Fig. 8(b) shows that wind tunnel experiments can generate integral length scales as much as double those predicted by the ESDU correlations. The divergence between L_u^x results are most likely because of the scaling issues in wind tunnels and the different techniques used for calculating integral length scales in previous studies. The method commonly used in wind tunnel experiments approximates L_u^x by fitting the von Karman power spectrum to the measured spectra, however Flay and Stevenson (1988) concluded that this method is limited due to difficulties in locating the peaks of the measured spectra. Hence, in the current study L_u^x was estimated using the correlation approach by integrating under the R_u curve to the first-zero crossing (τ_0) because of clearly defined limits of integration, as well as consistent fluctuation of R_u about zero after τ_0, and relatively smaller errors compared to the spectral-fit technique.

Force measurements on the model heliostat were taken using four three-axis Bestech load cells mounted on a rotary turntable, as shown in Fig. 9. Each load cell has a capacity of 500 N with a sampling frequency of 1 kHz in all three axes and an accuracy of ± 0.5% of full scale. The heliostat mirror was simply modelled as a thin flat plate in the absence of a support structure, since Gong et al. (2013) showed that the shielding effect of the support structure had a less significant effect on the fluctuating wind pressures on a stowed heliostat exposed to parallel flow (β = 0°) than standard operating positions and for wind angles β between 90° and 180°. A series of six square aluminium plates with

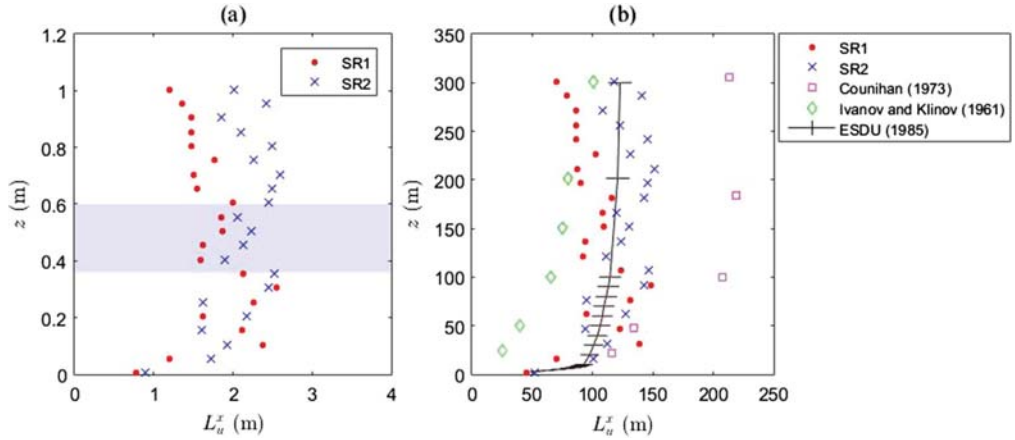

Fig. 8. Longitudinal integral length scale profiles: (a) Integral length scales calculated from the first-zero crossing of the autocorrelation function in the current study (δ = 1.2 m). Shaded region indicates the height at which the heliostat mirror was stowed in the current study; (b) Comparison of full-scale integral length scales with those measured in full-scale ABLs. Error bars on the ESDU curve indicate a maximum 8% error in the variation of L_u^x with changes in mean wind speed.

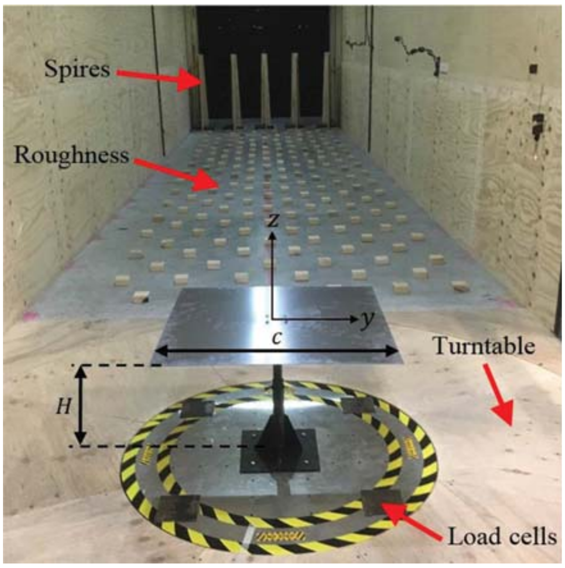

Fig. 9. Experimental setup in the wind tunnel showing spire and roughness configuration SR2 for generation of the lower ABL upstream of a 1:40 scale model heliostat in stow position of 0.8 m chord length (c) and 0.5 m elevation axis height (H).

3 mm thickness and chord length c ranging from 300 mm to 800 mm in 100 mm increments were manufactured and mounted on a common pylon with a telescopic design that allows the elevation axis height H to vary between 0.35 m and 0.6 m (H/δ = 0.3–0.5) and H/c to vary between 0.5 and 1.3.

Pressure measurements were taken on the upper and lower surfaces of a thick hollow aluminium facet containing 24 Honeywell high-frequency differential pressure sensors, as shown in Fig. 10(a). Each sensor has a pressure range of ± 1 psi (6.9 kPa) with an accuracy of ± 0.2% of full scale. The layout of the pressure taps on the surface of the heliostat is shown in Fig. 10(b). Differential pressures at each of the 24 tap locations were acquired simultaneously at a sampling frequency of 1 kHz for consistency with velocity and force data. To ensure simultaneous measurement and synchronisation of pressure signals at all of the locations on the stowed heliostat, individual channels were connected into two slots of a data acquisition chassis and a trigger was implemented using LabVIEW software to start sampling all of the signals at the same time.

2.2. Calculation of integral length scales

The integral length scales represent the sizes of the relevant eddies in the longitudinal direction that correspond to the largest magnitudes of the turbulent power spectra (Milbank et al., 2005; Watkins, 2012). The lower end of the power spectra represents the largest eddies, however these low-frequency eddies may have smaller energies than those at the peaks of the power spectra. Although the lowest frequencies of the turbulent power spectra in the ABL cannot be replicated in the wind tunnel (Milbank et al., 2005; Pfahl et al., 2015), the eddy scales of highest energy are assumed to have the largest impact on the integral length scale. Several different techniques have been used for calculating integral length scales, such as the commonly used spectral-fit method, however there are large uncertainties associated with locating the peaks of the measured spectra at low frequencies (Farell and Iyengar, 1999; Flay and Stevenson, 1988). Hence, the autocorrelation of velocity measurements was used to estimate the longitudinal integral length scales, L_u^x, in the current study because of clearly-defined limits of integration and consistent fluctuation of R_u about zero after τ_0, and relatively smaller errors compared to the spectral-fit technique. Point velocity measurements in the current study, obtained as a function of time, are transformed to spatially-distributed data by Taylor's hypothesis. This assumes that eddies are embedded in a frozen turbulence field convected downstream at the mean wind speed $\overline{U}$ (m/s) in the streamwise x direction, and hence do not evolve with time (Kaimal and Finnigan, 1994; Milbank et al., 2005). The longitudinal integral length scale L_u^x (m) at a given height H is defined in Fig. 11 as the average streamwise spacing between the largest two-dimensional spanwise eddies with a Rankine velocity distribution, which is calculated as (Milbank et al., 2005; Swamy et al., 1979)

$$L_u^x = T_u^x \overline{U}, \tag{2}$$

where T_u^x (s) is the integral time scale representing the time taken for the largest eddies to traverse a single point in the ABL. The integral time scale is calculated using Eq. (3) by the integral of the autocorrelation function in Eq. (4) up to its first-zero crossing τ_0, assuming that $R(\tau)$ fluctuates close to zero after this point (Swamy et al., 1979). Here $u' = u - \overline{U}$ defines the fluctuating component of streamwise velocity and σ_u^2 is the variance of the streamwise velocity fluctuations.

$$T_u^x = \int_0^\infty R(\tau)d\tau \approx \int_0^{\tau_0} R(\tau)d\tau, \tag{3}$$

$$R(\tau) = \frac{\overline{u'(t)u'(t+\tau)}}{\sigma_u^2} \tag{4}$$

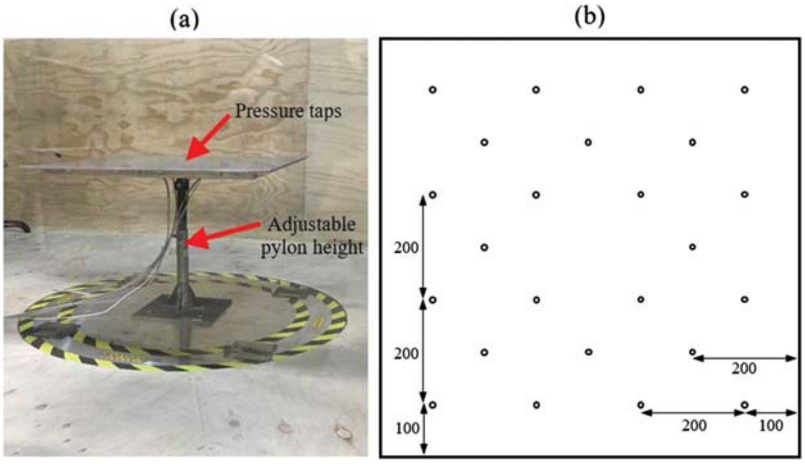

Fig. 10. (a) Experimental setup for surface pressure measurements showing the heliostat facet (c = 0.8 m) containing pressure sensors; (b) Layout of 24 pressure taps on the heliostat facet surface.

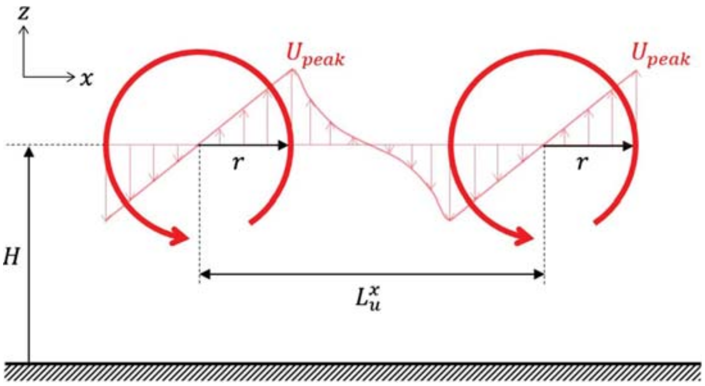

Fig. 11. Schematic diagram of two vortices with a Rankine velocity distribution and the definition of the longitudinal integral length scale L_u^x at elevation axis height H in the flow direction x.

2.3. Calculation of wind load coefficients

Mean and peak lift coefficients on the stowed heliostat are calculated from force data using the following equation:

$$c_L = \frac{L}{1/2\rho\overline{U}^2A}. \tag{5}$$

Here $L = L_{heliostat}-L_{pylon}$ (N) is the lift force on the flat plate calculated as the difference between the measured lift force on the stowed heliostat and the measured lift force on the pylon without the plate, ρ (kg/m^3) is density, $\overline{U}$ (m/s) is the mean wind speed at elevation axis height H and $A = c \times c$ (m^2) is the area of the flat plate projected onto the x–y plane. The peak lift forces were determined using the three-sigma approach, $L_{peak} = L_{mean} + 3\sigma_L$, for a sampling duration of 1 min at model scale (10 min equivalent full scale) at a sampling frequency of 1 kHz. The pressure coefficients at each pressure tap location i on the stowed heliostat surface are calculated from the measured differential pressures as:

$$C_{P_i} = \frac{P_i^f - P_i^b}{1/2\rho\overline{U}^2}, \tag{6}$$

where P_i^f (Pa) is the pressure on the upper surface of the stowed heliostat mirror and P_i^b (Pa) is the pressure on the lower surface of the stowed heliostat mirror.

Mean and peak hinge moments on the stowed heliostat are calculated as the product of the lift force on the plate and the distance of the centre of pressure from the centre of the plate defined in Fig. 1. The hinge moment coefficients are defined following Peterka and Derickson (1992):

$$c_{M_{Hy}} = \frac{M_{Hy}}{1/2\rho\overline{U}^2Ac}. \tag{7}$$

Here $M_{Hy} = L \times l_p$ (N·m) is the calculated hinge moment on the flat plate aligned parallel to the ground, L (N) is the lift force on the plate, c (m) is the plate chord length and l_p (m) is the distance to the centre of pressure in the streamwise direction of the mean flow in Fig. 1, defined as:

$$l_p = \frac{\int_0^c xp(x)dx}{\int_0^c p(x)dx}. \tag{8}$$

Here $p(x)$ is the non-uniform pressure distribution on the plate ($c = 0.8$ m) in the streamwise direction x (m). The time-averaged location of the centre of pressure was calculated to be $l_p = 0.12\,c$ for SR1 and $l_p = 0.15\,c$ for SR2 using the pressure distributions on the instrumented heliostat (Fig. 10).

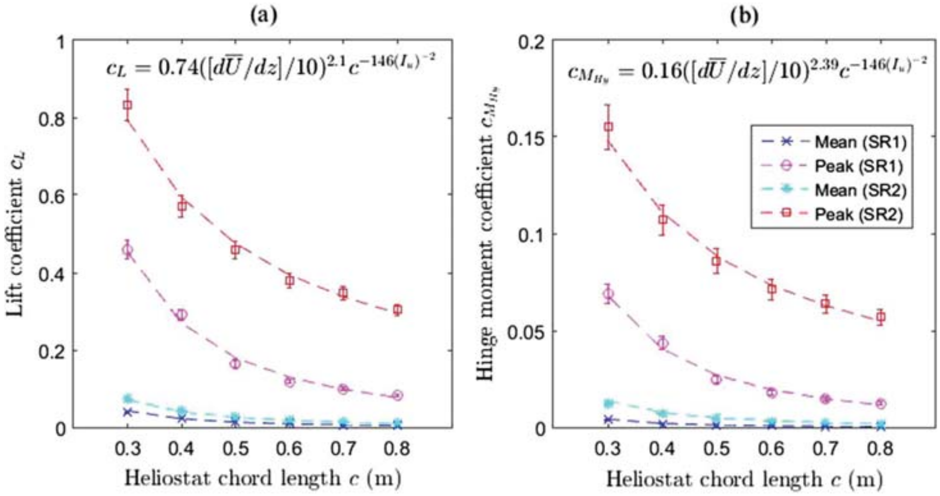

Fig. 12. Mean and peak wind load coefficients on a stowed heliostat as a function of square mirror chord length c for two spire and roughness configurations SR1 and SR2 at $U_\infty \approx 11$ m/s and $H/\delta \approx 0.3$ ($\delta = 1.2$ m): (a) Lift coefficient c_L; (b) Hinge moment coefficient $c_{M_{Hy}}$.

3. Results and discussion

3.1. Analysis of peak wind load coefficients

Fig. 12 shows the variation of mean and peak wind load coefficients for the two spire and roughness configurations on the heliostat mirror as a function of chord length c when stowed at a constant height (H/δ) in the ABL. Both mean and peak lift coefficients in Fig. 12(a) increased logarithmically with increasing chord length c from 0.3 m to 0.8 m. The ratio of peak-to-mean lift coefficients varied between 12 and 20 over the range of c tested. A similar exponential trend was observed in Fig. 12(b) for the hinge moment coefficients, as the peak-to-mean ratios were between 15 and 20 for comparison with the ratio of 10 reported in wind tunnel experiments by Peterka et al. (1989) and Peterka and Derickson (1992). Since the peak wind loads are decisive for the design of heliostats in stow position, the following equations have been developed for the peak lift and peak hinge moment coefficients as a function of the velocity gradient ($d\bar{U}/dz$), turbulence intensity I_u (%) and heliostat chord length c (m):

$$c_L = 0.74([d\bar{U}/dz]/10)^{2.1} c^{-146 I_u^{-2}}, \tag{9}$$

$$c_{M_{Hy}} = 0.16([d\bar{U}/dz]/10)^{2.39} c^{-146 I_u^{-2}}. \tag{10}$$

By assuming that the peak wind loads are caused by the break-up of vortices at the leading edge of the heliostat mirror and the resulting pronounced pressure near the leading edge, it can be shown that an increase of the peak lift force results from an increase in the width b of the mirror panel while it is rather independent of the height H of the mirror. As the chord length c is proportional to H, L is also proportional to H or c, respectively. Hence with constant k and $p_{dyn} = 1/2\rho\bar{U}^2$:

$$\begin{aligned} L \propto b &\Rightarrow L = kb = c_L p_{dyn} bc \\ &\Rightarrow c_L = k/p_{dyn} c \\ &\Rightarrow c_L \propto 1/c \end{aligned} \tag{11}$$

The hinge moment also depends on the distance $l_p(c)$ of the high pressure region near the leading edge to the centre of the mirror panel and it follows similar:

$$\begin{aligned} M_{Hy} \propto bc &\Rightarrow M_{Hy} = kbl_p(c) = c_{M_{Hy}} p_{dyn} bc^2 \\ &\Rightarrow c_{M_{Hy}} = k/p_{dyn} c \\ &\Rightarrow c_{M_{Hy}} \propto 1/c \end{aligned} \tag{12}$$

These inverse relationships derived in Eqs. (11) and (12) are approximately in accordance with the peak wind load coefficients in Fig. 12(a) and (b), respectively.

Fig. 13 presents the peak lift coefficient c_L and peak hinge moment coefficient $c_{M_{Hy}}$ as a function of the ratio of elevation axis height to chord length H/c at three different heights, non-dimensionalised with the ABL thickness H/δ, when exposed to SR1 (Fig. 13(a) and (c)) and SR2 (Fig. 13(b) and (d)). The effect of increasing the height at which the heliostat mirror is stowed in the ABL, H/δ, from 0.3 to 0.5 results in a vertical shift of peak c_L and peak $c_{M_{Hy}}$ to larger magnitudes at constant H/c. The effect of this upward shift increases with increasing H/c, hence the effect of H/δ becomes small at $H/c \leqslant 0.5$. Both peak c_L and peak $c_{M_{Hy}}$ increase exponentially with increasing H/c at a constant H/δ. Conventional heliostats are commonly designed for the ratio H/c of 0.5 (Téllez et al., 2014), however $H/c \approx 0.7$ for a heliostat with a horizontal primary axis. Additionally, $H/c > 0.5$ is required for those heliostats that are moved to the normal position for cleaning and washing of the mirror. Since heliostats would never be required to reach the normal position in the operation of a heliostat field, Fig. 13 shows that the minimum stow design wind loads and thus the lowest capital cost of manufacturing the components of a heliostat can be achieved by designing for H/c of 0.5 for the range of chord lengths tested in the current study. For example, reductions of approximately 50% in c_L and 40% in $c_{M_{Hy}}$ are possible by lowering H/c from 0.7 to 0.5 for a heliostat without a horizontal primary axis. Hence, the overall mass and strength of the heliostat can be reduced as the length of the pylon required is shorter. Designing for the smaller H/c of 0.5 can therefore lead to savings in the cost of manufacturing and installation of the heliostat.

Fig. 14 presents the peak wind loads on the stowed heliostat as a function of the longitudinal turbulence intensity using data for SR1 and SR2 at different heights in the simulated ABL for the six chord lengths tested. Peak lift coefficients in Fig. 14(a) increased linearly at $I_u \geq 10\%$ for the range of chord lengths c between 0.3 m and 0.8 m. The effect of I_u on peak lift coefficient becomes larger with decreasing c because of

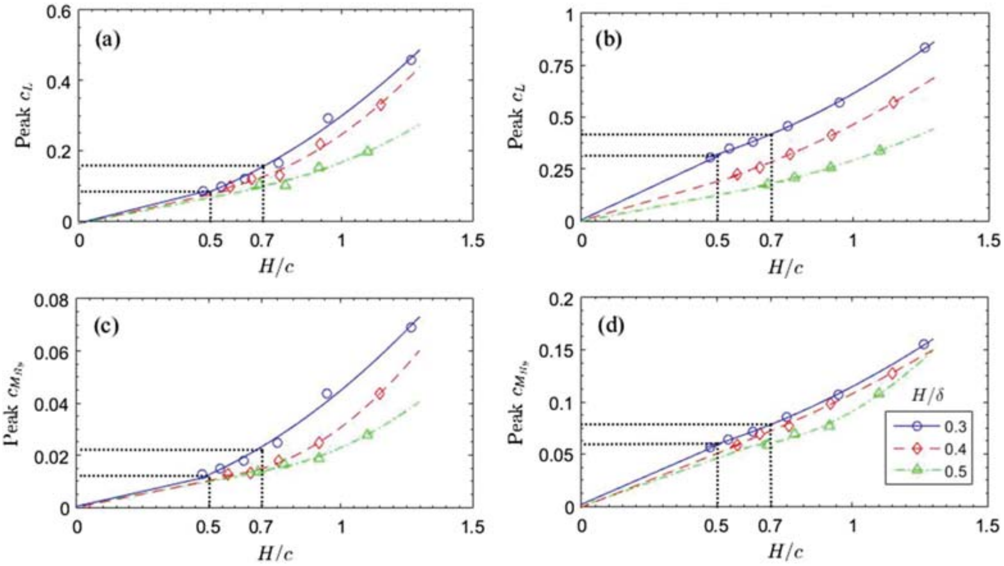

Fig. 13. Effect of the ratio of the elevation axis height to chord length (H/c) on the peak wind load coefficients on a heliostat mirror stowed at three different heights (H/δ) in the simulated ABL at a freestream velocity U_∞ of 11 m/s and Reynolds number Re_∞ of 8.8×10^5: (a) Peak lift coefficient c_L for SR1; (b) Peak lift coefficient c_L for SR2; (c) Peak hinge moment coefficient $c_{M_{Hy}}$ for SR1; (d) Peak hinge moment coefficient $c_{M_{Hy}}$ for SR2.

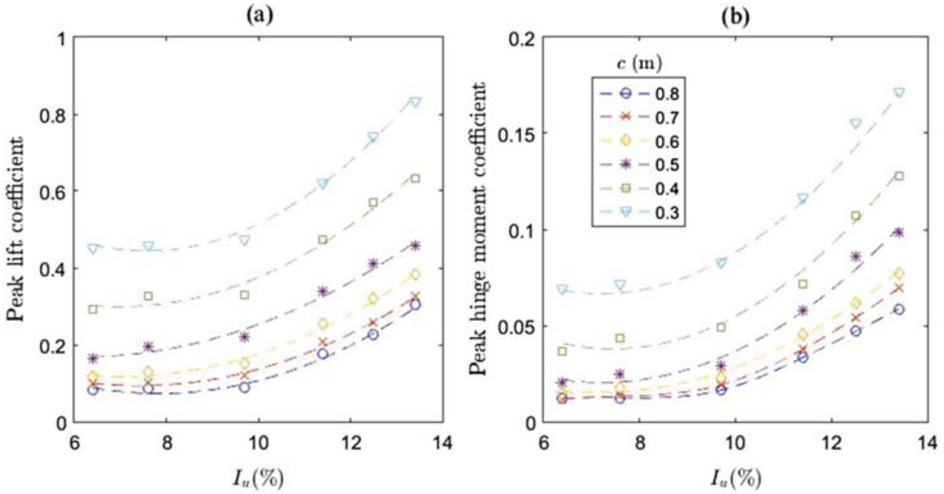

Fig. 14. Effect of turbulence intensity I_u on: (a) peak lift coefficient; (b) peak hinge moment coefficient on a stowed heliostat as a function of heliostat mirror chord length c.

larger length scale ratios L_u^x/c. In comparison, Fig. 14(b) shows that the peak hinge moment coefficients also increased significantly at $I_u \geq 10\%$. The pronounced linear increase of the peak wind load coefficients on stowed heliostats at turbulence intensities larger than 10% in the current study is in agreement with a similar finding by Peterka et al. (1989) for the peak drag and lift coefficients on heliostats in operating positions.

The peak lift and hinge moment coefficients on the smallest stowed heliostat ($c = 0.3$ m) exposed to the maximum I_u of 13.4% in the current study were 8% and 15% smaller, respectively, than those measured by Peterka et al. (1989) at a larger turbulence intensity I_u of 18%. In comparison, the peak lift and hinge moment coefficients on the stowed heliostat with $c = 0.5$ m were 13% and 23% smaller, respectively than those measured by Pfahl et al. (2015) at I_u of 13% similar to SR2 in the current study, as shown in Table 1. The main differences between this study and those by Pfahl et al. (2015) and Peterka et al. (1989) were the elevation axis height to boundary layer thickness ratio H/δ and the integral length scales representing the size of the largest eddies at a given height in the simulated ABL. The lowest value of H/δ of 0.3 in the current study is approximately double that of these previous experimental studies, however their integral length scales were not reported and can vary depending on the fetch length, spire geometry and incoming flow quality. Hence, these differences indicate that BLWT data can lead to uncertainties in the load measurements as the length scales that can be generated are limited by the size of the wind tunnel and the largest length scales that exist in the ABL cannot be simulated.

Fig. 15 presents the effect of the ratio of longitudinal integral length scale to heliostat chord length L_u^x/c on the mean and peak lift and hinge moment coefficients using data for SR1 and SR2 at different heights in the simulated ABL for the six chord lengths tested. It can be seen in Fig. 15(a) that the peak lift coefficient increases linearly from 0.1 to 0.8 as L_u^x/c increases from 2.5 to 10. In comparison, the peak hinge moment coefficient in Fig. 15(b) increases linearly from 0.02 to 0.12 as L_u^x/c increases to 10. These linear relationships of the peak lift and hinge moment coefficients with L_u^x/c can be approximated by the following equations:

$$c_L = 0.1(L_u^x/c) - 0.113 \tag{13}$$

$$c_{M_{Hy}} = 0.022(L_u^x/c) - 0.032 \tag{14}$$

Fig. 16 presents the peak lift and hinge moment coefficients, averaged for SR1 and SR2, as a function of turbulence intensity I_u and freestream Reynolds number Re_∞ for a stowed heliostat of three different chord lengths c. Fig. 16(a) shows that increasing freestream Reynolds number by 40% leads to average increases of 13%, 15% and 21% in c_L for c of 0.3 m, 0.5 m and 0.8 m, respectively, at a constant turbulence intensity I_u ranging from 6.5% to 13%. In comparison, the average increases in $c_{M_{Hy}}$ are 14%, 16% and 25%, respectively for the same values of c, as shown in Fig. 16(b). These relative changes in peak wind load coefficients are considerably less than the dependence on L_u^x/c in Fig. 15, providing confidence that the hypothesis proposed by Holdø et al. (1982) regarding the peak drag coefficient at turbulence intensities between 2% and 25%, can be confirmed for the peak lift coefficient with a larger range of freestream velocities or boundary layer thicknesses. The limited tunnel size would not allow major changes to the thickness of the simulated ABL, lower freestream velocities could not be tested due to increasing uncertainties in the force measurements, and higher freestream velocities could not be used due to instability of the spires and roughness elements.

3.2. Surface pressure distributions on stowed heliostat

Fig. 17 shows the contours of mean, RMS and peak pressure coefficients C_P calculated using Eq. (6) at each of the 24 pressure taps and linearly interpolated between the points on the stowed heliostat for SR2. Large magnitudes of C_P were concentrated in the frontal 10% of the plate behind the leading edge due to the break-up of large eddies at the leading edge. This can result in large lift forces close to the leading edge of the mirror, thus resulting in the maximum hinge moments that can potentially lead to failure with insufficient structural integrity and strength of the mirror and supporting structure. The high intensity area of peak C_P in Fig. 17(c) is concentrated on the central 0.5 m of the

Table 1
Peak wind load coefficients on stowed heliostats ($H/c = 0.5$) in wind tunnel experiments.

Turbulence intensity **I_u** (%)	Height in boundary layer **H/δ**	Peak lift coefficient **c_L**	Peak hinge moment coefficient **$c_{M_{Hy}}$**	Source
12.5	0.3	0.4	0.1	Current study (SR2)
18	0.15	0.9	0.2	Peterka et al. (1989)
13	0.15	0.46	0.13	Pfahl et al. (2015)

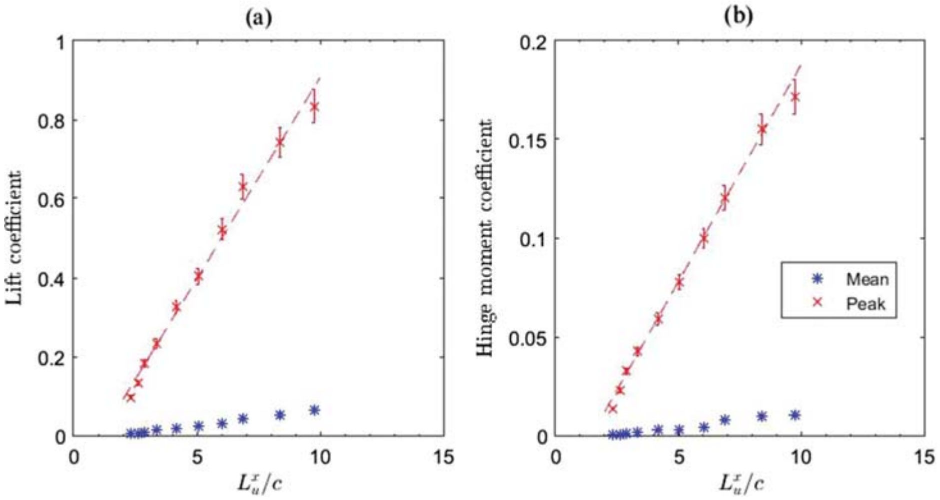

Fig. 15. Effect of length scale ratio L_u^x/c on the mean and peak wind load coefficients on a stowed heliostat with chord length c: (a) Lift coefficient; (b) Hinge moment coefficient.

leading edge that results in a peak lift coefficient of 0.26. This confirms the finding by Gong et al. (2013) that the leading edge of a stowed heliostat is most vulnerable to wind-induced mirror damage from the interaction with large vortices. This case is also important for serviceability considerations in the design of heliostats for multiple cycles of up-lift loading in the stow position.

Fig. 18(a) presents the time histories of measured differential pressure fluctuations about a zero-mean value at four points along the heliostat mirror surface from the leading edge to the trailing edge, as shown in Fig. 17(a). Table 2 shows that the largest amplitudes of pressure fluctuations in Fig. 18(a) occur at points A and D near the leading and trailing edges, respectively. The peak power spectrum of the pressure signals at point A is over 6 times the magnitude of the other three points, as shown in Fig. 18(b). The peak power spectra values occur at frequencies of 2.4 Hz near the leading edge are shifted to higher frequencies with downstream distance along the mirror surface to 21 Hz near the trailing edge. Fig. 18(c) presents the cross-correlations between two points in the along-wind direction (x) as a function of time lag τ between the instantaneous pressure signals. The pressure fluctuations are most highly correlated between points A and B with a peak normalised cross-correlation coefficient of 0.88 and the shortest phase delay of 0.018 s in Table 3. Although pressure fluctuations become less correlated further along the plate as the phase delay increases, the peak coefficient only decreases by 15% from A-B to A-D. This suggests the presence of a vortex-heliostat interaction near the leading edge of the mirror surface, as illustrated by the pressure coefficient contours in Fig. 17. Since the fluctuating pressures corresponded to low-frequency peaks on the power spectra and remain highly correlated across the along-wind length of the mirror, large-scale spanwise vortices can cause progressive failure initiating at the leading edge.

4. Discussion and conclusions

Calculations of peak wind load coefficients have established that the sizes of the vortices corresponding to the largest energies within the flow were at least double the heliostat mirror chord length in the current study. This study varied the length scale ratio L_u^x/c using smaller-sized heliostat mirrors modelled as thin flat plates. The break-up of the large vortices at the leading edge of the mirror results in a non-uniform pressure distribution $p(x)$ along the mirror surface. As L_u^x/c increased

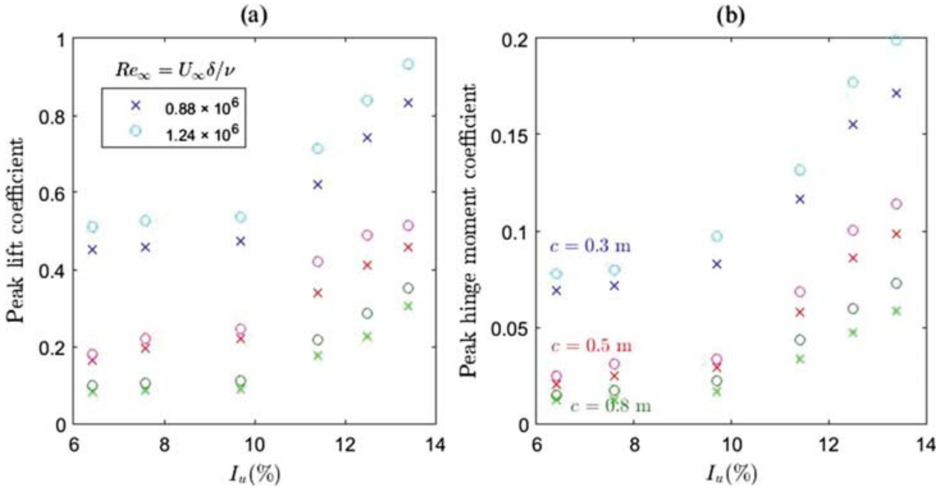

Fig. 16. Effect of freestream Reynolds number $Re_\infty = U_\infty\delta/\nu$ as a function of turbulence intensity I_u on: (a) Peak lift coefficient; (b) Peak hinge moment coefficient.

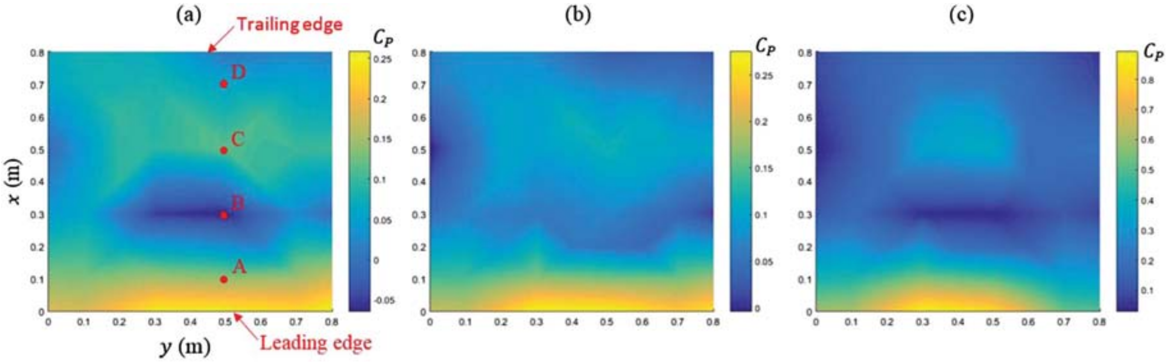

Fig. 17. Surface pressure coefficient C_P contours on the stowed heliostat for SR2: (a) Mean; (b) RMS; (c) Peak.

from 2.5 to 5, the peak wind loads increased linearly as the large suctions caused by the large-eddy break-up at the leading edge increase in magnitude. The most significant increase, resulting in a doubling of the peak lift and hinge moment coefficients, occurred for L_u^x/c between 5 and 10. Contours of wind pressure coefficients in Fig. 17 confirmed that large pressures at the leading edge need to be considered for critical failures of the heliostat in the stow position. The lower frequencies of the fluctuating pressure signals are of the order of 2 Hz close to the leading edge, which is within the range of the natural frequencies of 2–5 Hz measured on stowed heliostats by Gong et al. (2012). Hence, the leading edge is more likely to be exposed to resonance effects that can lead to excessive deflections and stresses that commonly result in structural failure.

Turbulence intensity and the sizes of the largest vortices were found to have a more pronounced effect on peak wind load coefficients than freestream parameters such as mean velocity and Reynolds number. Both peak lift and hinge moment coefficients were calculated to be at least ten times the size of their mean coefficients, confirming those found by Peterka et al. (1989) for a stowed heliostat. Peak wind load coefficients increased linearly and by approximately double in magnitude with an increase of I_u from 10% to 13% and as L_u^x/c increased from 5 to 10. Increasing freestream Reynolds number by 40% at constant turbulence intensity only resulted in maximum increases of 21% in peak lift coefficient and 25% in peak hinge moment coefficient. Hence, the integral length scales of the approaching eddies with the largest energies and their size relative to the heliostat chord length must be considered for the design of heliostats in the stow position so that they can withstand maximum wind loads during high-wind events.

Table 2
Characteristics of stowed heliostat surface pressure fluctuations.

Measurement point and coordinates (x, y)	Maximum amplitude P' (Pa)	Frequency of peak power spectra f (Hz)
A (0.1 m, 0.5 m)	39.1	2.4
B (0.3 m, 0.5 m)	11.1	2.5
C (0.5 m, 0.5 m)	16.6	6.8
D (0.7 m, 0.5 m)	18.4	21

Table 3
Cross-correlation statistics of stowed heliostat surface pressure fluctuations.

Two points for cross-correlation	Phase delay τ (s)	Peak normalised cross-correlation coefficient R_{p1p2}
A-B	0.018	0.88
A-C	0.034	0.82
A-D	0.071	0.75

Lowering the height at which the heliostat is stowed in the simulated ABL from H/δ of 0.5 to 0.3 was found to halve the hinge moment coefficient, despite there being a 10% increase in peak lift coefficient. Additionally, the lowest wind load coefficients were found when the elevation axis height of the heliostat was designed to be half that of the mirror chord length (H/c = 0.5). Although heliostats are commonly

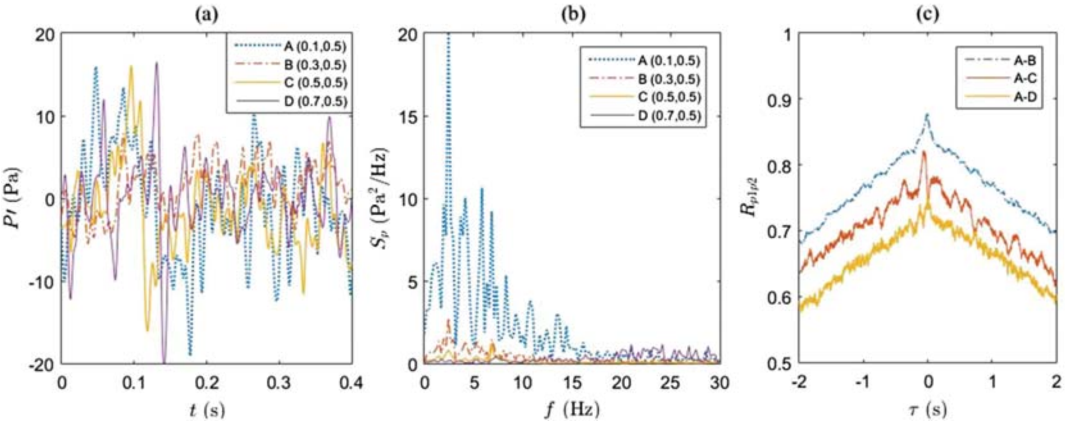

Fig. 18. (a) Time history of pressure fluctuations P' (Pa) between the upper and lower surfaces at four points along the stowed heliostat mirror surface; (b) Power spectra of pressure fluctuations S_p (Pa^2/Hz) at four points along the stowed heliostat mirror surface; (c) Normalised cross-correlation coefficients R_{p1p2} of pressure fluctuations between two points from the leading edge to the trailing edge of the mirror surface.

designed for a minimum H/c of 0.5, larger ratios of H/c are required for heliostats with a horizontal primary axis or for ground clearance if they are cleaned in the normal position. In the current study, reductions of up to 50% in c_L and 40% in $c_{M_{Hy}}$ were found by lowering H/c from 0.7 to 0.5 by manufacturing a heliostat without a horizontal primary axis. This provides the opportunity to lower the critical stow design wind loads for the mirror, drives and support structure, thus lowering the overall mass and strength of the heliostat with a shorter pylon length, and potentially offset the higher capital cost of the drives in a conventional heliostat. The peak lift and peak hinge moment coefficients of the smallest stowed heliostat in the current study were approximately a half and a third, respectively, of those reported by Pfahl et al. (2015) under similar turbulence conditions. These discrepancies may be explained by differences in integral length scales between these studies and the elevation axis height in the ABL ($H/\delta = 0.3$) in the current study that was double that in experiments by Peterka et al. (1989) and Pfahl et al. (2011). The chord length of the heliostat mirrors tested in this study was also found to have a significant influence on the mean and peak wind load coefficients. Reducing the chord length by half of its size resulted in the peak lift coefficient increasing from 0.3 to 0.57 and the peak hinge moment coefficient increasing from 0.05 to 0.09. Therefore, optimisation of the sizes of the mirror chord length and the elevation axis height for the characteristics of the turbulence approaching a stowed heliostat can significantly reduce design wind loads for high-wind events in the atmospheric surface layer. This optimisation can result in significant cost reductions for the manufacturing and installation of the wind-sensitive heliostat components.

Acknowledgements

Support for the work has been provided by the Australian Government Research Training Program Scholarship and by the Australian Solar Thermal Research Initiative (ASTRI) through funding provided by the Australian Renewable Energy Agency (ARENA). The authors would also like to acknowledge the constructive and insightful comments by the anonymous reviewers of the paper.

References

ASCE 7-02. Minimum Design Loads for Buildings and Other Structures. American Society of Civil Engineers, Reston, Virginia, USA.

Banks, D., 2011. Measuring peak wind loads on solar power assemblies. In: 13th International Conference on Wind Engineering, Amsterdam, Netherlands.

Cook, N.J., 1978. Determination of the model scale factor in wind-tunnel simulations of the adiabatic atmospheric boundary layer. J. Wind Eng. Ind. Aerodyn. 2, 311–321.

Cook, N.J., 1985. The designer's guide to wind loading of building structures, Part 1: Background, damage survey, wind data and structural classification. Building Research Establishment, Garston, UK.

Counihan, J., 1973. Simulation of an adiabatic urban boundary layer in a wind tunnel. Atmos. Environ. 7, 673–689.

Coventry, J., Pye, J., 2014. Heliostat cost reduction–where to now? Energy Procedia 49, 60–70.

De Bortoli, M., Natalini, B., Paluch, M., Natalini, M., 2002. Part-depth wind tunnel simulations of the atmospheric boundary layer. J. Wind Eng. Ind. Aerodyn. 90, 281–291.

Emes, M.J., Arjomandi, M., Kelso, R.M., Ghanadi, F., 2016. Integral length scales in a low-roughness atmospheric boundary layer. In: 18th Australasian Wind Engineering Society Workshop, Adelaide, Australia.

Emes, M.J., Arjomandi, M., Nathan, G.J., 2015. Effect of heliostat design wind speed on the levelised cost of electricity from concentrating solar thermal power tower plants. Sol. Energy 115, 441–451.

ESDU 85020, 1985. Characteristics of Atmospheric Turbulence near the Ground – Part II: Single Point Data for Strong Winds (Neutral Atmosphere). Engineering Sciences Data Unit, London, UK.

Farell, C., Iyengar, A.K., 1999. Experiments on the wind tunnel simulation of atmospheric boundary layers. J. Wind Eng. Ind. Aerodyn. 79, 11–35.

Flay, R.G.J., Stevenson, D.C., 1988. Integral length scales in strong winds below 20 m. J. Wind Eng. Ind. Aerodyn. 28, 21–30.

Gong, B., Li, Z., Wang, Z., Wang, Y., 2012. Wind-induced dynamic response of Heliostat. Renew. Energy 38, 206–213.

Gong, B., Wang, Z., Li, Z., Zang, C., Wu, Z., 2013. Fluctuating wind pressure characteristics of heliostats. Renew. Energy 50, 307–316.

Greenway, M.E., 1979. An analytical approach to wind velocity gust factors. J. Wind Eng. Ind. Aerodyn. 5, 61–91.

Hinkley, J.T., Hayward, J.A., Curtin, B., Wonhas, A., Boyd, R., Grima, C., Tadros, A., Hall, R., Naicker, K., 2013. An analysis of the costs and opportunities for concentrating solar power in Australia. Renew. Energy 57, 653–661.

Holdø, A.E., Houghton, E.L., Bhinder, F.S., 1982. Some effects due to variations in turbulence integral length scales on the pressure distribution on wind-tunnel models of low-rise buildings. J. Wind Eng. Ind. Aerodyn. 10, 103–115.

Holmes, J.D., Kwok, K.C.S., Ginger, J.D., 2012. Wind Loading Handbook for Australia and New Zealand: Background to AS/NZS 1170.2 Wind Actions. Australasian Wind Engineering Society, Sydney, Australia.

IRENA, 2013. Renewable Power Generation Costs in 2012: An Overview. IRENA, Bonn, Germany.

IRENA, 2015. The Power to Change: Solar and Wind Cost Reduction Potential to 2025. IRENA, Bonn, Germany.

Irwin, H., 1981. The design of spires for wind simulation. J. Wind Eng. Ind. Aerodyn. 7, 361–366.

Jain, A., Jones, N.P., Scanlan, R.H., 1996. Coupled flutter and buffeting analysis of long-span bridges. J. Struct. Eng. 122, 716–725.

Kaimal, J.C., Finnigan, J.J., 1994. Atmospheric Boundary Layer Flows: Their Structure and Measurement. Oxford University Press, New York, USA.

Kolb, G.J., Ho, C.K., Mancini, T.R., Gary, J.A., 2011. Power tower technology roadmap and cost reduction plan. In: SAND2011-2419. Sandia National Laboratories, Albuquerque, New Mexico, USA.

Kolb, G.J., Jones, S.A., Donnelly, M.W., Gorman, D., Thomas, R., Davenport, R., Lumia, R., 2007. Heliostat Cost Reduction Study. In: SAND2007-3293. Sandia National Laboratories, Albuquerque, USA.

Kristensen, L., Casanova, M., Courtney, M., Troen, I., 1991. In search of a gust definition. Bound.-Layer Meteorol. 55, 91–107.

Lovegrove, K., Stein, W., 2012. Concentrating Solar Power Technology: Principles, Developments and Applications. Woodhead Publishing Limited, Cambridge, UK.

Mendis, P., Ngo, T., Haritos, N., Hira, A., Samali, B., Cheung, J., 2007. Wind loading on tall buildings. EJSE Special Issue: Load. Struct. 3, 41–54.

Milbank, J., Loxton, B., Watkins, S., Melbourne, W., 2005. Replication of Atmospheric Conditions for the Purpose of Testing MAVs: MAV Flight Environment Project Final Report. Royal Melbourne Institute of Technology.

Nakamura, Y., 1993. Bluff-body aerodynamics and turbulence. J. Wind Eng. Ind. Aerodyn. 49, 65–78.

Peterka, J.A., Derickson, R.G., 1992. Wind load design methods for ground-based heliostats and parabolic dish collectors. In: SAND92-7009. Sandia National Laboratories, Albuquerque, USA.

Peterka, J.A., Tan, Z., Cermak, J.E., Bienkiewicz, B., 1989. Mean and peak wind loads on heliostats. J. Sol. Energy Eng. 111, 158–164.

Pfahl, A., Buselmeier, M., Zaschke, M., 2011. Wind loads on heliostats and photovoltaic trackers of various aspect ratios. Sol. Energy 85, 2185–2201.

Pfahl, A., Randt, M., Meier, F., Zaschke, M., Geurts, C., Buselmeier, M., 2015. A holistic approach for low cost heliostat fields. Energy Procedia 69, 178–187.

Plate, E.J., 1974. Aerodynamic Characteristics of Atmospheric Boundary Layers. US Atomic Energy Commission, Springfield, Virginia, USA.

Roadman, J.M., Mohseni, K., 2009. Gust characterization and generation for wind tunnel testing of micro aerial vehicles. AIAA Paper 1290 4166.

AS/NZS 1170.2. Structural Design Actions – Part 2: Wind actions. Standards Australia and Standards New Zealand, Sydney, Australia.

Swamy, N.V.C., Gowda, B.H.L., Lakshminath, V.R., 1979. Auto-correlation measurements and integral time scales in three-dimensional turbulent boundary layers. Appl. Sci. Res. 35, 237–249.

Téllez, F., Burisch, M., Villasente, Sánchez, M., Sansom, C., Kirby, P., Turner, P., Caliot, C., Ferriere, A., Bonanos, C.A., Papanicolas, C., Montenon, A., Monterreal, R., Fernández, J., 2014, State of the Art in Heliostats and Definition of Specifications. In: 609837, STAGE-STE Project, Madrid, Spain.

Watkins, S., 2012. Turbulence characteristics of the atmospheric boundary layer and possibilities of replication for aircraft. In: Third Symposium ‘Simulation of Wing and Nacelle Stall’, Braunschweig, Germany.

Chapter 6

Peak Wind Loads on Tandem Heliostats

6.1. Section Overview

This chapter reports an experimental investigation of the peak wind load coefficients on a second downstream heliostat in stow position relative to an isolated heliostat, discussed in Chapter 5, and their sensitivity to turbulence characteristics in the atmospheric surface layer to determine the optimal spacing between the heliostats and characteristic lengths of their pylons and mirrors. Maximum values of the normalised peak lift and peak hinge moments occurred at high turbulence intensities and were significantly dependent on the ratio of integral length scale to mirror chord length and the separation distance between the two heliostats. Wind load reductions of up to 40% on the second downstream heliostat occurred at low field densities, however peak wind loads were up to 12% larger than those on an isolated heliostat at high field densities. The results can be used to further optimise the size and thus cost of manufacturing heliostats with respect to the turbulence approaching the heliostat field at a given site.

6.2. Experimental Measurements in a Simulated ABL

Statement of Authorship

Title of Paper	Investigation of peak wind loads on tandem heliostats in stow position
Publication Status	☐ Published ☐ Accepted for Publication ☑ Submitted for Publication ☐ Unpublished and Unsubmitted work written in manuscript style
Publication Details	Emes, M.J., Ghanadi, F., Arjomandi, M. and Kelso, R.M., 2017, Investigation of peak wind loads on tandem heliostats in stow position, Renewable Energy.

Principal Author

Name of Principal Author (Candidate)	Matthew Emes		
Contribution to the Paper	Carried out wind tunnel experiments, performed data analysis and interpretation, wrote manuscript and acted as corresponding author.		
Overall percentage (%)	70		
Certification:	This paper reports on original research I conducted during the period of my Higher Degree by Research candidature and is not subject to any obligations or contractual agreements with a third party that would constrain its inclusion in this thesis. I am the primary author of this paper.		
Signature		Date	3/11/17

Co-Author Contributions

By signing the Statement of Authorship, each author certifies that:

i. the candidate's stated contribution to the publication is accurate (as detailed above);

ii. permission is granted for the candidate in include the publication in the thesis; and

iii. the sum of all co-author contributions is equal to 100% less the candidate's stated contribution.

Name of Co-Author	Farzin Ghanadi		
Contribution to the Paper	Supervised development of work, assisted in carrying out wind tunnel experiments, helped in data interpretation and manuscript evaluation.		
Signature		Date	03/11/2017

Name of Co-Author	Maziar Arjomandi		
Contribution to the Paper	Supervised development of work, helped in data interpretation and manuscript evaluation.		
Signature		Date	3/11/17

Name of Co-Author	Richard Kelso		
Contribution to the Paper	Supervised the research and contributed in academic discussion and manuscript review.		
Signature		Date	3/11/'17

Investigation of peak wind loads on tandem heliostats in stow position

Matthew J. Emes*, Farzin Ghanadi, Maziar Arjomandi and Richard M. Kelso

School of Mechanical Engineering, The University of Adelaide, SA 5005, Australia

Abstract

This paper investigates the effects of turbulence in the atmospheric boundary layer (ABL) on the peak wind loads on heliostats in stow position in isolation and in tandem configurations with respect to the critical scaling parameters of the heliostats. The heliostats were exposed to a part-depth ABL in a wind tunnel using two configurations of spires and roughness elements to generate a range of turbulence intensities and integral length scales. Force measurements on different-sized heliostat mirrors at a range of heights found that both peak lift and hinge moments were reduced by up to 30% on the second tandem heliostat when the spacing between the heliostat mirrors was close to the mirror chord length and converged to the isolated heliostat values when the spacing was greater than 5 times the chord length. Peak wind loads on the tandem heliostat increased to above those on an isolated heliostat for an integral-length-scale-to-chord-length ratio L_u^x/c of less than 5, whereas tandem loads were 30% lower than an isolated heliostat at L_u^x/c of 10. The reduced loads on the tandem heliostat corresponded to a shift to higher frequencies of the fluctuating pressure spectra, due to the break-up of large eddies by the upstream heliostat.

Keywords: Stowed heliostat; Wind load; Atmospheric boundary layer; Gap ratio

Nomenclature

A	Heliostat mirror area (m^2)
α	Power law roughness exponent
b	Spire base width (m)
c	Heliostat mirror chord length (m)
c_L	Peak lift coefficient
$c_{M_{Hy}}$	Peak hinge moment coefficient
c_P	Pressure coefficient
D	Spire base depth (m)
D_I	Peak drag force on an isolated heliostat in stow position (N)
D_T	Peak drag force on a second downstream heliostat in a tandem arrangement (N)
d	Separation distance between two tandem heliostat mirrors in stow position (m)
d/c	Longitudinal gap ratio for tandem heliostat mirrors in stow position
δ	ABL thickness (m)
f	Frequency of velocity/pressure fluctuations (Hz)
H	Elevation axis height of stowed heliostat mirror above the ground (m)
h	Spire height (m)
I_u	Turbulence intensity (%)
l_p	Distance to the centre of pressure in the flow direction (m)
L_u^x	Longitudinal integral length scale (m)
L_I	Peak lift force on an isolated heliostat in stow position (N)
L_T	Peak lift force on a second downstream heliostat in a tandem arrangement (N)
M_{HyI}	Peak hinge moment on an isolated heliostat in stow position (N·m)
M_{HyT}	Peak hinge moment on a second downstream heliostat in a tandem arrangement (N·m)
M_{yI}	Peak overturning moment on an isolated heliostat in stow position (N·m)
M_{yT}	Peak overturning moment on downstream heliostat in a tandem arrangement (N·m)
P_i^f	Pressure fluctuations on the upper surface of the stowed heliostat mirror (Pa)
P_i^b	Pressure fluctuations on the lower surface of the stowed heliostat mirror (Pa)
S_p	Power spectrum of pressure fluctuations (Pa^2/Hz)
S_u	Power spectrum of velocity fluctuations (m^2/s^3)
T_u^x	Longitudinal integral time scale (s)
U_∞	Freestream velocity (m/s)
$\bar{U}(z)$	Mean velocity profile (m/s)
u	Streamwise velocity fluctuations (m/s)
x	Longitudinal direction (m)
y	Spanwise direction (m)
z	Height above the ground (m)
z_0	Surface roughness height (m)

1. Introduction

The concentrating solar thermal (CST) power tower (PT) is one of the most promising renewable technologies for large-scale electricity production. Although the intermittency of solar irradiation is a practical limitation of CST systems, PT plants can be deployed with thermal energy storage or as a hybrid system with existing fossil fuel power plants for a base-line power supply (Hinkley et al., 2013). PT systems consist of a field of heliostat mirrors reflecting sunlight to the top of a beam-up or beam-down tower containing a receiver. Heliostats are arranged in rows on one side of an anti-polar facing cavity receiver in a polar field or surrounding a cylindrical receiver in a surround field. The main limitation of PT systems is their significantly larger levelised cost of electricity (LCOE). The LCOE of a conventional molten-salt receiver PT plant was estimated by NREL (Mehos et al., 2016) to be 0.14 USD/kWh in 2015, but this could be further reduced to 0.1 USD/kWh with near-term advanced heliostats at \$97/m^2 in a 2017 tower configuration (Mehos et al., 2017). In comparison, base-load energy systems, such as fossil fuel power plants, have an LCOE in the range of 0.06-0.13 USD/kWh in 2011 (IRENA, 2013). To reduce the LCOE of PT systems there is a need to lower the capital cost of a PT plant, of which the largest cost is the heliostat field, with an estimated contribution of between 40% and 50% (Coventry and Pye, 2014; Hinkley et al., 2013; IRENA, 2015; Kolb et al., 2007). During operation heliostat mirrors are inclined with respect to the horizontal and are exposed to large drag forces and overturning moments that are directly proportional to the wind speed with a large projected frontal area to the wind (Yu et al., 2016). Heliostats are aligned parallel to the ground in the stow position during periods of high wind speeds to minimise the frontal area and thus the drag forces, as shown for a tandem arrangement in Fig. 1. A cost analysis of quasi-static wind loads by Emes et al. (2015) found that the heliostat cost of a PT plant in Alice Springs (central Australia) was reduced by 18% by lowering the design wind speed for stowing the heliostats from 22 m/s to 13 m/s for only a 2% reduction in capacity factor of the heliostat field. While the operating wind load can be reduced by changing the stow wind speed, the survival wind speed that a heliostat is designed to withstand in the stow position cannot be varied based on the maximum site wind speed. Hence, there is a significant potential to minimise the capital cost and LCOE of a PT plant through optimisation of the structural design of heliostats in the stow position. This paper investigates the sensitivity of peak wind loads on a heliostat in stow position (Fig. 1) to: (1) the chord length (c) and elevation axis height (H) of a single heliostat mirror and spacing (d) between two heliostat mirrors in a tandem arrangement; (2) the turbulence characteristics in the ABL.

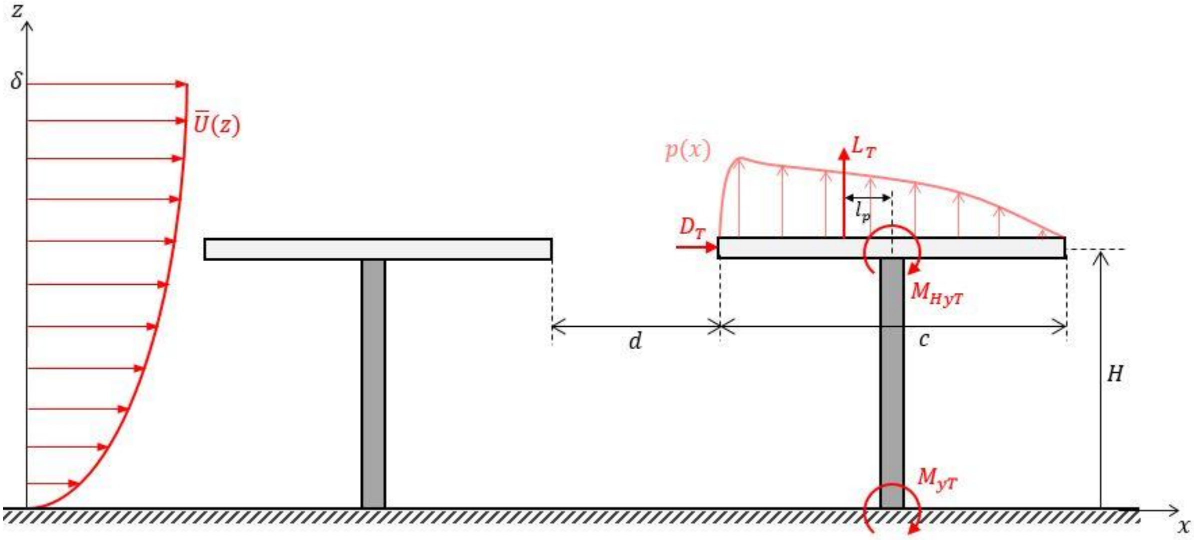

Fig. 1. Peak wind loads due to a non-uniform pressure distribution p on a second stowed heliostat in a tandem arrangement with identical mirrors of chord length c and elevation axis height H separated by a gap distance d and exposed to a logarithmic mean velocity profile $\overline{U}(z)$ in the ABL.

Static wind loads on isolated heliostats in operating and stow positions have previously been calculated using mean and peak wind load coefficients derived from experimental data in systematic wind-tunnel studies. Peterka et al. (1989) found that the peak lift and hinge moment coefficients on a 1:40 scale heliostat modelled as a thin flat plate were approximately 10 times their mean values in stow position at a longitudinal turbulence intensity I_u, defined by the ratio of the root-mean-square of fluctuating velocity to the mean velocity, of 18% commonly observed in the open country terrain surrounding heliostat fields (Peterka and Derickson, 1992). This indicates the significance of gust and amplification effects on survival high-wind conditions for heliostats in stow position. Peterka et al. (1989) and Pfahl et al. (2011a) showed that peak wind load coefficients increase significantly at I_u above 10%. Analysis of peak wind loads obtained from wind tunnel experiments has previously yielded the most realistic results by matching turbulence intensities (Pfahl et al., 2015), however the sizes of the relevant eddies also significantly affect the peak wind loads on heliostats. Emes et al. (2017) found that the peak lift coefficient and peak hinge moment coefficient on an isolated heliostat in stow position increased linearly and approximately doubled when the ratio of the longitudinal integral length scale to the mirror chord length L_u^x/c increased from 5 to 10 at a constant turbulence intensity. Previous experimental studies have focused on the effects of the temporal characteristics of ABL turbulence on isolated heliostats in stow position, but further knowledge of the relationships between the temporal and spatial characteristics of ABL turbulence and the peak wind loads on isolated and tandem heliostats is required. Hence, the first objective of this study is to improve the understanding of the peak wind loads on an isolated heliostat in stow position and two stowed heliostats in tandem. The sensitivity of the peak wind loads on a second downstream heliostat in a tandem arrangement, relative to an isolated heliostat, to L_u^x/c is investigated to determine the effect of the critical scaling parameters of the upstream heliostat on the sizes of the turbulent eddies in the ABL that reach the second downstream heliostat.

The design and layout of heliostat fields have previously been optimised with respect to the optical efficiency of heliostats in operational positions, however static wind loads have also been found to be highly dependent on the spacing between heliostats relative to mirror chord length, defined by the longitudinal gap ratio d/c and the heliostat field density, defined by the ratio of mirror area to land area. Peterka et al. (1987) measured mean and peak wind loads on 1:60 scale-models of a tandem arrangement of five consecutive heliostats in rows of a high-density region of the Barstow heliostat field. In addition, Pfahl et al. (2011b) measured peak wind loads on 1:20 scale-models of a tandem arrangement of four consecutive heliostats, each of 30 m^2 mirror area, in operating and stow positions for field densities of 10% and 50%, corresponding to gap ratios (d/c) between the mirrors of 5.5 and 1.5, respectively. Peterka et al. (1987) and Pfahl et al. (2011b) reported reductions of up to 50% in peak drag and lift forces on a second operating heliostat relative to the first heliostat at high field densities of 50% ($d/c \approx$ 1.5). In comparison, Pfahl et al. (2011b) found that the peak lift forces and hinge moments on a second heliostat were 20% and 60% lower, respectively, relative to the first heliostat in tandem at high field density ($d/c \approx$ 1.5). However, a smaller reduction of 20% in peak hinge moment and a 30% increase in peak lift force relative to the first heliostat was measured on the second heliostat at a low field density of 10% ($d/c \approx$ 5.5). In the case of two square prisms in tandem, Sakamoto et al. (1987) found that the lift coefficient on the downstream prism was larger than an identical upstream prism at smaller gap ratios ($d/c < 3$), however the lift coefficient on the downstream prism became smaller than the upstream prism above the critical gap ratio $d/c = 3$ due to suppression of the fluctuating pressures from reattachment of the separated shear layer. The effect of the downstream prism became negligible at $d/c \geq 6$, so that the fluctuating lift coefficient on the upstream prism was equal to that on an isolated prism exposed to a uniform flow with $I_u = 0.19\%$ (Alam et al., 2002). Coustols et al. (1989) investigated the use of single and tandem thin flat plates as a wake manipulator of a turbulent boundary layer with freestream velocity $U_\infty = 24$ m/s, boundary layer thickness $\delta = 17$ mm and Reynolds number based on the momentum thickness $Re_\theta = 2400$. In the wake of a single flat plate with chord length $c/\delta = 0.75$ thickness $t/\delta = 0.007$ at a height $H/\delta = 0.35$ above the surface of the flat plate, I_u showed a maximum decrease from 6.5% (without the plate) to 4.5% at a distance $x = 5.3\delta = 1.9H$ downstream of the trailing edge of the plate. In addition, power spectra of the streamwise velocity fluctuations showed an excess of energy at high frequencies due to the production of new energetic small-scale eddies and a deficit of energy at low frequencies leading to the damping of large-scale structures (Coustols et al., 1989). In the case of two thin flat plates in a tandem configuration, Coustols et al. (1989) found that the skin friction coefficient c_f at $x = 52\delta$ was reduced by a maximum of 15% for a tandem spacing d/δ of 10 or a gap ratio d/c of 12, compared with a 8.4% reduction for a single plate. Previous wind tunnel experiments (Peterka et al., 1987; Pfahl et al., 2011b) on tandem heliostats have focused on operating positions, such as in the normal position, with a limited analysis of the stow position. These experimental studies investigated the wind loads on normal heliostats in several rows of a field at different field densities, however there is limited knowledge on the relationship between the longitudinal gap ratio and the peak wind loads on tandem stowed heliostats in the rows of a field. Hence, the second objective of this study is to investigate the effect of gap ratio on the aerodynamic loads on two tandemly-arranged thin flat plates aligned parallel to the ground and exposed to turbulence intensities above 10%, representing heliostats in stow position in the ABL.

Another objective of this paper will focus on is the dynamic wind loads on stowed heliostats due to interaction with atmospheric instabilities. Knowledge of the aerodynamic loads on heliostats during high-wind events such as gusts is critical for their design to maintain structural integrity in stow position.

This knowledge requires an understanding of the turbulent effects of the neutrally stratified wind over flat, uniform terrain in the ABL. Oscillatory instabilities such as galloping and flutter, arising from one or more vibrational modes at a critical wind velocity can lead to structural failure from excessive deflections and stresses (Jain et al., 1996; Mendis et al., 2007). Nakamura (1993) found that galloping and torsional flutter tend to occur on short rectangular cylinders of height D ($Re_{\infty} = \overline{U}D/\nu$ from 0.14 to 30 × 10^4) at frequencies of the order of 1 Hz when the turbulence length scales are comparable to the size of the body ($L_u^x/D \approx 1$). This has particular significance for heliostats with natural frequencies of the order of 1 Hz (Gong et al., 2012; Griffith et al., 2015) when stowed at heights below 10 m in the atmospheric surface layer. Gong et al. (2013) found that large negative peak wind pressure coefficients occurred at the leading edge of the heliostat mirror surface in stow position, suggesting that this region is the most vulnerable to wind-induced mirror damage. Measurements by Sment and Ho (2014) of the turbulence intensity between six consecutive rows of a heliostat field found that the turbulence intensity increased to over 50% between the third and fifth rows by factors of 3 and 6 for elevation angles of 90° and 45°, respectively. In the stow position however, turbulence intensities ahead of heliostats in downstream rows remained below a maximum of 20% approaching the first row at the outer boundary of the field (Sment and Ho, 2014). Previous experimental studies on tandem heliostats in the rows of a field have investigated the mean wind loads on stowed heliostats in tandem arrangements representing the rows of a heliostat field. However, the presence and cause of these unsteady loads due to non-uniform distributions of fluctuating pressures on the mirror surface requires further investigation. A longitudinal plate installed parallel to the flow can be used as a large-eddy break-up device (LEBU) with a 13% reduction of both the friction velocity and the root-mean-square wall pressure fluctuation in the turbulent boundary layer along a flat plate (Beeler, 1986). Chin et al. (2015) confirmed that a LEBU attenuated the energies of the largest eddies and shifted the energy to moderate length scales at higher frequencies. Therefore, the third objective of this paper is to investigate the dynamic wind loads and the peak spectral energies arising from differences in fluctuating pressures and the dominant sizes and frequencies of eddies interacting with the surface of an isolated heliostat in stow position and a second downstream mirror in a tandem configuration. Pressure distributions over the surface of the second downstream heliostat are used to compare peak spectral energies and frequencies with an isolated heliostat, particularly at the leading edge of the mirror, due to the interaction with large vortices that can lead to critical failures.

The overall aim of this paper is to investigate the static and dynamic wind loads on an isolated heliostat and on a second downstream heliostat in a tandem arrangement relative to the isolated heliostat. The results will be used to further understand the effects of vortex shedding and flow penetration between the heliostat mirror and the ground. Further, the derived relationships can be used to optimise the spacing between heliostats at different field densities and the chord length and elevation axis height of the stowed heliostat mirror, based on known characteristics of the approaching turbulence in a given ABL.

2. Experimental Method

Experimental measurements were taken in a closed-return wind tunnel at the University of Adelaide. The test section of the tunnel has a cross-section of 3 m × 3 m. The tunnel walls diverge to allow for a pressure gradient resulting from the growth of the wall boundary layers. The tunnel can be operated at speeds of up to 20 m/s with a moderate level of turbulence intensity, ranging between 1% and 3%. The unperturbed boundary layer formed in smooth flow is 0.2 m thick at the location of the turntable, 15 m from the start of the working section. Accurate representation of a part-depth ABL in the wind tunnel is required to replicate similar turbulence properties that heliostats are exposed to in the lower surface layer of the ABL. The mean velocity profile can be accurately modelled by the power law and log law to a theoretical maximum gradient or freestream velocity U_∞ at the boundary layer thickness δ (Kaimal and Finnigan, 1994), however Banks (2011) noted that replication of the turbulent power spectra in boundary layer wind tunnels cannot be achieved due to discrepancies in scaling between heliostat models (typically 1:10 to 1:50) and the turbulent eddy length scales (typically 1:100 to 1:300). It is generally accepted that the most effective wind tunnel simulation of the velocity and turbulence intensity profiles in the ABL is obtained when a flow passes over a rough surface producing a natural-growth boundary layer (Cook, 1978; De Bortoli et al., 2002; Reinhold et al., 1978; Sarkar, 2013). The most commonly-used passive devices include spires to generate turbulent mixing through separation of flow around their edges, fence barriers to increase the height of the boundary layer and floor roughness to develop the velocity deficit near the ground (Cook, 1978; Counihan, 1973). In the present study, spires and roughness elements, shown in Fig. 2 and Fig. 3, were used to generate a power law mean velocity profile of the form:

$$\bar{U}(z) = U_\infty \left(\frac{z}{\delta}\right)^\alpha, \tag{1}$$

where U_∞ (m/s) is the freestream velocity, δ is the boundary layer thickness and α is the power law exponent. Fig. 2 shows the flow configuration in the wind tunnel using spires and roughness elements to generate a power law velocity profile of the lower ABL with thickness δ. Roughness blocks and two different spire geometries, with dimensions shown in Table 1, were found to generate a range of turbulence intensities I_u and integral length scales L_u^x. The spires were separated in the spanwise direction (y) by a distance of 650 mm at their centrelines, and were followed by a 10 m fetch of roughness elements. Dimensions of the two different triangular spires, hereafter referred to as SR1 and SR2, were derived following a theoretical design method outlined by Irwin (1981) such that the height h, base width b and depth D of the spire could be determined based on the desired power law profile with exponent α of 0.2 and a boundary layer thickness δ of 1 m (chosen due to the wind tunnel limit of 1.2 m). This gives a ratio of boundary layer thickness to wind tunnel height of 0.33, for which Irwin (1981) showed that the experimental boundary layer velocity profile based on the spire dimensions ratio b/h can be generated to within 3% of a power law velocity profile. Lateral homogeneity of the boundary layer was found to occur after a minimum streamwise distance of 6 spire heights ($6h$) downstream of the spires, whereas the effect of the roughness elements on the velocity deficit of the boundary layer becomes smaller with increasing downstream distance. The mounting point of the upstream stowed heliostat (H1 in Fig. 2) is greater than $7h$ downstream for the two spires in the current study, hence the 10 m length of roughness elements is expected to be sufficient for lateral flow homogeneity to be achieved within a maximum error of ±5% (shown by error bars in Fig. 4).

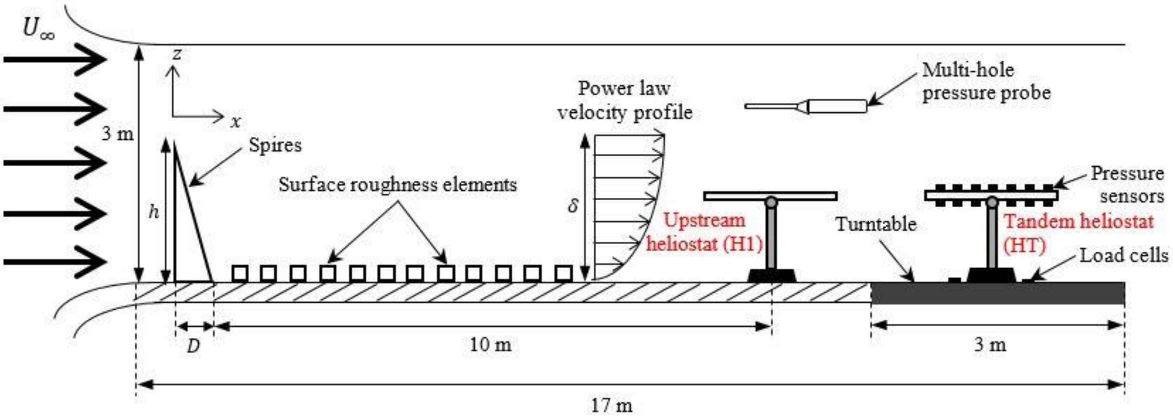

Fig. 2. Schematic diagram showing the flow configuration and dimensions of the wind engineering test section in the closed-return wind tunnel containing spires and roughness elements.

Table 1. Dimensions and characteristics of spire and roughness configurations

Configuration	Spire height $\boldsymbol{h}$ (m)	Spire base width $\boldsymbol{b}$ (m)	Spire depth $\boldsymbol{D}$ (m)	Roughness width $\boldsymbol{R_b}$ (m)	Roughness height $\boldsymbol{R_h}$ (m)
SR1	1.3	0.155	0.34	0.09	0.045
SR2	1.4	0.2	0.74	0.09	0.045

Three components of velocity were measured using a multi-hole pressure probe at a sampling frequency of 1 kHz with an oversampling ratio of 5 to satisfy the Nyquist criterion and prevent aliasing. Data were taken at a freestream velocity U_∞ of 11 m/s, corresponding to a freestream Reynolds number $Re_\infty = U_\infty \delta / \nu$ of 8.8×10^5, based on a boundary layer thickness δ of 1.2 m. The forces and pressures at these velocities fill the measurement span of the devices so that errors remain small.

Force measurements on the instrumented model heliostat (H2 in Fig. 2) were taken using four three-axis load cells mounted on a rotary turntable, as shown in Fig. 3(b). Each load cell has a capacity of 500 N with a sampling frequency of 1 kHz in all three axes and an accuracy of ±0.5% of full scale. Pressure measurements were taken on the upper and lower surfaces of a hollow aluminium heliostat facet containing 24 high-frequency differential pressure sensors. Each sensor has a pressure range of ± 1 psi (6.9 kPa) with an accuracy of ±0.2% of full scale. The layout of the pressure taps on the surface of the instrumented heliostat is indicated in Fig. 3(a). Differential pressures at each of the 24 tap locations on the mirror surface ($c = 0.8$ m) were acquired simultaneously for 1 minute at model scale (10 minutes equivalent full scale) at a sampling frequency of 1 kHz for consistency with velocity and force data. To ensure simultaneous measurement and synchronisation of pressure signals at all of the locations on the stowed heliostat, individual channels were connected into two slots of a data acquisition chassis and a trigger was implemented using LabVIEW software to start sampling all of the signals at the same time.

The heliostat mirror was simply modelled as a thin flat plate in the absence of a support structure, since Gong et al. (2013) showed that the shielding effect of the support structure had a less significant effect on the fluctuating wind pressures on a stowed heliostat exposed to parallel flow ($\beta = 0°$) than standard operating positions and for wind angles β between 90° and 180°. The longitudinal effects on the peak heliostat wind loads at $\beta = 0°$ were investigated in the current study, as they presumably lead to the maximum surface pressures near the leading edge of a stowed heliostat (Gong et al., 2013). A series of tests was performed on an isolated heliostat in stow position (HI) and on a second tandem heliostat (HT) downstream of an identical heliostat (H1) to ensure a reasonable comparison of peak wind loads. For each test, the heliostats were exposed to the simulated ABL using SR1 and SR2 to produce a wider range of turbulence intensities and integral length scales arising from different velocity profiles. The height of the pylon in each test was adjustable by using a telescopic design to allow elevation axis heights H between 0.39 m and 0.6 m, corresponding to non-dimensional heights in the ABL (H/δ) between 0.3 and 0.5. Wind loads were measured on HT of the tandem configuration with an identical heliostat H1 of mirror chord length c positioned upstream by a distance d in the flow direction, as shown in Fig. 1 and Fig. 3(b). Forces were measured on a series of seven square aluminium plates with 3 mm thickness and chord length c ranging from 200 mm to 800 mm in 100 mm increments. Different sizes of heliostat mirrors were used to vary the length-scale-to-chord-length ratio ($5 \leq L_u^x/c \leq 10$), the height-to-chord ratio ($0.5 \leq H/c \leq 1$) of both identical mirrors and the gap ratio ($0.1 \leq d/c \leq 5$) between the two heliostat mirrors. Table 2 outlines the values of these parameters for each of the test configurations of the stowed heliostat force measurements. Test configuration 1 investigates the effect of d/c at a constant height H/δ in the ABL and hence, constant turbulence intensity I_u and integral length scale L_u^x of the approaching flow. Test configuration 2 investigates the effect of I_u at different heights in the ABL for constant L_u^x/c, H/c and d/c. Test configuration 3 investigates the effect of L_u^x/c for different chord lengths at a constant height H/δ in the ABL for constant I_u and d/c. Pressures were measured on the surface of HI, shown in Fig. 3(a), and on the surface of HT with a heliostat H1 of the same size (c = 0.8 m) positioned upstream (Fig. 3(b)) at $d/c \approx 1$ for a tandem arrangement representing a high-density region of a heliostat field.

Table 2. Test configurations for stowed heliostat measurements

Test configuration	Spire and roughness configuration	Elevation axis height to ABL thickness $\boldsymbol{H/\delta}$	Turbulence intensity $\boldsymbol{I_u}$ (%)	Integral length scale to chord length ratio $\boldsymbol{L_u^x/c}$	Elevation axis height to chord length ratio $\boldsymbol{H/c}$	Longitudinal gap ratio $\boldsymbol{d/c}$
$1-\boldsymbol{d/c}$	SR1	0.3	8	6	0.5-1	0.1-5
	SR2	0.3	12	6	0.5-1	0.1-5
$2-\boldsymbol{I_u}$	SR1	0.3-0.5	6-9	6	1	3
	SR2	0.3-0.5	10-13	6	1	3
$3-\boldsymbol{L_u^x/c}$	SR1	0.5	8	5-7	1	3
	SR2	0.5	12	8-10	1	3

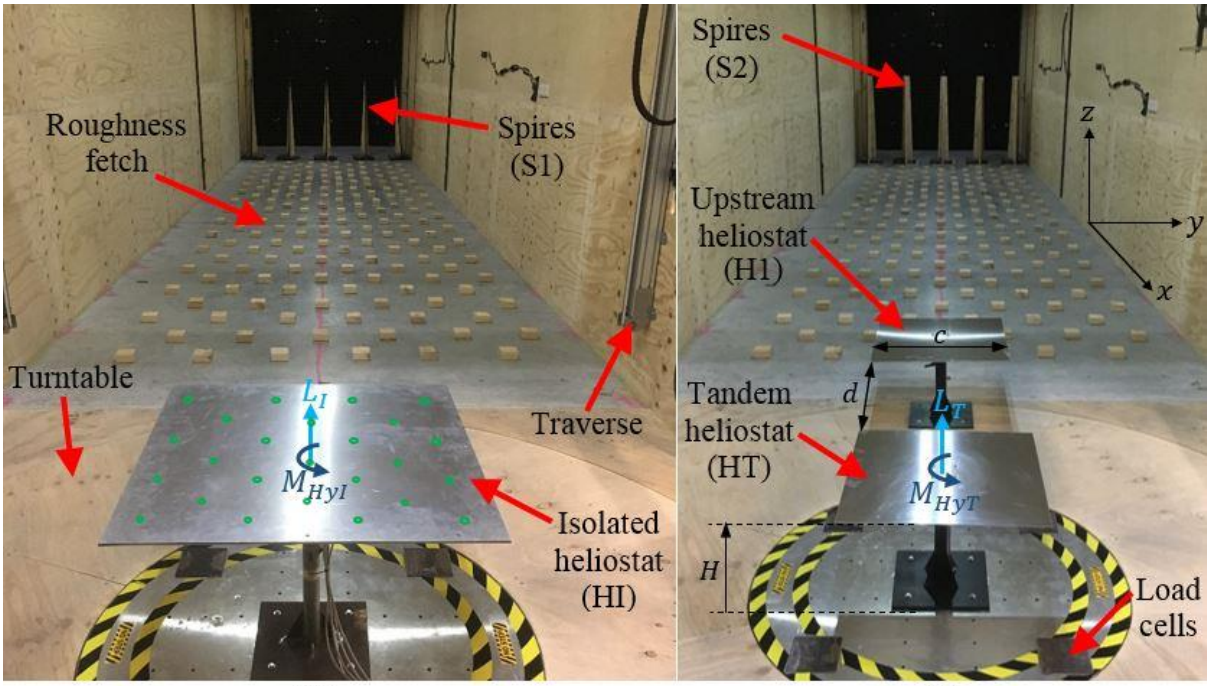

(a) (b)

Fig. 3. Experimental setup showing the two stowed heliostat configurations:
(a) Isolated heliostat in stow position (HI) with instrumented pressure sensors at the indicated tap locations, lift force L_I and hinge moment M_{HyI} exposed to the ABL generated by SR1;
(b) Tandem configuration of two identical heliostats in stow position with chord length c and elevation axis height H and their mirrors separated by a distance d. The heliostats are exposed to the ABL generated by SR2 and the lift force L_T and hinge moment M_{HyT} on the second tandem heliostat are measured using the load cells.

3. Simulated Atmospheric Boundary Layer

Fig. 4 presents the mean velocity and turbulence intensity profiles as a function of non-dimensional height z/δ at three spanwise locations in the ABL generated by SR1 with a freestream velocity U_∞ of 11 m/s, boundary layer thickness of δ of 1.2 m and Reynolds number Re_∞ of 8.8×10^5. Velocity profiles at the tunnel centreline ($y = 0$ m) in Fig. 4(a) show lateral homogeneity within an error of ±5% of the values at the outer boundaries of a 1 m × 1 m grid ($y = –0.5$ m and 0.5 m) at the position of the heliostat. This is considered to show sufficient lateral homogeneity for using centreline profiles for the calculation of turbulence parameters and wind loads. The heliostat had a ratio of elevation axis height to boundary layer thickness H/δ between 0.3 and 0.5, as shown by the shaded area in Fig. 4. Mean velocity profiles at this range of heights are well approximated by the power law curve $\overline{U}(z) = 11(z/1.2)^{0.12}$ to represent a low-roughness atmospheric surface layer. The power law curve can be shown to correspond to a logarithmic mean velocity profile with roughness height z_0 of 1 mm within a maximum 1% error. Turbulence intensities at the two outer lateral boundaries ($y = –0.5$ m and 0.5 m) in Fig. 4(b) are within 1% and 2% of the centreline values, respectively. Hence, the turbulence intensities are homogeneous in the spanwise direction in the area surrounding the heliostat mirror. Mean velocity and turbulence intensity profiles of SR2 were also found to be homogeneous.

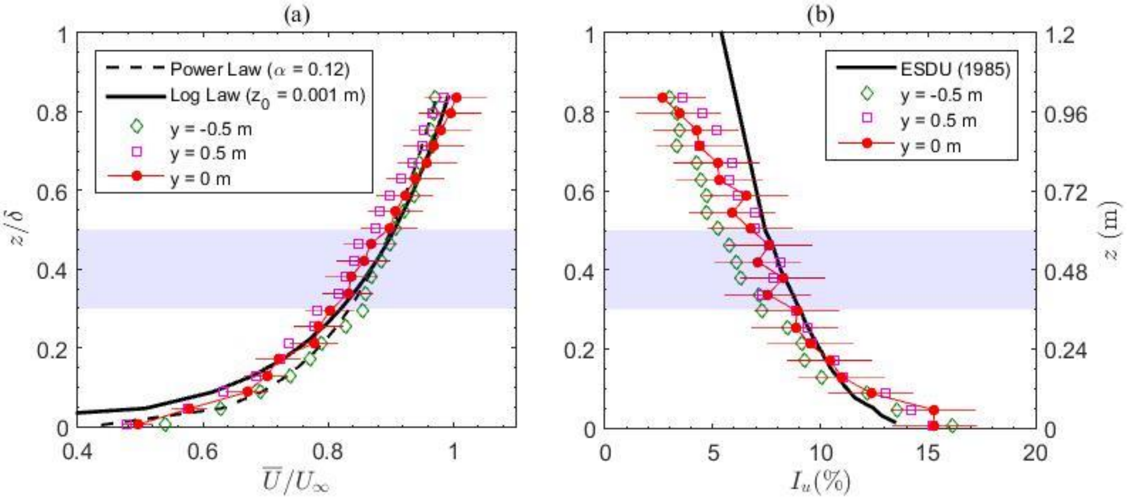

Fig. 4. Turbulence profiles at three spanwise y locations in the lower ABL generated using spire and roughness configuration SR1: (a) Mean velocity profiles normalised with respect to the freestream velocity U_∞ and compared with power law ($\alpha = 0.12$) and log law ($z_0 = 0.001$ m) profiles. Error bars indicate a maximum ±5% error in the centreline mean velocities; (b) Turbulence intensity I_u profiles compared with ESDU 85020 (1985) for $U_{10r} = 10$ m/s, $z_0 = 0.001$ m and assumed model scale of 1:150. Error bars indicate a ±2% error in the centreline I_u values. The shaded area shows the range of heights that the heliostat mirrors were positioned for force and pressure measurements.

Fig. 5 shows the mean velocity ($\overline{U}/U_\infty$) and turbulence intensity (I_u) profiles as a function of non-dimensional height z/δ behind the two different spire configurations with roughness elements. Fig. 5(a) shows that SR1 produces a mean velocity profile with a maximum error of ±5% with respect to the power law and log law profiles and within ±2% of I_u of ESDU 85020 (1985) data for a neutral ABL for $U_{10r} = 10$ m/s, $z_0 = 0.001$ m and $\delta = 350$ m. In contrast, the mean velocity profile produced by SR2 is closely linear in the part-depth simulated ABL and the turbulence intensity profile of SR2 is well approximated by the Engineering Sciences Data Unit (1985) profile for $z_0 = 0.015$ m and an assumed model scale of 1:150 at the range of elevation axis heights ($0.3 < z/\delta < 0.5$) of the stowed heliostat mirror shown by the shaded area in Fig. 5(b). Hence, the effects of two flow types could be generated to investigate the sensitivity of the peak wind loads on the heliostat mirror to the turbulence characteristics at different heights: (1) a power law velocity profile in a canonical turbulent boundary layer flow at moderate turbulence intensities (5% $< I_u <$ 10%) using SR1; (2) a wake flow with a linear velocity profile at larger uniform turbulence intensities ($I_u >$ 10%) using SR2.

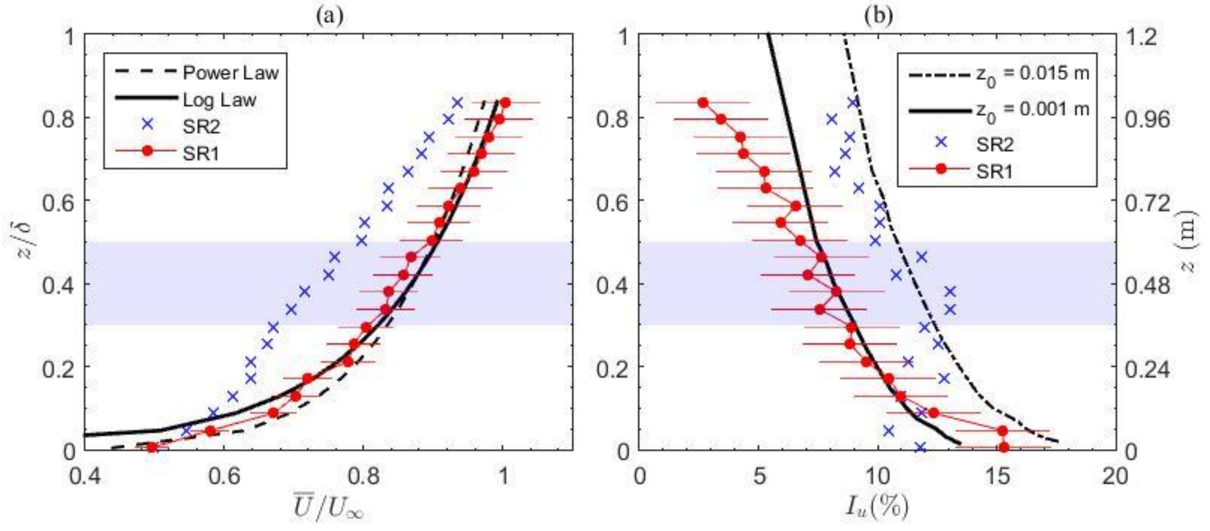

Fig. 5. Centreline profiles using two spire and roughness configurations:
(a) Mean velocity profiles normalised with respect to the freestream velocity U_∞ and compared with power law ($\alpha = 0.15$) and log law ($z_0 = 0.015$ m) profiles. Error bars on SR1 indicate a maximum ±5% error of the SR1 velocity profile; (b) Turbulence intensity I_u profiles of SR1 and SR2 compared with ESDU 85020 (1985) profiles of roughness height z_0, $U_{10r} = 10$ m/s, and $\delta = 350$ m. Error bars on SR1 indicate a maximum error of ±2% error of I_u. The shaded area shows the range of heights that the heliostat mirrors were positioned for force and pressure measurements.

The integral length scales, representing the sizes of the largest eddies that correspond to the largest magnitudes of the power spectra at a given height z in the ABL (Milbank et al., 2005; Watkins, 2012), are calculated following Taylor's hypothesis that eddies embedded in a frozen turbulence field are convected downstream at the mean wind speed $\overline{U}$ (m/s) in the streamwise x direction, and hence do not evolve with time (Kaimal and Finnigan, 1994; Milbank et al., 2005). Point velocity measurements in the current study, obtained as a function of time, are transformed to spatially-distributed data to calculate the longitudinal integral length scale following the correlation method (Flay and Stevenson, 1988; Milbank et al., 2005) as:

$$L_u^x(z) = T_u^x(z)\overline{U}(z), \tag{2}$$

where T_u^x (s) is the integral time scale representing the time taken for the largest eddies to traverse a single point in the ABL. The integral time scale is calculated using Equation (3) by the integral of the autocorrelation function in Equation (4) up to its first-zero crossing τ_0, assuming that $R(\tau)$ fluctuates close to zero after this point (Swamy et al., 1979):

$$T_u^x = \int_0^\infty R(\tau)\, d\tau \approx \int_0^{\tau_0} R(\tau)\, d\tau, \tag{3}$$

$$R(\tau) = \frac{\overline{u'(t)u'(t+\tau)}}{{\sigma_u}^2}, \tag{4}$$

where $u' = u - \overline{U}$ defines the fluctuating component of streamwise velocity and ${\sigma_u}^2$ is the variance of the streamwise velocity fluctuations.

Fig. 6(a) presents the longitudinal integral length scales L_u^x, calculated using Equations (2-4) following the correlation method, as a function of non-dimensional height in the ABL ($\delta = 1.2$ m) for SR1 and SR2 to approximate the sizes of the largest vortices approaching the stowed heliostat. The values of L_u^x show considerable scatter at all heights and are approximately double those measured by Farell and Iyengar (1999) at the same height ($z = 0.6$ m) in an ABL with the same thickness, as shown by the filled data points in Fig. 6(a). At the shaded range of heights ($0.3 < z/\delta < 0.5$) where the stowed heliostat mirror is positioned, L_u^x varies from 1.6 m to 2 m for SR1 and from 1.9 m to 2.5 m for SR2. This indicates that the largest vortices approaching the stowed heliostat using SR2 were on average 21% larger and as much as double the size of those produced using SR1 in the current study. The divergence between the L_u^x results can be explained by differences in mean velocity profiles produced by the surface roughness height of the simulated ABL. Farell and Iyengar (1999) generated an urban terrain power law velocity profile with exponent α of 0.28 using a packing density of 7.84% for the roughness elements, generating larger velocity gradients and smaller L_u^x at lower heights in the simulated ABL than the open country terrain power law velocity profile ($\alpha = 0.18$) produced by SR1, which had a roughness packing density of 5% in the current study. In addition, the different techniques used for calculating integral length scales in semi-empirical models, use spectral-fit methods that have large uncertainties associated with the location of the peaks of the measured spectra at low frequencies (Farell and Iyengar, 1999; Flay and Stevenson, 1988). In the current study therefore, L_u^x was estimated using the correlation method because of clearly-defined limits of integration, as well as consistent fluctuation of R_u about zero after τ_0, and relatively smaller errors compared to the spectral-fit technique.

Calculated values of L_u^x for SR1 and SR2 were compared in Fig. 6(a) with the predicted L_u^x by the Engineering Sciences Data Unit (ESDU) 85020 model for a full-scale ABL with $z_0 = 0.015$ m. The predicted L_u^x by ESDU 85020 over-estimated L_u^x by 40% for SR1 and by 17% for SR2 on average over the range of heights ($0.3 < z/\delta < 0.5$). Overall, the values of L_u^x calculated for SR1 and SR2 are below the stated ±8% error of the ESDU 85020 correlations, however this is expected because of the limitation of producing the largest length scales of the ABL in a wind tunnel. Hence, the values of L_u^x for SR1 and SR2 are considered reasonable for wind-load analysis within the highlighted range of heights of the stowed heliostat.

Fig. 6(b) compares the non-dimensional power spectra in the longitudinal direction fS_u/σ_u^2 as a function of non-dimensional frequency $fL_u^x/\overline{U}$, at a non-dimensional height $z/\delta = 0.5$ for SR1 and SR2 in the current study, with the fitted von Karman spectrum reported by Farell and Iyengar (1999). The non-dimensional spectra of the two flow types in the current study closely follow the von Karman spectrum at high frequencies, however the peak spectral values of SR1 and SR2 at low frequencies are 24% and 40% larger, respectively. These peaks are reflected in integral length scales L_u^x increasing from 0.8 m to 2 m and 2.5 m for SR1 and SR2, respectively, as indicated by the three filled data points at $z = 0.6$ m ($z/\delta = 0.5$) in Fig. 6(a). The spectral peaks corresponding to these values of L_u^x are shifted from 5 Hz to the lower frequencies of 2 Hz and 1 Hz for SR1 and SR2 respectively (filled data points in Fig. 6(b)). This indicates that the largest eddies at a constant height in the simulated ABL ($z/\delta = 0.5$) of the current study correspond to frequencies that are approximately half those of an urban terrain ABL simulated by Farell and Iyengar (1999) in a wind tunnel. The peak magnitudes of the longitudinal and vertical power spectra in the current study were previously shown by Emes et al. (2017) to be consistent with Engineering Sciences Data Unit (1985) data of a low-roughness full-scale ABL at I_u of 6% and 10% for SR1 and SR2, respectively. Despite the horizontal shift of the power spectra to higher frequencies because the low frequency region of the full-scale turbulent power spectra cannot be replicated in boundary layer wind tunnel experiments (Banks, 2011; Pfahl et al., 2015), velocity fluctuations measured at the frequencies corresponding to the peak values of the power spectra (Fig. 6(b)) were considered sufficient for the calculation of longitudinal integral length scales L_u^x to provide a measure of the largest eddies in the flow.

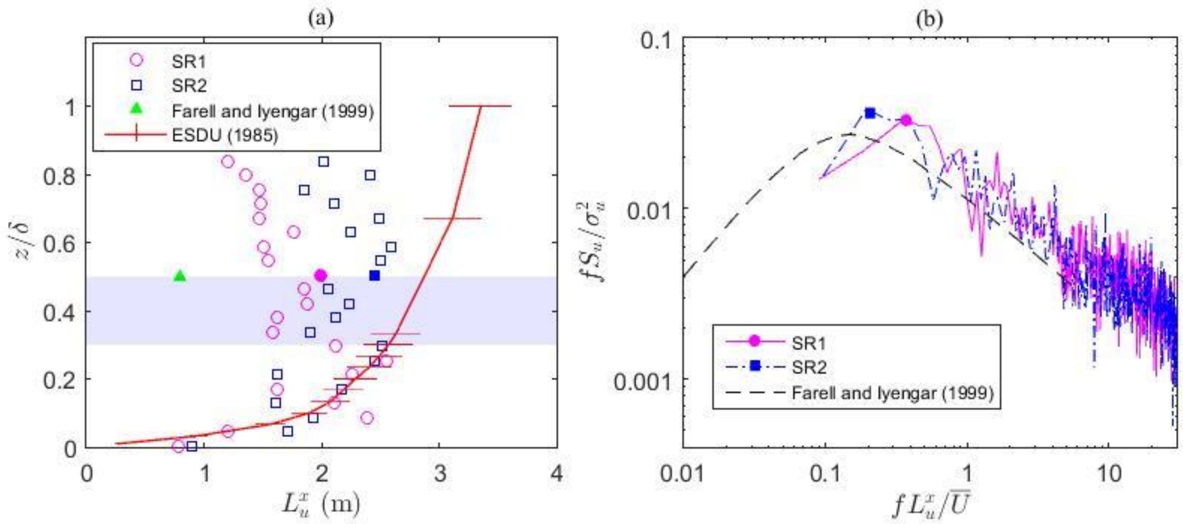

Fig. 6. Frequency characteristics of the simulated ABL ($\delta = 1.2$ m) compared with literature:
(a) Integral length scale profiles calculated using the correlation integral method for SR1 and SR2 in comparison with one wind tunnel measurement by Farell and Iyengar (1999) and those predicted by ESDU (1985) correlations for an assumed 1:150 model scale. Error bars on the ESDU curve ($z_0 = 0.015$ m) indicate a maximum ±8% error in the variation of L_u^x with changes in mean velocity. The shaded area shows the range of heights that the heliostat mirrors were positioned for force and pressure measurements;
(b) Non-dimensional power spectra as a function of non-dimensional frequency $fL_u^x/\overline{U}$ using the filled data points at $z = 0.6$ m ($z/\delta = 0.5$) for SR1 and SR2 compared with the von Karman equation fitted by Farell and Iyengar (1999) to the wind tunnel data at the filled data point in Fig. 6(a). Peak values of the power spectra for SR1 and SR2 are indicated by filled data points.

4. Calculation of Peak Wind Loads on a Heliostat in Stow Position

Drag forces on a heliostat in stow position are relatively small compared to those in operating positions because of the very small projected frontal area, however lift forces and moments about the hinge of the mirror are critically large for stowed heliostats when exposed to large eddies corresponding to low frequencies in the ABL (Emes et al., 2017). The peak forces and moments on stowed heliostats are influenced by the presence of large vortices in the embedded turbulence, leading to a peak lift force L and a peak hinge moment M_{Hy} due to the vertical wind pressures acting on the mirror surface at the mirror elevation axis height H. The pressure coefficient at each pressure tap location i on the stowed heliostat surface in Fig. 3(a) is calculated from the differential pressure measured as:

$$C_{P_i} = \frac{P_i^f - P_i^b}{1/2\rho\bar{U}^2}. \tag{5}$$

Peak lift coefficients on the stowed heliostat are calculated from force data using the following equation:

$$c_L = \frac{L}{1/2\rho\bar{U}^2 A}. \tag{6}$$

Here L(N) is the the measured lift force on the stowed heliostat, ρ (kg/m^3) is density, $\bar{U}$ (m/s) is the mean wind speed at elevation axis height H and $A = c \times c$ (m^2) is the area of the flat plate projected onto the x-y plane. The peak lift forces were determined using the three-sigma approach, $L_{peak} = L_{mean} + 3\sigma_L$, for a sampling duration of 1 minute at model scale (10 minutes equivalent full scale) at a sampling frequency of 1 kHz. Alternatively, the lift coefficient at a wind angle β of 0° can be calculated as a function of the pressure coefficients in Equation (5) as:

$$c_L = \oint -C_{P_i}\, dA. \tag{7}$$

Peak hinge moments on the stowed heliostat are calculated as the product of the measured lift force on the stowed heliostat and the distance of the centre of pressure (l_p) from the centre of the plate defined in in Fig. 1. The hinge moment coefficients are defined following Peterka and Derickson (1992):

$$c_{M_{Hy}} = \frac{M_{Hy}}{1/2\rho\bar{U}^2 Ac}. \tag{8}$$

Here $M_{Hy} = L \times l_p$ (N·m) is the calculated hinge moment on the flat plate aligned parallel to the ground, L (N) is the lift force on the plate, c (m) is the plate chord length and l_p (m) is the distance to the centre of pressure from the central elevation axis of the heliostat in the streamwise direction of the mean flow in Fig. 1, defined as:

$$l_p(x) = \frac{\int_0^c xp(x)\,dx}{\int_0^c p(x)\,dx}. \tag{9}$$

Here $p(x)$ is the non-uniform pressure distribution on the plate ($c = 0.8$ m) in the streamwise direction x (m) from the leading edge of the plate. The location of the centre of pressure for peak lift forces was calculated to be $l_p = 0.12c$ for SR1 and $l_p = 0.15c$ for SR2 using the instantaneous pressure distributions on the instrumented heliostat in Fig. 3(a).

5. Results and Discussion

Peak wind loads on heliostats in stow position were investigated for two cases: (1) an isolated heliostat (HI), and (2) the second downstream heliostat (HT in Fig. 2) for two heliostats in a tandem arrangement. Section 5.1 reports the effect of the characteristic dimensions of the heliostats, including the sensitivity of peak static wind loads to the spacing between tandem heliostat mirrors defined by the gap ratio d/c. Section 5.2 reports the sensitivity of peak static wind loads to the characteristics of the turbulence in the ABL approaching isolated and tandem heliostats in stow position, including turbulence intensity I_u and the ratio of longitudinal integral length scale to mirror chord length L_u^x/c. This is followed in Section 5.3 by an analysis of the fluctuating pressure distributions and their effect on the dynamic wind loads on isolated and tandem heliostats.

5.1. Effect of the gap ratio of tandem heliostats

Fig. 7 presents the effect of the gap ratio (d/c) between two stowed heliostat mirrors ($0.5 < H/c < 1$) on the normalised peak wind loads on a second tandem heliostat (HT) relative to an isolated heliostat (HI) stowed at constant height ($H/\delta = 0.3$) in the ABL. The normalised peak lift forces L_T/L_I decrease from 1.1 at $d/c \leq 1$ to 0.7 and 0.8 for SR1 and SR2, respectively at $d/c \approx 3$, as shown in Fig. 7(a). At $d/c > 3$, the peak lift forces on HT increase so that L_T approaches L_I at $d/c \approx 5$. Similar results are shown for the ratio of hinge moments M_{HyT}/M_{HyI} in Fig. 7(b), as the peak hinge moment on HT increases by 6% and 9% for SR1 and SR2, respectively, relative to that on HI at $d/c < 1$. Values of L_T/L_I and M_{HyT}/M_{HyI} are relatively different than the ratios reported by Pfahl et al. (2011b) on low-and high-density heliostat fields with an external barrier fence that causes a tripping of the generated ABL, whereas the tandem configurations in the current study could be used to study the longitudinal spacing (d/c) of thin flat plates. The heliostat models in the current study were constructed of a thin flat aluminium plate with no support structure, however the presence of back structure on the lower side of the stowed heliostat is expected to have a significant impact on separation and thus the tandem heliostat loads at different gap ratios. In the case of two square prisms in a tandem arrangement, Sakamoto et al. (1987) found that the peak lift coefficient on the downstream prism was 6 times that on an upstream prism at d/c of 1, but decreased to be less than the upstream prism at $d/c > 3$ and approximately half that of the upstream prism at $d/c \geq 10$. Although these ratios of lift forces on the upstream prism to those on the downstream prism are larger than found in the current study, the differences can be explained for a stowed heliostat mirror modelled as a thin flat plate. At smaller gap ratios ($d/c < 1$), the flow is very stable around the upstream plate and a recirculation region forms between the two plates. As a result, separated shear layers from the upstream plate shed onto the side surfaces of the downstream plate, leading to large fluctuating pressures on the downstream plate so that $L_T > L_I$ and $M_{HyT} > M_{HyI}$ at $d/c < 1$. At larger gap ratios ($d/c > 3$), periodic vortex shedding occurs from both the upstream and downstream plates and hence the wake fluctuates at larger turbulence intensities, leading to large fluctuating pressures on both the upstream and downstream plates. The suppression of fluctuating pressures at the side surface of a thin flat plate with maximum aspect ratio (t/c) of 0.015 has a smaller effect at larger gap ratios ($d/c > 3$) compared to the two-dimensional square prism of Sakamoto et al. (1987) with a significantly larger aspect ratio of 9.5. Hence, the lift forces on the downstream heliostat in a tandem configuration converge to that of an isolated heliostat as the distance between the two heliostats increases ($d/c > 5$). Lift forces and hinge moments on in-field heliostats in the high-density ($d/c \approx 1.5$) inner regions of a heliostat field are likely to be larger than those on in-field heliostats in the low-density ($d/c \approx 5.5$) outer regions of a field. Both peak lift forces and peak hinge moments on the second downstream heliostat can be up to 12% larger than an isolated heliostat in stow position at small gap ratios ($d/c < 1$) and as much as 32% and 45% lower at larger gap ratios ($d/c \approx 3.5$). Although the high field densities corresponding to these gap ratios generally lead to a higher field efficiency, they are less favourable to optimise the design of in-field heliostats for stow wind loads. Hence, the low and high field densities commonly adopted in existing heliostat fields produce a favourable result that the wind loads on a second downstream heliostat are usually equal to or lower than an isolated heliostat in stow position.

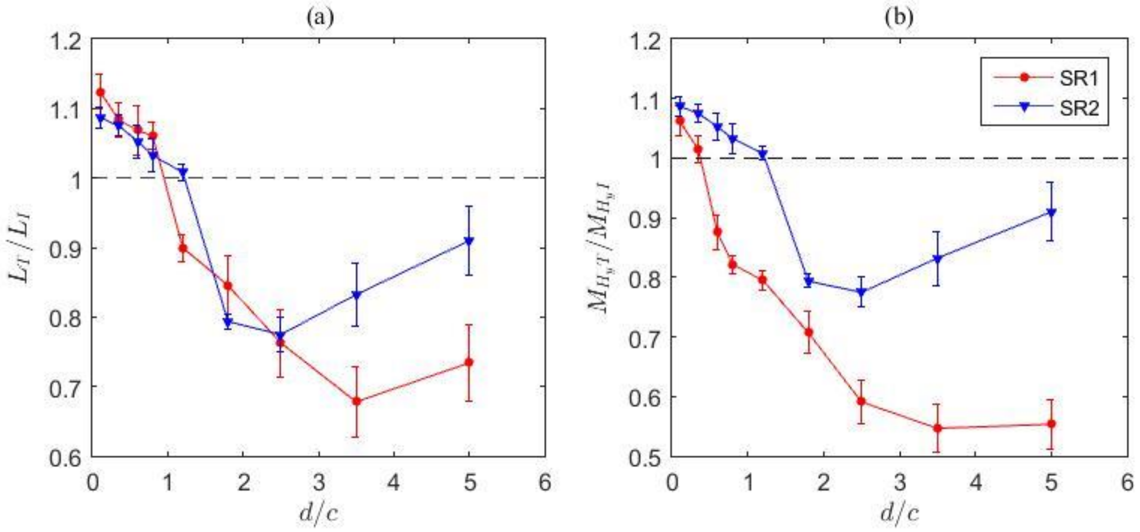

Fig. 7. Effect of the gap ratio (d/c) between two stowed heliostat mirrors ($H/\delta = 0.3$ and $0.5 < H/c < 1$) of chord length c on the normalised peak wind loads on a second tandem heliostat relative to an isolated heliostat in stow position for SR1 ($I_u = 8\%$) and SR2 ($I_u = 12\%$) at a freestream velocity U_∞ of 11 m/s and Reynolds number of 8.8×10^5:
(a) Normalised lift forces L_T/L_I; (b) Normalised hinge moments M_{HyT}/M_{HyI}.

5.2. *Effect of the approaching turbulence characteristics in the simulated ABL*

Fig. 8 presents the effect of turbulence intensity (I_u) on the peak wind loads on tandem heliostats in stow position at $d/c \approx 3$ and $H/c \approx 1$. Peak lift and hinge moment coefficients, calculated using Equations (6) and (8), on an isolated heliostat in stow position increase significantly at $I_u \geq 10\%$ (Emes et al., 2017). In contrast, the peak wind loads on a second tandem heliostat converge closer to those on an isolated heliostat in stow position at $I_u \geq 10\%$. The ratio of peak lift forces increases from $L_T/L_I = 0.64$ to 1.03 when I_u increases from 6.4% to 13% in Fig. 8(a). Fig. 8(b) shows a similar increase of the normalised peak hinge moments M_{HyT}/M_{HyI} from 0.6 to 1as I_u increases from 10% to 13%. Hence, the ratios of peak wind loads on a second tandem heliostat to an isolated heliostat in stow position show that the largest load reductions of 40-50% on a second tandem heliostat occur at smaller turbulence intensities, whereas the peak wind loads approach those on an isolated heliostat at $I_u \geq 10\%$.

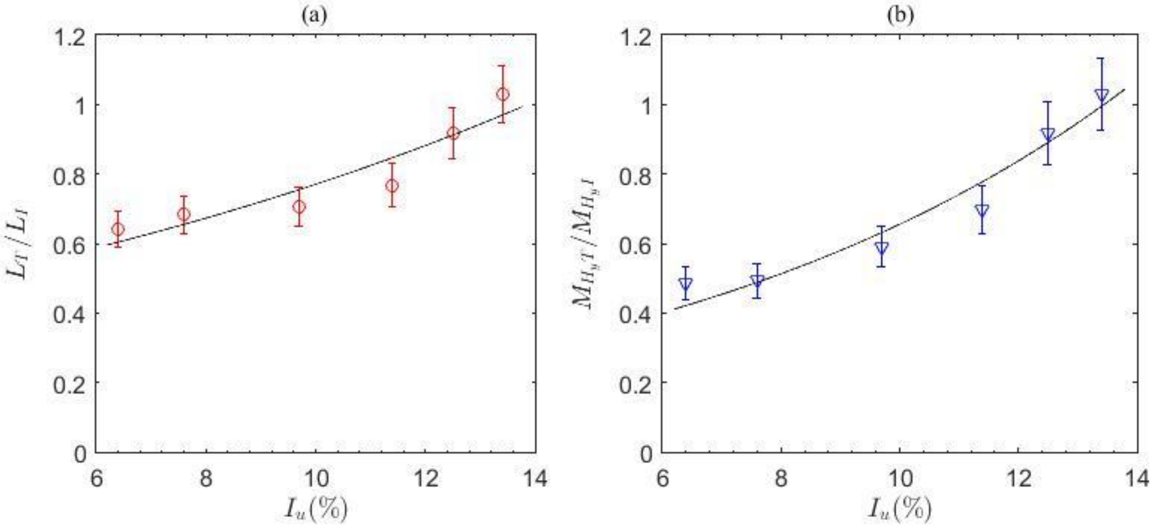

Fig. 8. Effect of turbulence intensity I_u on the peak wind loads on tandem ($d/c \approx 3$ and $H/c \approx 1$) heliostats in stow position:
(a) Normalised peak lift forces on a second tandem heliostat relative to an isolated heliostat L_T/L_I;
(b) Normalised peak hinge moments on a second tandem heliostat relative to an isolated heliostat M_{HyT}/M_{HyI}.
The error bars indicate the experimental uncertainty in the load measurements on isolated and tandem heliostats.

Fig. 9 presents the effect of the ratio of integral length scale to mirror chord length (L_u^x/c) on the peak wind loads on tandem heliostats in stow position at $d/c \approx 3$ and $H/c \approx 1$. Both ratios of peak lift forces L_T/L_I in Fig. 9(a) and peak hinge moments M_{HyT}/M_{HyI} in Fig. 9(b) on a second tandem heliostat, relative to an isolated heliostat, decrease with increasing L_u^x/c from 5 to 10. At the larger L_u^x/c ratio of 10 that leads to maximum wind loads on an isolated heliostat (Emes et al., 2017), such as in the outer row of a field, the lift forces and hinge moments on a heliostat in the second in-field row are as much as 30% and 34% lower, respectively. This suggests that the upstream stowed heliostat is effective at breaking up the larger eddies and thus reducing the vertical components of turbulence that cause lower peak lift forces on the tandem heliostat. Hence, there is a trade-off between lowering the peak wind loading on heliostats in the outermost row of a field and those positioned in the second in-field row. The peak wind loads on heliostats in the two outer rows of a field are strongly dependent on the sizes of vortices approaching the outermost row.

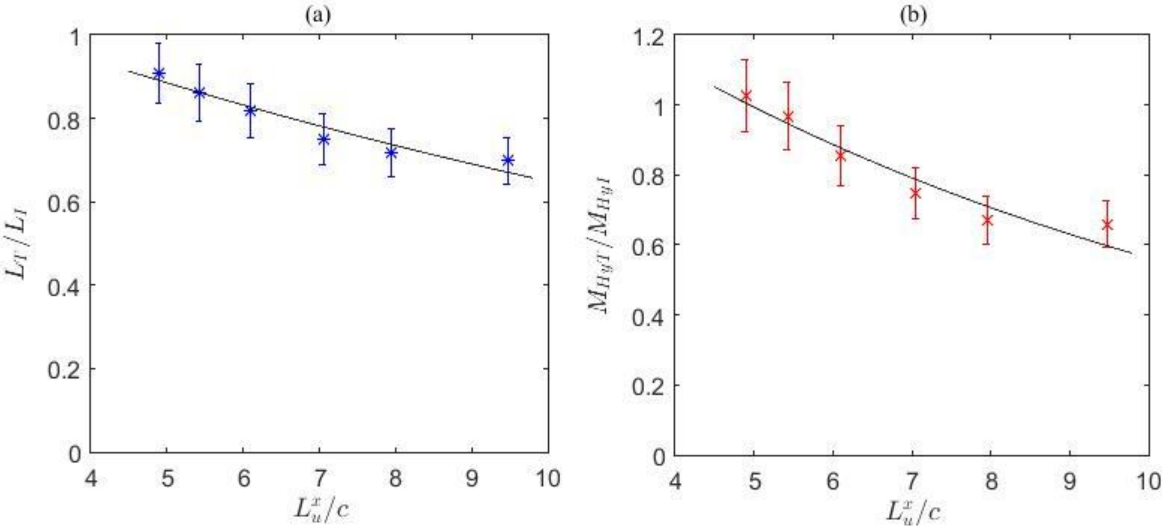

Fig. 9. Effect of the ratio of integral length scale to mirror chord length L_u^x/c on the peak wind loads on a tandem heliostat ($d/c \approx 3$ and $H/c \approx 1$) relative to an isolated heliostat in stow position:
(a) Normalised peak lift forces L_T/L_I;
(b) Normalised peak hinge moments M_{HyT}/M_{HyI}.

5.3. Dynamic wind loads

Fig. 10 shows the contours of peak pressure coefficients C_P, calculated as three-sigma values using Equation (5) at each of the 24 pressure taps and linearly interpolated between the points on the stowed heliostat exposed to SR2. There is a region of high C_P along the leading edge near point A (0.1 m, 0.5 m) on the isolated heliostat (HI), as shown in Fig. 10(a). These large differences in surface pressures, caused by the break-up of large eddies at the leading edge, result in large lift forces near the leading edge of the mirror that can lead to significant hinge moments and vibrations with insufficient structural integrity and strength of the mirror. In contrast, Fig. 10(b) shows significantly reduced magnitudes of C_P on the second tandem heliostat (HT) at $d/c = 1$, resulting in a 47% lower lift coefficient of 0.15 compared to HI in Fig. 10(a). This is most likely caused by the break-up of the largest turbulent eddies by HI, although some turbulent structures are still reaching HT with regions of high C_P at both corners of the leading edge of HT. Lower magnitudes of peak C_P near the leading edge of the downstream heliostat suggests that the turbulence intensity is lower, as found by Sment and Ho (2014), and the vortices shed from the first heliostat are likely to be smaller than those approaching the isolated heliostat. Hence, peak wind loads on an isolated heliostat are likely to be significantly larger than those on a heliostat in the second row of a field, particularly in the inner rows at high field densities. Although manufacturing and installation costs are minimised by using identical heliostats over the whole field at larger production volumes, reductions of over 30% in dynamic wind loads on in-field heliostats are not translated to cost reductions due to the use of uniform heliostat designs within a field.

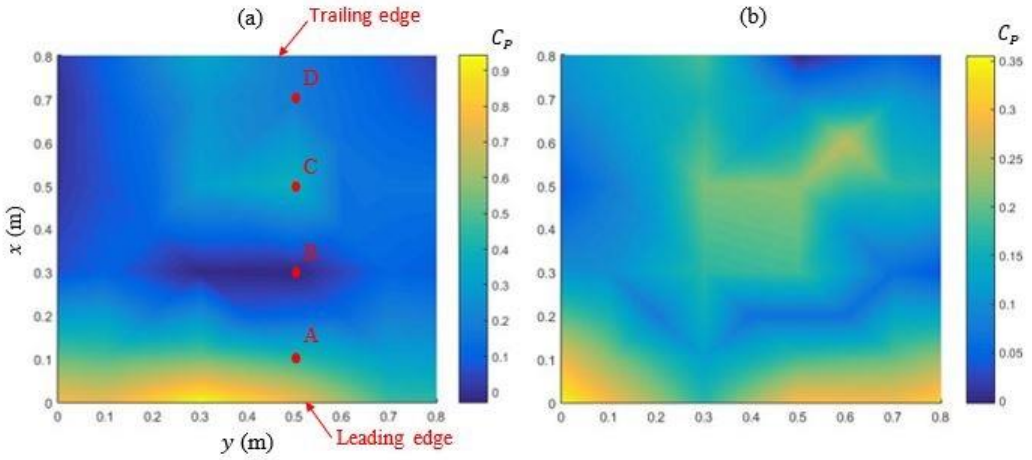

Fig. 10. Peak surface pressure coefficient C_P contours on a stowed heliostat ($H/\delta = 0.4$) for SR2: (a) Single isolated heliostat HI; (b) Second tandem heliostat HT ($d/c = 1$).

Fig. 11 presents the power spectra of the measured differential pressure signals (S_p) at four locations on the stowed heliostat mirror surface defined in Fig. 10(a). The peak value of S_p at point A is over 10 times the peak magnitude of differential pressure fluctuations measured at the other three points in Fig. 10 for both an isolated heliostat (HI) and a downstream tandem heliostat (HT), as shown in Fig. 11(a) and Fig. 11(b), respectively. It is also shown in Fig. 11(b) that the peak values of S_p for HI are an order of magnitude larger than those for HT, and that the peaks of the power spectra distributions on HT are shifted to higher frequencies which correspond to smaller eddies. The frequencies of the peak S_p of the pressure fluctuations measured near the leading edge at point A on HI, shown in Table 3 for SR1 and SR2, closely correspond to the frequencies of 2 Hz and 1 Hz of the most energetic eddies in the flow represented by the peaks of the power spectra for SR1 and SR2, respectively (Fig. 6(b)). The peaks of S_p are shifted to higher frequencies greater than 3 Hz at point A on HT for both SR1 and SR2 (Table 3), which indicates that the largest turbulent eddies of low frequencies are destroyed by HI and only the resulting smaller eddies caused by separation at HI reach HT. This is supported by the reduced magnitudes and the smaller regions of peak C_P near the corners of HT in Fig. 10. Hence, reduced sizes of the largest vortices at the leading edge of HT are less likely to cause progressive failure, however flutter and resonance effects remain possible if the frequencies of the pressure fluctuations match the resonant frequency of the heliostat structure.

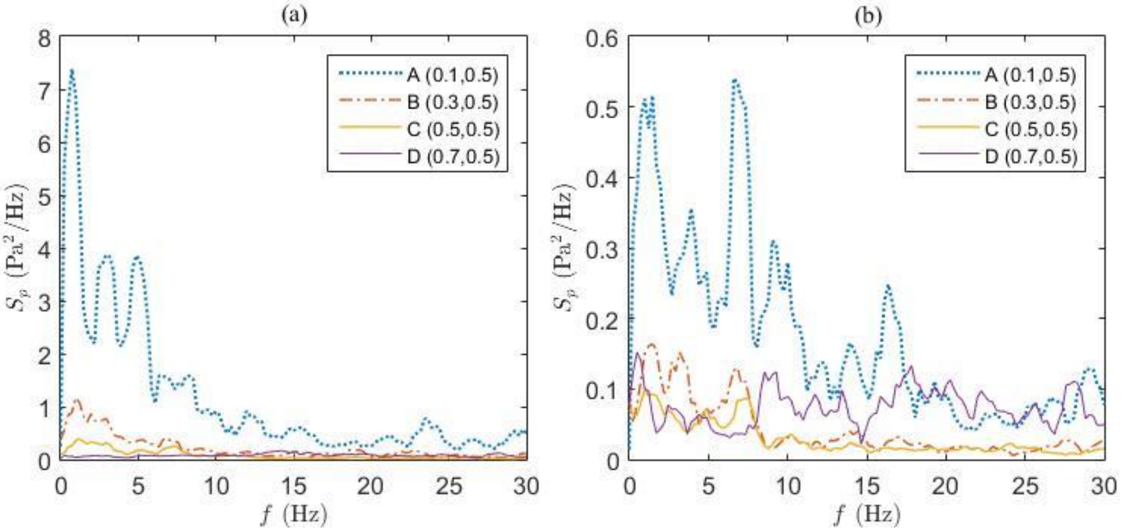

Fig. 11. Power spectra of pressure fluctuations S_p (Pa^2/Hz) at four points along the stowed heliostat mirror surface exposed to SR2: (a) Single isolated heliostat HI; (b) Second tandem heliostat HT.

Table 3. Frequency characteristics of stowed heliostat surface pressure fluctuations

Measurement point and coordinates (x, y)	Frequency of peak power spectra f (Hz)			
	SR1		SR2	
	HI	HT	HI	HT
A (0.1 m, 0.5 m)	1.5	4.0	0.7	6.6
B (0.3 m, 0.5 m)	2.5	5.1	1.0	6.8
C (0.5 m, 0.5 m)	6.8	7.5	2.9	7.3
D (0.7 m, 0.5 m)	20.0	9.3	14.2	8.8

6. Conclusions

Force measurements on two stowed heliostat mirrors in tandem have established that the spacing between the mirrors significantly influences the peak wind loads on stowed heliostats in the two outer rows of a field. For a small spacing between the two heliostat mirrors in tandem, defined by gap ratios $d/c \leq 1$ and corresponding to a high-density region of a heliostat field, peak wind loads on the second heliostat in tandem are up to 10% larger than those on an isolated heliostat in stow positon. In contrast at the gap ratio $d/c \approx 2$, the peak lift forces and hinge moments on the tandem heliostat are as much as 30% and 40% smaller than those on an isolated heliostat, respectively. Peak lift forces on the downstream heliostat in a tandem configuration were found to converge to the values for an isolated heliostat above the gap ratio $d/c \approx 5$ as the distance between the two heliostat mirrors is increased. Hence, lift forces and hinge moments on in-field heliostats in the high-density inner regions of a field are likely to be larger than in-field heliostats in the low-density outer regions of a field.

Turbulence characteristics approaching tandem heliostats were found to have a significant effect on the peak wind loads in stow position. Peak lift coefficients and peak hinge moment coefficients on a second downstream heliostat were found to increase significantly as the turbulence intensity I_u approaching the first heliostat was increased above 10%. Peak wind loads on both isolated and tandem heliostats in the two outer rows of a field were also found to be strongly dependent on the sizes of the turbulent ABL vortices approaching the outermost row. The ratio of the peak loads on a second tandem heliostat relative to those on an isolated heliostat occur decreases as L_u^x/c increases from 5 to 10, such that a reduction of over 30% in peak wind loads was found at the L_u^x/c ratio of 10 corresponding to the maximum wind loads on an isolated heliostat. Hence, the maximum wind loads on stowed heliostats in the outermost row of a field result from larger vortices relative to the chord length of the heliostat mirror than those positioned in the second in-field row.

The dynamic wind loads were found to differ considerably on an isolated heliostat and a second downstream heliostat in a tandem arrangement. Maximum energy in the differential pressure fluctuations was distributed at low frequencies around 1 Hz near the leading edge of the isolated heliostat, corresponding to the same order as the natural frequency of a heliostat. Peaks in the measured pressure spectra on the downstream mirror surface in tandem were an order of magnitude smaller than those for an isolated heliostat and were shifted to higher frequencies centred around 10 Hz and above 4 Hz near the leading edge of the tandem heliostat due to the break-up of large turbulent eddies by the upstream heliostat. Pressure spectra peaks at the leading edge of the mirror were an order of magnitude smaller on the tandem heliostat than the isolated heliostat, leading to a 47% reduction in the peak lift coefficient. The reduced sizes of the largest vortices at the leading edge of the downstream heliostat in tandem are less likely to cause progressive failure, however flutter and resonance effects remain possible if the frequencies of the pressure fluctuations match the resonant frequency of the heliostat structure. Hence, the reduced sizes of vortices that interact with the mirror of a second downstream heliostat through turbulent buffeting in the ABL and from vortex shedding behind the upstream heliostat are less likely to cause progressive failure. Flutter and resonance effects when the frequencies of the pressure fluctuations match the resonant frequency of the heliostat structure are therefore most likely to occur on an isolated heliostat in the first row of a field. The results provide an insight into the differences in loads on heliostats in the outermost two rows of a field, such that their characteristic dimensions can be optimised with respect to the size of the largest eddies in the ABL approaching a heliostat field.

Acknowledgements

Support for the work has been provided by the Australian Government Research Training Program Scholarship and by the Australian Solar Thermal Research Initiative (ASTRI) through funding provided by the Australian Renewable Energy Agency (ARENA). The authors would also like to acknowledge the insightful and constructive comments by the anonymous reviewers of the paper.

References

Alam, M.M., Moriya, M., Takai, K. and Sakamoto, H., 2002, Suppression of fluid forces acting on two square prisms in a tandem arrangement by passive control of flow, Journal of Fluids and Structures 16, 1073-1092.

Banks, D., 2011, Measuring peak wind loads on solar power assemblies, in: 13th International Conference on Wind Engineering, Amsterdam, Netherlands.

Beeler, G., 1986, Turbulent boundary-layer wall pressure fluctuations downstream of a tandem LEBU, AIAA journal 24, 689-691.

Chin, C., Monty, J., Hutchins, N., Ooi, A., Orlu, R. and Schlatter, P., 2015, Simulation of a large-eddy-break-up device (LEBU) in a moderate Reynolds number turbulent boundary layer, in: Proc. Turbulence and Shear Flow Phenomena 9, Melbourne, Australia.

Cook, N.J., 1978, Determination of the model scale factor in wind-tunnel simulations of the adiabatic atmospheric boundary layer, Journal of Wind Engineering and Industrial Aerodynamics 2, 311-321.

Counihan, J., 1973, Simulation of an adiabatic urban boundary layer in a wind tunnel, Atmospheric Environment 7, 673-689.

Coustols, E., Tenaud, C. and Cousteix, J., 1989. Manipulation of turbulent boundary layers in zero-pressure gradient flows: detailed experiments and modelling, in: Turbulent Shear Flows 6, Springer, pp. 164-178.

Coventry, J. and Pye, J., 2014, Heliostat cost reduction–where to now?, Energy Procedia 49, 60-70.

De Bortoli, M., Natalini, B., Paluch, M. and Natalini, M., 2002, Part-depth wind tunnel simulations of the atmospheric boundary layer, Journal of Wind Engineering and Industrial Aerodynamics 90, 281-291.

Emes, M.J., Arjomandi, M., Ghanadi, F. and Kelso, R.M., 2017, Effect of turbulence characteristics in the atmospheric surface layer on the peak wind loads on heliostats in stow position, Solar Energy 157, 284-297.

Emes, M.J., Arjomandi, M. and Nathan, G.J., 2015, Effect of heliostat design wind speed on the levelised cost of electricity from concentrating solar thermal power tower plants, Solar Energy 115, 441-451.

ESDU 85020, 1985, Characteristics of atmospheric turbulence near the ground - Part II: single point data for strong winds (neutral atmosphere), Engineering Sciences Data Unit, London, UK.

Farell, C. and Iyengar, A.K., 1999, Experiments on the wind tunnel simulation of atmospheric boundary layers, Journal of Wind Engineering and Industrial Aerodynamics 79, 11-35.

Flay, R.G.J. and Stevenson, D.C., 1988, Integral length scales in strong winds below 20 m, Journal of Wind Engineering and Industrial Aerodynamics 28, 21-30.

Gong, B., Li, Z., Wang, Z. and Wang, Y., 2012, Wind-induced dynamic response of Heliostat, Renewable Energy 38, 206-213.

Gong, B., Wang, Z., Li, Z., Zang, C. and Wu, Z., 2013, Fluctuating wind pressure characteristics of heliostats, Renewable energy 50, 307-316.

Griffith, D.T., Moya, A.C., Ho, C.K. and Hunter, P.S., 2015, Structural dynamics testing and analysis for design evaluation and monitoring of heliostats, Journal of Solar Energy Engineering 137, 021010.

Hinkley, J.T., Hayward, J.A., Curtin, B., Wonhas, A., Boyd, R., Grima, C., Tadros, A., Hall, R. and Naicker, K., 2013, An analysis of the costs and opportunities for concentrating solar power in Australia, Renewable Energy 57, 653-661.

IRENA, 2013, Renewable Power Generation Costs in 2012: An Overview, Bonn, Germany.

IRENA, 2015, The Power to Change: Solar and Wind Cost Reduction Potential to 2025, Bonn, Germany.

Irwin, H., 1981, The design of spires for wind simulation, Journal of Wind Engineering and Industrial Aerodynamics 7, 361-366.

Jain, A., Jones, N.P. and Scanlan, R.H., 1996, Coupled flutter and buffeting analysis of long-span bridges, Journal of Structural Engineering 122, 716-725.

Kaimal, J.C. and Finnigan, J.J., 1994, Atmospheric Boundary Layer Flows: Their Structure and Measurement, Oxford University Press, New York, USA.

Kolb, G.J., Jones, S.A., Donnelly, M.W., Gorman, D., Thomas, R., Davenport, R. and Lumia, R., 2007, Heliostat Cost Reduction Study, In: SAND2007-3293, Sandia National Laboratories, Albuquerque, USA.

Mehos, M., Turchi, C., Jorgenson, J., Denholm, P., Ho, C. and Armijo, K., 2016, On the Path to SunShot. Advancing Concentrating Solar Power Technology, Performance, and Dispatchability, In: National Renewable Energy Laboratory (NREL), Golden, Colorado, USA.

Mehos, M., Turchi, C., Vidal, J., Wagner, M., Ma, Z., Ho, C., Kolb, W., Andraka, C. and Kruizenga, A., 2017, Concentrating Solar Power Gen3 Demonstration Roadmap, In: National Renewable Energy Laboratory (NREL), Golden, Colorado, USA.

Mendis, P., Ngo, T., Haritos, N., Hira, A., Samali, B. and Cheung, J., 2007, Wind loading on tall buildings, EJSE Special Issue: Loading on Structures 3, 41-54.

Milbank, J., Loxton, B., Watkins, S. and Melbourne, W., 2005, Replication of Atmospheric Conditions for the Purpose of Testing MAVs: MAV Flight Environment Project Final Report, Royal Melbourne Institute of Technology.

Nakamura, Y., 1993, Bluff-body aerodynamics and turbulence, Journal of Wind Engineering and Industrial Aerodynamics 49, 65-78.

Peterka, J.A., Bienkiewicz, B., Hosoya, N. and Cermak, J.E., 1987, Heliostat mean wind load reduction, Energy 12, 261-267.

Peterka, J.A. and Derickson, R.G., 1992, Wind load design methods for ground-based heliostats and parabolic dish collectors, In: SAND92-7009, Sandia National Laboratories, Albuquerque, USA.

Peterka, J.A., Tan, Z., Cermak, J.E. and Bienkiewicz, B., 1989, Mean and peak wind loads on heliostats, Journal of solar energy engineering 111, 158-164.

Pfahl, A., Buselmeier, M. and Zaschke, M., 2011a, Wind loads on heliostats and photovoltaic trackers of various aspect ratios, Solar Energy 85, 2185-2201.

Pfahl, A., Buselmeier, M. and Zaschke, M., 2011b, Determination of wind loads on heliostats, in: Proceedings of the 17th SolarPACES Conference, Granada, Spain.

Pfahl, A., Randt, M., Meier, F., Zaschke, M., Geurts, C. and Buselmeier, M., 2015, A holistic approach for low cost heliostat fields, Energy Procedia 69, 178-187.

Reinhold, T., Tieleman, H. and Maher, F., 1978, Simulation of the urban neutral boundary layer for the model study of wind loads on tall buildings, NASA STI/Recon Technical Report N 78, 31278.

Sakamoto, H., Hainu, H. and Obata, Y., 1987, Fluctuating forces acting on two square prisms in a tandem arrangement, Journal of Wind Engineering and Industrial Aerodynamics 26, 85-103.

Sarkar, P.P., 2013, Advances in wind tunnel simulation, techniques and tools for assessing extreme-wind hazard to structures, in: The Eighth Asia-Pacific Conference on Wind Engineering, Chennai, India.

Sment, J. and Ho, C., 2014, Wind patterns over a heliostat field, Energy Procedia 49, 229-238.

Swamy, N.V.C., Gowda, B.H.L. and Lakshminath, V.R., 1979, Auto-correlation measurements and integral time scales in three-dimensional turbulent boundary layers, Applied Scientific Research 35, 237-249.

Watkins, S., 2012, Turbulence Characteristics of the Atmospheric Boundary Layer and Possibilities of Replication for Aircraft, in: Third Symposium "Simulation of Wing and Nacelle Stall", Braunschweig, Germany.

Yu, J.S., Arjomandi, M., Ghanadi, F. and Kelso, R.M., 2016, The Effect of Inclination Angle on the Flow Characteristics of Tandem Bluff Plates, In: *Proc., 20th Australasian Fluid Mechanics Society Conference,* Perth, Australia.

Chapter 7

Conclusions and Future Work

The effect of turbulence characteristics in the atmospheric boundary layer (ABL) on the peak wind loads on heliostats in stow position has been investigated in this study. The research has included theoretical and experimental studies, focusing on the design wind loads on heliostats required for structural integrity in the stow position. The primary contribution of the current thesis is the analysis of the peak wind loads on stowed heliostats for a range of temporal and spatial variations in turbulence conditions. Maximum wind loads on both an isolated heliostat and a second downstream heliostat in a tandem arrangement were investigated to optimise the critical scaling parameters of heliostats with respect to the approaching turbulent flow. Optimisation of the chord length and the elevation axis height of the heliostat mirror above the ground to the peak wind loads in stow position can lead to savings in manufacturing costs of the heliostats. Furthermore, the row spacing between tandem heliostats in the field can be optimised to reduce the wind loads. The following sections outline the major conclusions and outcomes drawn from each part of the present research.

7.1. Stow Design Wind Speed of Heliostats

There is a significant opportunity to lower the levelised cost of electricity (LCOE) in windy sites by careful choice of both the design wind speed at which heliostats are parked in stow position and the size of the heliostats. Lowering the design wind speed has the potential to reduce the LCOE of a PT plant at windy sites because of the strong dependence of the cost of the heliostat field on the design wind speed. The relative cost of the structural components increases from 6% to 23% as the design wind speed is increased from 1 m/s to 15 m/s. A larger range of observed wind speeds at three Australian sites showed that a significant reduction in the design wind speed is associated with only a small reduction to the capacity factor, thus lowering the LCOE. For example, lowering the design wind speed by 9 m/s from the maximum 22 m/s measured wind speed at Alice Springs yields a 0.3% lower capacity factor and a 18% reduction in LCOE. The optimal size of a heliostat is also dependent on the design wind speed. For example, the optimal heliostat size is 50 m^2 for a design wind speed of 10 m/s, while it is only 25 m^2 for a design wind speed of 20 m/s. Hence, the design wind speed and the size of the heliostat need to be considered together because the optimal heliostat area decreases with increasing design wind speed, based on the assumptions of quasi-static loads for the heliostat design and the independence of heliostat maintenance costs on the wind speed. Additionally, heliostat costs can be minimised in regions of wind speeds above 10 m/s by manufacturing smaller heliostats than those commonly employed today. However, this requires that the heliostat structure be optimised to account for wind speed, which would reduce the number of sites to which any given design applies and, in turn, reduce the economies of scale. Large heliostats are more cost efficient (lower \$/m^2) than smaller heliostats due to the ‘economies of scale’, however the structural stiffness and strength required to withstand the maximum wind loads is considerably larger. A larger mass production of smaller heliostats with a highly automated production facility may lead to lower labour costs per heliostat, but the maintenance costs associated with additional field setup and wiring will increase. This suggests that there may be a trade-off between site-specific designs and a more robust design that is applicable at all practical sites, such as a heliostat with an increased mirror area at a low wind-speed site. Furthermore, if no wind data is available at the site or at a nearby automatic weather station at the standard measurement height of 10 m, regional design wind speeds are usually specified in design wind codes and standards based on regions that are exposed to cyclonic and synoptic (non-cyclonic) winds. The smaller scales of surface-layer turbulence, on the order of 20 m in the lowest 100 m of the ABL, are most accurately captured by measuring wind velocities using sonic, cup or propeller anemometers mounted on towers or masts. At least 1 year of local high-quality DNI data, measured at 1 minute intervals, is necessary for the calculation of the capacity factor and heliostat field power output in the developed model.

7.2. Turbulence Characteristics in the Atmospheric Surface Layer

Stowed heliostats are exposed to the effects of turbulence from the wind in the atmospheric surface layer (ASL) within the lowest 100 m of the neutral atmospheric boundary layer (ABL). Short-duration wind fluctuations (gusts) and amplification effects during high-wind conditions need to be considered in the design of heliostat components to maintain their structural integrity. The gust factor method relating the peak gust velocity to mean velocity generally gives a good approximation of the design wind loads for standard building shapes. However, the gust factor can underestimate the peak wind loads on stowed heliostats with large dynamic responses due to the large amplitude velocity fluctuations at heights below 10 m in the ASL. Hence, the differences in the expected gust factor due to a change in the gust period, and thus the filtering frequency of the velocity fluctuations, were investigated using a transfer function between the time and frequency domains. The effect of ground surface roughness on the spatial characteristics of turbulence in the ASL, including the integral length scales of turbulence, were analysed based on field velocity measurements in a low-roughness surface layer in the Utah desert.

For the purposes of studying the effects of gusts in a neutrally-stratified ABL, the mean velocity profile in the SLTEST field experiment agrees well with the logarithmic law within a 10% experimental error in the estimate of friction velocity and Reynolds stresses close to the ground. Turbulence intensity profiles in the streamwise, spanwise and vertical directions show good agreement with the laboratory data for a smooth-wall turbulent boundary layer, when the height is non-dimensionalised with respect to an estimated surface layer thickness δ_s of 60 m. The skewness and kurtosis of the PDF of vertical velocity w are consistent with previous surface layer measurements at lower heights in the neutrally-stratified atmospheric boundary layer, where positive skewness of w indicates the presence of low-speed streaks with prevailing narrow updrafts over wider downdraft motions in the Utah desert.

Large eddies are elongated significantly in the longitudinal direction due to the extremely small scale of the w-component fluctuations in the desert surface layer. The variation of the longitudinal integral scale L_u^x with height in the SLTEST field experiment was consistent with semi-empirical models (Counihan, 1975; Engineering Sciences Data Unit, 1985; Solari and Piccardo, 2001), however these models over-predict the size of the largest eddies by more than double in the lowest 10 m of the low-roughness desert surface layer. Hence, the sizes of eddies close to the ground in the surface layer in a low-roughness desert ABL appear to differ considerably from rural, open country and urban terrains that have commonly been the basis of semi-empirical models.

For the purposes of deriving design wind loads on physical structures in the ABL from the calculation of the gust factor, the longitudinal PSD functions at the 9 measurement heights in the SLTEST surface layer are considered to be reasonably close to the von Karman spectrum. The maximum gust velocity is less than 9 m/s for the range of gust periods tested in the desert terrain, however the velocity gust factor at a 10 m height increases by 3% as the gust period is lowered from 3 s to 0.2 s, such as in the redefinition of the equivalent moving average in AS/NZS 1170.2. Gust factor calculated using the Ashcroft (1994) equation is consistent with the expected gust factor following Holmes et al. (2014) for short-duration 0.2-second gusts, however it tends to under-predict the peak wind speeds of low-frequency gusts in the low-roughness SLTEST desert terrain compared to open country terrains with an order of magnitude larger roughness height.

7.3. Peak Wind Loads on a Stowed Heliostat

Wind tunnel experiments were carried out to measure wind loads and pressure distributions on a heliostat in stow position exposed to gusty wind conditions in a simulated part-depth atmospheric boundary layer (ABL) of thickness δ. The experiments investigated the sensitivity of the peak lift coefficient c_L and peak hinge moment coefficient $c_{M_{Hy}}$ on a stowed heliostat to the critical scaling parameters of the heliostat chord length c and elevation axis height H and the turbulence characteristics in the ABL. The sizes of the largest vortices with respect to the heliostat size, defined by the ratio of longitudinal integral length scales to heliostat chord length (L_u^x/c), were found to have a more pronounced effect on the peak wind load coefficients than freestream parameters such as mean velocity and Reynolds number. Maximum increases of 21% in c_L and 25% in $c_{M_{Hy}}$ were observed with a 40% increase in freestream Reynolds number, compared to a linear increasing and doubling in magnitude of c_L and $c_{M_{Hy}}$ with increasing L_u^x/c from 5 to 10. The linear increase of the peak coefficients with increasing L_u^x/c was caused by the distribution of larger negative pressures over the surface of the heliostat mirror. Contours of wind pressure coefficients confirmed that large negative pressures at the leading edge, caused by the break-up of large eddies, need to be considered for critical failures of the heliostat in the stow position. The values of L_u^x/c in the lowest 10 m of open country terrains surrounding heliostat fields are expected to range between 5 and 10, hence L_u^x/c can be reduced by stowing the heliostat mirror at lower heights and increasing the size of heliostat mirrors.

The effects of the critical scaling parameters of the heliostat on the peak wind load coefficients were investigated for moderate turbulence intensities I_u in the range of low-roughness desert terrains. Peak c_L and $c_{M_{Hy}}$ increased linearly and approximately doubled as I_u increased from 10% to 13%. The chord length of the heliostat mirror was also found to have a significant influence on the peak wind load coefficients. Reducing the chord length to half its size from 0.8 m to 0.4 m resulted in peak c_L increasing from 0.3 to 0.57 and peak $c_{M_{Hy}}$ increasing from 0.05 to 0.09 at a constant turbulence intensity. Both peak lift and hinge moment coefficients were at least ten times the magnitude of their mean coefficients, confirming those found by Peterka et al. (1989) for a stowed heliostat. Lowering the elevation axis height H at which the heliostat is stowed in the simulated ABL of constant thickness δ from H/δ of 0.5 to 0.3 was found to result in a vertical shift of peak c_L and peak $c_{M_{Hy}}$ to larger magnitudes because of the 'ground effect' at lower heights with constant H/c. Reductions of up to 50% in c_L and 40% in $c_{M_{Hy}}$ were found by lowering H/c from 0.7 to 0.5 by manufacturing a heliostat without a horizontal primary axis. Although heliostats are commonly designed for a minimum H/c of 0.5, heliostats with a horizontal primary axis require H/c of 0.7. Lowering H/c to 0.5 provides the opportunity to lower the critical stow design wind loads for the mirror, drives and support structure, thus lowering the overall mass and strength of the heliostat with a shorter pylon length, and ultimately reducing the capital cost of manufacturing these components. The peak c_L and $c_{M_{Hy}}$ of the stowed heliostat with $c = 0.5$ m in the current study were 13% and 23% smaller, respectively than those reported by Pfahl et al. (2015) at a similar turbulence intensity. In comparison, the peak lift and hinge moment coefficients on the smallest stowed heliostat ($c = 0.3$ m) exposed to the maximum I_u of 13.4% in the current study were 8% and 15% smaller, respectively, than those measured by Peterka et al. (1989) at a larger turbulence intensity I_u of 18%. These discrepancies may be explained by differences in integral length scales between these studies and the elevation axis height in the ABL (H/δ = 0.3) in the current study that was double that used in experiments by Peterka et al. (1989) and Pfahl et al. (2011a). Therefore, optimisation of the mirror chord length and the elevation axis height for the characteristics of the turbulence approaching a stowed heliostat can significantly reduce design wind loads for high-wind events in the atmospheric surface layer and the cost of manufacturing the heliostat components.

7.4. Peak Wind Loads on Tandem Stowed Heliostats

Force measurements on two heliostat mirrors have established that the chord length c and elevation axis height H of the heliostat mirror significantly influence the peak wind loads on stowed heliostats in the two outermost rows of a field. The peak lift forces and peak hinge moments on a second downstream heliostat can be reduced by as much as 40% and 50%, respectively, relative to an isolated stowed heliostat, by designing for H/c of less than or equal to 0.5 and reducing the height in the ABL (H/δ) at which the mirrors are stowed. Peak wind loads on both heliostats were optimal on an isolated heliostat at H/c of 0.5. Although the stiffness of a concrete pylon is preferred in contemporary heliostat designs (Pfahl et al., 2017a), the lowering of the heliostat mirror using a spindle drive to the ground in stow during high-wind conditions can reduce the wind load requirements and the cost of a cantilever-sandwich heliostat (Pfahl et al., 2017b). The use of a telescopic pylon design in the current study can also be used to lower the stow position and hence reduce peak loading. This provides the potential to reduce the capital cost of manufacturing the heliostat components by lowering the mass and strength of the heliostat to withstand the maximum wind loads in the stow position.

The spacing between the two stowed heliostat mirrors in tandem, defined by the gap ratio d/c, was found to have a significant effect on the peak lift forces L and peak hinge moments M_{Hy} on the second downstream heliostat. The experimental study investigated longitudinal gap ratios in the range $0.1 \leq d/c \leq 5$ and found that the peak wind loads on a second downstream heliostat were up to 12% larger relative to an isolated heliostat at $d/c < 1$. At moderate gap ratios $d/c \approx 3$, L and M_{Hy} on the second downstream heliostat were reduced by up to 30% and 50%, respectively, relative to an isolated heliostat in stow position. At larger gap ratios $d/c > 5$ in the low-density outer regions of a heliostat field, both L and M_{Hy} were found to converge to the values for an isolated heliostat. Hence, the gap ratios corresponding to high-density fields can lead to peak wind loads on in-field stowed heliostats being larger than those in the outermost rows. The field densities commonly adopted in existing heliostat fields typically produce the favourable result that designing for the maximum wind loads on an isolated heliostat in stow position can account for the maximum loads on the outermost two rows in a heliostat field. The tandem configuration of two outermost heliostats can be applied for any row of the field, provided that the effect of heliostats in neighbouring rows is negligible.

Turbulence characteristics approaching tandem heliostats were found to have a significant effect on the peak wind loads in stow position. Peak lift coefficients and peak hinge moment coefficients on a second downstream heliostat were found to increase significantly as the turbulence intensity I_u approaching the first heliostat was increased above 10%. Extrapolation of the fitted exponential expressions to higher I_u indicated that the peak wind loads on a second downstream heliostat would increase above those of an isolated heliostat at $I_u > 12\%$. Peak wind loads on both isolated and tandem heliostats in the two outer rows of a field were found to be strongly dependent on the sizes of the turbulent ABL vortices approaching the outermost row. The peak wind loads on a second tandem heliostat were similar to those on an isolated heliostat at L_u^x/c less than 5. In contrast, a reduction of over 30% in peak wind loads was found at the L_u^x/c ratio of 10, corresponding to the maximum wind loads on an isolated heliostat. Values of L_u^x/c less than 3 tend to occur in the lowest 10 m of very low roughness terrains such as deserts, whereas L_u^x/c between 5 and 10 are expected in open country terrains surrounding heliostat fields. Therefore, the maximum wind loads on stowed heliostats in the outermost two row of a field are significantly dependent on the size of the largest vortices relative to the chord length of the heliostat.

The dynamic wind loads were found to differ considerably on an isolated heliostat and a second downstream heliostat in a tandem arrangement. Maximum energy in the differential pressure fluctuations was distributed at low frequencies around 1 Hz near the leading edge of the isolated heliostat that closely correspond to the frequencies of the largest eddies in the flow. Peaks in the measured pressure spectra on the downstream mirror surface in tandem were an order of magnitude smaller than those for an isolated heliostat and were shifted to higher frequencies above 3 Hz near the leading edge. This indicated the presence of smaller vortices that interact with the second downstream heliostat through buffeting by boundary layer vortices and vortex shedding behind the upstream heliostat at frequencies around 10 Hz. Pressure spectra peaks at the leading edge of the mirror were 6 times the magnitude at the trailing edge for both the isolated heliostat and the second downstream heliostat in a tandem arrangement. Hence, the propagation of structural failure of the heliostat is likely to be initiated at the leading edge of the mirror from the interaction with the largest eddies in the ABL.

7.5. Significance of Present Work

Previous research on heliostat wind loads has focused on the effects of turbulence intensity and temporal characteristics of turbulence in the ABL by adopting a simplified gust factor calculation of mean and peak load coefficients from experimental data in systematic wind tunnel studies. This allows for the estimation of design wind loads on heliostats in stow position, however the spectral distribution of the velocity fluctuations with frequency has a significant effect on the dynamic wind loads on physical structures exposed to turbulence in the ABL. Thus, the research in the current thesis investigates the spatial distribution of velocity fluctuations using a defined integral length scale at lower heights in the surface layer where heliostat mirrors are stowed. Further, the effect of the sizes of the largest eddies on the unsteady pressure fluctuations on the heliostat mirror resulting from short-duration gusts was investigated. The findings from the current research allow more accurate determination of static and dynamic wind loads on stowed heliostats to further optimise the dimensions of the heliostat mirror, pylon and support structure with respect to the approaching turbulence characteristics at a particular field site. Furthermore, the spacing between rows of heliostats in the field can be optimised to minimise the wind loads on in-field heliostats and thus reduce the cost and land area required for the installation of a solar field in a power tower plant.

7.6. Recommendations for Future Work

The results of this study provided a detailed analysis of the turbulence characteristics in the lower atmospheric boundary layer (ABL) and investigated how the critical scaling parameters of a heliostat can be optimised to the maximum wind loads in stow position. This study focused on improving the accuracy and versatility of the current methods used for calculating the ultimate design wind loads on heliostats, however further effective techniques to reduce the wind load on heliostats in the stow position are required to lower the cost of the support structure and drive mechanisms. The following recommendations of passive and active techniques have been proposed by the author for future investigations to complement and further develop the research presented in the current thesis.

7.6.1. Field Measurements of Turbulence Characteristics in the Surface Layer

Wind tunnel experiments in the current research investigated the effects of turbulence in the atmospheric boundary layer (ABL) on the peak wind loads on scale-model stowed heliostats. However, field measurements in the full-scale ABL are needed to improve the accuracy and versatility of the current methods used for calculating the ultimate design wind loads on stowed heliostats. This would involve characterisation of the temporal and spatial turbulence characteristics of gusts in the atmospheric surface layer (ASL), such as an investigation of the coherent vortices at heights below 10 m where heliostats will be installed. Turbulent vortices can be most accurately characterised using spanwise and wall-normal arrays of three-component sonic anemometers to measure all three components of velocity and temperature. Neutral stability of the ASL required for comparison with statistically stationary data from the canonical turbulent boundary layer can be confirmed with a negligible vertical heat-flux. Systematic errors in the measurement of source data used in semi-empirical models (Ashcroft, 1994; Cheung and Melbourne, 2004; Cook, 1985; Engineering Sciences Data Unit, 1985) are most likely the reason for discrepancies in predicted gust factors and integral length scales in full-scale ASLs in different studies. Sonic anemometers can accurately measure the spectral content of the wind and are thus are most suitable for capturing the high frequency velocity fluctuations of the large eddies in the ASL. Therefore, sonic anemometers are recommended for spectral analysis, including the calculation of integral length scales and gust factor. Obtaining data from field site measurements would allow the dimensions and strength of the heliostat components to be optimised based on known characteristics of the approaching turbulence that stowed heliostats are exposed to in the lowest 10 m of a full-scale ABL.

7.6.2. Vibration of the Heliostat Facet

The dynamic wind loads on an isolated heliostat were found to be strongly correlated to the dominant frequencies of the largest eddies in the approaching flow within the simulated ABL. Peak wind loads on the stowed heliostat, modelled as a thin flat plate, were determined for different flow conditions and critical scaling parameters of the heliostat, however the vibration of the stowed heliostat was not measured. Vibrations of the heliostat facet in the stow position from gravitational and dynamic loadings can degrade optical pointing accuracy and fatigue the structural components. Dynamic loads due to the turbulence in the atmospheric surface layer (ASL) can be investigated by instrumenting heliostats with accelerometers in the wind tunnel. The displacement of the heliostat mirror needs to be measured as a function of mirror size, pylon thickness and height, turbulence intensity and integral length scales. Displacement measurements can help identify the vibrational modes of the stowed heliostat and allow correlation of these modes with the peak lift forces and hinge moments measured using the load cells. Consequently, the turbulent characteristics that most significantly influence large displacements of the heliostat facet and lead to structural failure can be determined.

Experimental measurements would be complemented with predictive structural models using fluid-structure interactions that can reduce the time and costs associated with the alignment process of nominally-identical heliostats in a single field. In addition, the effect of the heliostat support structure on the dynamic wind loads could be investigated by measuring the vibrations after adding support structure to the thin flat plates investigated in the current research.

7.6.3. Flow Visualisations of the Heliostat Field

Flow measurements in the wind tunnel experiments in the current research were limited by point velocity measurements at different positions in a spanwise y-z plane using a two-dimensional traverse, however the turbulent vortices in the wakes of heliostats can be observed in a water channel experiment of a small-scale heliostat. The current research calculated the integral length scale profiles from the integration of the autocorrelation function to its first-zero crossing, however any relationships between eddy sizes and turbulence intensities and the turbulent phenomena associated with flutter and resonance effects requires further investigation. The estimated size of the large eddies embedded in the turbulence approaching heliostats can be estimated using particle image velocimetry (PIV) techniques in a water channel to map the velocity and vorticity contours within the turbulent flow in the ABL. PIV analysis could also be used to track the impingement of vortices shed from upstream heliostats and interacting with downstream heliostats in tandem arrangements of field configurations. Coupling of simultaneous measurements of velocity, vorticity and displacements using accelerometers on instrumented heliostats would allow for the correlation of wind-induced response with the size and strength of eddies interacting with the heliostat.

7.6.4. Development of a Validated Computational Model

The effect of the critical scaling parameters, such as the chord length c and elevation axis height H, of the stowed heliostat and the gap ratio d/c defining the spacing between two heliostat mirrors in a tandem arrangement, were investigated within a range of freestream velocities and turbulence intensities that were limited by the wind tunnel specifications. For example, the telescopic design of the heliostat allowed a minimum ratio of elevation axis height to chord length H/c of 0.5 and the working section length of the tunnel allowed for a maximum d/c of 5.5. The results from wind tunnel experiments can be complemented by the development of a validated computational modelling tool for investigation of the topographic interactions within the embedded turbulence approaching heliostats and the flow behaviour in the vicinity of heliostats. The flow characteristics of the ABL, such as the mean velocity profile and turbulence intensities, can be easily adjusted in a three-dimensional unsteady turbulence model to simulate different conditions observed in full-scale ASLs. Direct Numerical Simulation (DNS) is considered the most accurate model to resolve the large-scale turbulent eddies motions in the ABL. Large Eddy Simulation (LES) is a more suitable model as it requires less computational effort than DNS, however further analysis of how to control the length scales of eddies in a simulated ABL is required to achieve realistic results that are simulated in the wind tunnel using conventional passive techniques, such as spires and roughness elements. Experimental measurements on only two heliostats in tandem could be tested in the current research due to the limited size of the wind tunnel. Validated numerical models could be used to extend experimental wind load measurements to subsequent rows after the first and second rows at the outer boundary of a heliostat field. Experimental data can also be used as an input to the model to investigate the flow behaviour around multiple heliostats. The results from computational fluid dynamics (CFD) modelling and finite element analysis (FEA) can be used to improve the management of existing fields and to guide the decision making processes for the future placement of heliostats.

7.6.5. Active Turbulence Generation Technique

Conventional passive techniques, such as spires and roughness elements used in this study, have effectively modelled the lower region of the atmospheric boundary layer (ABL) in wind tunnels. However, this passive technique was limited to the generation of turbulence intensities less than 13% within the range of heights at which the scale-model heliostats were stowed. Stationary fences have also been used to increase the height of the tripped boundary layer, however the generation of large two-dimensional spanwise vortices with high coherence has been most effectively achieved by the forcing of periodic motions in the boundary layer. Time-averaged and phase-averaged velocity measurements would allow the identification and characterisation of large-scale spanwise vortices behind an oscillating fence. Furthermore, the vortex-heliostat interaction could be analysed from the correlation of velocity measurements with force and pressure measurements on an instrumented heliostat.

References for Chapter 7

Ashcroft, J., 1994, The relationship between the gust ratio, terrain roughness, gust duration and the hourly mean wind speed, Journal of Wind Engineering and Industrial Aerodynamics 53, 331-355.

Cheung, J.C.K. and Melbourne, W.H., 2004, Wind Gust Factors with Various Turbulence Intensities and Length Scales, in: Australasian Wind Engineering Society Workshop (11th: 2004: Darwin, Australia).

Cook, N.J., 1985, The designer's guide to wind loading of building structures, Part 1: Background, damage survey, wind data and structural classification, In: Building Research Establishment, Garston, UK.

Counihan, J., 1975, Adiabatic atmospheric boundary layers: a review and analysis of data from the period 1880–1972, Atmospheric Environment 9, 871-905.

ESDU 85020, 1985, Characteristics of atmospheric turbulence near the ground - Part II: single point data for strong winds (neutral atmosphere), Engineering Sciences Data Unit, London, UK.

Holmes, J.D., Allsop, A.C. and Ginger, J.D., 2014, Gust durations, gust factors and gust response factors in wind codes and standards, Wind and Structures 19, 339-352.

Peterka, J.A., Tan, Z., Cermak, J.E. and Bienkiewicz, B., 1989, Mean and peak wind loads on heliostats, Journal of solar energy engineering 111, 158-164.

Pfahl, A., Buselmeier, M. and Zaschke, M., 2011a, Wind loads on heliostats and photovoltaic trackers of various aspect ratios, Solar Energy 85, 2185-2201.

Pfahl, A., Coventry, J., Röger, M., Wolfertstetter, F., Vásquez-Arango, J.F., Gross, F., Arjomandi, M., Schwarzbözl, P., Geiger, M. and Liedke, P., 2017a, Progress in heliostat development, Solar Energy 152, 3-37.

Pfahl, A., Gross, F., Liedke, P., Hertel, J., Rheinländer, J., Mehta, S., Vásquez-Arango, J.F., Giuliano, S. and Buck, R., 2017b, Reduced to Minimum Cost: Lay-Down Heliostat with Monolithic Mirror-Panel and Closed Loop Control, In: *Proc., SolarPACES 2017*, Santiago, Chile.

Pfahl, A., Randt, M., Meier, F., Zaschke, M., Geurts, C. and Buselmeier, M., 2015, A holistic approach for low cost heliostat fields, Energy Procedia 69, 178-187.

Solari, G. and Piccardo, G., 2001, Probabilistic 3-D turbulence modeling for gust buffeting of structures, Probabilistic Engineering Mechanics 16, 73-86.

Appendix A

Field Experiment Velocity Measurements

A.1. Section Overview

This appendix reports some characteristics of the turbulence in a low-roughness atmospheric surface layer (ASL). The temporal and spatial characteristics of turbulence were calculated using field velocity measurements taken in a low-roughness surface layer in the Utah desert during near-neutral conditions. These characteristics were analysed and discussed in relation to semi-empirical models developed for homogenous, isotropic turbulence over open country terrains in a neutrally-stable ABL. Calculated gust factor profiles following the approach used in wind codes and standards for buildings showed that the peak wind speeds of low-frequency gusts were under-predicted in the low-roughness terrain. Hence, these discrepancies highlight the uncertainties associated with using the quasi-steady gust factor method to approximate the peak wind loads on heliostats.

A.2. Turbulence Characteristics in the Atmospheric Surface Layer

Statement of Authorship

Title of Paper	Integral Length Scales in a Low-Roughness Atmospheric Boundary Layer
Publication Status	☑ Published ☐ Accepted for Publication ☐ Submitted for Publication ☐ Unpublished and Unsubmitted work written in manuscript style
Publication Details	Emes, M. J., Arjomandi, M., Kelso, R. M. and Ghanadi, F., 2016, 'Integral Length Scales in a Low-Roughness Atmospheric Boundary Layer', *18th Australasian Wind Engineering Society Workshop*, Adelaide, Australia.

Principal Author

Name of Principal Author (Candidate)	Matthew Emes		
Contribution to the Paper	Performed data analysis and interpretation, wrote manuscript and acted as corresponding author.		
Overall percentage (%)	70		
Certification:	This paper reports on original research I conducted during the period of my Higher Degree by Research candidature and is not subject to any obligations or contractual agreements with a third party that would constrain its inclusion in this thesis. I am the primary author of this paper.		
Signature		Date	3/11/17

Co-Author Contributions

By signing the Statement of Authorship, each author certifies that:

i. the candidate's stated contribution to the publication is accurate (as detailed above);

ii. permission is granted for the candidate in include the publication in the thesis; and

iii. the sum of all co-author contributions is equal to 100% less the candidate's stated contribution.

Name of Co-Author	Maziar Arjomandi		
Contribution to the Paper	Supervised development of work, helped in data interpretation and manuscript evaluation.		
Signature		Date	3/11/17

Name of Co-Author	Richard Kelso		
Contribution to the Paper	Supervised the research and contributed in academic discussion and manuscript review.		
Signature		Date	3/11/17

Name of Co-Author	Farzin Ghanadi		
Contribution to the Paper	Supervised the research and contributed in academic discussion and manuscript review.		
Signature		Date	03/11/2017

Integral Length Scales in a Low-Roughness Atmospheric Boundary Layer

M.J. Emes, M. Arjomandi, R.M. Kelso and F. Ghanadi

School of Mechanical Engineering
University of Adelaide, Adelaide, South Australia 5005, Australia

Abstract

This paper discusses the integral length scales in a low-roughness atmospheric boundary layer (ABL), based on the high-fidelity measurements of wind velocity. Results from the analysis shows that longitudinal integral length scales follow a linear relationship with height in a low-roughness ABL that deviates significantly from semi-empirical Engineering Sciences Data Unit (ESDU) 85020 model derived for open country and urban terrains with larger surface roughness heights. Although the model accurately predicts the integral length scales non-dimensionalised relative to the boundary layer thickness for the majority of the profile, they are over-predicted by more than double in the lowest 10% of the ABL, corresponding to the atmospheric surface layer (ASL). The analysis shows that the largest eddies at lower heights in the ASL over a very low roughness desert terrain have length scales similar to the characteristic lengths of physical structures positioned on the ground, which corresponds to the maximum wind loads for buildings. Hence, it is recommended that the integral length scales in the ASL are characterised over an estimated range at each of the four terrain categories in AS/NZS 1170.2 to ensure that buildings and other large physical structures can be optimised in terms of their size and location.

Introduction

Wind codes and standards for low- to medium-rise buildings adopt a simplified gust factor approach that assumes quasi-steady wind loads based on a maximum gust wind speed, which can lead to significant errors for very tall buildings with large dynamic responses to the large amplitude fluctuations during high-wind events such as gusts over short time intervals (Mendis et al., 2007). Current design methods in AS/NZS 1170.2 for estimating the peak wind loads on buildings are based on the peak wind speed associated with gusts over a short duration known as the gust period. Analysis of quasi-static wind loads by Emes et al. (2015) found that the the cost of heliostats in a concentrating solar thermal (CST) power tower plant becomes significant at design wind speeds above 10 m/s, beyond which a 5 m/s increase in design wind speed leads to a 34% increase in the total capital cost of a 120 m^2 heliostat. The frequency of gusts in the ABL has been accounted for by the gust factor method, however the length scales of turbulent eddies relative to the characteristic length of the structure is also known to significantly affect the peak wind loads (Holdø et al., 1982). Small eddies result in pressures on various parts of a structure that become uncorrelated with distance of separation, however large eddies whose size is comparable with the structure result in well correlated pressures over its surface, leading to maximum wind loads (Greenway, 1979; Mendis et al., 2007). Galloping and torsional flutter tend to occur when the turbulent eddies are comparable to the size of the body at small frequencies of the order of 1 Hz (Nakamura, 1993), which corresponds to the natural frequency of large buildings in the ABL (Arakawa and Yamamoto, 2004). Hence, consideration of the size of large-scale eddies in the ABL relative to the characteristic length of the structure can lead to significant savings in costs due to the reduced design wind loading.

The size of the largest eddies in the ABL has a significant effect on the fluctuating pressures on structures, which can result in fatigue damage and can lead to structural collapse. The integral length scale is a measure of the longest correlation distance between two points in the flow field that are separated by either distance or time (O'Neill et al., 2004). The longitudinal integral length scale ${}^{x}L_u$ is defined in Figure 1 at a given height z in the ABL as the streamwise spacing between two-dimensional spanwise eddies orientated in the axial direction (Emes et al., 2016). Holdø et al. (1982) found that the maximum base pressure coefficient on wind tunnel models of low-rise buildings of height D occurs at ${}^{x}L_u/D \approx 2.8$ when exposed to turbulence in the ABL compared to ${}^{x}L_u/D \approx 1.6$ for a uniform approaching flow. Designing for the larger ratio results in a 10% increase in drag coefficient on low-rise buildings (Holdø et al., 1982). Hence, the overall aim of this paper is to calculate longitudinal integral length scales using the autocorrelation function in a low-roughness ABL to determine the accuracy of a semi-empirical Engineering Sciences Data Unit (2002) model. This will be used to provide recommendations for improving the accuracy and versatility of the current methods in AS/NZS 1170.2 for calculating wind loads on permanent structures exposed to gusty wind conditions in the ABL.

Atmospheric Boundary Layer Characteristics

Records of wind velocities show that there are gusts or highly turbulent flow at all heights in the ABL, including the lowest 10% of the ABL known as the atmospheric surface layer (ASL) where permanent building structures are positioned on the ground. Turbulent phenomena such as gusts are very complex, however some characteristics of the fully-developed boundary layer wind over flat homogenous terrain can be modelled mathematically as a stationary random process with a zero mean value (Xu, 2013). The instantaneous wind speed can be decomposed as

$$U(z,t) = \overline{U}(z) + u'(z,t), \qquad (1)$$

where $\overline{U}(z)$ is the mean wind speed component at height z above the ground and $u'(z,t)$ is the turbulent wind fluctuation component averaged over the gust period t.

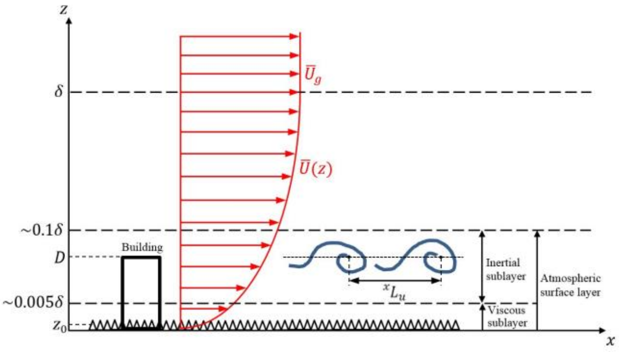

Figure 1. Turbulence characteristics and definition of integral length scale ${}^{x}L_u$ in the atmospheric boundary layer (Emes et al., 2016).

The mean wind speed profile in the ABL has been modelled to various degrees of accuracy by the power law, logarithmic law and Deaves-Harris model (Mendis et al., 2007). The power law has been found to be appropriate for heights around 30-300m, hence it is commonly used for the calculation of wind loads on buildings and other large structures (Cook, 1997). For the design of structures with height D less than 100m in the ABL, the logarithmic law is most appropriate for modelling the mean velocity profile under the assumption of asymptotic similarity in a neutral ABL (Sun et al., 2014).

$$\bar{U}(z) = \left(\frac{U_\tau}{k}\right) \ln\left(\frac{z}{z_0}\right) \tag{2}$$

Here U_τ (m/s) is the friction velocity representing the Reynolds shear stress $-\rho\overline{u'w'}$ at the surface, k is von Karman's constant (0.4) and z_0 (m) is the surface roughness height as a function of the average height of roughness elements on the ground in Figure 1, which can vary in scale from millimetres in a flat desert to metres in a dense urban area (Xu, 2013). The design wind speed at the height of structures is normally calculated in wind load design codes and standards, such as AS/NZS 1170.2 (Standards Australia, 2011) using an ultimate limit state wind speed with a 5% probability of being exceeded in a 50 year period (Emes et al., 2015; Mendis et al., 2007).

Turbulence intensity is commonly used to describe the level of turbulence in the time domain of the ABL, defined by the ratio of the root-mean-square of the fluctuating component of the instantaneous wind speed and the mean wind speed in Equation (2). However, the distribution of energy in the turbulent flow fluctuations is proposed by similarity theory to give rise to a cascade of eddies spanning a frequency domain and a large range of length scales (Tennekes and Lumley, 1972). Turbulent flow fluctuations are often characterised as coherent eddies in order to simplify the descriptions of the random three-dimensional eddying fluid motions in the ABL over a wide range of length scales. Coherent eddies exist for sufficient time periods to have a significant influence on the time-averaged statistics of a turbulent flow field (Venditti et al., 2013). The size of the largest eddies is defined by the integral length scale ${}^{x}L_u$ at the lower bound of the inertial subrange frequency domain in the ABL (Kaimal and Finnigan, 1994).

The largest eddies in the ABL are spatially extensive structures that require analysis of many points in space. Point velocity measurements as a function of time are transformed to spatially distributed data by adopting Taylor's hypothesis that eddies are embedded in a frozen turbulence field, which is convected downstream at the mean wind speed $\bar{U}$ (m/s) in the streamwise x direction and hence do not evolve with time (Kaimal and Finnigan, 1994). The integral length scale at a given height in the ABL is therefore calculated as (O'Neill et al., 2004; Swamy et al., 1979).

$${}^{x}L_u = {}^{x}T_u\bar{U}, \tag{3}$$

where ${}^{x}T_u$ (s) is the integral time scale representing the time taken for the largest eddies to traverse the inertial subrange in the ABL before they are dissipated by viscosity at the Kolmogorov length scale η. Larger integral length scales cause slower variations in the time series and are thus associated with longer integral time scales. Integral time scales are commonly estimated from the covariance of single point velocity data between two different times using the normalised autocorrelation function $R_u(\tau)$ of the fluctuating component of the turbulence velocity (Kaimal and Finnigan, 1994)

$$R_u(\tau) = \frac{\overline{u'(t)u'(t+\tau)}}{\overline{u'(t)u'(t)}} \tag{4}$$

Here $\boldsymbol{\tau}$ (s) is the time lag with respect to time $\boldsymbol{t}$ over which $\boldsymbol{R(\tau)}$ decreases in magnitude from one to zero as $\boldsymbol{u'(t+\tau)}$ becomes uncorrelated and statistically independent of $\boldsymbol{u'(t)}$. The autocorrelation function is calculated from the velocity data using the xcorr function in Matlab. The integral time scale is defined by

$${}^{x}T_u = \int_0^\infty R_u(\tau)\,d\tau \approx \int_0^{\tau_0} R_u(\tau)\,d\tau, \tag{5}$$

where the integral is taken to the first-zero crossing τ_0 of the autocorrelation function by assuming that $R(\tau)$ fluctuates very close to zero after this point (Swamy et al., 1979). Alternatively ${}^{x}T_u$ has been approximated by integrating to the point when $R(\tau)$ reaches a value of $1/e \approx 0.37$ or from the frequency at the peak of the Engineering Sciences Data Unit (2002) power spectral density (PSD) function derived from the von Karman spectral equations and fitted to the measured data (Flay and Stevenson, 1988). Analysis of these three methods for calculating ${}^{x}T_u$ by Flay and Stevenson (1988) showed that ${}^{x}L_u$ is largely underpredicted in an open country terrain (z_0 = 30mm) because of uncertainties in a fitted model PSD curve. A large portion of the autocorrelation function is not accounted for in the integral to the upper limit $1/e$ (O'Neill et al., 2004). Hence, the first-zero crossing serves as an upper estimate for ${}^{x}L_u$ that is most appropriate for a low-roughness ABL where smaller ${}^{x}L_u$ means that $R(\tau)$ will approach zero more quickly (Emes et al., 2016).

Integral Length Scales in a Low-Roughness ABL

High fidelity measurements of wind velocity were acquired from a field experiment study carried out by Hutchins et al. (2012) at the SLTEST facility in the western Utah Great Salt Lake desert. The mean velocity and turbulence intensity profiles lie within a 10% experimental error of the logarithmic law profile in Equation (2) for a mildly transitional rough surface with friction velocity $U_\tau =$ 0.19 m/s and equivalent sand grain roughness height $k_s^+ \approx 22$ or surface roughness height $z_0 \approx$ 1.8mm (Marusic et al., 2013). Velocity data during the field experiment (Hutchins et al., 2012) were obtained during a one hour period of neutral buoyancy and steady wind conditions, such that the velocity profiles are expected to be generated by a shear-driven wall-bounded flow (Marusic and Hutchins, 2008). Velocities were measured using sonic anemometers at logarithmically-spaced heights in the ABL with thickness $\delta \approx$ 60m estimated from two-point correlations of velocity data and prior radiosonde measurements (Metzger et al., 2007). Sonic anemometers tend to degrade significantly in accuracy at lower heights where the vertical velocity gradients are typically the largest and the eddy scales of interest are too small to be resolved accurately (Kaimal and Finnigan, 1994). However, they are preferred for spectral analysis of integral length scales in the ABL compared to the widely-used cup anemometer. Hence, sonic anemometers are the most appropriate measurement device for dynamic and vibrational responses on buildings and large structures in the ABL arising from the interaction with large eddies of a similar size.

Figure 2 compares the autocorrelation function R_u calculated using Equation (4) at three heights in the low-roughness ABL. The amplitude of the fluctuation of R_u about zero increases with increasing height in the ABL. This indicates that there is a wider range distribution of eddy sizes at larger heights in the ABL. For the analysis of dynamic wind loads on large physical structures, the largest eddies at each height need to be determined. The integral time scales are calculated using Equation (5) for the following three domains:

1. Integrate over the entire domain τ_∞
2. Integrate to the first-zero crossing τ_0
3. Integrate to where R_u falls to $1/e$

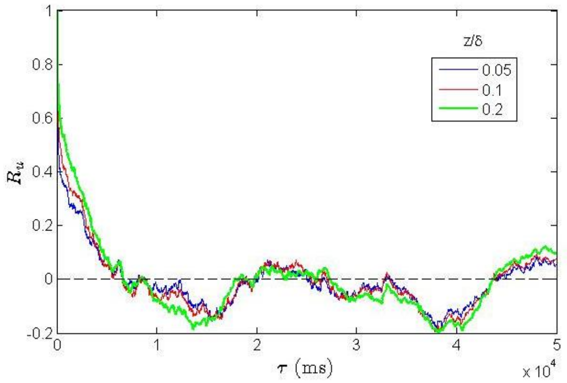

Figure 2. Autocorrelation function $R_u(\tau)$ of velocity data at 3 heights in a low-roughness ABL in Utah, USA.

Figure 3 presents the integral length scales calculated for three different integration domains using velocity data collected by Hutchins et al. (2012) in a low-roughness ABL in Utah, USA. The integration of the full time domain is less than to the first-zero crossing as expected from observation of the significant portion below the x-axis in the autocorrelation functions in Figure 2. Integral length scales are significantly under-predicted, particularly at lower heights, using the third integration domain to $1/e$. This suggests that an insufficient amount of the time domain is covered to capture the size of the largest eddies with low frequencies covered using this method. Comparison of the other two methods shows a 27% difference at the lowest measurement height of 1.42m (z/δ = 0.024) and a 67% difference at the largest measurement height of 25.69m (z/δ = 0.43). These differences in the estimated ${}^xL_u$ show the effect of the fluctuation of R_u after the first-zero crossing. The integral length scale profile calculated to τ_0 follows closer to a linear trend at lower heights, however the profile appears to become more logarithmic when integrating R_u over the whole time domain. The autocorrelation function is expected to decay to zero within a sufficiently large spatial domain, hence the use of the whole domain may lead to erroneous results for ${}^xL_u$ in cases such as Figure 2 where there are random fluctuations in R_u after the first-zero crossing. O'Neill et al. (2004) showed that ${}^xL_u$ becomes independent of the domain size when the spatial domain is at least six times larger than ${}^xL_u$. In the case of a low-roughness ABL with a sufficiently large spatial domain, the first-zero crossing is the most appropriate integration domain for ${}^xT_u$ where smaller ${}^xL_u$ means that $R(\tau)$ will approach zero more quickly.

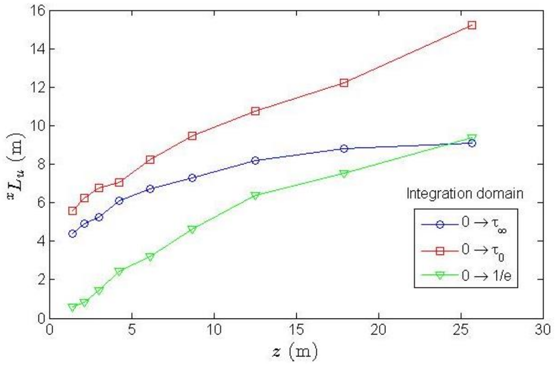

Figure 3. Integral length scales determined using three different integration domains of $R_u(\tau)$ as a function of height z in a low-roughness ABL in Utah, USA.

The majority of integral length scale data available in the literature has been obtained from field-site anemometer velocity measurements in large-scale ABLs, however there are few recognised standards due to the diverse nature and scales of ABLs. Table 1 presents the reference atmospheric conditions for the semi-empirical data developed by Engineering Sciences Data Unit (ESDU) 85020 for the integral length scales of atmospheric turbulence over uniform terrain in a neutral ABL. This data set extends previous empirical formulations for ${}^xL_u$ to higher equivalent design wind speeds up to 30 m/s at heights corresponding to taller buildings for which dynamic effects are more significant (Engineering Sciences Data Unit, 2002). A correction factor k_L is used to account for the variation of ${}^xL_u$ with a change in mean wind speed $\bar{U}_{10r}$ = 6.19 m/s at a 10m height in the field experiment ABL (Hutchins et al., 2012) within an estimated ±8% error (Engineering Sciences Data Unit, 2002) such that the integral length scales predicted by the ESDU model can be compared with the field experiment data in Figure 4.

$\bar{U}_{10r}$	f	z_0
20 m/s	1×10^{-5} rad/s	0.03 m

Table 1. Reference ABL characteristics for ESDU 85020 integral length scale data (Engineering Sciences Data Unit, 2002).

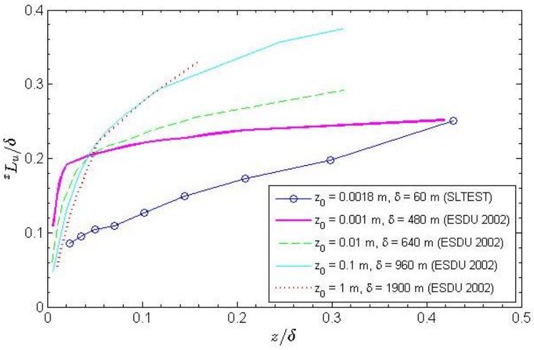

Figure 4. Comparison of integral length scales calculated for a low-roughness ABL with those predicted from ESDU 85020 (2002) correlations as a function of non-dimensional height z/δ in the ABL.

The results from a low-roughness ABL in the field experiment in Figure 4 show that ${}^xL_u/\delta \approx 0.1$ at $z/\delta \approx 0.05$, corresponding to half that of the predicted ${}^xL_u/\delta \approx 0.2$ by the ESDU 85020 model (Emes et al., 2016). The linear relationship between ${}^xL_u$ and z in Figure 4 suggests that physical structures positioned on the ground in a low-roughness ABL are exposed to eddies that are a similar size (${}^xL_u/D \approx 1$), leading to the maximum wind loads due to turbulent buffeting (Greenway, 1979; Mendis et al., 2007). The significance of the relationship between ${}^xL_u$ and z_0 has major implications for the dynamic wind loads on low-rise buildings exposed to gusts in the ABL, which can lead to 10% over-prediction of the drag coefficient for $I_u = 25\%$ at $z/\delta = 0.1$ (Holdø et al., 1982). The characteristics of low-roughness ABLs appear to differ considerably from urban terrains with larger roughness heights. Further understanding of how unsteady wind loads vary with the ratio ${}^xL_u/D$ would allow for optimisation of the sizes of buildings and structures based on the largest eddies that they are likely to be exposed to at a given height in the ABL. This could be achieved through full-scale measurements of ${}^xL_u$ at each of the characteristic z_0 values corresponding to the main terrain categories in building design standards. For example, estimation of ${}^xL_u$ at each of the four terrain categories in AS/NZS 1170.2 would ensure that buildings and other large physical structures can be optimised in terms of their size and location.

Changes in surface roughness are shown in Figure 4 to have a significant effect on integral length scales that can vary by as much as an order of magnitude from 10m to 100m, hence the specification of integral length scales in wind load codes and design standards such as AS/NZS 1170.2 would allow for optimisation of the size and location of a physical structure such that the maximum wind loads from the exposure to large eddies of a similar size can be minimised. More accurate prediction of the variation of ${}^{x}L_u$ with height in the lowest 100m of the ABL is required for low-roughness terrains, which tend to deviate from semi-empirical models developed for high roughness terrains such as urban environments. Calculation of the estimated range of integral length scales from sonic anemometer velocity measurements at each of the four terrain categories in AS/NZS 1170.2 (z_0 = 0.002m, 0.02m, 0.2m, 2m) would ensure that buildings and other large structures are not overdesigned following Engineering Sciences Data Unit (2002) models that predict eddies over double the size of those that exist in low-roughness ABLs.

Conclusions

Longitudinal integral length scales in the lowest 10% of the ABL predicted by the Engineering Sciences Data Unit (2002) model are over double those calculated from autocorrelation of velocity measurements in a low-roughness ABL in the Utah desert. Although ESDU correlations have been shown to be an upper bound on integral length scales calculated in full-scale ABLs, the predicted logarithmic relationship with non-dimensional height in the ABL is not appropriate for low-roughness ABLs where a linear relationship is observed. The sizes of the largest eddies that physical structures are exposed to at a given height in the ABL are not taken into account in the calculation of design wind loads in wind codes and standards following the quasi-steady gust factor method. However, knowledge of the estimated size of the largest eddies that a physical structure is exposed to at a given location can assist in the optimisation of the critical scaling parameters of the structure during the design stage. The present analysis shows that the largest eddies at lower heights in the ASL over a very low roughness desert terrain have length scales similar to the characteristic lengths of physical structures positioned on the ground, which corresponds to the maximum wind loads for buildings.

Acknowledgments

The authors would like to acknowledge Nicholas Hutchins and others at the University of Melbourne for their contribution of velocity data obtained from the SLTEST facility in Utah, USA. Support for the work has been provided by the Australian Solar Thermal Research Initiative (ASTRI), through funding provided by the Australian Renewable Energy Agency (ARENA).

References

Arakawa, T., Yamamoto, K., 2004, Frequencies and damping ratios of a high rise building based on microtremor measurement, in: Proc., 13 th World Conference on Earthquake Engineering.

Cook, N.J., 1997, The Deaves and Harris ABL model applied to heterogeneous terrain, Journal of Wind Engineering and Industrial Aerodynamics 66, 197-214.

Emes, M.J., Arjomandi, M., Kelso, R.M., Ghanadi, F., 2016, Understanding of the relationship between gust factor, turbulence intensity and integral length scales in the atmospheric boundary layer, submitted to Journal of Wind Engineering and Industrial Aerodynamics.

Emes, M.J., Arjomandi, M., Nathan, G.J., 2015, Effect of heliostat design wind speed on the levelised cost of electricity from concentrating solar thermal power tower plants, Solar Energy 115, 441-451.

Engineering Sciences Data Unit, 2002, Characteristics of atmospheric turbulence near the ground - Part II: single point data for strong winds (neutral atmosphere), London, ESDU 85020.

Flay, R., Stevenson, D., 1988, Integral length scales in strong winds below 20 m, Journal of Wind Engineering and Industrial Aerodynamics 28, 21-30.

Greenway, M., 1979, An analytical approach to wind velocity gust factors, Journal of Wind Engineering and Industrial Aerodynamics 5, 61-91.

Holdø, A., Houghton, E., Bhinder, F., 1982, Some effects due to variations in turbulence integral length scales on the pressure distribution on wind-tunnel models of low-rise buildings, Journal of Wind Engineering and Industrial Aerodynamics 10, 103-115.

Hutchins, N., Chauhan, K., Marusic, I., Monty, J., Klewicki, J., 2012, Towards reconciling the large-scale structure of turbulent boundary layers in the atmosphere and laboratory, Boundary-layer meteorology 145, 273-306.

Kaimal, J.C., Finnigan, J.J., 1994, Atmospheric boundary layer flows: their structure and measurement,

Marusic, I., Hutchins, N., 2008, Study of the log-layer structure in wall turbulence over a very large range of Reynolds number, Flow, Turbulence and Combustion 81, 115-130.

Marusic, I., Monty, J.P., Hultmark, M., Smits, A.J., 2013, On the logarithmic region in wall turbulence, Journal of Fluid Mechanics 716, R3.

Mendis, P., Ngo, T., Haritos, N., Hira, A., Samali, B., Cheung, J., 2007, Wind loading on tall buildings, EJSE Special Issue: Loading on Structures 3, 41-54.

Metzger, M., McKeon, B., Holmes, H., 2007, The near-neutral atmospheric surface layer: turbulence and non-stationarity, Philosophical Transactions of the Royal Society of London A: Mathematical, Physical and Engineering Sciences 365, 859-876.

Nakamura, Y., 1993, Bluff-body aerodynamics and turbulence, Journal of Wind Engineering and Industrial Aerodynamics 49, 65-78.

O'Neill, P., Nicolaides, D., Honnery, D., Soria, J., 2004, Autocorrelation functions and the determination of integral length with reference to experimental and numerical data, in: 15th Australasian Fluid Mechanics Conference The University of Sydney, Sydney, Australia, pp. 13-17.

Standards Australia, 2011, Structural design actions, Part 2: Wind actions, AS/NZS 1170.2.

Sun, H., Gong, B., Yao, Q., 2014, A review of wind loads on heliostats and trough collectors, Renewable and Sustainable Energy Reviews 32, 206-221.

Swamy, N., Gowda, B., Lakshminath, V., 1979, Auto-correlation measurements and integral time scales in three-dimensional turbulent boundary layers, Applied Scientific Research 35, 237-249.

Tennekes, H., Lumley, J.L., 1972, A first course in turbulence, MIT press.

Venditti, J.G., Best, J.L., Church, M., Hardy, R.J., 2013, Coherent Flow Structures at Earth's Surface, John Wiley & Sons.

Xu, Y.L., 2013, Wind Characteristics in Atmospheric Boundary Layer, Wind Effects on Cable-Supported Bridges 25-59.

Appendix B

Generation of Large-Scale Vortices

B.1. Section Overview

This appendix describes an experimental technique for the generation of large-scale vortices in a wind tunnel to analyse a method for the controlled generation of vortices of a given size in the atmospheric boundary layer (ABL). A sinusoidal oscillation of a wall-mounted fence in the direction of the flow allowed the forcing of periodic motions in the reattached shear layer with a controlled length scale. Mean velocity, normal stress, Reynolds stress and integral length scales profiles were calculated downstream of fences of four different heights that spanned the width of the tunnel. The amplitude and frequency of the fence oscillation were controlled to determine their effect on the sizes of the largest eddies in the reattached shear layer. It was found that the height of the fence had the largest effect on the integral length scales non-dimensionalised with fence height. Although the oscillation amplitude of the fence had a negligible effect on the integral length scales, the largest vortices in the middle region of the reattached shear layer were generated at an oscillation frequency of 5 Hz closely corresponding to the average vortex passage frequency of the stationary fence. The generation of large-scale vortices with a controlled length scale can provide further knowledge on the dynamic wind loads arising from the effects of resonance-induced vibrations and vortex-structure interaction of small physical structures, such as heliostats and MAVs in the lowest 6 m of the ABL.

B.2. Experimental Technique using an Oscillating Fence

Statement of Authorship

Title of Paper	An Experimental Technique for the Generation of Large-Scale Spanwise Vortices in a Wind Tunnel	
Publication Status	☑ Published ☐ Submitted for Publication	☐ Accepted for Publication ☐ Unpublished and Unsubmitted work written in manuscript style
Publication Details	Emes, M. J., Ghanadi, F., Arjomandi, M. and Kelso, R. M., 2016, 'An Experimental Technique for the Generation of Large-Scale Spanwise Vortices in a Wind Tunnel', *20th Australasian Fluid Mechanics Society Conference*, Perth, Australia.	

Principal Author

Name of Principal Author (Candidate)	Matthew Emes		
Contribution to the Paper	Performed data analysis and interpretation, wrote manuscript and acted as corresponding author.		
Overall percentage (%)	70		
Certification:	This paper reports on original research I conducted during the period of my Higher Degree by Research candidature and is not subject to any obligations or contractual agreements with a third party that would constrain its inclusion in this thesis. I am the primary author of this paper.		
Signature		Date	3/11/17

Co-Author Contributions

By signing the Statement of Authorship, each author certifies that:

i. the candidate's stated contribution to the publication is accurate (as detailed above);

ii. permission is granted for the candidate in include the publication in the thesis; and

iii. the sum of all co-author contributions is equal to 100% less the candidate's stated contribution.

Name of Co-Author	Farzin Ghanadi		
Contribution to the Paper	Supervised development of work, helped in data interpretation and manuscript evaluation.		
Signature		Date	3/11/17

Name of Co-Author	Maziar Arjomandi		
Contribution to the Paper	Supervised development of work, helped in data interpretation and manuscript evaluation.		
Signature		Date	3/11/17

Name of Co-Author	Richard Kelso		
Contribution to the Paper	Supervised the research and contributed in academic discussion and manuscript review.		
Signature		Date	3/11/17

An Experimental Technique for the Generation of Large-Scale Spanwise Vortices in a Wind Tunnel

M.J. Emes, F. Ghanadi, M. Arjomandi and R.M. Kelso

Department of Mechanical Engineering
University of Adelaide, Adelaide, South Australia 5005, Australia

Abstract

The presence of large-scale vortices with high spanwise coherence has been observed in the atmospheric boundary layer (ABL). This study investigates an innovative technique to generate a large-scale spanwise vortex from the oscillation of a surface-mounted fence in a wind tunnel. Characteristics of the large vortex with a well-defined length scale and its development with downstream distance behind the fence were investigated. Time-averaged profiles of velocity, normal and Reynolds stresses were measured to determine the dominant frequencies of the large vortices in the wake of the oscillating fence. Longitudinal length scales of the spanwise vortices were calculated using the autocorrelation of velocity data. It was found that the size of the largest spanwise vortices are most significantly influenced by the height of the fence, such that the integral length scales increased by 52mm for a 20mm increase in fence height. Spanwise vortices were also found to be 11mm larger when oscillating the fence at the vortex shedding frequency behind a stationary fence. The oscillation amplitude of the fence was found to have a negligible effect on the size of the large spanwise vortices.

Introduction

Characterisation of coherent structures in the lower atmospheric boundary layer (ABL) requires an understanding of turbulent phenomena that are responsible for gusts on small physical structures such as heliostats and dynamic wind loads on large civil structures. Wind codes and standards adopt a quasi-steady gust factor approach based on a maximum gust wind speed and turbulence intensity for the estimation of peak wind loads, however the dynamic response of large civil structures is more significantly influenced by the frequency distribution of the longitudinal velocity and the size of the largest eddies in the ABL [5]. There exists a wide range of turbulent structures within the ABL, such as very large superstructures observed as counter-rotating pairs of horseshoe vortices in the logarithmic region [6, 11]. Spanwise vortices with an axis of rotation perpendicular to the flow are components of these superstructures resulting from the interaction of separating and reattaching shear layers and tripping around obstacles on the ground [17]. The presence of large-scale eddies with high spanwise coherence has been observed in the shear layer, even for significant levels of free-stream turbulence from small-scale buffeting [20]. Coherent structures within canonical turbulent boundary layers have typically been quantified through the measurement of planar vortices such as spanwise vortices, however these structures are yet to be fully quantified from high resolution velocity measurements in the ABL because of the limited number of vertical data points along the height of a wind mast [16].

Large-scale spanwise vortices have been found to be responsible for most of the entrainment in the naturally occurring shear layer, leading to dynamic responses of large structures such as buildings and bridges. Large eddies of a similar size to the structure result in well correlated pressures over its surface as the eddy engulfs the structure, leading to maximum wind loads [4, 12]. Structural failure due to excessive deflections and stresses from galloping and torsional flutter tend to occur at small frequencies of the order of 1 Hz when the turbulence length scales are comparable to the size of the body, however the effect becomes negligible when turbulence scale is increased beyond the order of magnitude of the body scale [13]. The size of the largest eddies is defined by the integral length scale in the inertial subrange of frequencies in the ABL [7]. The longitudinal integral length scale ${}^{x}L_{u}$ (m) at a given height is defined as the streamwise spacing between two-dimensional spanwise vortices orientated in the axial direction. Hence, the aim of this paper is to characterise the size of a large spanwise vortex that physical structures are likely to be exposed to in the ABL.

Time-averaged and phase-averaged measurements of velocity characteristics have previously been used to identify, analyse and characterise large-scale vortex structures within the separated shear layer in turbulent flows such as behind bluff bodies [15]. The near wake behind bluff bodies is affected by flow separation and reattachment and vortex shedding, with the associated length scales of the shear layer thickness and the spacing between the two separated shear layers given by the body height respectively [13]. Periodic motions in the form of a von Karman vortex street behind circular cylinders and flat plates have been widely studied in the literature through flow visualisation, conditional averaging techniques and spectral analyses. A body is defined as bluff if there is separated flow over a substantial proportion of its surface, however the isolation of a single coherent large-scale vortex in the wake of bluff bodies has proven to be difficult at high Reynolds numbers above 20,000 because of the development of instabilities and the interaction of unsteady vortices [1]. The generation of large two-dimensional spanwise vortices has been most effectively produced by the forcing of periodic motions in the shear layer [8]. This has previously been investigated using several dynamic methods, such as oscillating cylinders and airfoils to generate large spanwise vortex structures. However, the limitation of cylindrical bluff bodies with a change of surface curvature is that shed vortices exhibit larger spanwise waviness and dispersion in streamwise spacing [10]. Alternatively, there is a straight line of flow separation from a rectangular plate that is fixed at its edges, leading to more coherent vortices with well-defined length scales. Small-amplitude sinusoidal oscillations of a floor-mounted normal plate in the streamwise direction have previously been demonstrated by Kelso *et al.* [9] to generate large-scale spanwise vortices with improved coherence and periodicity compared to a stationary fence. Hence, the scope of this study is to investigate the effect of oscillation amplitude, oscillation frequency and height of a floor-mounted normal flat plate on the integral length scales of the largest vortices behind the oscillating fence.

Experimental Setup

Oscillating Fence in Boundary Layer Rig

Experimental measurements were taken in a closed return wind tunnel at the University of Adelaide. Figure 1 shows the schematic layout of the boundary layer rig containing an acrylic flat plate with an elliptical leading edge for minimal flow separation from the plate and smooth development of the boundary layer. The flat plate has previously been designed with a 0.5 m × 0.3 m cross-section and 2.15 m test section length. Plexiglass side walls of the test section are adjustable to control pressure gradient along the flat plate. An adjustable angle trailing edge flap of 0.2 m length is also used to ensure the stagnation point is on the measurement side of the plate and the boundary layer is developed smoothly. The upstream boundary layer was perturbed using a 3 mm trip wire, giving a boundary layer thickness δ of 25 mm (δ/h = 0.31) at the position of the fence. The free-stream turbulence intensity at the tunnel's centreline was measured at 0.5%.

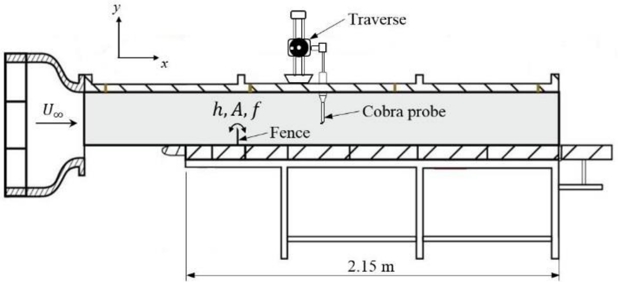

Figure 1. Schematic diagram of the traversing mechanism and the boundary layer rig in the wind tunnel.

A thin rectangular plate of 60mm height (h) with aspect ratio (w/h) of 4.17 was mounted spanwise to the surface of the acrylic plate using hinges in the boundary layer rig, as shown in Figure 2. One end of the aluminium fence was connected to a high-torque JR ES579 servo motor via a horn pin, as shown inset in Figure 2. The servo motor was controlled by an Arduino Uno microcontroller through Matlab to oscillate the fence at frequencies from 1-10 Hz and amplitudes between 2mm and 12mm. Velocities were measured in the wake using a high-frequency Cobra probe for over 25 oscillation cycles of the fence. The free-stream Reynolds number Re_∞ was approximately 28,000 based on the fence height and the freestream velocity U_∞ = 7 m/s. The Reynolds number Re_x based on the distance x behind the fence was in the range between 100,000 and 280,000. The top edge of the fence was chamfered at 30° to ensure clean separation and controlled generation of spanwise vortices was achieved by oscillating the fence at a peak-to-peak amplitude A of 4mm (A/h = 0.03) and forcing frequency f = 5 Hz corresponding to a Strouhal number of 0.043 and fence-tip velocity of approximately 0.04 m/s.

Flow Measurement Technique

A Turbulent Flow Instrumentation (TFI) Cobra pressure probe was used to measure the flow in the wake of the oscillating fence. The multi-hole probe with 2.5 kPa pressure transducers was dynamically calibrated by the manufacturer to allow accurate flow measurements up to 90 m/s and provide a frequency response up to 2 kHz as a more robust alternative to hot-wire anemometers. The probes were able to resolve the three orthogonal components of velocity and static pressure, as long as the flow vector was contained within a cone of ±45° around the probe x-axis [19]. This enabled resolution of the constantly fluctuating velocity vector in the turbulent flow when the probe was approximately aligned with the freestream flow direction and the turbulence intensities were not excessively large ($I_u < 30\%$).

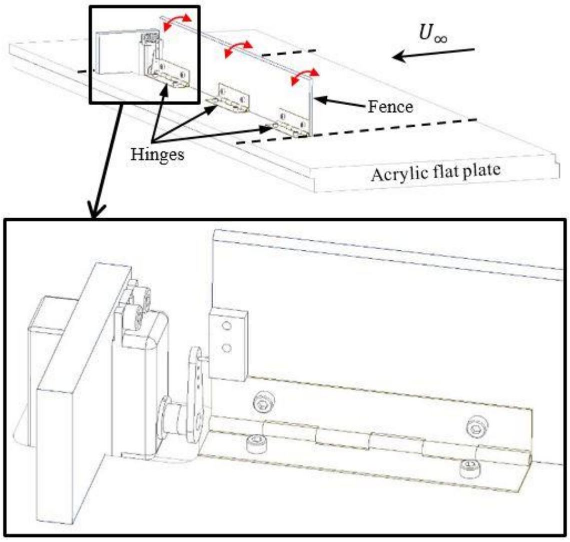

Figure 2. Schematic diagram showing the oscillating fence hinged to the acrylic flat plate. Dashed lines indicate the location of the Plexiglass side walls of the boundary layer rig. The inset shows the connection of the servo motor to the fence via a servo horn pin.

Integral Length Scales

The sizes of the largest eddies in the wake of the oscillating fence are defined by the integral length scale ${}^{x}L_u$ at the lower bound of the inertial subrange frequency domain in the ABL [7]. Point velocity measurements as a function of time are transformed to spatially distributed data by adopting Taylor's hypothesis that eddies are embedded in a frozen turbulence field, which is convected downstream at the mean wind speed $\overline{U}$ (m/s) in the streamwise x-direction and hence do not evolve with time [7]. The integral length scale at a given height in the ABL is therefore calculated as [14, 18]

$$ {}^{x}L_u = {}^{x}T_u \overline{U}, \tag{1}$$

where ${}^{x}T_u$ (s) is the integral time scale representing the time taken for the largest eddies to traverse the inertial subrange in the ABL before they are dissipated by viscosity at the Kolmogorov length scale η. Integral time scales are commonly estimated from the covariance of single point velocity data between two different times using the normalised autocorrelation function $R_u(\tau)$ of the fluctuating turbulent component of the velocity [7]

$$R_u(\tau) = \frac{\overline{u'(t)u'(t+\tau)}}{\overline{u'(t)u'(t)}} \tag{2}$$

Here τ (s) is the time lag with respect to time t over which $R(\tau)$ decreases in magnitude from one to zero as $u'(t+\tau)$ becomes uncorrelated and statistically independent of $u'(t)$. The autocorrelation function is calculated from the velocity data using the *xcorr* function in Matlab. The integral time scale is defined by

$$ {}^{x}T_u = \int_0^\infty R_u(\tau)\, d\tau \approx \int_0^{\tau_0} R_u(\tau)\, d\tau, \tag{3}$$

where the integral is taken to the first-zero crossing τ_0 of the autocorrelation function by assuming that $R(\tau)$ fluctuates very close to zero after this point [14, 18]. Alternatively ${}^{x}T_u$ is approximated from the frequency at the peak of the Engineering Sciences Data Unit [2] power spectral density (PSD) function derived from the von Karman spectral equations and fitted to the measured data [3].

Results

Time-Averaged Velocity and Stress Profiles

Figure 4 presents the time-averaged u and v velocity profiles in the streamwise x and vertical y directions, which have been non-dimensionalised with respect to the freestream velocity U_∞. Mean u-velocity profiles in Figure 4(a) at the two closest positions behind the fence are negative for $y/h \leq 1$, which shows that there is recirculation in the near-wake region directly behind the fence as the shear layer has detached from the wall surface around the oscillating fence. The mean streamwise velocity u at the closest measurement height to the ground (y/h = 0.1) is approximately zero at x/h = 8, which indicates that the reattachment length is approximately $8h$ for the oscillating fence, compared to $10h$ for the stationary fence. It is also apparent from Figure 4(a) that measurements did not extend to the height of the shear layer where $\bar{u}/U_\infty$ = 1 at all streamwise positions. Mean vertical v-velocity profiles in Figure 3(b) are close to zero and show some scatter in the recirculation region, however they become negative with increasing height as the shear layer reattaches downstream.

The time-averaged profiles of Reynolds stresses as a function of the streamwise position behind the fence have also been investigated. As shown in Figure 4(a), the peak stresses occur at the middle of the shear layer around y/h = 1.5 at the two nearest positions behind the fence and show a general decrease in magnitude with streamwise distance. The maximum Reynolds shear stress occurs at x/h = 5, which is in an indication of turbulent stress production and rapid shear layer growth from the direct roll-up of large-scale eddies. The stress profiles at x/h = 8 and 10 in Figure 4(b) show that the shear stresses are comparable to those measured by Kelso *et al.* [9], however the maximum Reynolds stresses are 13% lower due to the smaller forcing velocity of the fence relative to the freestream velocity in this study.

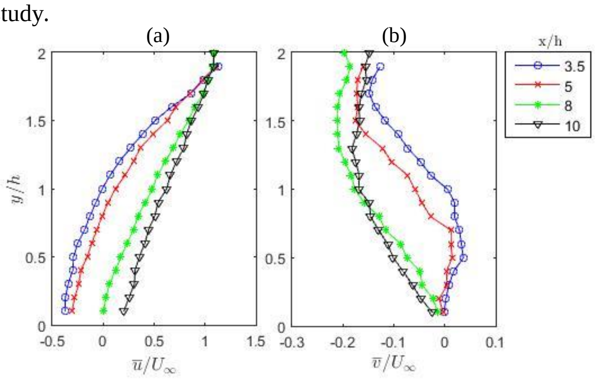

Figure 3. Time-averaged velocity profiles: (a) Streamwise, (b) Vertical; normalised to the freestream velocity U_∞ at four downstream distances of the 60mm oscillating fence (A/h = 0.03, f = 5 Hz).

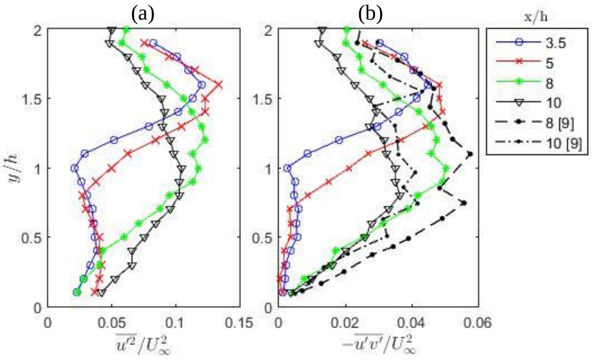

Figure 4. (a) Streamwise normal stress $\overline{u'^2}/U_\infty^2$; (b) Reynolds shear stress $-\overline{u'v'}/U_\infty^2$ compared with experimental data [9].

Integral Length Scales

Figure 5(a) shows that the length scales of eddies are the order of the fence height, increasing with height in the reattaching shear layer to $1.27h$ and $1.37h$ respectively at x/h = 8 and 10 respectively. The maximum gradient in the shear layer occurs further upstream at x/h = 3.5, where the spanwise vortices roll up and merge as the separated shear layer develops downstream. Hence, the largest eddies are expected to be developed into a well-organised shape in the region around reattachment at $x/h \geq 8$. With further distance downstream at $x/h \geq 12$, the vortices become elongated and hence the longitudinal integral length scale ${}^xL_u$ increases to a maximum value of $2h$.

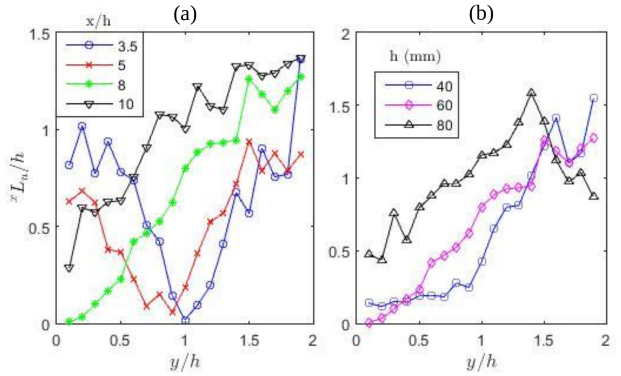

Figure 5. (a) Integral length scale profiles calculated using the autocorrelation function as a function of downstream distance (x/h) and non-dimensionalised with the height of the oscillating fence (h = 60 mm); (b) Effect of fence height on integral length scales at x/h = 8 downstream of the oscillating fence (A/h = 0.03, f = 5 Hz).

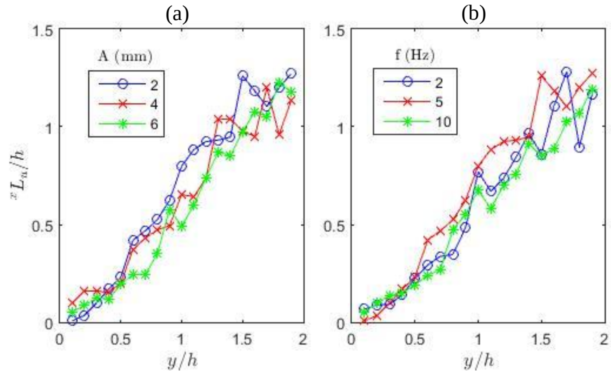

Figure 6. Effect of oscillation (a) amplitude A, and (b) frequency f on integral length scales at x/h = 8 downstream of the 60mm fence.

Figure 5(b) shows that the size of the largest spanwise vortices at x/h = 8 and the largest gradients of increasing ${}^xL_u$ occur at heights around the middle of the reattaching shear layer (0.5 < y/h < 1.5). The integral length scale non-dimensionalised by the fence height ${}^xL_u/h$ increases with height to a peak value shown in Table 1, before decreasing and fluctuating after this point. The position of the largest spanwise vortices become closer to the wall with increasing fence height at x/h = 8. This is believed to be due to increased blockage of the tunnel with increasing fence height.

h (mm)	**${}^xL_u/h$**	**y/h**
40	1.41	1.6
60	1.26	1.5
80	1.59	1.4

Table 1. Sizes of the largest spanwise vortices and their position within the shear layer at x/h = 8 as a function of fence height.

Figure 6(a) shows that the integral length scale profiles at x/h = 8 are not significantly influenced by a change in the amplitude of the sinusoidal oscillation of the 60mm fence. However, the largest spanwise vortices are generated at an oscillation frequency of 5 Hz in Figure 6(b), which is close to the vortex shedding frequency for a stationary fence. Forcing the shear layer at this frequency appears to cause the direct roll-up of large-scale two-dimensional vortices [9], Hence, a 5 Hz oscillation frequency was used as the operating point in this study.

Discussion

It is clear that the forcing of the fence leads to substantial change in the development of the shear layer, leading to more rapid shear layer growth and turbulent stress production. The maximum Reynolds shear stresses show that the development of large-scale vortices through merging and direct roll-up mechanisms at x/h = 5-8 corresponds to the vortices with the largest integral length scales. The largest vortices continue to increase in size after shear layer reattachment at x/h = 8 as they become elliptical due to vortex stretching.

The results show that the largest spanwise vortices are most significantly affected by changes in the fence height. The maximum integral length scale increases by 52mm (26%) in the middle of the shear layer when the fence height increases from 60mm to 80mm. In comparison, the length scales in the middle of the shear layer ($0.5 < y/h < 1.5$) are 11mm (18%) larger for a 5 Hz oscillation frequency than for 2 Hz and 10 Hz. This suggests that this frequency of oscillation has enhanced the roll-up mechanism of vortices from the tip of the fence that have developed to become larger further downstream.

There are some experimental errors in the calculation of integral length scales. Time samples of the order of 10 minutes to 1 hour would usually be required in the ABL, however only 5 second time samples were possible in this study due to the large quantity of measurements required. Taylor's hypothesis of frozen turbulence implies the assumption that the constant mean velocity is large with respect to the turbulence fluctuations and combined with the 2 m/s lower measurement limit of the Cobra probe, the integral length calculated for $y/h < 0.7$ at x/h = 8 are considered to be a rough estimate with a larger error. The limitation of the probe's cone of acceptance also leads to uncertainty of the length scales in the recirculation region at x/h = 3.5 and 5. However, after reattachment at x/h = 8 and 10 the integral length scales calculated using the first-zero crossing method are estimated to have a 95% confidence interval assuming a Gaussian distribution.

Conclusion

Wind tunnel results have shown that large spanwise vortices are generated by the forcing of the shear layer behind an oscillating fence. The integral length scales of these vortices are significantly affected by the fence height, such as a 26% increase in the maximum length scale when increasing the fence height from 60mm to 80mm. The amplitude of the fence oscillation has a negligible influence on the size of the largest vortices at the downstream position of shear layer reattachment. However, the average integral length scale of vortices in the middle region of the shear layer can be increased by 18% when the frequency of oscillation is approximately equal to the vortex shedding frequency for a stationary fence.

Acknowledgments

This work has been supported by the Australian Solar Thermal Research Initiative (ASTRI), through funding provided by the Australian Renewable Energy Agency (ARENA).

References

[1] Bearman, P.W., Vortex shedding from oscillating bluff bodies, *Annual review of fluid mechanics*, **16**, 1984, 195-222.
[2] Engineering Sciences Data Unit, ESDU 85020: Characteristics of Atmospheric Turbulence Near the Ground. Part II: Single Point Data for Strong Winds, 2001.
[3] Flay, R.G.J. & Stevenson, D.C., Integral length scales in strong winds below 20 m, *Journal of Wind Engineering and Industrial Aerodynamics*, **28**, 1988, 21-30.
[4] Greenway, M.E., An analytical approach to wind velocity gust factors, *Journal of Wind Engineering and Industrial Aerodynamics*, **5**, 1979, 61-91.
[5] Holdø, A.E., Houghton, E.L. & Bhinder, F.S., Some effects due to variations in turbulence integral length scales on the pressure distribution on wind-tunnel models of low-rise buildings, *Journal of Wind Engineering and Industrial Aerodynamics*, **10**, 1982, 103-115.
[6] Hutchins, N. & Marusic, I., Evidence of very long meandering features in the logarithmic region of turbulent boundary layers, *Journal of Fluid Mechanics*, **579**, 2007, 1-28.
[7] Kaimal, J.C. & Finnigan, J.J., *Atmospheric Boundary Layer Flows: Their Structure and Measurement*, Oxford University Press, 1994.
[8] Kelso, R.M., A Study of Free Shear Flows Near Rigid Boundaries, Thesis: Doctor of Philosophy in Mechanical Engineering, University of Melbourne, 1991.
[9] Kelso, R.M., Lim, T.T. & Perry, A.E., The effect of forcing on the time-averaged structure of the flow past a surface-mounted bluff plate, *Journal of Wind Engineering and Industrial Aerodynamics*, **49**, 1993, 217-226.
[10] Kiya, M. & Matsumura, M., Incoherent turbulence structure in the near wake of a normal plate, *Journal of Fluid Mechanics*, **190**, 1988, 343-356.
[11] Marusic, I. & Hutchins, N., Study of the log-layer structure in wall turbulence over a very large range of Reynolds number, *Flow, Turbulence and Combustion*, **81**, 2008, 115-130.
[12] Mendis, P., Ngo, T., Haritos, N., Hira, A., Samali, B. & Cheung, J., Wind loading on tall buildings, *EJSE Special Issue: Loading on Structures*, **3**, 2007, 41-54.
[13] Nakamura, Y., Bluff-body aerodynamics and turbulence, *Journal of Wind Engineering and Industrial Aerodynamics*, **49**, 1993, 65-78.
[14] O'Neill, P.L., Nicolaides, D., Honnery, D. & Soria, J., Autocorrelation functions and the determination of integral length with reference to experimental and numerical data, in *15th Australasian Fluid Mechanics Conference*, 2004, 13-17.
[15] Perry, A.E. & Steiner, T.R., Large-scale vortex structures in turbulent wakes behind bluff bodies. Part 1. Vortex formation processes, *Journal of fluid mechanics*, **174**, 1987, 233-270.
[16] Rosi, G.A., Martinuzzi, R.J. & Rival, D.E., A conditional analysis of spanwise vortices within the lower atmospheric log layer, *Journal of Wind Engineering and Industrial Aerodynamics*, **119**, 2013, 89-101.
[17] Sarkar, P.P., Techniques and tools for assessing extreme-wind hazard to structures, in *8th Asia-Pacific Conference on Wind Engineering*, 2013, 131-172.
[18] Swamy, N.V.C., Gowda, B.H.L. & Lakshminath, V.R., Auto-correlation measurements and integral time scales in three-dimensional turbulent boundary layers, *Applied Scientific Research*, **35**, 1979, 237-249.
[19] Watkins, S., Turbulence Characteristics of the Atmospheric Boundary Layer and Possibilities of Replication for Aircraft, in *Joint Symposium of DFG and DLR-Airbus "Third-Symposium-Simulation of Wing and Nacelle Stall"*, 2012, 21-22.
[20] Wygnanski, I., Oster, D., Fiedler, H. & Dziomba, B., On the perseverance of a quasi-two-dimensional eddy-structure in a turbulent mixing layer, *Journal of Fluid Mechanics*, **93**, 1979, 325-335.

Appendix C

Turbulence Characteristics in the ABL

C.1. Section Overview

This appendix reports the variations of turbulence characteristics in a part-depth atmospheric boundary layer (ABL) in a wind tunnel. Two spires with different geometries and four stationary fences spanning the tunnel with different heights were used to generate a range of turbulence characteristics. Mean velocity, longitudinal turbulence intensity and longitudinal integral length scale profiles were measured in the wake of the different passive devices. These turbulent characteristics were analysed and discussed in relation to the field measurements in a low-roughness atmospheric surface layer in Chapter 4 and Appendix A. Spires were found to generate logarithmic velocity profiles and relatively constant turbulence intensity profiles that provided an effective comparison with the field measurements in the ASL and would therefore be suitable for sensitivity studies relevant to wind codes and standards. In contrast, fences generated closely linear velocity profiles and larger turbulence intensities and integral length scales in the lowest 50% of the simulated ABL. Hence, fences were considered to provide a controlled method to generate large eddies of a given longitudinal integral length scale and may be suited to investigate the effect of large vortices on the dynamic wind loads arising from the vortex-blade interactions on wind turbines.

C.2. Experimental Generation of a Part-Depth ABL

Statement of Authorship

Title of Paper	Wind tunnel investigation of turbulence characteristics in the atmospheric surface layer
Publication Status	☑ Published ☐ Accepted for Publication ☐ Submitted for Publication ☐ Unpublished and Unsubmitted work written in manuscript style
Publication Details	Emes, M. J., Arjomandi, M., Ghanadi, F. and Kelso, R. M., 2017, 'Wind tunnel investigation of turbulence characteristics in the atmospheric surface layer', *Wind Energy Science Conference 2017*, Copenhagen, Denmark.

Principal Author

Name of Principal Author (Candidate)	Matthew Emes		
Contribution to the Paper	Performed data analysis and interpretation, wrote manuscript and acted as corresponding author.		
Overall percentage (%)	70		
Certification:	This paper reports on original research I conducted during the period of my Higher Degree by Research candidature and is not subject to any obligations or contractual agreements with a third party that would constrain its inclusion in this thesis. I am the primary author of this paper.		
Signature		Date	3/11/17

Co-Author Contributions

By signing the Statement of Authorship, each author certifies that:

i. the candidate's stated contribution to the publication is accurate (as detailed above);

ii. permission is granted for the candidate in include the publication in the thesis; and

iii. the sum of all co-author contributions is equal to 100% less the candidate's stated contribution.

Name of Co-Author	Maziar Arjomandi		
Contribution to the Paper	Supervised development of work, helped in data interpretation and manuscript evaluation.		
Signature		Date	3/11/17

Name of Co-Author	Farzin Ghanadi		
Contribution to the Paper	Supervised development of work, helped in data interpretation and manuscript evaluation.		
Signature		Date	3/11/17

Name of Co-Author	Richard Kelso		
Contribution to the Paper	Supervised the research and contributed in academic discussion and manuscript review.		
Signature		Date	3/11/17

Wind tunnel investigation of turbulence characteristics in the atmospheric surface layer

M. J. Emes[1], M. Arjomandi, F. Ghanadi and R. M. Kelso

Further understanding of turbulence characteristics in the lowest 100 m of the atmospheric boundary layer (ABL), known as the atmospheric surface layer (ASL), is required for analysis of the dynamic effects of gusts on physical structures such as wind turbines. Galloping and torsional flutter tend to occur at frequencies of the order of 1 Hz, corresponding to the natural frequencies of buildings[1] and large wind turbines[2], when the turbulence length scales are comparable to the size of the structure[3]. Generation of a part-depth ABL in the wind tunnel has previously been achieved using passive devices include spires and fences to generate turbulent mixing through sudden separation of flow around their edges[4]. This experimental study investigates the effect of different-sized spires and fences on turbulence characteristics in the ASL including mean velocity, turbulence intensity and integral length scale profiles. Velocity measurements were obtained using a high-frequency Cobra probe in a closed-return wind tunnel with a freestream turbulence intensity of 1%.

Figure 1 presents the turbulent flow characteristics of the simulated ASL generated using two spires (S) and four fences (F) of different heights compared with SLTEST field measurements by Hutchins et al.[5] in a low-roughness ASL. The mean velocity profiles using S2 most closely represents the lowest 50% of the low-roughness SLTEST ASL, as shown in Figure 1(a). The velocity gradient close to the ground in the lowest 10% of the ASL was not accurately produced using any of the spires or fences, however this could be generated with the addition of surface roughness elements. The longitudinal turbulence intensity profile of S1 closely matches the SLTEST data in Figure 1(b), whereas the fence profiles significantly increase in the lower half of the simulated ASL to greater than 20% with increasing fence height. Thus, it was found that fences provide a wider range of high turbulence conditions, similar to those observed in urban terrains that cannot be simulated using conventional spires. By contrast, spires are limited to turbulence intensities of less than 10% observed in low-roughness terrains. Longitudinal integral length scales in Figure 1(c) were between 20-40% of the surface layer thickness using the two spires and 20-60% using the four fences compared to a range of 20-30% in the SLTEST data. This confirms that spires are the most suitable for representing a low-roughness terrain such as a desert, whereas fences can generate larger vortices and higher turbulence intensities corresponding to the larger mean velocity gradients observed in a high-roughness ASL such as a city. Wind turbines are commonly positioned in open-country terrains with flat grassy plains, hence their structural design can be optimised to withstand high-wind events by using spires or fences in a wind tunnel to generate the turbulence characteristics at a given site.

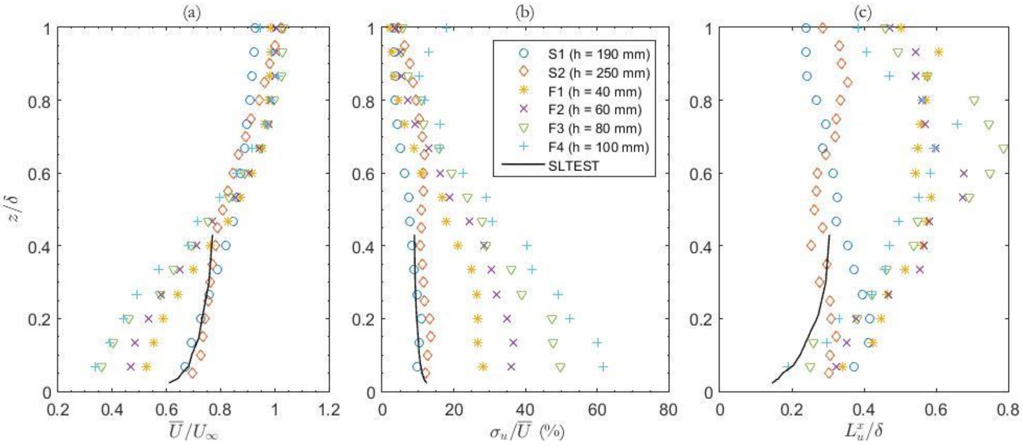

Figure 1: Flow characteristics within surface layer thickness for U_∞ = 10 m/s: (a) Mean streamwise velocity (b) Longitudinal turbulence intensity (c) Longitudinal integral length scales.

---

1 Dep. Mechanical Engineering, University of Adelaide, Adelaide, SA, Australia.

[1] Arakawa and Yamomoto, *Proc. 13th World Conference on Earthquake Eng.*, Vancouver (2004).

[2] van der Tempel et al., *Wind Eng.* **26**, 4 (2002).

[3] Nakamura, *JWEIA* **49**, 1-3 (1993).

[4] Cook, *JWEIA* **3**, 2-3 (1978).

[5] Hutchins et al., *Boundary-Layer Met.* **145**, 2 (2012).

Appendix D

Optimisation of the Size and Cost of Heliostats

D.1. Section Overview

This appendix reports the optimisation of the peak wind load coefficients on a heliostat in stow position from a wind tunnel experiment in a simulated part-depth atmospheric boundary layer (ASL). The effect of the critical scaling parameters of the stowed heliostat were investigated using force measurements on different-sized plates at a range of elevation axis heights. Peak wind load coefficients showed an inverse proportionality with the chord length of the heliostat mirror, so that a halving of the mirror chord length resulted in a doubling of the coefficients. The peak lift and hinge moment coefficients on the stowed heliostat could be reduced by 21% and 23%, respectively, by lowering the elevation axis height of the heliostat mirror by 30% in the simulated ABL. Hence, the peak wind loads on stowed heliostats during high-wind conditions in the ABL are highly sensitive to the critical scaling parameters of the heliostat and should be carefully considered depending on the turbulence characteristics of the site.

D.2. Peak Wind Loads on Stowed Heliostats

Statement of Authorship

Title of Paper	Optimisation of the size and cost of heliostats in a concentrating solar thermal power tower plant
Publication Status	☑ Published ☐ Accepted for Publication ☐ Submitted for Publication ☐ Unpublished and Unsubmitted work written in manuscript style
Publication Details	Emes, M., Ghanadi, F., Arjomandi, M. and Kelso, R., 2017, 'Optimisation of the size and cost of heliostats in a concentrating solar thermal power tower plant', *The European Conference on Sustainability, Energy & the Environment 2017*, Brighton, U.K.

Principal Author

Name of Principal Author (Candidate)	Matthew Emes		
Contribution to the Paper	Carried out wind tunnel experiments, performed data analysis and interpretation, wrote manuscript and acted as corresponding author.		
Overall percentage (%)	70		
Certification:	This paper reports on original research I conducted during the period of my Higher Degree by Research candidature and is not subject to any obligations or contractual agreements with a third party that would constrain its inclusion in this thesis. I am the primary author of this paper.		
Signature		Date	3/11/17

Co-Author Contributions

By signing the Statement of Authorship, each author certifies that:

i. the candidate's stated contribution to the publication is accurate (as detailed above);

ii. permission is granted for the candidate in include the publication in the thesis; and

iii. the sum of all co-author contributions is equal to 100% less the candidate's stated contribution.

Name of Co-Author	Farzin Ghanadi		
Contribution to the Paper	Supervised development of work, helped in data interpretation and manuscript evaluation.		
Signature		Date	03/11/17

Name of Co-Author	Maziar Arjomandi		
Contribution to the Paper	Supervised development of work, helped in data interpretation and manuscript evaluation.		
Signature		Date	3/11/17

Name of Co-Author	Richard Kelso		
Contribution to the Paper	Supervised the research and contributed in academic discussion and manuscript review.		
Signature		Date	3/11/17

Optimisation of the size and cost of heliostats in a concentrating solar thermal power tower plant

Matthew Emes, The University of Adelaide, Australia
Farzin Ghanadi, The University of Adelaide, Australia
Maziar Arjomandi, The University of Adelaide, Australia
Richard Kelso, The University of Adelaide, Australia

The European Conference on Sustainability, Energy & the Environment 2017
Official Conference Proceedings

Abstract

Concentrating solar thermal (CST) power tower (PT) is one of the most promising renewable technologies for large-scale electricity production, however the main limitation of PT systems is their significantly larger levelised cost of electricity (LCOE) relative to base load energy systems. One opportunity to lower the LCOE is to reduce the capital cost of heliostats through optimisation of the size and position of heliostat mirrors to withstand maximum wind loads during high-wind conditions when aligned parallel to the ground in the stow position.

Wind tunnel experiments were carried out to measure the forces on thin flat plates of various sizes at a range of heights in a simulated part-depth atmospheric boundary layer (ABL). Calculated peak wind load coefficients on the stowed heliostat showed an inverse proportionality with the chord length of the heliostat mirror, which suggests that the coefficients could be optimised by increasing the size of the heliostat mirror relative to the sizes of the relevant eddies approaching the heliostat. The peak lift coefficient and peak hinge moment coefficient on the stowed heliostat could be reduced by as much as 23% by lowering the elevation axis height of the heliostat mirror by 30% in the simulated ABL. A significant linear increase of the peak wind load coefficients occurred at longitudinal turbulence intensities greater than 10% in the simulated ABL. Hence, the critical scaling parameters of the heliostat should be carefully considered depending on the turbulence characteristics of the site.

Keywords: heliostat, stow position, turbulence, atmospheric boundary layer

Introduction

Current energy systems, based primarily on the combustion of fossil fuels, are unsustainable in the long term, so that a transition to an environmentally-sustainable energy system with the integration of renewable energy sources is necessary (Hernández-Moro & Martínez-Duart, 2012). Concentrating solar thermal (CST) is one of the most promising renewable technologies capable of large scale electricity production (Hinkley et al., 2013). A CST system operates by focusing direct solar radiation to obtain higher energy densities and thus an improved Carnot efficiency at higher temperatures. Heat collected in the receiver is typically used to heat a working fluid to generate supercritical steam that drives a turbine for electricity generation (IRENA, 2015); although a wide range of alternative power cycles is under development including Brayton and CO_2 power cycles. Parabolic trough systems are the most commercially-deployed CST technology, however power tower (PT) systems have been identified as an emerging concept that can operate at higher concentration ratios and higher working fluid temperatures than parabolic troughs, thus allowing for higher power cycle efficiency (IEA-ETSAP & IRENA, 2013). Although the intermittency of solar irradiation is a practical limitation of CST systems, PT plants can be deployed with thermal energy storage or as a hybrid system with existing fossil fuel power plants for a base-line power supply (Hinkley et al., 2013; Kolb, Ho, Mancini, & Gary, 2011).

The main limitation of PT systems is their significantly larger levelised cost of electricity (LCOE), in the range of 0.15-0.19 USD/kWh in 2015 (IRENA, 2015), compared to base-load energy systems such as fossil fuel power plants in the range of 0.06-0.13 USD/kWh in 2011 (IRENA, 2013). To reduce the LCOE of PT systems there is a need to lower the capital cost of a PT plant, of which the largest cost is the heliostat field, with an estimated contribution of between 40% and 50% (Coventry & Pye, 2014; Hinkley et al., 2013; IRENA, 2015; Kolb et al., 2007). Government-funded initiatives that support the research and development of CST systems to make them competitive with base-load energy rates include the SunShot Initiative by the Department of Energy (DOE) in the USA, with a goal LCOE of 0.06 USD/kWh by 2020 (Kolb et al., 2011), and the Australian Solar Thermal Research Initiative (ASTRI) targeting a LCOE of 0.12 AUD/kWh by 2020. Currently, the total installed cost of a 150 MW PT plant is 5700 USD/kW. Figure 1 shows that the total cost of PT plants is projected to be reduced by 37% to 3600 USD/kW by 2025, compared with a projected 33% reduction in parabolic troughs (IRENA, 2015). The largest reduction of 24% in the cost of the solar field is expected to be achieved through the optimisation of the structural design of heliostats to wind loading. Hence, the aim of this paper is to optimise the size and cost of heliostats to withstand the maximum wind loads during high-wind conditions in the stow position.

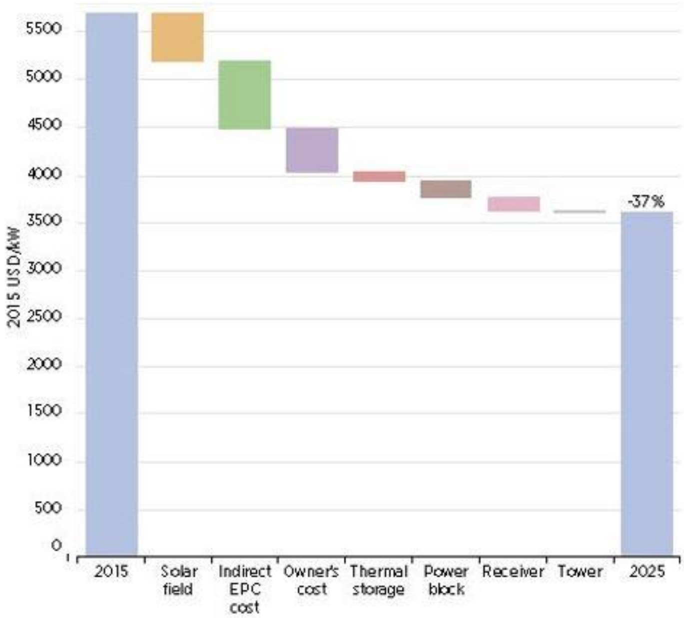

Figure 1: Projected reduction in capital cost (USD/kW) of a 150 MW PT plant from 2015 to 2025 (IRENA, 2015).

Kolb et al. (2007) concluded that the optimum heliostat size for a molten-salt PT plant is between 50 m^2 and 150 m^2, however there is no consensus on the optimal size of a heliostat mirror. This is because the optimum heliostat size is dependent on many factors associated with the production volume and manufacturing processes, ease of access to the electricity network in the region and the terrain type and wind conditions at the site. Therefore, further understanding of the relationships between the heliostat cost and the wind loading on heliostats needs to be developed. One opportunity to lower the heliostat cost is through optimisation of the size and position of heliostat mirrors to withstand maximum wind loads during high-wind conditions. Heliostats are aligned parallel to the ground in the stow position during periods of high wind speeds to minimise the frontal area and the large drag forces that the heliostat are exposed to in operating positions, however stowed heliostats must withstand maximum lift forces and hinge moments due to the effects of vortex structures embedded within the turbulence in the atmospheric boundary layer. The motor drives, support structure and mirror must all withstand any forces and moments, applied to the heliostat from the wind. These wind-sensitive structural components account for up to 80% of the heliostat capital cost according to research by Kolb et al. (2011). A cost analysis of quasi-static wind loads on individual heliostat components by Emes, Arjomandi, and Nathan (2015) found that the sensitivity of the total heliostat cost to the stow design wind speed increased by 34% for an increase in mean wind speed from 10 m/s to 15 m/s. Following the linear cost-load proportionality developed by McMaster Carr, a 40% reduction in the peak hinge moment on the elevation drive of a conventional heliostat can lead to a 24% saving in the representative gear reducer cost (Lovegrove & Stein, 2012). Hence, this paper investigates the effect of the critical scaling parameters of the heliostat on the peak wind loads in stow position.

Methodology

Experimental measurements were taken in a closed-return wind tunnel at the University of Adelaide. Figure 2 shows the test section of the tunnel with a development length of 17 m and a cross-section expanding to 3 m × 3 m to allow for a pressure gradient resulting from growth of the boundary layer. The tunnel can be operated at speeds of up to 20 m/s with a low level of turbulence intensity, ranging between 1% and 3%. Accurate representation of a part-depth ABL in the wind tunnel is required to replicate similar turbulence properties that heliostats are exposed to in the lower surface layer of the ABL, including a logarithmic mean velocity profile. It is generally accepted that the most effective wind tunnel simulation of the ABL is obtained when a flow passes over a rough surface producing a natural-growth boundary layer (De Bortoli, Natalini, Paluch, & Natalini, 2002). The most commonly-used passive devices include spires to generate turbulent mixing through separation of flow around their edges, fence barriers to increase the height of the boundary layer and floor roughness to develop the velocity deficit near the ground (Cook, 1978; Counihan, 1973). Two different triangular spire designs and timber roughness blocks are shown in Table 1. These dimensions were derived following a theoretical design method outlined by Irwin (1981) such that the height h, base width b and depth d of the spires could be determined based on the desired power law profile with exponent α of 0.2 and boundary layer thickness δ of 1.2 m. Velocity measurements for the two configurations of spire and roughness in Table 1 were taken at different height using a multi-hole pressure probe and a traverse. The operating conditions of the tunnel were a freestream velocity $U_\infty = 11$ m/s and Reynolds number $Re_\infty = U_\infty \delta / \nu = 8.8 \times 10^5$.

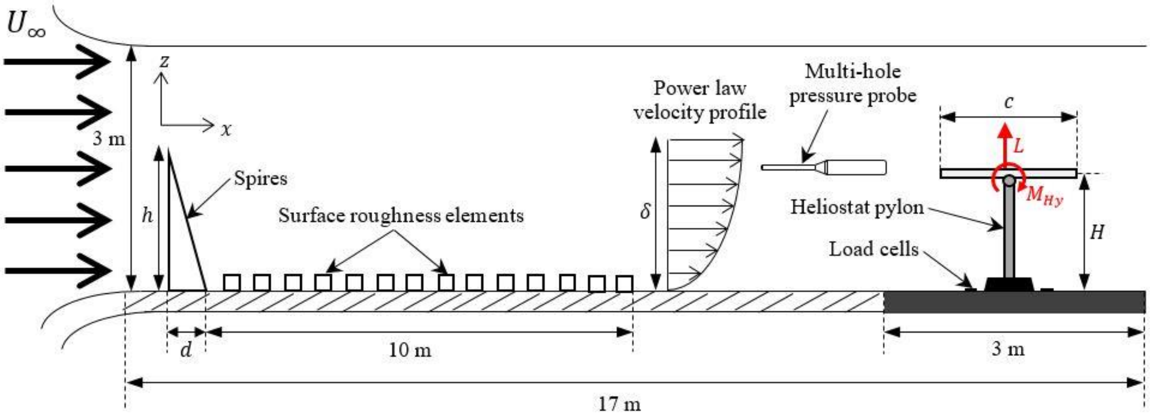

Figure 2: Schematic of the experimental setup for generation of the ABL in the wind tunnel and force measurements on the heliostat model.

Configuration	Spire height **h** (m)	Spire base width **b** (m)	Spire depth **D** (m)	Roughness width **R_b** (m)	Roughness height **R_h** (m)
SR1	1.3	0.155	0.34	0.09	0.045
SR2	1.4	0.2	0.74	0.09	0.045

Table 1: Dimensions and characteristics of spires and roughness elements

Figure 3(a) and (b) show the mean velocity and turbulence intensity profiles, respectively, of the two spire and roughness configurations in Table 1. The mean velocity profiles generated by SR1 are within a maximum error of ±5% of a power law ($\alpha = 0.18$) velocity profile. The turbulence intensities generated by SR1 are within ±2% of ESDU 85020 (1985) data for a neutral ABL with a mean wind speed of 10 m/s at a 10 m height, surface roughness height $z_0 = 0.002$ m and boundary layer thickness $\delta = 350$ m. In contrast, the mean velocity profile generated by SR2 is close to linear in the part-depth simulated ABL and generated turbulence intensities above 10%. Hence, the two spire and roughness configurations, SR1 and SR2, can be used to investigate the effect of turbulence intensity on the peak wind loads on the heliostat mirror that was stowed at a range of heights ($0.3 < z/\delta < 0.5$) indicated by the shaded region in Figure 3.

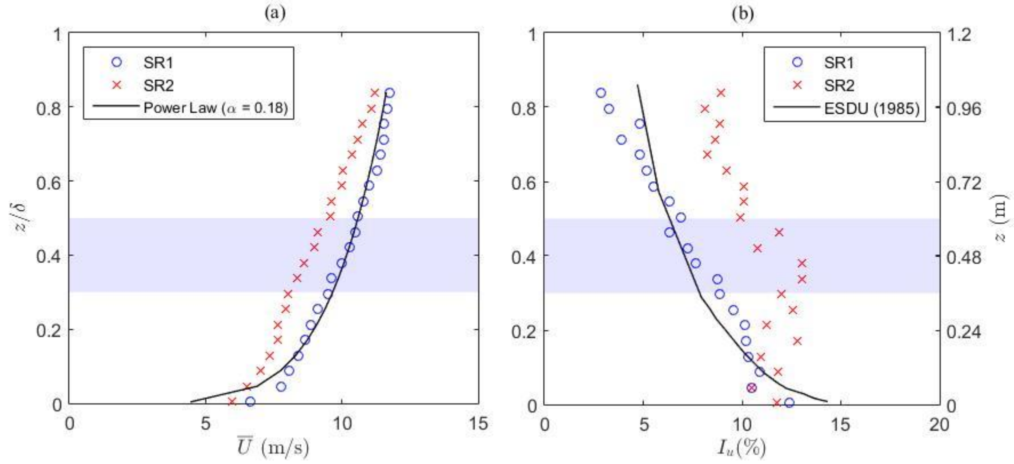

Figure 3: (a) Mean velocity profiles of the two spire configurations compared with the power law profile of a low-roughness terrain; (b) Longitudinal turbulence intensity profiles compared with the ESDU (1985) profile of a low-roughness terrain. The shaded area indicates the heights at which the heliostat mirror was stowed.

Force measurements on the model heliostat were taken using four three-axis load cells, mounted on a rotary turntable in Figure 2. Each load cell has a capacity of 500 N with a sampling frequency of 1 kHz in all three axes and an accuracy of ±0.5% of full scale. The heliostat was modelled as a thin flat plate in the absence of a support structure. A series of six square aluminium plates with 3 mm thickness and chord length (c) ranging from 300 mm to 800 mm were manufactured and mounted on a common pylon with a telescopic design to allow the elevation axis height H of the plate to vary between 0.35 m and 0.6 m. The peak lift force on the plate (L in Figure 2) was determined from the difference between the measured lift forces on the heliostat (plate mounted to pylon) and those on the heliostat pylon in the absence of a mounted plate. The peak hinge moments on the plate (M_{Hy} in Figure 2) were calculated from the product of the peak lift force on the plate and the longitudinal distance from the centre of pressure to the centre of the plate. The peak lift coefficient and peak hinge moment coefficients on the plate were calculated following Peterka and Derickson (1992) as:

$$c_L = \frac{L}{1/2\rho\bar{U}^2 A} \quad (1)$$

$$c_{M_{Hy}} = \frac{M_{Hy}}{1/2\rho\bar{U}^2 Ac} \quad (2)$$

Here ρ (kg/m^3) is the density of air, $\bar{U}$ (m/s) is the mean wind speed at the heliostat elevation axis height H, $A = c^2$ (m^2) is the heliostat mirror area and c is the heliostat chord length.

Results

Figure 4 shows the effect of the heliostat chord length on the peak wind load coefficients on a heliostat in stow position exposed to SR1 and SR2. The peak lift coefficients for SR2 in Figure 4(a) and the peak hinge moment coefficients in Figure 4(b) are approximately double those for SR1. Both the peak lift and peak hinge moment coefficients increase by approximately double as the chord length is halved from 0.8 m to 0.4 m. This indicates that there is an inverse proportionality between the wind load coefficients and the chord length of the heliostat mirror.

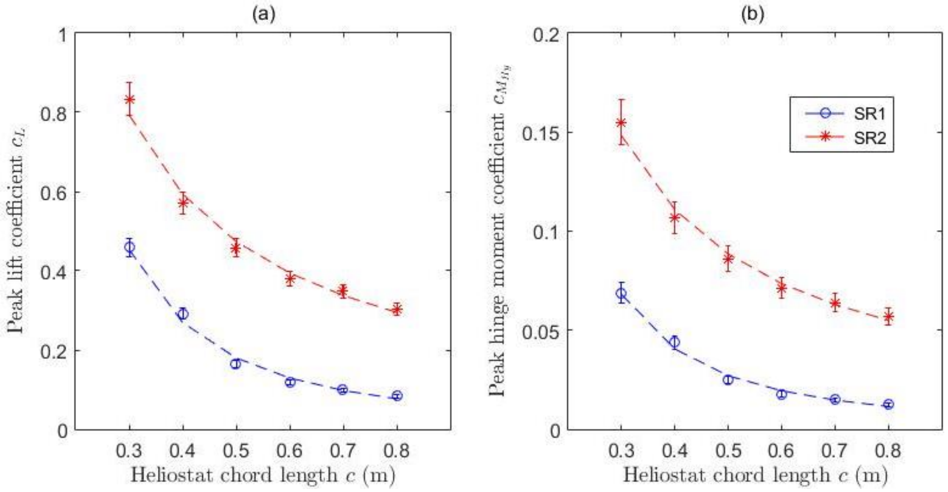

Figure 4: Effect of the heliostat chord length for SR1 and SR2 on (a) peak lift coefficient; (b) peak hinge moment coefficient on a stowed heliostat.

Figure 5 shows the effect of the elevation axis height on the peak wind load coefficients on stowed heliostats of two different chord lengths exposed to SR1. Both the peak lift coefficients in Figure 5(a) and the peak hinge moment coefficients in Figure 5(b) increase linearly with the elevation axis height of the heliostat. Hence, the peak wind load coefficients can be reduced by 21% and 23% for chord lengths of 0.5 m and 0.8 m, respectively, by lowering the elevation axis height of the heliostat by 30%.

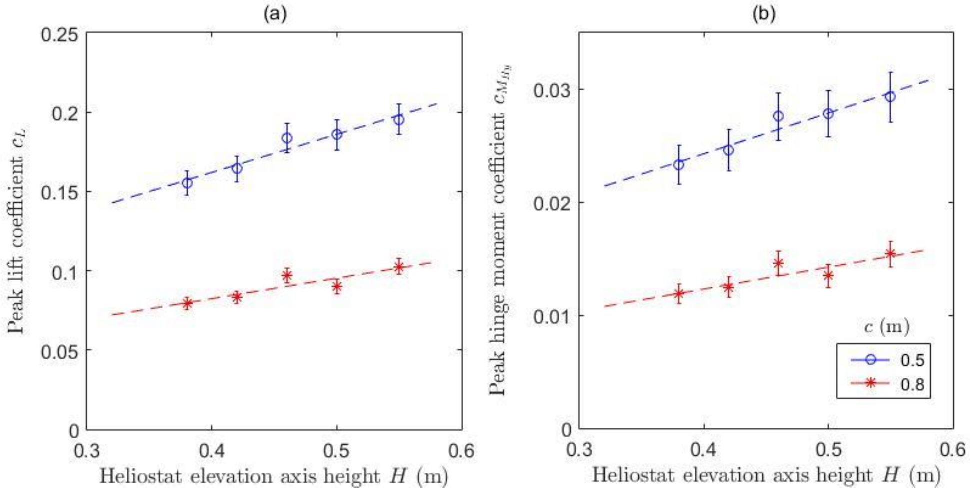

Figure 5: Effect of the heliostat elevation axis height for SR1 on (a) peak lift coefficient; (b) peak hinge moment coefficient on a stowed heliostat.

Figure 6 shows the effect of the outer diameter and thickness of the heliostat pylon for a heliostat mirror with chord length of 0.8 m stowed at different elevation axis heights and exposed to SR1. Both the peak lift coefficient (Figure 6(a)) and the peak hinge moment coefficient (Figure 6(b)) can be reduced by approximately 10% by increasing the outer diameter of the pylon from 33 mm to 42 mm and increasing the thickness of the pylon from 5 mm to 6 mm.

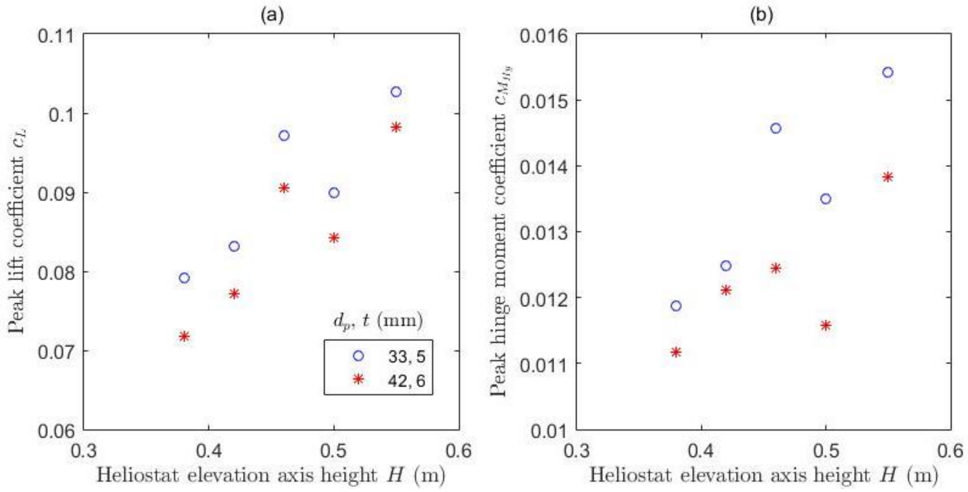

Figure 6: Effect of the heliostat pylon diameter on (a) peak lift coefficient; (b) peak hinge moment coefficient on a stowed heliostat with a chord length of 0.8 m.

Figure 7 shows the effect of longitudinal turbulence intensity on the peak wind load coefficients for comparison with the coefficients reported by Pfahl et al. (2015) at a turbulence intensity of 13%. At a similar turbulence intensity of 12.5%, the peak lift coefficient (Figure 7(a)) and peak hinge moment coefficient (Figure 7(b)) on the heliostat with chord length of 0.5 m in the current study were 13% and 23% lower, respectively than those measured by Pfahl et al. (2015). The pronounced linear increase of the peak wind load coefficients on stowed heliostats at turbulence intensities larger than 10% in the current study is in agreement with a similar finding by Peterka, Tan, Cermak, and Bienkiewicz (1989) for the peak drag and lift coefficients on heliostats in operating positions.

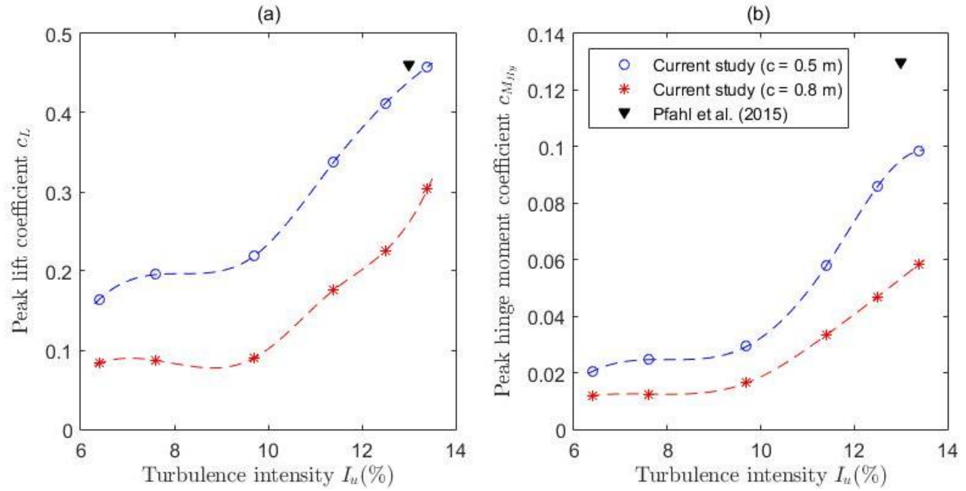

Figure 7: Effect of longitudinal turbulence intensity on (a) peak lift coefficient; (b) peak hinge moment coefficient on a stowed heliostat.

Conclusions

The effect of the critical scaling parameters of a heliostat on the peak lift coefficient and peak hinge moment coefficient on a stowed heliostat was investigated using force measurements on different-sized plates at a range of elevation axis heights. Peak wind load coefficients showed an inverse proportionality with the chord length of the heliostat mirror, so that a halving of the mirror chord length resulted in a doubling of the coefficients. This suggests that the coefficients can be optimised by increasing the size of the heliostat mirror relative to the sizes of the relevant eddies approaching the heliostat. The peak lift coefficient and peak hinge moment coefficient on the stowed heliostat could be reduced by 21% and 23%, respectively, by lowering the elevation axis height of the heliostat mirror by 30% in the simulated ABL. In comparison, the peak wind load coefficients were reduced by less than 10% with an increase in the outer diameter and thickness of the heliostat pylon. A significant linear increase of the peak wind load coefficients occurred at longitudinal turbulence intensities greater than 10% in the simulated ABL. Hence, the peak wind loads on stowed heliostats during high-wind conditions in the ABL are highly sensitive to the critical scaling parameters of the heliostat and should be carefully considered depending on the turbulence characteristics of the site. Optimisation of the ultimate design wind loads can lead to cost reductions in the manufacturing of heliostats from lower strength and lighter materials.

Acknowledgements

Support for the work has been provided by the Australian Government Research Training Program Scholarship and by the Australian Solar Thermal Research Initiative (ASTRI) through funding provided by the Australian Renewable Energy Agency (ARENA).

References

Cook, N. J. (1978). Determination of the model scale factor in wind-tunnel simulations of the adiabatic atmospheric boundary layer. *Journal of Wind Engineering and Industrial Aerodynamics,* 2(4), 311-321.

Counihan, J. (1973). Simulation of an adiabatic urban boundary layer in a wind tunnel. *Atmospheric Environment,* 7(7), 673-689.

Coventry, J., & Pye, J. (2014). Heliostat cost reduction–where to now? *Energy Procedia,* 49, 60-70.

De Bortoli, M., Natalini, B., Paluch, M., & Natalini, M. (2002). Part-depth wind tunnel simulations of the atmospheric boundary layer. *Journal of Wind Engineering and Industrial Aerodynamics,* 90(4), 281-291.

Emes, M. J., Arjomandi, M., & Nathan, G. J. (2015). Effect of heliostat design wind speed on the levelised cost of electricity from concentrating solar thermal power tower plants. *Solar Energy,* 115, 441-451.

Hernández-Moro, J., & Martínez-Duart, J. M. (2012). CSP electricity cost evolution and grid parities based on the IEA roadmaps. *Energy Policy,* 41, 184-192.

Hinkley, J. T., Hayward, J. A., Curtin, B., Wonhas, A., Boyd, R., Grima, C., . . . Naicker, K. (2013). An analysis of the costs and opportunities for concentrating solar power in Australia. *Renewable Energy,* 57, 653-661.

IEA-ETSAP, & IRENA. (2013). *Concentrating Solar Power Technology Brief.*

IRENA. (2013). Renewable Power Generation Costs in 2012: An Overview. *Bonn, Germany.*

IRENA. (2015). The Power to Change: Solar and Wind Cost Reduction Potential to 2025. *Bonn, Germany.*

Irwin, H. (1981). The design of spires for wind simulation. *Journal of Wind Engineering and Industrial Aerodynamics,* 7(3), 361-366.

Kolb, G. J., Ho, C. K., Mancini, T. R., & Gary, J. A. (2011). *Power Tower Technology Roadmap and Cost Reduction Plan* (SAND2011-2419). Albuquerque, USA.

Kolb, G. J., Jones, S. A., Donnelly, M. W., Gorman, D., Thomas, R., Davenport, R., & Lumia, R. (2007). *Heliostat Cost Reduction Study* (SAND2007-3293). Albuquerque, USA.

Lovegrove, K., & Stein, W. (2012). *Concentrating solar power technology: principles, developments and applications*. Cambridge, UK: Woodhead Publishing Limited.

Peterka, J. A., & Derickson, R. G. (1992). *Wind load design methods for ground-based heliostats and parabolic dish collectors* (SAND92-7009). Albuquerque, USA.

Peterka, J. A., Tan, Z., Cermak, J. E., & Bienkiewicz, B. (1989). Mean and peak wind loads on heliostats. *Journal of Solar Energy Engineering,* 111(2), 158-164.

Pfahl, A., Randt, M., Meier, F., Zaschke, M., Geurts, C., & Buselmeier, M. (2015). A holistic approach for low cost heliostat fields. *Energy Procedia*, 69, 178-187.

Contact email: matthew.emes@adelaide.edu.au